Capturing Gravitational Waves in a World of Noise

Tapia San Martín, E.N.

Publication date
2024
Document Version
Final published version

Capturing Gravitational Waves in a World of Noise

Enzo Nicolás Tapia San Martín

Gravitational Waves
Nikhef
Universiteit van Amsterdam

Capturing Gravitational Waves in a World of Noise

ACADEMISCH PROEFSCHRIFT

ter verkrijging van de graad van doctor
aan de Universiteit van Amsterdam
op gezag van de Rector Magnificus
prof. dr. ir. P.P.C.C. Verbeek

ten overstaan van een door het College voor Promoties
ingestelde commissie, in het openbaar
te verdedigen in de Agnietenkapel
op maandag 25 november 2024, te 10.00 uur

door Enzo Nicolás Tapia San Martín
geboren te Almendral, Valparaíso

Promotor:

Prof. dr. F.L. Linde	Universiteit van Amsterdam

Copromotor:

Dr. M. Tacca	NWO-I Nikhef

Beoordelingscommissie:

Prof. dr. A.P. Colijn	Universiteit van Amsterdam
Prof. dr. M.P. Decowski	Universiteit van Amsterdam
Prof. dr. S.C.M. Bentvelsen	Universiteit van Amsterdam
Dr. S.M. Nissanke	Universiteit van Amsterdam
Prof. dr. A. Freise	Vrije Universiteit Amsterdam
Dr. B.L. Swinkels	NWO-I Nikhef
Dr. H. Heitmann	Artemis, Nice

Printed by Gildeprint
ISBN: 978-94-6496-255-0

Faculteit der Natuurwetenschappen, Wiskunde en Informatica

Acknowledgements

As I approach the end of this long journey in gravitational wave research, I reflect on the many people who have supported and inspired me along the way. This thesis is the result of nearly five years of hard work, but it would not have been possible without the encouragement, wisdom and friendship of many remarkable individuals.

My journey began in Japan, where I took my first steps as an engineer. I owe deep gratitude to Mark, Fabian, Hirata-san and all my colleagues at NAOJ/KAGRA who nurtured my early passion for science and engineering. It was an incredible foundation and I will always cherish the friendships I made during that time.

Moving to the Netherlands opened a new chapter in my career. The gravitational wave community here welcomed me with open arms. I am deeply grateful to Matteo and Frank for their constant guidance, support and incredible patience. You both deserve extra credit for keeping me focused on the tasks, especially when my curiosity led me down paths far outside my research! Thanks for reeling me back in. To all my colleagues at Nikhef, especially Bas and Alessandro, thank you for the countless discussions, for answering my never-ending questions and for pushing me to grow as a scientist. I'm also thankful to my treasured friends Yuefan, Manuel and Shi for sharing this journey with me. You made me feel at home, and together we navigated the highs and lows of this intense journey.

My time in Amsterdam has been incredibly enriched by the wonderful community of friends I've found here. Thank you to my amazing Latin friends who made Amsterdam one of the most vibrant and fun places to live. I also want to give a special shout-out to my capoeira friends in Amsterdam. Capoeira has been my escape after long office days, allowing me to unwind, stay active and practice a sport I am passionate about.

Italy became a significant part of my life as I pursued my PhD. I am grateful

to my colleagues at Virgo, especially Julia, Diego and Maddalena, for their support both in the control room and for their patience to explain the Virgo machine. I'd also like to mention my dear friend Matthieu for making Pisa one of the most exciting places to live in.

To my family in Chile, even though we have been separated by distance, you have always been close in my heart. Thank you for your endless love and encouragement. I have missed you all dearly and your presence in my life has been a constant reminder of where I come from. To my mom, Pamela, words cannot truly capture how thankful I am for everything you've done for me. You have been my constant source of strength, love and encouragement. From the very beginning, you believed in me even when I doubted myself.

To my friends in Chile thank you for sharing in this adventure with me. Although I couldn't see many of you as often as I would have liked, our shared memories and experiences have carried me through. Your friendship means the world to me.

Finally, I must save my most profound gratitude for my wife, Giselle. You have been with me since the beginning, through every step of this incredible journey. Your tenacious love, patience and belief in me have given me the strength to keep going, even in the most challenging moments. This thesis would not exist without you. You are my greatest supporter, my partner and my best friend. I am eternally grateful for everything you have done and I look forward to every future adventure we will share.

Contents

Introduction

The detection of gravitational waves has started a new era in astronomy, providing a new way to observe and understand some of the most violent and energetic events in the Universe. These waves, predicted by Einstein's theory of general relativity, are ripples in the fabric of spacetime and can be caused by massive celestial events such as black hole mergers and neutron star collisions. The detection and analysis of gravitational waves require extremely sensitive instruments capable of distinguishing these faint signals from background noise. The sensitivity of these detectors is defined by fundamental noises, but ultimately limited by technical noises. This thesis focuses on the study of technical noises in current ground-based detectors to reduce them, with particular emphasis on the Advanced Virgo Plus detector, and on the preliminary study to cope with fundamental noises in future gravitational-wave detectors. Interferometric gravitational-wave detectors employ optical cavities within their design. These cavities are crucial components where laser light is bounced back and forth between highly reflective mirrors. Maintaining these cavities at the precise operating point is essential to achieve the desired performance. Consequently, all longitudinal and angular degrees of freedom must be carefully controlled. This presents the challenge of managing a system with multiple inputs and outputs.

This work describes the control of the main longitudinal degrees of freedom of the Advanced Virgo Plus interferometer using a Multiple-Input Multiple-Output (MIMO) approach, which allows also the define the cross-couplings among them. The aim is to employ this approach for system identification and for designing filters that mitigate noise re-injection caused by cross-couplings. Using this MIMO model of the detector as a core, we develop a frequency domain noise budget that can dynamically monitor the interferometer status and help to mitigate technical noises. Additionally, other essential systems of the detector are analyzed, highlighting the necessity of applying a MIMO

approach across various interferometer components. The study also explores an experimental setup to evaluate materials for the coatings of the mirrors for future gravitational-wave detectors like the Einstein Telescope.

The first chapter, *"Foundation of gravitational radiation"*, sets the stage by introducing the fundamental principles behind the gravitational-wave propagation. It starts with a short review of general relativity and focuses on how gravitational waves are predicted as solutions of the Einstein field equations. The properties of these waves, including their speed, polarization, and interaction with matter, are explored. This chapter also delves into the history of gravitational-wave detection, highlighting major milestones such as the first detection done by Advanced LIGO and subsequent observations by Advanced Virgo. The implications of these discoveries for astronomy and cosmology are briefly discussed, illustrating how gravitational-wave detection has become a pivotal field in astrophysics and how the era of multi-messenger astronomy begun.

In the second chapter, *"Gravitational-wave detectors"*, the focus shifts to the technological aspects of gravitational-wave detectors. The response of interferometric detectors to the passage of gravitational waves are explained in detail. This chapter includes a discussion on the basic operational principles of laser interferometry. Furthermore, the specific sources of noise that impact the sensitivity of the detectors are addressed, such as seismic activity, thermal noise, and quantum fluctuations. Moreover, sources of technical noises are described. These noises pose limits and challenges during the commissioning and operation of these detectors. Understanding these noise sources is crucial for developing effective strategies to mitigate their effects, which is critical for increasing the reliability and accuracy of gravitational-wave detection.

Chapter three, *"A MIMO approach for longitudinal sensing and control noise projections of Advanced Virgo gravitational-wave detector"*, introduces a MIMO model based on simulations to study cross-couplings among the various degrees of freedom and to design de-coupling filters to enhance the sensitivity of the Advanced Virgo Plus detector. This chapter explains the theoretical foundation of the description of MIMO systems in the frequency domain and their adaptation for the main longitudinal degrees of freedom of the Advanced Virgo Plus detector. It discusses how these systems can effectively manage and mitigate cross-couplings and other complex noise sources within the detector setup.

In Chapter four, *"Longitudinal cross-couplings in Advanced Virgo Plus"*, the

practical implementation of these decoupling filters in the Advanced Virgo Plus detector is explored, including the challenges faced and the solutions developed. The benefits of implementing MIMO control systems, such as improved noise handling and enhanced detection capabilities, are evaluated, demonstrating their significant impact on the operational efficiency of the detector.

Chapter five, *"Frequency domain noise budget tool for Advanced Virgo Plus"*, delves into the development and application of a frequency domain noise budget tool for the Advanced Virgo Plus detector. This chapter underscores the critical importance of accurately identifying and quantifying various noise sources to enhance the detector's sensitivity and reliability. The noise budget tool serves as a comprehensive framework for mapping out all significant noise contributions, allowing researchers to isolate true gravitational-wave signals from background disturbances. This chapter begins with a detailed explanation of how gravitational-wave detectors employ noise budgets to maintain and improve their performance. Then, it focuses on the implementation of a "real-time" noise budget tool, designed to offer dynamic monitoring and analysis capabilities. By integrating various noise sources and employing advanced modeling techniques, this tool aims to provide a robust and user-friendly platform for ongoing noise management and mitigation efforts in gravitational-wave detection.

In Chapter six, *"A MIMO system identification approach for the longitudinal control of the Filter Cavity of the Advanced Virgo Gravitational-wave Detector"*, the focus shifts to a specific case of a MIMO system. The chapter starts with a description of the principles of frequency dependent squeezing and details the operational principles of the filter cavity system, illustrating how it manipulates squeezed states of light to reduce the broadband quantum noise of the detector. The control of the filter cavity of Advanced Virgo Plus exhibits strong cross-couplings. This chapter examines the application of system identification techniques to understand and optimize the filter cavity's performance. The chapter elucidates the transition from a Single-Input Single-Output (SISO) to a MIMO system identification method, highlighting the superiority of the second one in capturing the intricate dynamics of the system and ensuring robust control.

Chapter seven, *"Toward direct measurement of Coating Thermal Noise for Future Gravitational-wave Detectors"*, introduces the preliminary experimental setup designed to directly measure the thermal noise of the coatings for future gravitational-wave detectors at cryogenic temperature. This chapter

outlines the working principle of the optical setup. It provides a comprehensive look at the experimental setup, highlighting the challenges that could be encountered along the way. The chapter also discusses the implications of these measurements for future detector designs and the potential for incorporating new materials and technologies to further reduce thermal noise. By directly addressing this fundamental noise source, the research contributes to broader efforts to enhance the detector sensitivity, paving the way for more precise and reliable gravitational-wave detection in future observatories.

Chapter 1

Foundation of gravitational radiation

February 2016, the Advanced Laser Interferometer Gravitational-wave Observatory (aLIGO) [1] announced the first direct observation of a gravitational-wave (GW) signal [2]. This observation took place nearly 100 years after Einstein's General Relativity (GR) theory [3], which predicted these waves. This first directly detected GW signal, referred to as GW150914, was traced back to the coalescence of two black holes occurring about 1.3 billion years ago. Thus, this observation unveiled an entire new frontier for the field of physics.
In 2017 both Advanced LIGO and Advanced Virgo [4] observed the first GW signal originated from a binary neutron star (BNS) coalescence, GW170817 [5]. Light from this event was observed as well by several telescopes worldwide. Moreover the Fermi Gamma-ray Space Telescope [6] and the INTErnational Gamma-Ray Astrophysics Laboratory (INTEGRAL) [7] detected the gamma-ray burst originated from this merger [8]. GW170817 signal is the keystone that marked the start of the era of the multi-messenger astronomy. The first part of this chapter briefly describes the derivation of GWs from GR. Then, typical sources of GWs will be introduced to finally describe the main events that started the era of the multi-messenger astronomy.

1.1 Summary of General Relativity

1.1.1 Introduction

The laws of motion and gravitation described in Newton's Principia [9] have been accepted for centuries and used for theories of mechanics and gravity. In these laws, gravity has been considered as static and described as a pulling force

between objects with mass. This states that an object with a mass M_1 would exert a force $\vec{F_{12}}$ on another object with mass M_2 at a distance $\vec{r}_{12} = \vec{r}_1 - \vec{r}_2$. This gravitational force is defined as:

$$\vec{F_{12}} = G\frac{M_1 M_2}{|\vec{r}_{12}|^2}\hat{r}_{12}, \tag{1.1}$$

where $\hat{r}_{12}$ is the unit vector from object two to object one and G is the universal gravitational constant. This description of gravity is sufficiently precise for numerous practical applications, hence is extensively used for instance in science classes, structural and aerospace engineering. However, it lacks an explanation on the origin of the gravitational force and assumes instantaneous actions at any distance.

In the last century, this understanding was altered by Einstein's theory of General Relativity (GR), a generalization of the theory of Special Relativity (SR) [10], which describes gravity as a consequence of curved space-time in presence of mass [3]. In both SR and GR, for any frame of reference, the speed of light remains constant for all observers and space-time is described as a four-dimensional framework, which is the integration of the traditional three-dimensional spatial coordinates with time as the fourth dimension. As a result, space and time are relative to the observers conducting their measurements. Additionally, in SR, the laws of physics are covariant when applied in flat space-time, within non-accelerated frames of reference. In GR, Einstein introduces the notion of covariance also for accelerated frames. In this context, the gravitational attraction between masses is a consequence of the curvature of space-time, and this curvature emerges due to the presence of mass. For this four-dimensional coordinate system, one can define a measure of the distance between two points:

$$ds^2 = -(cdt)^2 + dx^2 + dy^2 + dz^2, \tag{1.2}$$

where c is the speed of light. This four-dimensional manifold allows to describe the curvature of space-time by the use of the metric $g_{\mu\nu}$ tensor, where the indices $(\mu, \nu) \in \{0, 1, 2, 3\}$ refer to the space-time coordinates ($x^0 = ct, x^1 = x, x^2 = y, x^3 = z$). The same rule applies to other subscripts and superscripts mentioned in this chapter.

A sign convention given by $(-, +, +, +)$ is used for the metric tensor. For example, in Cartesian coordinates, the Minkowski metric tensor $\eta_{\mu\nu}$ is given by $\eta_{\mu\nu} = diag(-1, 1, 1, 1)$, where the speed of light c is set to unity. Subsequently,

using the Einstein summation convention, where an index appearing both as sub- and superscript in a single term implies summation over all its possible values, the distance ds between two points can be rewritten as:

$$ds^2 = \eta_{\mu\nu} dx^\mu dx^\nu. \tag{1.3}$$

In SR, space is typically treated as Euclidean. As a result, free falling objects follow straight paths. On the other hand, in GR, in the four-dimensional curved space-time, free falling objects move along geodesics. A geodesic is the shortest path between two points in space-time. To derive the geodesics equation, we have to introduce the four-position vector $\vec{S} = (ct, x, y, z)$ and the path parameter λ of the manifold. Assuming that free falling objects are not accelerated along straight lines, the second derivative of the four-position vector $\vec{S}$ satisfies the following condition:

$$\frac{\partial^2 \vec{S}}{\partial \lambda^2} = \vec{0}. \tag{1.4}$$

Thus, it follows that the general geodesics equation for any coordinate system is given by:

$$0 = \frac{d^2 x^\sigma}{d\lambda^2} + \Gamma^\sigma_{\mu\nu} \frac{dx^\mu}{d\lambda} \frac{dx^\nu}{d\lambda}, \tag{1.5}$$

where σ is another tensor index and $\Gamma^\sigma_{\mu\nu}$ are the Christoffel symbols or connection coefficients. These coefficients describe how the basis vectors change in a curved space-time. To simplify the notation, using the metric tensor and rewriting the partial derivatives with respect to a space-time variable as $\frac{\partial}{\partial x^\mu} = \partial_\mu$, the connection coefficients become:

$$\Gamma^\sigma_{\mu\nu} = \frac{1}{2} g^{\sigma\rho} \left(\partial_\nu g_{\mu\rho} + \partial_\mu g_{\nu\rho} - \partial_\rho g_{\mu\nu} \right), \tag{1.6}$$

where ρ is another tensor index and $g^{\mu\nu}$ is the inverse of the metric tensor $g_{\mu\nu}$. Such that $g^{\mu\rho} g_{\rho\nu} = \delta^\mu_\nu$, with δ^μ_ν being the Kronecker delta.

The measure of the curvature of space-time can be described using the Riemann curvature tensor:

$$R^\rho_{\sigma\mu\nu} = \partial_\mu(\Gamma^\rho_{\nu\sigma}) - \partial_\nu(\Gamma^\rho_{\mu\sigma}) + \Gamma^\rho_{\mu\alpha}\Gamma^\alpha_{\nu\sigma} - \Gamma^\rho_{\nu\alpha}\Gamma^\alpha_{\mu\sigma}, \tag{1.7}$$

where α is another tensor index. The Ricci curvature tensor $R_{\sigma\nu}$ is the contraction of the Riemann tensor $R^\rho_{\sigma\mu\nu}$, meaning that $R_{\sigma\nu} = R^\mu_{\sigma\mu\nu}$, and gives

information about volume changes along geodesics. Next, the contraction of the remaining two indices in the Ricci tensor gives the Ricci scalar, which compares the area of a circumference in curved space-time as it travels along geodesics with the area of a circumference in flat space-time, and is defined as:

$$R = g^{\mu\nu} R_{\mu\nu}. \tag{1.8}$$

From this point, as defined in GR, the curvature of space-time is encoded in the Einstein tensor $G_{\mu\nu}$, and defined by the Einstein field equations, as:

$$G_{\mu\nu} := R_{\mu\nu} - \frac{1}{2} g_{\mu\nu} R = \frac{8\pi G}{c^4} T_{\mu\nu}, \tag{1.9}$$

where $T_{\mu\nu}$ represents the energy-momentum tensor of matter, which describes the energy and momentum of a given region in space-time. Essentially, this means that energy and momentum cause curvature in space-time. The Einstein field equations consist of ten coupled differential equations, and not sixteen since $T_{\mu\nu}$ and $G_{\mu\nu}$ are symmetric. These equations are non-linear but, since they have a well-defined initial-value structure, then $g_{\mu\nu}$ can be determined from given initial data. However, there exist four arbitrary degrees of freedom related to the choice of coordinates. Therefore, to determine all ten equations from initial data is not possible, since it will depend on the selection of coordinates. Thus, the Einstein equations reduce to finally six independent differential equations for six components within the metric tensor $g_{\mu\nu}$.

1.1.2 Weak-field Einstein equations

In the absence of mass and, therefore, a gravitational field, space-time is flat. An analytical solution of the Einstein field equations can be obtained only under specific cases, such as in flat space Minkowski metric. In this context, for a weak gravitational field and for nearly Lorentz coordinates, the metric for a slightly curved space-time can be expressed as:

$$g_{\mu\nu} = \eta_{\mu\nu} + h_{\mu\nu}, \tag{1.10}$$

where $\eta_{\mu\nu}$ is the Minkowski metric tensor of flat space-time and $|h_{\mu\nu}| \ll 1$ is a small perturbation, which is a first order linear correction of the metric. Other conditions that hold for the $h_{\mu\nu}$ are $h_{\sigma\rho} h_{\mu\nu} \approx 0$, $|\partial_\rho h_{\mu\nu}| \ll 1$, $(\partial_\sigma h_{\alpha\beta})(\partial_\rho h_{\mu\nu}) \approx 0$ and $h_{\alpha\beta}(\partial_\rho h_{\mu\nu}) \approx 0$. With these assumptions, it can be shown that the inverse of the metric $g_{\mu\nu}$ is described as:

$$g^{\mu\nu} = \eta^{\mu\nu} - h^{\mu\nu}, \tag{1.11}$$

where $h^{\mu\nu} = h_{\sigma\rho}\eta^{\sigma\mu}\eta^{\rho\nu}$ and $|h^{\mu\nu}| \ll 1$.

For regions of space-time with weak gravitational field, it holds that $\partial_\sigma g_{\mu\nu} = \partial_\sigma h_{\mu\nu}$. Therefore, the connection coefficients, or Christoffel symbols, can be written as:

$$\Gamma^\sigma_{\mu\nu} = \frac{1}{2}\eta^{\sigma\rho}\left(\partial_\nu h_{\mu\rho} + \partial_\mu h_{\nu\rho} - \partial_\rho h_{\mu\nu}\right). \tag{1.12}$$

Moreover, for linearized gravity, the product of the connection coefficients can be assumed to be nearly zero. Thus, the Riemann tensor expressed in equation (1.7) can be written as:

$$R^\rho_{\sigma\mu\nu} \approx \partial_\mu(\Gamma^\rho_{\nu\sigma}) - \partial_\nu(\Gamma^\rho_{\mu\sigma}). \tag{1.13}$$

Using equation (1.12), and reusing the auxiliary tensor index α, the Riemann tensor can be simplified to:

$$R^\rho_{\sigma\mu\nu} = \frac{1}{2}\eta^{\rho\alpha}\left(\partial_\mu\partial_\sigma h_{\alpha\nu} + \partial_\nu\partial_\alpha h_{\mu\sigma} - \partial_\mu\partial_\alpha h_{\nu\sigma} - \partial_\nu\partial_\sigma h_{\alpha\mu}\right). \tag{1.14}$$

Thanks to the symmetries and properties of the Riemann tensor, it can be contracted to obtain the Ricci tensor. The upper index and the lower middle index become the same, and $R_{\sigma\nu} = R^\mu_{\sigma\mu\nu}$. Moreover, using the property $\eta^{\mu\nu}h_{\mu\sigma} = h^\nu_\sigma$ we can contract indices in the expression of the Riemann tensor. Furthermore, the d'Alembertian operator is defined as $\Box = \eta^{\mu\alpha}\partial_\mu\partial_\alpha = \partial_\mu\partial^\mu$. Finally, another definition is the trace h of the perturbation metric, given by $h = h^\mu_\mu = \eta^{\mu\alpha}h_{\mu\alpha}$. With these definitions, the Ricci tensor in linearized gravity takes the following form:

$$R_{\sigma\nu} = \frac{1}{2}\left(\partial_\mu\partial_\sigma h^\mu_\nu + \partial_\nu\partial_\alpha h^\alpha_\sigma - \Box h_{\nu\sigma} - \partial_\nu\partial_\sigma h\right). \tag{1.15}$$

Contracting the remaining indices in the Ricci tensor, it is possible to obtain the Ricci scalar, defined as:

$$\begin{aligned} R &= \eta^{\sigma\nu}R_{\sigma\nu} \\ &= \partial_\mu\partial_\sigma h^{\mu\sigma} - \Box h. \end{aligned} \tag{1.16}$$

Hence, one can rewrite the Einstein field equations for linearized gravity using equations (1.10), (1.15), (1.16) and reusing the auxiliary tensor indices previously introduced as:

$$G_{\mu\nu} = \frac{1}{2}\left(\partial_\sigma\partial_\mu h^\sigma_\nu + \partial_\nu\partial_\sigma h^\sigma_\mu - \Box h_{\mu\nu} - \partial_\mu\partial_\nu h - \eta_{\mu\nu}\partial_\sigma\partial_\rho h^{\sigma\rho} + \eta_{\mu\nu}\Box h\right). \tag{1.17}$$

Lowering the indices and introducing the term $\bar{h}_{\mu\nu} \equiv h_{\mu\nu} - \frac{1}{2}\eta_{\mu\nu}h$, equation (1.17) becomes:

$$G_{\mu\nu} = \frac{1}{2}\left(\partial^\sigma\partial_\mu\bar{h}_{\sigma\nu} + \partial^\sigma\partial_\nu\bar{h}_{\mu\sigma} - \eta_{\mu\nu}\partial^\sigma\partial^\rho\bar{h}_{\sigma\rho} - \Box\bar{h}_{\mu\nu}\right) = \frac{8\pi G}{c^4}T_{\mu\nu}. \tag{1.18}$$

To further simplify the field equations, one can impose the Lorentz gauge condition, in which the divergence of the metric perturbation is set to zero ($\partial^\mu h_{\mu\nu} = 0$). Then, equation (1.18) results in:

$$G_{\mu\nu} = \frac{1}{2}\left(0 + 0 - 0 - \Box\bar{h}_{\mu\nu}\right) = \frac{8\pi G}{c^4}T_{\mu\nu}. \tag{1.19}$$

Finally, the expression for the linearized Einstein's field equations, in this condition, becomes:

$$\Box\bar{h}_{\mu\nu} = -\frac{16\pi G}{c^4}T_{\mu\nu}. \tag{1.20}$$

1.1.3 Gravitational Radiation

In vacuum, where $T_{\mu\nu} = 0$, and for a weak gravitational field, the linearized Einstein field equations are given by:

$$\Box\bar{h}_{\mu\nu} = 0. \tag{1.21}$$

Developing the d'Alembertian operator and separating the spacial and time terms, we can obtain:

$$-\frac{\partial^2\bar{h}_{\mu\nu}}{\partial(x^0)^2} + \frac{\partial^2\bar{h}_{\mu\nu}}{\partial(x^1)^2} + \frac{\partial^2\bar{h}_{\mu\nu}}{\partial(x^2)^2} + \frac{\partial^2\bar{h}_{\mu\nu}}{\partial(x^3)^2}\bar{h}_{\mu\nu} = 0, \tag{1.22}$$

which can be re-written as:

$$\frac{1}{c^2}\frac{\partial^2 \bar{h}_{\mu\nu}}{\partial t^2} = \nabla^2 \bar{h}_{\mu\nu}, \tag{1.23}$$

where ∇^2 is the Laplacian operator. Thus, equation (1.23) shows that the components of $\bar{h}_{\mu\nu}$ satisfy the wave equation. Hence, the Einstein field equations predict the presence of waves that travel through the space-time curvature at the speed of light c as small perturbations to the flat Minkowski metric.
The straightforward solutions of equation (1.23) are plane waves, which can be written in the following form:

$$\begin{aligned} \bar{h}_{\mu\nu} &= A\cos\left(\eta_{\mu\sigma}k^{\mu}x^{\sigma}\right) \\ &= Re\left[Ae^{i\eta_{\mu\sigma}k^{\mu}x^{\sigma}}\right], \end{aligned} \tag{1.24}$$

where k^{μ} represents the wave vector components. In linearized gravity, the linear metric perturbation $h_{\mu\nu}$ has 16 components. Therefore, the amplitude A of the plane-wave solutions is instead a four by four symmetric matrix. Then, equation (1.24) becomes:

$$\bar{h}_{\mu\nu} = Re\left[A_{\mu\nu}e^{ik_{\sigma}x^{\sigma}}\right], \tag{1.25}$$

where $A_{\mu\nu}$ is a symmetric matrix, reducing the number of independent components to ten. Furthermore, the Lorentz gauge condition, imposes that $\partial^{\mu}\bar{h}_{\mu\nu} = 0$, giving four constraint equations, reducing the amount of independent components to six. In the framework of the Lorentz gauge condition, we can introduce a particular coordinate system called the Transverse-Traceless (TT) gauge, where we consider only the part of the perturbation of the metric that is perpendicular to the propagation, meaning that $k_{\mu}\bar{h}^{\mu\nu} = 0$ and $A_{\mu\nu}k^{\mu} = 0$. Moreover, in the TT gauge, the perturbations do not cause any overall expansion or contraction of space as they propagate, meaning that $\bar{h}^{\mu}_{\mu} = 0$. As a consequence, the amount of independent components reduces to two. Furthermore, it is possible to show that in the TT gauge $\bar{h} = -h = 0$, thus, $\bar{h}_{\mu\nu} = h_{\mu\nu}$. In this way, the original metric perturbation introduced in equation (1.10) can be expressed as $h_{\mu\nu} = A_{\mu\nu}e^{ik_{\sigma}x^{\sigma}}$.
Thus, the set of equations for the plane wave amplitudes take the following form:

$$\begin{bmatrix} 0 & 0 & 0 & 0 \\ 0 & A_{xx} & A_{xy} & 0 \\ 0 & A_{yx} & A_{yy} & 0 \\ 0 & 0 & 0 & 0 \end{bmatrix} \begin{bmatrix} k^t \\ k^x \\ k^y \\ k^z \end{bmatrix} = \begin{bmatrix} 0 \\ 0 \\ 0 \\ 0 \end{bmatrix}. \tag{1.26}$$

Given the traceless conditions of this choice of coordinates, we have that $A^\mu_\mu = \eta^{\mu\nu} A_{\mu\nu} = 0$, meaning that $\eta^{xx} A_{xx} + \eta^{yy} A_{yy} = 0$, and $A_{xx} = -A_{yy}$. Moreover, since the matrix $A_{\mu\nu}$ is symmetric, then $A_{xy} = A_{yx}$. Finally, the wave amplitude matrix $A_{\mu\nu}$ has only two independent components, which can be expressed as A_+ and $A_\times$:

$$\begin{bmatrix} 0 & 0 & 0 & 0 \\ 0 & A_+ & A_\times & 0 \\ 0 & A_\times & -A_+ & 0 \\ 0 & 0 & 0 & 0 \end{bmatrix} = \begin{bmatrix} 0 & 0 & 0 & 0 \\ 0 & A_+ & 0 & 0 \\ 0 & 0 & -A_+ & 0 \\ 0 & 0 & 0 & 0 \end{bmatrix} + \begin{bmatrix} 0 & 0 & 0 & 0 \\ 0 & 0 & A_\times & 0 \\ 0 & A_\times & 0 & 0 \\ 0 & 0 & 0 & 0 \end{bmatrix}. \tag{1.27}$$

Where the subscripts denote the "Plus" and "Cross" polarization modes of the gravitational waves respectively. In conclusion, the perturbation of the space-time metric, i.e. the gravitational-wave, in the TT gauge coordinate system, can be expressed as:

$$h_{\mu\nu} = \begin{bmatrix} 0 & 0 & 0 & 0 \\ 0 & A_+ & A_\times & 0 \\ 0 & A_\times & -A_+ & 0 \\ 0 & 0 & 0 & 0 \end{bmatrix} e^{ik_\sigma x^\sigma}. \tag{1.28}$$

1.1.4 Effects of gravitational radiation on free particles

The perturbations on the metric, denoted by $h_{\mu\nu}$ are no other than ripples in the curvature of space-time. Considering free falling particles distributed in an (x, y, z) coordinate system, a wave travelling along the z axis has an expansion and contraction effect on x and y axes distribution of the particles. In order to test this hypothesis, one has to study the proper length (L_0) between two neighbour geodesics. For a displacement vector $\vec{r}$ between two neighbour points over the $x - y$ plane in space-time, the proper length is given by:

$$\begin{aligned} L_0 &= \int |\frac{d}{d\lambda}| d\lambda \\ &= \int \sqrt{-\left(\frac{dx}{d\lambda}\frac{\partial}{\partial x} + \frac{dy}{d\lambda}\frac{\partial}{\partial y}\right) \cdot \left(\frac{dx}{d\lambda}\frac{\partial}{\partial x} + \frac{dy}{d\lambda}\frac{\partial}{\partial y}\right)} d\lambda \\ &= \int_0^1 \sqrt{-(r^x)^2 g_{xx} + (r^x)(r^y) g_{xy} + (r^y)^2 g_{yy}} d\lambda \\ &= |\vec{r}|, \end{aligned} \tag{1.29}$$

where λ is the path parameter of the manifold. Therefore, to calculate the proper distance, it is necessary to take the dot product of this vector $\vec{r}$ with itself, defined as:

$$\vec{r} \cdot \vec{r} = (r^\mu \vec{e_\mu}) \cdot (r^\nu \vec{e_\nu}), \tag{1.30}$$

where $\vec{e_\mu}$ and $\vec{e_\nu}$ are basis vectors. Then, summing only over the $x - y$ plane, the expression in equation (1.29) becomes:

$$\begin{aligned} L_0 &= \vec{r} \cdot \vec{r} \\ &= r^x r^x g_{xx} + r^x r^y g_{xy} + r^y r^x g_{yx} + r^y r^y g_{yy} \\ &= (r^x)^2(\eta_{xx} + h_{xx}) + 2 r^x r^y (\eta_{xy} + h_{xy}) + (r^y)^2(\eta_{yy} + h_{yy}). \end{aligned} \tag{1.31}$$

Using the plane-wave solution in equation (1.28) of the metric perturbation and the Minkowski metric for flat space-time, the expression (1.31) turns into:

$$L_0 = -[(r^x)^2 + (r^y)^2] + [A_+((r^x)^2 - (r^y)^2) + 2A_\times r^x r^y] e^{ik_\sigma x^\sigma}, \tag{1.32}$$

where the first term is the standard result for a Minkowski metric of flat space-time and the second term corresponds to the effect of perturbations of the metric due to GWs. Therefore, the separation between adjacent geodesics changes due to fluctuations in the form of $h_{\mu\nu}$, despite the fact that the geodesics have constant space-time coordinates in the TT gauge.
In order to illustrate this effect, one can first align the displacement vector $\vec{r}$, between two geodesics, along the x axis. In this scenario, the changes on the separation results in $\Delta = A_+(r^x)^2 e^{ik_\sigma x^\sigma}$. On the other hand, if this displacement vector is aligned along the y axis, this variation results in $\Delta = A_+(r^y)^2 e^{ik_\sigma x^\sigma + \pi}$.

This means that the variations due to the "Plus" polarization, along the x and y axes, occur simultaneously, but they are phase-shifted by half a cycle. In a similar way, one can study the results of placing the distance vector $\vec{r}$ in a diagonal direction, for r^x and r^y with the same sign. This results in a change of the separation of these geodesics of $\Delta = 2A_\times |r^x r^y| e^{ik_\sigma x^\sigma}$. Then, if this vector $\vec{r}$ is oriented diagonally, but for r^x and r^y with opposite signs, the variation of the proper length results in $\Delta = 2A_\times |r^x r^y| e^{ik_\sigma x^\sigma + \pi}$. This means that the variations due to the "Cross" polarization also occur simultaneously and they are phase-shifted by half a cycle.
This can be summarized in the diagram in *Fig. 1.1*, which shows the effect of a passing GW on a ring of free falling particles.

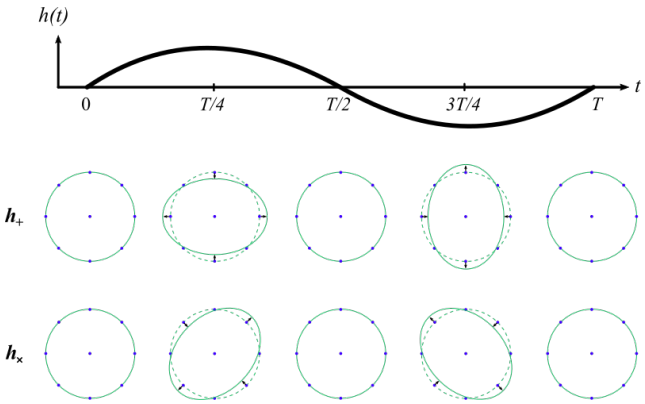

Figure 1.1: Effect of Cross-Plus Polarization gravitational waves passing by a ring of free falling particles.

Note that GWs have two polarization modes. However, these are the first order polarizations that GWs can have, since this study has been performed for linearized gravity. In fact, under a different analysis it can be shown that GWs can have up to six different polarization modes [11].

1.2 Generation of gravitational waves

When interested in studying the conditions that give rise to GWs, the energy-momentum tensor $T_{\mu\nu}$ has to be considered because at the GW source, where the mass and energy are concentrated, curvature effects are significant. A solution for the Einstein's field equations (1.20) can be found by imposing boundary conditions to the source geometry, defining a finite space, and by

integrating over the source. Then, the tensor $h_{\mu\nu}$ can be expressed as:

$$h_{\mu\nu}(t, \vec{x} - \vec{x}') = \frac{4G}{c^4} \int \frac{T_{\mu\nu}(\vec{x}, t - |\vec{x} - \vec{x}'|/c)}{|\vec{d}|} d^3x', \tag{1.33}$$

where $\vec{x}'$ is a vector from a point of the source and $\vec{x}$ is the vector identifying the observer position. For a source located in the origin of the coordinate system, at large distances from the source, it is possible to assume that $|\vec{x} - \vec{x}'| \approx |\vec{x}| = r$. In this condition the energy momentum tensor can be expressed as $T_{\mu\nu}(\vec{x}, t - r/c)$. For this type of energy-momentum tensor and if the gravitational impact to the total energy is small, then equation (1.33) can be simplified to the quadrupole formula in the weak field limit on the TT gauge as [12]:

$$h_{\mu\nu}(t, r) = \frac{2G}{c^4} \frac{1}{r} \frac{\partial^2 I_{\mu\nu}}{dt^2}(t - r/c) \tag{1.34}$$

where $I_{\mu\nu} = \int \rho(\vec{x}) x_\mu x_\nu d^3x$ represents the quadrupole moment tensor and ρ is the mass density of the object under study. Equation (1.34) suggests that gravitational radiation is generated by sources that undergo accelerated motion, as long as their distribution changes over time, and their symmetry is nor spherical neither rotational.

1.3 Gravitational waves sources

As shown in equation (1.34), the magnitude of GWs is directly connected to the mass of the system emitting these waves, and it is inversely proportional to the distance from the source. Thus, a rough estimate for this amplitude can be given by $h \sim \frac{2G}{c^4} \frac{M_{system}}{r}$, which for a non-spherical system with a mass of the order of one solar mass $\mathrm{M}_\odot$, with kinetic energy E_{sys} at a distance of 1 Mpc (Mega parsec), can be given by:

$$h \sim 10^{-19} \left(\frac{E_{sys}}{\mathrm{M}_\odot \mathrm{c}^2} \right) \left(\frac{1\,\mathrm{Mpc}}{r} \right), \tag{1.35}$$

where it has been assumed that a large fraction of kinetic energy is converted to gravitational radiation. While a rough estimate, equation (1.35) serves to define an upper limit for GW amplitudes from a source located within the Local Group of galaxies [13].

Typically, in GW astronomy possible sources are classified into four categories: Compact Binaries, Continuous waves, Stochastic and Burst sources.

1.3.1 Compact binary coalescence sources

Compact objects engaged in a cosmic dance abound in the known Universe. These objects can be white dwarfs, neutron stars (NS), black holes (BH), among others. Under specific conditions, these binary systems can emit powerful GWs, which can be and have been observed by GW detectors such as Advanced LIGO [1] and Advanced Virgo [4]. These systems generate GWs at the cost of losing energy and angular momentum, getting closer and closer together in smaller orbits until the two objects collide and merge into a single entity. This process can be divided into three phases, which are the inspiral, the merger and the ringdown, as shown in *Fig. 1.2*, taken from [14].

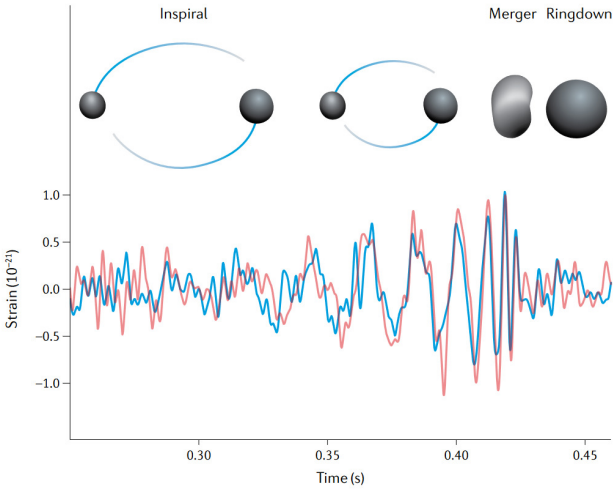

Figure 1.2: The upper inset provides an artistic representation of the merger, illustrating the evolution of black hole event horizons during the coalescence and merger process. The lower inset shows the gravitational-wave strain amplitude over time for GW150914 detected by both the LIGO Hanford and Livingston observatories on September 14, 2015.

The inspiral phase can take millions of years, and it is mainly characterized by a consistent increase of both amplitude and frequency of the GW being emitted. The frequency of these waves just before the merger is of the order of hundred of Hz. For this reason and for the likelihood of this types of events to occur, the design sensitivity for Earth based GW detectors reach their peak around hundred of Hz. After the inspiral phase the merger comes, which takes place in just some milliseconds [15]. This rapid increase in frequency and amplitude is also known as the chirp. In this stage there is no longer space

between the objects and they merge into one single compact object. Finally, the ringdown describes that a new formed object settles to a stationary state. After this phase finishes, the object ceases its gravitational radiation. These waves can be generated by the merger of two BHs, Binary Black Hole (BBH), the merger of two NSs, Binary Neutron Star (BNS) or by the merger of a BH and a NS. The first indirect proof of GWs emission was indeed by studying a BNS system. In the 1970s, Russell Hulse and Joseph Taylor discovered a binary pulsar [16], a pair of neutron stars orbiting each other. Over the years, they observed a gradual decrease in the orbital period of these stars, which matched the predictions of energy loss due to gravitational-wave emission, as described by GR. Additionally, for this binary pulsar system, they noted a cumulative shift in the periastron, the point of closest approach in the orbit of the stars, which aligned with relativistic predictions, as shown in *Fig. 1.3*, taken from [17]. This indirect evidence of gravitational waves demonstrated a previously theoretical phenomenon. For their discovery and work, Hulse and Taylor were awarded the Nobel Prize in Physics in 1993.

Compact binary coalescence (CBC) is one of the most frequent source of GWs that can be detected on Earth. The characteristic amplitude of these waves from inspiral binaries can be written as [18]:

$$h = 4.1 \times 10^{-22} \left(\frac{\mu}{\mathrm{M}_\odot}\right)^{\frac{1}{2}} \left(\frac{M}{\mathrm{M}_\odot}\right)^{\frac{1}{3}} \left(\frac{100\,\mathrm{Mpc}}{r}\right) \left(\frac{100\,\mathrm{Hz}}{f_{GW}}\right)^{\frac{1}{6}} \tag{1.36}$$

where r is the distance from the detector to the binary system and f_{GW} is the characteristic frequency of the GW, M is the sum of the masses of the objects ($M = M_1 + M_2$), and μ is the reduced mass of the objects, which is given by $\mu = M_1 M_2 / M$. For two objects of about one solar mass $\mathrm{M}_\odot$, orbiting at 100Hz and within the Local Group of galaxies ($r \leq 3.1\,\mathrm{Mpc}$), then the amplitude would be of $h \approx 1 \times 10^{-20}$, which could be detected by all current GW detectors in observing mode.

1.3.2 Continuous waves

A spinning compact object with non-axisymmetric deformations can emit continuous GWs [19]. A spinning NS with a distortion or without a perfect surface exhibits a quadrupole moment which varies over time, meaning that emits GWs. Some models have estimated the population of active pulsar in our

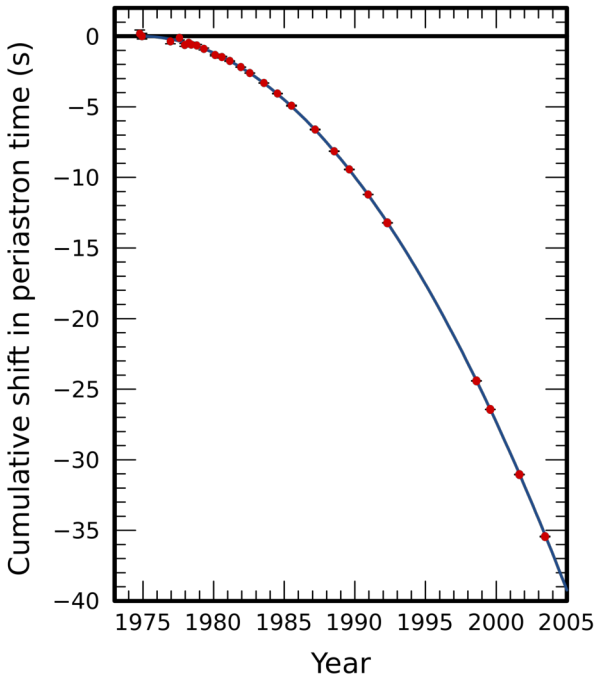

Figure 1.3: Orbital decay due to the loss of energy via gravitational radiation. The curve illustrates the expected shift in periastron time compared to an unchanging orbit, as predicted by GR.

Galaxy to be of the order of half a million, from which only about 2000 have been identified. In order to detect pulsars, their electromagnetic (EM) radiation has to point the Earth, that is the reason why we have detected only a small fraction of the estimated population. On the other hand, one could use GWs to study pulsars that do not point to the Earth with its EM emission. The expected strain amplitude h of such an object can be written as [20]:

$$h = 1.1 \times 10^{-24} \left(\frac{\epsilon}{10^{-6}}\right) \left(\frac{I_{zz}}{I_0}\right) \left(\frac{f_{GW}}{1\,\mathrm{kHz}}\right)^2 \left(\frac{1\,\mathrm{kpc}}{r}\right) \tag{1.37}$$

where I_0 is a nominal moment of inertia of a NS, ϵ is the mass quadrupole asymmetry of the star, f_{GW} is the characteristic frequency of the GW and r is the distance from the NS to the detector. For a spinning object with a mass quadrupole asymmetry $e \sim 10^{-6}$, within the vicinity of the Orion Arm ($r \leq 3.07\,\mathrm{kpc}$) and spinning at 1kHz, the amplitude would be of $h \approx 0.36 \times 10^{-24}$, which could be detected by the future generation of GW detectors.

1.3.3 Stochastic gravitational-wave background

The superposition of numerous independent sources could give origin to a stochastic GW background [21]. This background provides insights into the early moments of the Universe. The theory supports that this radiation was generated just fractions of a second after the Big Bang, well before the emergence of the Cosmic Microwave Background (CMB). In order to characterize the expected strain amplitude h of such stochastic waves, one starts by describing the GW spectrum in relation to the total energy density of all GWs over a logarithmic frequency range as [22]:

$$\Omega_{gw}(f) = \frac{1}{\rho_{critical}} \frac{d\rho_{gw}}{d\ln(f)}, \tag{1.38}$$

where ρ_{gw} is the energy density of the GW found within a specified frequency range, $\rho_{critical} = \frac{3c^2 H_0^2}{8\pi G}$ is the critical energy density to cover the Universe and H_0 is the Hubble constant. Then, as described in [18], a characteristic amplitude for a stochastic GW is:

$$h = 1.3 \cdot 10^{-18} \left(\frac{\rho_{critical}}{1.7 \times 10^{-8}\,\mathrm{erg\ cm^{-3}}} \right)^{\frac{1}{2}} \left(\frac{1\,\mathrm{Hz}}{f} \right) [\Omega_{gw}(f)]^{\frac{1}{2}}\,. \tag{1.39}$$

Observing stochastic GWs would offer a unique chance to test GR during the early stage of the Universe by detecting additional polarization modes of GWs [23]. Furthermore, the stochastic gravitational-wave background can provide insights into the formation and evolution of large-scale structures, the dynamics of early universe phase transitions, and the contribution from numerous unresolved binary systems, such as BBH and NSs, across the universe.

1.3.4 Burst emission of gravitational waves

Bursts are referred to brief duration events from sources that are either unidentified or unexpected. These events may also involve release of EM radiation as Gamma-ray bursts, which could originate from matter interactions with an accreting BH, a star core collapsing supernovae or even NS mergers. Modelling of gravitational collapse is a highly active field in astrophysics. However, modelling wave-forms of those effects is a complex task, since it involves uncertainties arising from violent processes, initial conditions, which means taking into account multiple variables. Nevertheless, estimates of a GW amplitude

generated by a supernova in our galaxy [24], emitting the energy (E) equivalent to $10^{-7}\,\mathrm{M}_{\odot}$, located at a distance of 10 kpc, at a frequency of 1 kHz and having a duration of 1 ms can be written as:

$$h \sim 6 \times 10^{-21} \left(\frac{E}{10^{-7}\,\mathrm{M}_{\odot}}\right)^{\frac{1}{2}} \left(\frac{1\,\mathrm{ms}}{T}\right)^{\frac{1}{2}} \left(\frac{1\,\mathrm{kHz}}{f}\right) \left(\frac{10\,\mathrm{kpc}}{r}\right). \tag{1.40}$$

This magnitude should be detectable with current detector sensitivities on Earth. However, such a supernova event in a vicinity of 10 kpc has a rate significantly low, making the detection unlikely.

1.4 LIGO-Virgo signal extraction and analysis

The task of analyzing data from GW detectors involves unique challenges, such as ensuring consistency across several GW antennas of the network that is crucial to mitigate instrumental background noise and to facilitate analysis of GW signals. Having detectors separated by vast distances helps to determine the direction of the source due to the different arrival times of the signal. Such a network plays a crucial role in discerning GW signals, exhibiting a correlated response across the network, from uncorrelated noise in each instrument, allowing for the distinction of signals from noise fluctuations. In addition, all-sky searches, analysis of polarization, analysis of a broad spectrum of frequencies and creating algorithms for multiple antennas are essential. Besides, the computational demands are significant due to the continuous data acquisition and due to the need of multiple filtering processes.

GW detection and understanding of physical parameters depend on knowing the expected signal shape and noise distribution. Due to the nature of GW signals, uncertainties in parameters can be considerable. A priori assumptions about the amplitudes and phase evolution of these signals can have a significant impact on the reconstructed waveform. Consequently, determining physical parameters like masses and spins of merging objects is achieved through Bayesian parameter estimation methods [25]. Wave-form models are created for different parameters and these are compared with the output data of the detector utilizing likelihood functions, to find the most likely solution. The study of residuals from the comparison between the observed and estimated values has to be consistent with noise properties. *Fig. 1.4*, taken from [25], shows an example of a comparison between the

data and wave-form model of a GW signal with the related residual. Since stationary Gaussian noise exhibits no correlation between frequency bins, and the noise present in the LIGO-Virgo detectors is generally stationary, then it is effective to analyze it in the frequency domain. Matched filters are used for GW data analysis. Window functions are employed to avoid spectral leakage and to prevent spurious correlations in phase between frequency bins [26]. In particular, Tukey windows are especially advantageous for analyzing transient data and cause minimal alteration to the data compared to other window functions [27]. The challenges to analyze this data arise from the fact that noise could have short and high transients referred to as glitches, that ultimately cause the noise to deviate from ideal Gaussian.

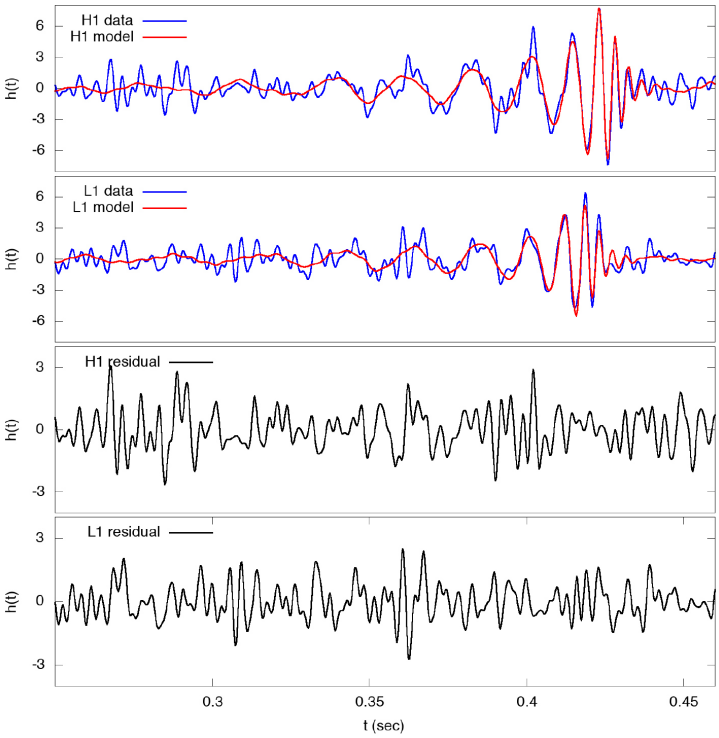

Figure 1.4: The two top panels display the whitened and band-passed data from the LIGO detectors for the signal GW150914. The data is overlaid with maximum likelihood whitened templates. The lower panels show the residuals obtained by subtracting the templates from the data. The y-axis of these panels represents strain measurements with an order of magnitude of 10^{-22}.

Initially, the output of the detector is subjected to calibration and it is converted to a GW strain measure in time. If the data is corrupted by environmental or technical noises, a flag is raised and, therefore, invalidated for analysis. If the data is not flagged as corrupted, then it is passed through search algorithms to define the quality of the obtained signal. Signals are ranked and undergo different analyses depending on their significance. These candidates are compared with the wave-forms previously generated and probability distributions are generated for all the properties of the source. Finally, after checking data quality and validations, the events are incorporated in a source catalog. A scheme, which summarizes this process, is shown in *Fig. 1.5*.

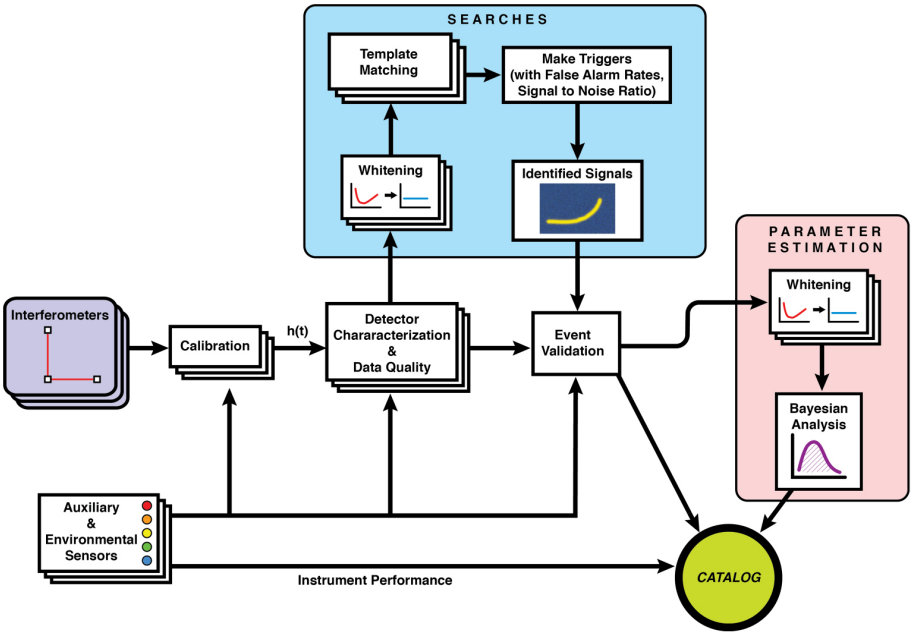

Figure 1.5: A simplified diagram outlining the primary stages in LIGO-Virgo data processing, starting from detector data.

.

1.5 Gravitational-wave detection

During the last decade, astronomy has undergone a remarkable revolution, with three GW landmarks standing out. First, in 2015 during the initial observing run, LIGO Livingston and LIGO Hanford detectors made history with a first direct detection of a GW, which was denoted as GW150914 [2]. This signal

was emitted by a BBH merger. This event was located at a luminosity distance of 410^{+160}_{-180} Mpc, corresponding to a redshift of $z = 0.09^{+0.03}_{-0.04}$. The initial BH masses were of $36^{+5}_{-4}\,M_\odot$ and $29^{+4}_{-4}\,M_\odot$ respectively, and the merger culminated in a BH with a mass of $62^{+4}_{-4}\,M_\odot$. Remarkably, this merger radiated energy equivalent to $3.0^{+0.5}_{-0.5}\,M_\odot$ in the form of GWs. The detected signal ascends in frequency from 35 to 250 Hz, reaching a peak GW strain of 1.0×10^{-21}. The signal-to-noise ratio (SNR) of this observation was of 24. *Fig. 1.6*, taken from [2], shows the time signals, the residuals and the spectrograms of the event GW150914 acquired by the two LIGO detectors.

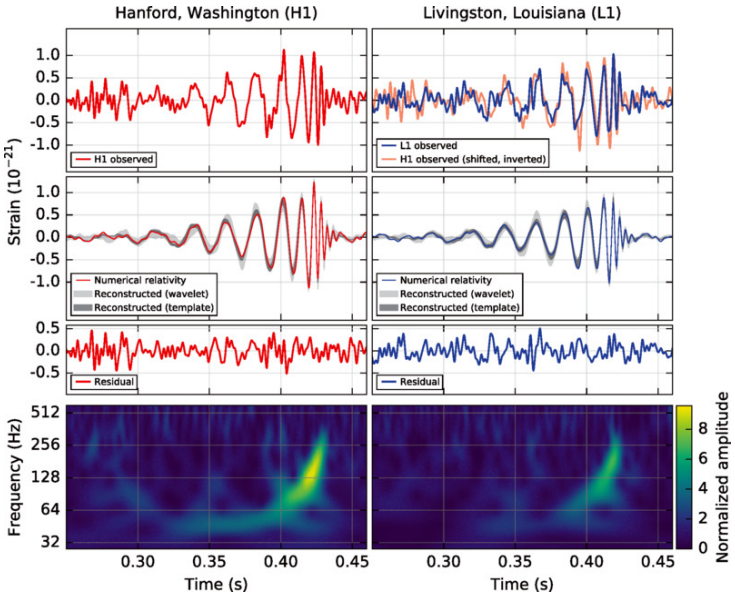

Figure 1.6: GW150914: First gravitational-wave detected by both LIGO Hanford (H1) and Livingston (L1) detectors on September 14, 2015, at 09:50:45 UTC. Filtering was applied to focus on the 35–350 Hz frequency range, and filters removed instrumental spectral lines. The top row shows H1 and L1 strains, with GW150914 arriving first at L1, delayed by 6.9 ms at H1. The second row displays the gravitational-wave strain projected onto each detector, accompanied by numerical relativity wave forms. Shaded areas represent 90 credible regions for waveform reconstructions, based on binary black hole templates. Residuals and a time-frequency representations are featured in the third and bottom rows, respectively.

The second landmark occurred nearly two years later. After having gone through a major sensitivity enhancement and expending nearly ten months of commissioning, Advanced LIGO detectors started a second observing run

(O2) on November 2016. This time Advanced Virgo entered the run, joining the network of detectors, in August 2017. A simultaneous detection of a GW, generated by a BBH, took place on August 14th by the three detectors. This signal is referred as GW170814 [28]. The source was located at an estimated luminosity distance of 540^{+130}_{-210} Mpc. The estimated masses of the initial BHs were $30.5^{+5.7}_{-3.0}\,M_\odot$ and $25.3^{+2.8}_{-4.2}\,M_\odot$, producing a final BH mass of $53.2^{+3.2}_{2.5}\,M_\odot$, therefore radiating the equivalent to $2.7^{+0.4}_{0.3}\,M_\odot$ in GWs. Utilizing a network of three detectors significantly enhanced the precision of the source localization, reducing the uncertainty area from $1160\,\mathrm{deg}^2$ to $60\,\mathrm{deg}^2$, as shown in *Fig. 1.7*, taken from [28].
Several subsequent investigations of the signal GW170814 were carried out by 25 detectors and observatories across various wavelengths, including neutrinos, gamma rays, X-rays, optical and near infrared detectors. However, no counterpart was found. Nevertheless, this detection provided an opportunity to test GW polarizations and new tests of gravity.

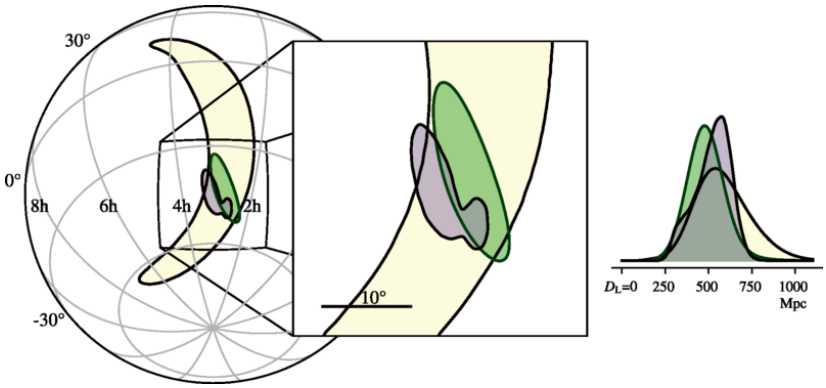

Figure 1.7: Localization of GW170814 visually represented in different panels: The initial localization based on Advanced LIGO data is shown in yellow, while the one obtained including data from Advanced Virgo is displayed in green. Using a fully coherent Bayesian localization and more sophisticated waveform models [29], the localization was updated and is represented in purple with 90% credible regions. Different projections in equatorial coordinates are used in the panels, and the inset on the right illustrates the posterior probability distribution for the luminosity distance across the entire celestial sphere.

Shortly after, the third landmark took place. On August 17, 2017, at 12:41:04 UTC, Advanced LIGO and Advanced Virgo jointly observed their first BNS inspiral, referred as GW170817 [5]. This signal had an estimated luminosity distance of 40^{+8}_{-14} Mpc and a combined SNR of 32.4, being the closest

and loudest GW signal detected so far. The estimated masses of the initial NSs were $1.26 - 1.60\,M_\odot$ and $1.17 - 1.36\,M_\odot$. The energy emitted (E_{rad}) in GW strongly depends on the equation of state (EOS) of the NS matter, therefore it was only possible to place a lower bound to it of $E_{rad} > 0.025\,M_\odot c^2$. In addition, using the detector network, the source of the signal was pinpointed to a region in the sky of $28\,\mathrm{deg}^2$ with 90% probability, as shown in *Fig. 1.8*, taken from [5].

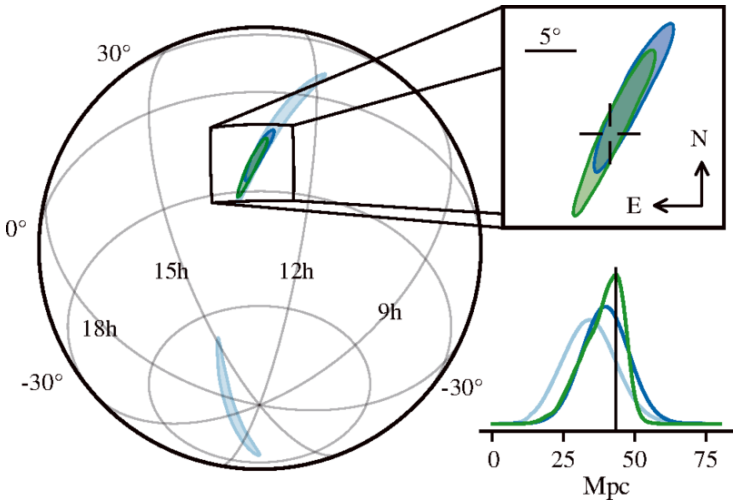

Figure 1.8: Sky localization of GW170817. With both LIGO Hanford and LIGO Livingstone detectors, the estimation of the localization results in $190\,\mathrm{deg}^2$. For Hanford-Livingstone-Virgo the localization is improved to $28\,\mathrm{deg}^2$. Bottom right panel shows an estimation of the luminosity distance of the GW source.

Every detector has certain areas of the sky where its sensitivity is limited due to its orientation. This particular fact plays a key aspect in narrowing down the localization of the source in the sky. As it can be seen in *Fig. 1.9*, taken from [5], this source was located in the blind spot of the Advanced Virgo detector.

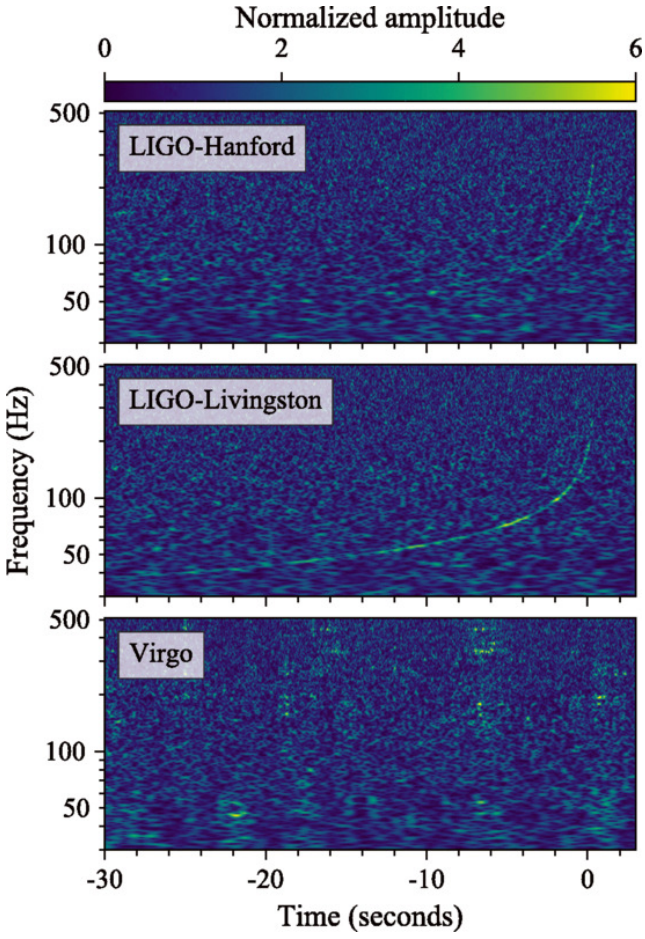

Figure 1.9: Time-frequency representations from the GW170817 event detected by LIGO-Hanford, LIGO-Livingston, and Virgo. Time is referenced to August 17, 2017, 12:41:04 UTC, with each detector's amplitude scale normalized to its noise amplitude spectral density. It can be seen that the signal in the spectrogram of Advanced Virgo, is null. This is due to the fact that the event was localized in the blind region of the sky for Advanced Virgo, which was fundamental for the small region for the sky localization.

As a result of this detection, an alert was sent to the astrophysical community, reporting a highly confident detection of a BNS GW signal.

Other notable events on this list are the detections of two neutron star-black hole (NS-BH) mergers in 2020, during the third observing run (O3) [30]. The fist of these events, GW200105, had a primary mass of $m_1 = 8.9^{+1.2}_{-1.5}\,\mathrm{M}_\odot$, consistent with predicted black hole masses. The secondary mass was estimated to

be $m_2 = 1.9^{+0.3}_{-0.2}\,\mathrm{M}_\odot$, consistent with neutron star masses observed in the Milky Way. The luminosity distance of this source was estimated to be $280^{+110}_{-110}\,\mathrm{Mpc}$.

Similarly, the second event, GW200115, had a primary mass of $m_1 = 5.7^{+1.8}_{-2.1}\,\mathrm{M}_\odot$, also consistent with predicted BH masses. The secondary mass was estimated to be $m_2 = 1.5^{+0.7}_{-0.3}\,\mathrm{M}_\odot$ respectively, consistent with NS masses observed in the Milky Way. The luminosity distance of this source was estimated to be $300^{+150}_{-100}\,\mathrm{Mpc}$.

The first event has been observed by only LIGO Livingston and Virgo, while the second one has been observed by the three detectors. For these events, there was no observed EM counterparts. Future observations of NS-BH systems, characterized by markedly unequal component masses, will offer new opportunities to investigate matter under extreme conditions. Additionally, these observations will offer possibilities to study potential deviations from GR.

GW190412, with a network signal-to-noise ratio (SNR) of 19 [31], stands out as another significant detection. This binary system is characterized by its asymmetric masses: a merger between a $\sim 30\,\mathrm{M}_\odot$ BH and an $\sim 8\,\mathrm{M}_\odot$ BH. The GW carried radiation oscillating not only at the dominant emission frequency of the binary system but also at other frequencies. This observation marked the first instance where higher-order GW modes were necessary to describe the signals [32].

Another notable detection was GW190521 [33], corresponding to the merger of two BHs with masses of $85^{+21}_{-14}\,\mathrm{M}_\odot$ and $66^{+17}_{-18}\,\mathrm{M}_\odot$. Following the merger, a black hole of $142^{+28}_{-16}\,\mathrm{M}_\odot$ was formed, which can be considered as an intermediate-mass black hole (IMBH) [34]. The network SNR of this detection was of 14.5 and the source luminosity distance was $5.3^{+2.4}_{-2.6}\,\mathrm{Gpc}$, corresponding to a redshift of $0.82^{+0.28}_{-0.34}\,\mathrm{Gpc}$.

In summary, during the past few years, three observing runs took place (O1, O2 and O3) detecting and collecting information about GW mergers. On November 2021, with these observing runs, an extensive catalog of mergers of NSs, BHs and NS-BH to this date was released [35]. It summarizes a total of 90 GW events observed by the LIGO-Virgo network. *Fig. 1.10* summarizes the observations performed in these runs classified in terms of initial and final masses.

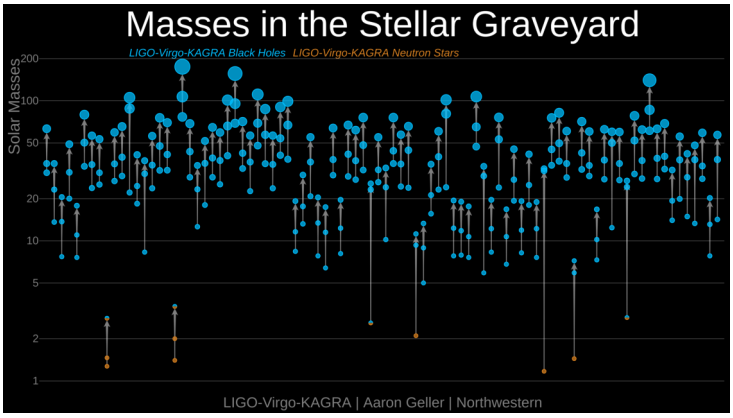

Figure 1.10: Masses of compact binaries identified by LIGO-Virgo network, showcasing BHs in blue and NSs in orange. Credit: LIGO-Virgo / Aaron Geller / Northwestern University.

1.6 Multi-messenger Astronomy

On August 17, 2017, at 12:41:06 there was a trigger in the Fermi Gamma-ray Burst Monitor (GBM) [36]. This signal, referred as GRB170817A [37, 38], was detected by the International Gamma-Ray Astrophysics Laboratory (INTEGRAL)[39] and was announced to the astrophysical community at 12:41:20 UTC that day. Only six minutes later, the astrophysical community received another alert, coming from the GW detector network, announcing a GW candidate product of a BNS merger. The signal GW170817 was recorded less than 2 s before the signal GRB170817A, as shown in *Fig. 1.11*, taken from [40]. Therefore, in response to these alerts, a broadband observing campaign was started across the EM spectrum. With the information collected with LIGO/Virgo, FERMI/GBM and INTEGRAL a very accurate estimation of the sky localization of the source, of about 28 $\deg^2$, was achieved, as shown in *Fig. 1.12*, taken from [8]. Due to its estimated localization, in the Southern Sky, the first bright optical counterpart was recorded by Las Campanas Observatory [41] in Chile.

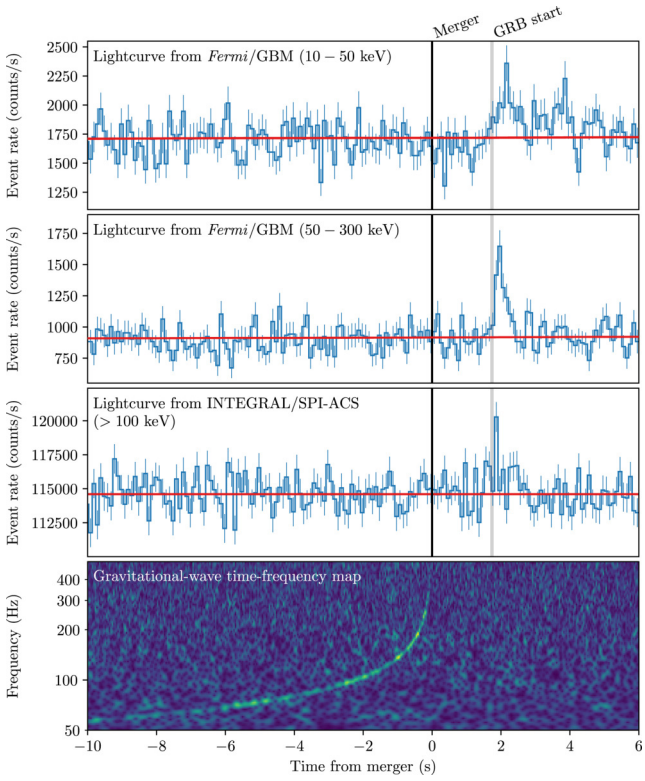

Figure 1.11: Joint detection of GW170817 and GRB170817A trough various detectors and observatories. The top panel depicts the detection of GRB in the energy band of $10 - 50\,\mathrm{keV}$. The second panel focuses in the $50 - 300\,\mathrm{keV}$ range. The third panel displays the detection of GRB signals for energy above $100\,\mathrm{keV}$. The bottom panel shows the frequency map of GW170817, detected by the LIGO-Virgo detector network.

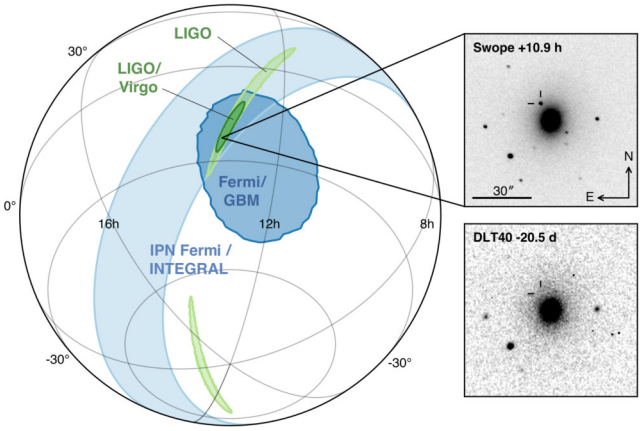

Figure 1.12: Sky localization of GW, GRB and optical signals. The left panel shows a 90% credible region of 190 $\deg^2$, and the improved localization to 28 $\deg^2$ by the LIGO-Virgo network. Together with triangulation from Fermi and INTEGRAL, the apparent host galaxy NGC 4993 could be identified (Bottom right). Later that day, 10.9 hr after the merger, a bright spot in the neighbourhood of the galaxy NGC4993 was observed (Top right).

.

Furthermore, the simultaneous observation of GWs and light emitted by the merging BNS system in GW170817 contributed independent estimations of distance and redshift. This enabled a direct calculation of the Hubble constant, H_0, without the assumption of a particular cosmological model. The Hubble constant is a key parameter used to describe the rate at which the Universe is expanding and it is defined as the ratio of the recession velocity of the source v and the distance from the observer D as:

$$v = H_0 D. \tag{1.41}$$

With the measurements taken from the event GW170817, GWs have emerged as a promising method for estimating the Hubble constant, thanks to their inherit properties as "standard sirens" [42, 43]. This designation arises because the energy dissipated during the collision of compact binary systems and the energy observed upon reaching Earth can be accurately determined from the GW signal, providing a direct measurement of distance. Finally with this method combined with the other cosmological models, the estimation of the Hubble constant was updated to $H_0 = 72.77^{+11.0}_{-7.55}$, km s^{-1} Mpc^{-1}.

Thanks to all the observations of the spectral energy distribution of this

event, as shown in *Fig. 1.13*, taken from [8], it was possible to determine the energy output, the ejected material and the environment of the explosion, concluding that the event was a kilonova [44]. In addition, this detection was followed by neutrino observatories such as IceCube [45], ANTARES [46] and Pierre Auger Observatory [47]. However, no neutrinos were found as a counter part of this event, information used to constrain the properties of the merger. This occurrence highlighted the significance of collaborative efforts, combining GW, EM and neutrino observations and gave place to the start of a new and exciting era in astrophysics, the multi-messenger era [8].

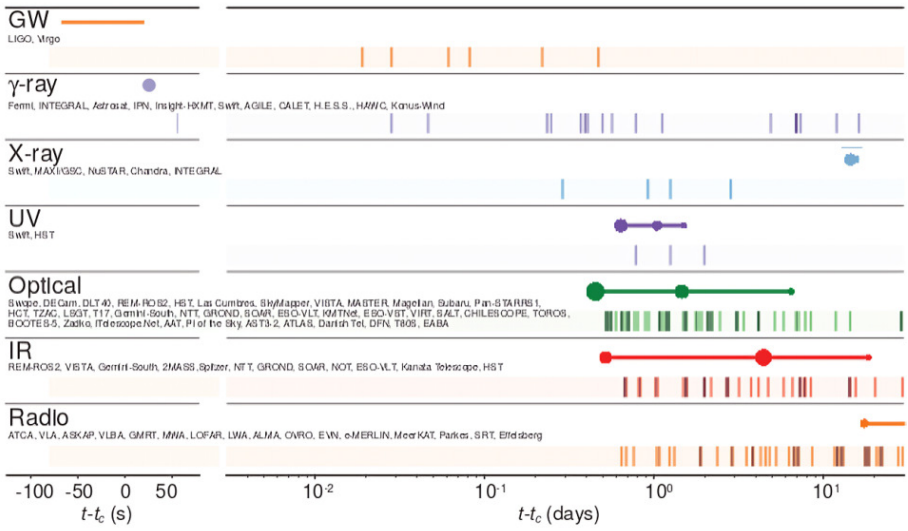

Figure 1.13: Time line of GW170817, GRB170817A and the follow-up detailed for different messengers, observatories and wavelength. Solid lines in the different messenger rows represent the times when the signal of the source system was detectable at least by one telescope.

Chapter 2

Gravitational-wave detectors

Due to its extremely small effect on matter and the required technology, GWs were initially considered to be impossible to measure. About four decades after the formulation of GR, J. Weber, fascinated by this theory and Einstein's prediction of GWs, started a campaign of experimental methods to directly detect these waves. This motivation led him to work on the innovative resonant mass detector [48]. Following this work, several groups around the globe joined the effort and several resonant bar detectors were developed for the hunt of such elusive waves [49, 50, 51]. Although having theoretically a sufficient sensitivity in a narrow bandwidth, these experiments did not record any gravitational-wave.

The transition to interferometric detectors began in the early 1970's with a laser interferometer proposed in 1971 [52]. Several advantages come with the choice of an interferometric detector over a resonant bar, as improved sensitivity and broader detection bandwidth. Therefore, interferometric detectors were considered more suitable for the analysis of the acquired data to study astrophysical phenomena. Some long baseline interferometers were designed, developed and implemented in the 1980's and 1990's such as TAMA [53], GEO600 [54].

During the last decades km-scale interferometric detectors, such as LIGO [1], Virgo [4], and KAGRA [55], have been developed and upgraded. The current upgrade of these interferometers is referred to as the 2^{nd} Generation (2G) of gravitational-wave detectors. The core of the 2G detectors is a Michelson interferometer [56], enhanced with the addition of a Fabry-Perot cavity on each arm. Moreover, two additional partially reflective mirrors are added at the input and output ports of the Michelson interferometer. This chapter describes

the working principle of ground-based interferometric detectors, with a detailed focus on the Advanced Virgo Plus detector. Future ground-based and space detectors will be introduced at the end of this chapter.

2.1 Working principle

2.1.1 Michelson Interferometer

The configuration of 2G detectors is a modified version of a Michelson interferometer. The main mirrors installed in these interferometers are suspended from wires. Therefore, they can be considered as free falling masses along the longitudinal axis given by the propagation direction of the main laser beam. In the configuration of a Michelson interferometer, as the one shown in *Fig. 2.1*, the incoming laser beam encounters a Beam Splitter (BS), dividing the beam into two beams of equal intensity. Note that equal intensities are mandatory to have symmetric arm powers needed to not degrade the sensitivity of the instrument. After having travelled along the interferometer's arms, these beams are reflected back by two mirrors positioned at the end of each arm. Upon their return, the beams are recombined at the BS, leading to an interference pattern based on their phase relationship.

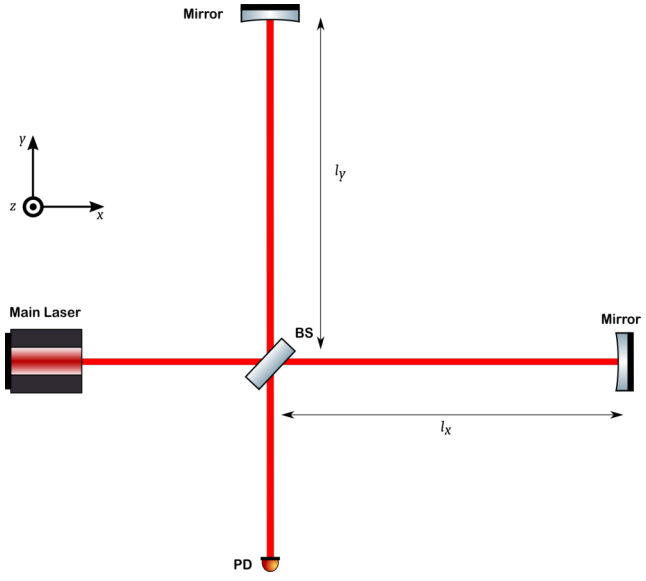

Figure 2.1: Scheme of a Michelson interferometer.

As detailed in Chapter 1, a passing GW will affect the Michelson interferometer by expanding one arm while shrinking the other one. This alteration in arm lengths modifies the path that the light beams travel. Such a change in the beam paths results in a phase difference between the two beams when they recombine at the BS, leading to a modified interference pattern. Consequently, in the context of interferometric GW detectors, this change in the interference pattern leads to a variation in the intensity that can be detected by a photodiode (PD) positioned at the output of the interferometer. For a Michelson interferometer with arm lengths l_x along the x axis and with l_y along the y axis, the difference in length can be expressed as $\delta l = l_x - l_y$. Then, the phase difference $\delta\phi$ between the beams traveling along the two arms and recombined at the BS can be expressed as:

$$\delta\phi = \frac{2\pi}{\lambda}\delta l = k\delta l, \tag{2.1}$$

where λ is the wavelength of the laser beam and k is the wave number.

To study the phase variation due to the passage of a GW, one can start by deriving the time difference for a round trip of a photon inside the interferometer. For a passing GW along the z axis, with a plus polarization mode and an interferometer detector with arms aligned with the x and y axes, as identified in *Fig. 2.1*, for light traveling along theses axes, the space-time distance ds, as detailed in Chapter 1 in equation (1.3), can be expressed as:

$$\begin{aligned} ds^2 &= g_{\mu\nu}dx^\mu dx^\nu \\ &= -(cdt)^2 + (1+h_+(t))dx^2 + (1-h_+(t))dy^2 + dz^2, \end{aligned} \tag{2.2}$$

which in this case is null, since in the framework of GR, light travels such that the time experienced by the light beam is zero, making the proper distance zero. Therefore, focusing on the beam traveling only along the x axis, equation (2.2) can be reduced to:

$$cdt = \sqrt{(1+h_+(t))}dx. \tag{2.3}$$

By integrating dx along the round trip path from the BS to the end mirror, we obtain:

$$\begin{aligned}\frac{2l_x}{c} &= \int_{t-\tau_{rt}}^{t} \frac{1}{\sqrt{1+h(\tau)}} d\tau \\ &\approx \int_{t-\tau_{rt}}^{t} \left(1 - \frac{h(\tau)}{2}\right) d\tau.\end{aligned} \tag{2.4}$$

Then, the round trip travel time τ_{rt} of the light, i.e. the time a photon needs to go from the BS to the end mirror and come back to the BS, is given by:

$$\tau_{rt} \approx \frac{2l_x}{c} + \frac{1}{2}\int_{t-2l_x/c}^{t} h(\tau)d\tau. \tag{2.5}$$

Thus, the total phase acquired in that round trip, along the x axis, is denoted by:

$$\phi_x(t) = \omega_0 \tau_{rt} = \frac{2\omega_0 l_x}{c} + \frac{\omega_0}{2}\int_{t-2l_x/c}^{t} h(\tau)d\tau, \tag{2.6}$$

where ω_0 is the angular frequency of the laser field. The first term represents the phase shift caused by the light traveling a distance of $2l_x$, while the second term indicates the phase variation induced by the passage of a GW. Analogously, the phase acquired in the distance l_y along the y axis can be expressed by:

$$\phi_y(t) = \frac{2\omega_0 l_y}{c} - \frac{\omega_0}{2}\int_{t-2l_y/c}^{t} h(\tau)d\tau. \tag{2.7}$$

Therefore, the phase difference acquired by the laser beams traveling in the two arms of the interferometer can be expressed as:

$$\begin{aligned}\delta\phi(t) &= \phi_x(t) - \phi_y(t) \\ &= \frac{2\omega_0(l_x - l_y)}{c} + \delta\phi_{GW},\end{aligned} \tag{2.8}$$

where the phase acquired for a passing GW $\delta\phi_{GW}$ is denoted by:

$$\delta\phi_{GW} = \omega_0 \int_{t-2l/c}^{t} h(\tau)d\tau. \tag{2.9}$$

Moreover, the second term in equations (2.6) and (2.7) have been approxi-

mated since the arm lengths are nearly identical, meaning that $l_x \approx l_y = l$.

Thus, the passage of a GW alters the condition of interference, resulting in observable power fluctuations at the PD. Furthermore, the passage of a GW with a long wavelength, i.e., one comparable to the arm length of the interferometer and corresponding to GWs in the kHz frequency range, leads to a phase shift that changes more slowly than the light round trip travel time. The related phase change can be approximated to:

$$\delta\phi_{GW} \approx \frac{2\omega_0 l}{c} h. \tag{2.10}$$

Considering a GW with an angular frequency $\omega_{GW} = 2\pi f_{GW}$, that produces a strain $h(t) = he^{i\omega_{GW}t}$, using equation (2.9), the phase shift becomes:

$$\begin{aligned} \delta\phi_{GW} &= \frac{2l\omega_0}{c} e^{-il\omega_{GW}/c} \frac{\sin(l\omega_{GW}/c)}{l\omega_{GW}/c} he^{i\omega_{GW}t} \\ &= H_{MICH}(\omega_{GW}, l) he^{i\omega_{GW}t}, \end{aligned} \tag{2.11}$$

where $H_{MICH}(\omega_{GW}, l)$ is the frequency response of the Michelson interferometer for the passage of a GW [57]. The trend of the phase shift due to the passage of a GW in a Michelson interferometer as a function of the frequency of the GW. This Transfer Function (TF) is shown in *Fig. 2.2*.

As expressed in equation (2.10), the longer the arms of the Michelson interferometer, the more sensitive it becomes to changes in path length. However, there are practical limitations to construct extremely long detectors. Therefore, to increase the effective path length traveled by the light, without physically extending the arms of the interferometer, Fabry-Perot (FP) cavities can be employed in the arms. Incorporating FP cavities allow the laser beam to be reflected back and forth multiple times within the arms of the interferometer, effectively increasing the arm lengths.

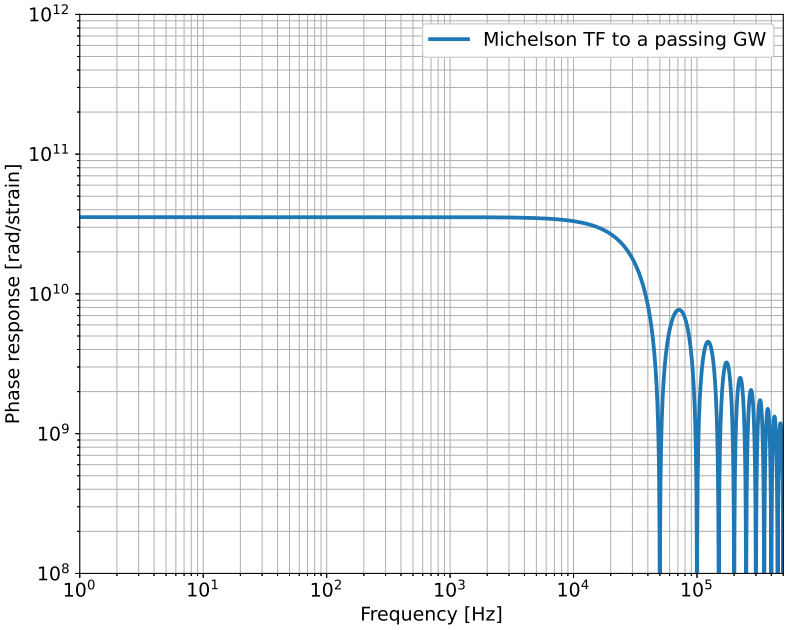

Figure 2.2: Michelson interferometer response to the passage of a GW. The interferometer parameters used for this figure are: $\mathrm{l} = 3\,km$ and wavelength of the laser beam $\lambda = 1064\,\mathrm{nm}$.

2.1.2 Fabry-Perot Cavity

A Fabry-Perot (FP) cavity consists of two mirrors facing each other, typically with a high reflectivity. Light is partially transmitted and partially reflected at each mirror. Inside the cavity, light undergoes multiple reflections building-up the intra-cavity electric field. A sketch of a FP cavity is shown in *Fig. 2.3*.

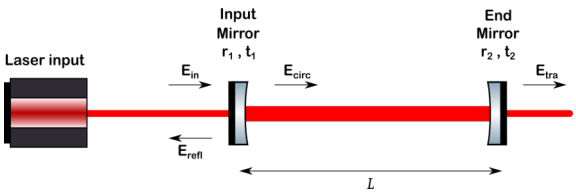

Figure 2.3: Sketch of a Fabry-Perot Cavity of length L including mirror parameters and characteristic electric fields.

For a FP cavity characterized by a length L, reflectivities (r_1, r_2) and transmissivities (t_1, t_2) of the input and end mirrors, respectively, the power circulating $P_{circ} = E_{circ} \cdot E^*_{circ}$ within the cavity is given by:

$$P_{circ} = \frac{t_1^2}{(1 - r_1 r_2)^2 + 4 r_1 r_2 \sin^2(kL)} P_{in}, \tag{2.12}$$

where $P_{in} = E_{in} \cdot E^*_{in}$ is the input power and $k = 2\pi/\lambda$ is the wave number. The resonance condition of the cavity is met when the optical path length is a multiple integer of the wavelength of the input light. It can be expressed as:

$$2\pi m = kL, \tag{2.13}$$

where m is an integer. In this condition, equation (2.12) becomes:

$$P_{circ} = \frac{t_1^2}{(1 - r_1 r_2)^2} P_{in}. \tag{2.14}$$

This resonance condition is met at each half-wavelength, which is defined as the Free Spectral Range (FSR) of the cavity. This characteristic parameter can be expressed also in frequency as:

$$\Delta f_{FSR} = \frac{c}{2L}. \tag{2.15}$$

The linewidth of a cavity, a key characteristic parameter, indicates the range of frequencies for which a laser beam is resonant. Typically defined by the Full Width at Half Maximum (FWHM) of the resonance peak, the linewidth is

calculated as follows:

$$FWHM = \frac{2\Delta f_{FSR}}{\pi} \arcsin\left(\frac{1 - r_1 r_2}{2\sqrt{r_1 r_2}}\right). \tag{2.16}$$

In resonant state, the power inside the cavity is enhanced. The enhancement in power is influenced by the finesse $\mathcal{F}$ of the cavity, which is defined as the ratio of the FSR to the linewidth:

$$\mathcal{F} = \frac{\Delta f_{FSR}}{FWHM} = \frac{\pi}{2 \arcsin\left(\frac{1-r_1 r_2}{2\sqrt{r_1 r_2}}\right)}. \tag{2.17}$$

In the context of GW detectors, where the reflectivities r_1 and r_2 are nearly 1, the argument of the arcsin function is small and equation (2.17) can be approximated to:

$$\mathcal{F} \approx \frac{\pi\sqrt{r_1 r_2}}{1 - r_1 r_2} \approx \frac{\pi}{1 - r_1 r_2}. \tag{2.18}$$

The storage time, or average time, τ_s, represents the time the photons remain in the cavity, is determined by the finesse as $\tau_s = 2L\mathcal{F}/c\pi$. Then, starting from the storage time we can define the cavity pole f_c as:

$$f_c = \frac{1}{2\pi\tau_s}. \tag{2.19}$$

The cavity pole denotes the frequency beyond which any induced change within the field of the cavity is canceled. The cavity pole originates from the fact that a cavity storage time is not infinite.

In order to study the response of a FP cavity to the passage of a GW, the reflected electric field should be defined. Considering the parameters of the cavity shown in *Fig. 2.3*, the reflected electric field can be expressed as:

$$E_{refl} = -\frac{r_1 - r_2(1 - \mathcal{L})e^{2ikL}}{1 - r_1 r_2 e^{2ikL}} E_{in}, \tag{2.20}$$

where $\mathcal{L}$ denotes the losses of the input mirror. The resonance condition of a FP cavity is given by $e^{2ikL} = 1$. For the case of a resonant cavity with a lossless input mirror and exposed to the passage of a GW inducing a change of length δL, equation (2.20) can be approximated to [58]:

$$E_{refl}(\delta L) = \frac{r_2 - r_1}{1 - r_1 r_2}\left(1 + i2k\delta L \frac{r_2(1-r_1)^2}{(1-r_1 r_2)(r_2 - r_1)}\right) \approx \frac{r_2 - r_1}{1 - r_1 r_2} e^{i\phi_{FP}(\delta L)}, \tag{2.21}$$

where $\phi_{FP}(\delta L)$ represents the phase shift in the reflected field by the FP cavity as a result of δL. For fully reflective end mirrors ($r_2 = 1$), $\phi_{FP}(\delta L)$ can be expressed as:

$$\phi_{FP}(\delta L) = \frac{2\mathcal{F}}{\pi} 2k\delta L. \tag{2.22}$$

Thus, employing resonant FP cavities in the arms of an interferometer can enhance the power circulating and magnify the phase shift induced by changes in the cavity length by a factor of $2\mathcal{F}/\pi$.

2.1.3 Fabry-Perot Michelson interferometer

For a given Michelson interferometer, the addition of FP cavities in each arm can effectively increase the sensitivity. A configuration of a FP-Michelson interferometer can be seen in *Fig. 2.4*: L_x denotes the length of the FP cavity along the x axis; L_y denotes the length of the FP cavity along the y axis.

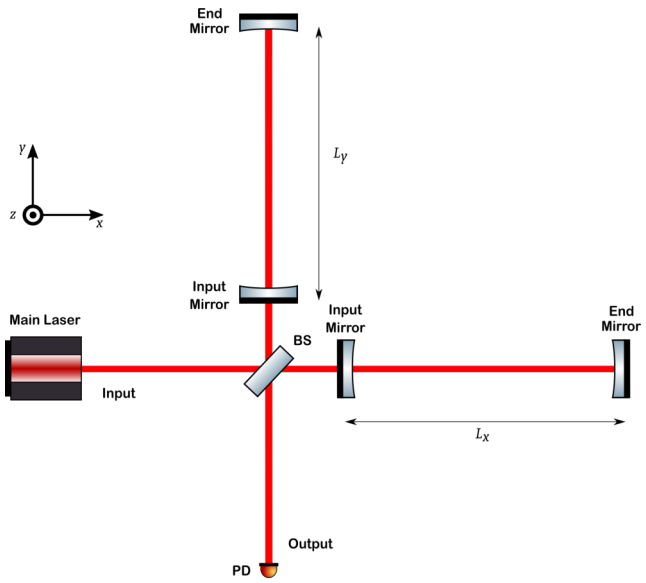

Figure 2.4: Fabry-Perot Michelson interferometer

For the arm aligned with the x axis, the phase change $\delta\phi_{FP,x}$ induced by a

length variation δL_x between the two mirrors of the FP cavity, caused by the passage of a GW propagating perpendicular to the $x-y$ plane and having a plus polarization, is given by:

$$\delta\phi_{FP,x} \approx \frac{4k\mathcal{F}}{\pi}\delta L_x. \tag{2.23}$$

Similarly, the phase shift along the arm aligned with the y axis can be obtained by inverting the sign of the phase shift induced along the x arm ($\delta\phi_{FP,y} = -\delta\phi_{FP,x}$). Then, the overall phase shift in a Michelson interferometer with FP cavity arms is described as:

$$\delta\phi_{FP-MICH} = \phi_{FP,x} - \phi_{FP,y} = 2\delta\phi_{FP,x} = \frac{8k\mathcal{F}}{\pi}\delta L_x. \tag{2.24}$$

Assuming that the two FP cavities in the arms are identical, taking into account the cavity storage time for the photons, the pole of the cavity f_c and the response of the Michelson interferometer to a passing GW described in equation (2.11), equation (2.24) becomes:

$$\delta\phi_{FP-MICH} = \frac{4\mathcal{F}}{\pi}\frac{1}{\sqrt{1+(f_{GW}/f_c)^2}}H_{MICH}he^{i\omega_{GW}t}. \tag{2.25}$$

Therefore, adding FP cavities alters the response of the Michelson interferometer to the passage of a GW and enhances its sensitivity. *Fig. 2.5* shows a comparison between the frequency response of a Michelson interferometer and the one of a FP-Michelson interferometer.

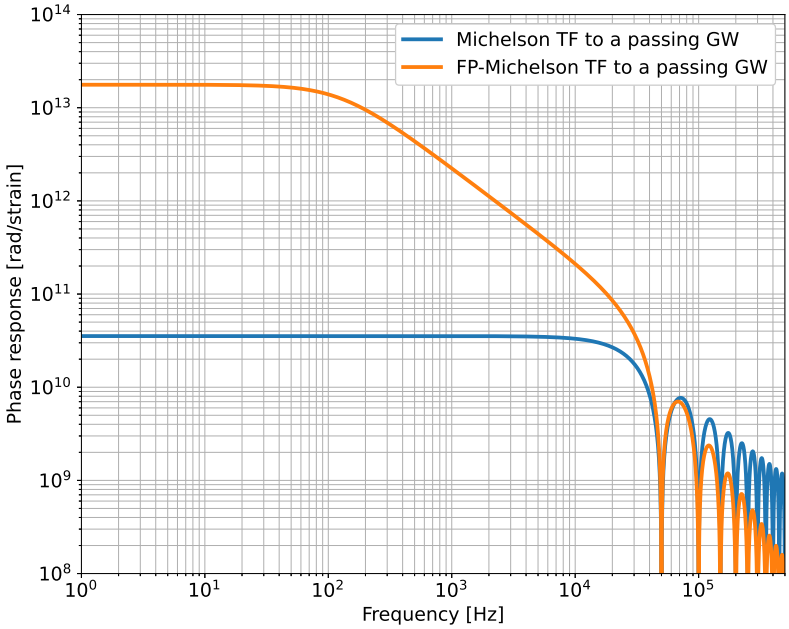

Figure 2.5: Comparison between a Michelson interferometer and a FP-Michelson interferometer Transfer Functions (TFs) to the passage of a GW. The interferometer parameters used for this figure are: arm length of 3 km and wavelength of the laser beam of 1064 nm. The addition of FP cavities in the arms of a Michelson interferometer modifies its response and enhances the sensitivity at lower frequencies (below 10 kHz). In this case by a factor of ~ 500.

2.1.4 Power-Recycling Cavity

The working point of a GW detector is tuned to have a destructive interference for the light beams coming back from the arm cavities, the so-called Dark Fringe (DF) configuration [59, 60]. In this configuration, resulting in minimal or zero intensity of the laser beam at the output, most of the light is reflected back towards the input port of the interferometer and lost. In order to not waste this light and re-inject it into the system, a semi-reflective mirror, the Power Recycling Mirror (PRM), is installed between the laser source and the BS. Thereby, the installation of the PRM boosts the effective power inside the interferometer. This configuration is shown in the left side of *Fig. 2.6*: l_{pr} is the distance between the PRM and the BS; l_x and l_y are the distances between the BS and the input mirrors along the x and y axes, respectively; L_x denotes the length of the FP cavity along the x axis; L_y denotes the length of the FP cavity along the y axis.

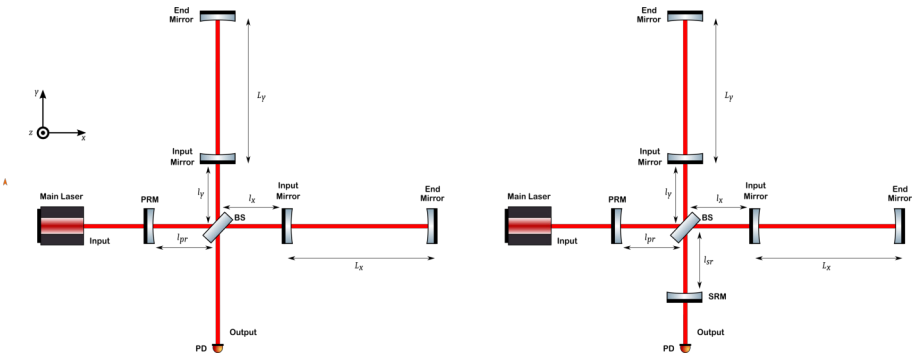

Figure 2.6: Left: Power Recycling FP Michelson interferometer. Right: Dual Recycling FP Michelson interferometer.

In order to study the behaviour of the updated configuration of the detector, we can make some simplifications: since FP cavities can be treated as an equivalent reflective mirror [61], the same can be applied to a Michelson interferometer with FP cavity arms. In this framework, the interferometer acts as a mirror with reflectivity and transmissivity that change depending on the resonance condition of the FP cavities and the working point of the Michelson interferometer. In this perspective, the entire FP-Michelson interferometer can modeled as a single mirror that, together with the PRM, forms a FP cavity, as shown in *Fig. 2.7*.

When the system is on resonance, the circulating power in the detector is

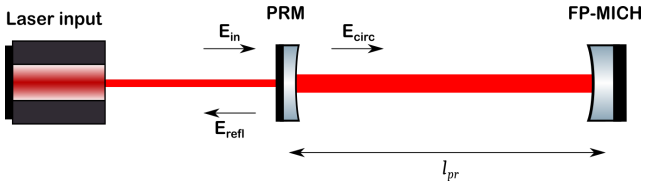

Figure 2.7: Cavity made by the PRM and the compound FP-Michelson interferometer.

increased by a gain factor g_{PR}, which is given by [62]:

$$g_{PR} = \frac{1 - r_{PR}^2}{\left(1 - r_{PR} r_{FP-MICH}\right)^2}, \tag{2.26}$$

where r_{PR} represents the reflectivity of the PRM and $r_{FP-MICH}$ denotes the reflectivity of the compound FP-Michelson interferometer.

2.1.5 Signal-Recycling Cavity

In a Fabry-Perot-Michelson interferometer enhanced with the installation of a PRM, placing a partially reflective mirror, the Signal Recycling Mirror (SRM), between the BS and the output port allows to shape the sensitivity of the detector. A sketch of a GW detector including a SRM is shown on the right side of *Fig. 2.6*: l_{sr} is the distance between the SRM and the BS. The installation of a SRM creates another optical cavity with the input mirrors: the Signal Recycling Cavity (SRC). The SRM effectively shifts the frequency of the cavity pole to a higher value, therefore broadening the frequency range over which the detector's response to the passage of GWs is optimized.

The impact of a passing GW on the laser beam is to create differential signal side-bands in the light that travels through the two arms. These side-bands have identical amplitudes but opposite signs. When they are constructively recombined at the BS, they move toward the SRM. Here, the differential side-bands encounter an equivalent input mirror, comprising the FP input mirror (IM) and the SRM. The reflection and transmission coefficients, labeled r_{SRC} and t_{SRC}, for this equivalent mirror are influenced by the precise adjustment of the signal recycling cavity's length, affecting the phase of the beam as it passes through this cavity. The signal recycling cavity length is the distance between the SRM and the input mirror, given by $l_{sr} + \frac{l_x + l_y}{2}$. The phase of the beam in the signal recycling cavity is given by:

$$\phi_{SRC} = k[l_{sr} + \frac{l_x + l_y}{2}]. \tag{2.27}$$

The reflection coefficient is expressed as:

$$r_{SRC} = \frac{r_{IM} - r_{SR}e^{2i\phi_{SRC}}}{1 - r_{IM}r_{SR}e^{2i\phi_{SRC}}}, \tag{2.28}$$

and the transmission coefficient is given by:

$$t_{SRC} = \frac{t_{IM}t_{SR}e^{i\phi_{SRC}}}{1 - r_{IM}r_{SR}e^{2i\phi_{SRC}}}, \tag{2.29}$$

where r_{IM}, r_{SR} and t_{IM}, t_{SR} are the reflectivity and transmissivity of the IM and SRM, respectively.

When ϕ_{SRC} equals zero, the signal recycling cavity is tuned for resonance with the carrier field. In this configuration, the reflectivity of the equivalent input mirror is lower than the one of the FP input mirror, decreasing the finesse of the FP cavity seen by the passing GW side-band signals. In this working point the pole of the cavity is shifted to higher frequencies, enhancing the bandwidth sensitivity of the detector.

2.2 Achieving the working point

2.2.1 Control Theory

To obtain the maximum sensitivity of the GW detectors, all the optical cavities must be on resonance, requiring the implementation of several control loops.

Control theory is an interdisciplinary field that deals with the behavior of dynamical systems. Typically, the systems under study are denoted as the *plant* (G), which has inputs (u), outputs (y), and internal dynamics. To maintain a desired working point, given by a *reference* or *set point* signal (r), a controller manipulates the input signal by applying a correction signal. The input for this controller is denoted as *error signal* (e), which is the difference between the reference signal and the output signal of the plant. A block diagram of a control loop system is shown in *Fig. 2.8*.

For a Linear Time-Invariant (LTI) system [63], the Laplace transform can be used to represent relations between signals with algebraic equations in the s-domain. This simplifies the analysis and the design of control systems. In the Laplace transform, the dynamics of the systems can be described using transfer

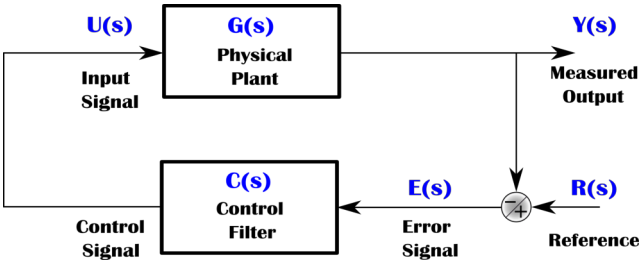

Figure 2.8: Block diagram of a control loop system.

functions (TFs). For the system presented in *Fig. 2.8*, the transfer functions of the plant and the controller are denoted by $G(s)$ and $C(s)$, respectively. The Laplace transforms of the reference, error, input, and output signals are given by $R(s)$, $E(s)$, $U(s)$ and $Y(s)$, respectively.

Open Loop Transfer Functions (OLTFs) and Closed Loop Transfer Functions (CLTFs) are crucial tools for system analysis and design. OLTFs provide insights into the intrinsic characteristics of the system, which can be used to assess stability, examine transients, and evaluate frequency response [63]. In contrast, CLTFs consider the system's behaviour under feedback control, allowing for precise tuning of the system to meet specific performance and maintain stability, even in the presence of disturbances. For the basic feedback system illustrated in *Fig. 2.8*, the OLTF and CLTF can be derived using the following relations:

$$\begin{aligned} E(s) &= R(s) - Y(s) \\ U(s) &= C(s)E(s) \\ Y(s) &= G(s)U(s). \end{aligned} \tag{2.30}$$

Thus, the relation between the set point $R(s)$ and the output $Y(s)$ is given by:

$$\frac{Y(s)}{R(s)} = T(s) = \frac{G(s)C(s)}{1 + G(s)P(s)} = \frac{G(s)C(s)}{1 + L(s)}, \tag{2.31}$$

where $T(s)$ is the CLTF and $L(s) = G(s)P(s)$ is the OLTF. The denominator of the CLTF represents the characteristic equation of the system. If this denominator equals zero, the system becomes unstable.

Different approaches can be used to design control loops. For simple systems and simple control tasks, one can use a Single-Input Single-Output (SISO)

approach. On the other hand, Multiple-Input Multiple-Output (MIMO) can be used in more complex scenarios, where several variables, and internal dynamics must be considered and need to be controlled simultaneously.

In control engineering, systems are often classified based on the number of inputs and outputs they have. A SISO system is characterized by having only one input and one output. In essence, this implies that there is a single control signal that affects a single process or plant, resulting in a single measured output. In a SISO system, the control algorithm processes the feedback from the output to adjust the input signal, aiming to regulate the system's behavior and achieve the desired performance. The simplicity of SISO systems makes them easier to be analyzed, designed, and implemented compared to more complex systems. However, real physical systems are characterized by internal couplings and multiple dynamics that, can not be fully described by using just one input and one output.

On the other hand, a MIMO system has numerous inputs and numerous outputs. In MIMO systems, multiple control signals can affect multiple processes simultaneously, resulting in multiple measured outputs. MIMO systems are often encountered in complex industrial processes or aerospace systems. GW detectors can also be described using a MIMO approach, since interactions among various inputs and outputs are significant as it will be shown in Chapter 3. Designing control algorithms for MIMO systems requires careful consideration of these interactions to ensure stability, performance, and robustness. While MIMO systems offer more flexibility and capability to address complex control tasks, they also pose greater challenges in terms of analysis, design, and implementation compared to SISO systems due to their increased complexity and mutual interactions.

For SISO feedback systems, and for a single pair of inputs and outputs in MIMO systems, a typical tool for studying stability is the Bode plot [63], which consists of the Magnitude and Phase trends in frequency of the TFs. A key aspect of this plot is the Unity Gain Frequency (UGF), where $|G(s)C(s)| = 1$, which is the frequency at which the magnitude of the OLTF equals one (or 0 dB). At this frequency, one determines the Phase Margin, which indicates the amount of additional phase lag required for the system to become unstable. A greater phase margin suggests that the system is more resistant to changes and disturbances. Another important aspect is the Phase Crossover Frequency, which is where the phase crosses -180 deg. At this frequency, one determines the Gain Margin, indicating the maximum increase of gain for the

system allowed to remain stable. A greater gain margin indicates a more stable system. An example of a Bode plot for a feedback system, indicating its stability margins, is shown in *Fig. 2.9*.

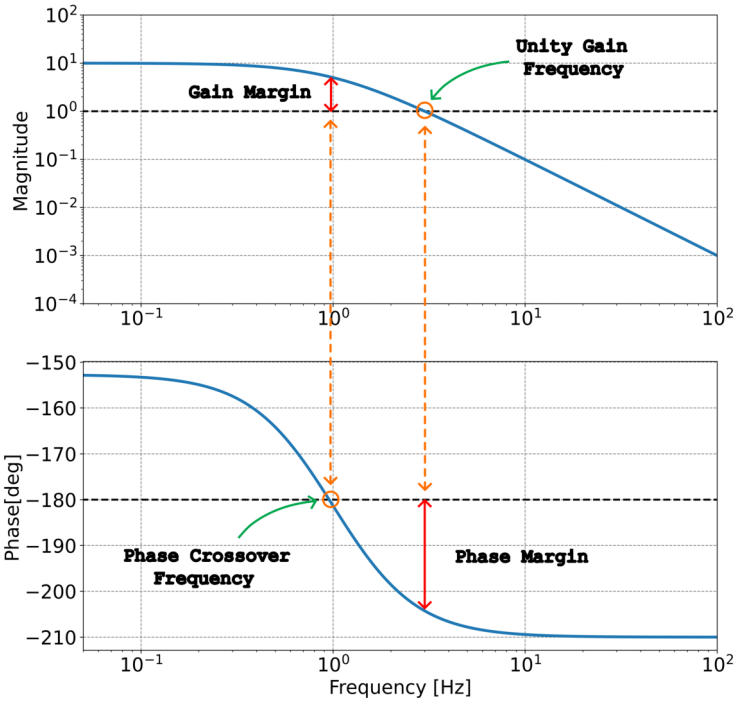

Figure 2.9: Bode plot of a simple feedback system: the top plot shows the magnitude and the bottom one shows the phase.

2.2.2 Pound-Drever-Hall Technique

The Pound-Drever-Hall (PDH) technique [64] is a commonly used method for stabilizing laser frequency and controlling optical cavity length, as the one shown in *Fig. 2.10*. This technique is broadly used in GW detectors. Essentially, it enables the generation of an error signal that can either stabilize the frequency of the laser source when the cavity length is constant or control and stabilize the cavity length when the frequency of the laser source is stable. In this technique, an Electro-Optic Modulator (EOM) is used to phase modulate

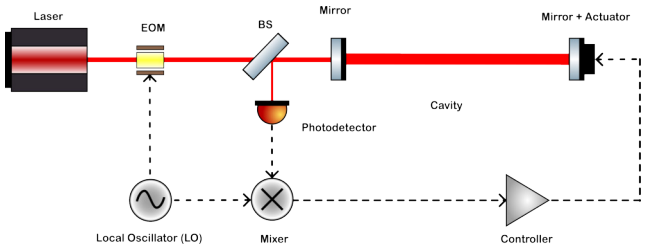

Figure 2.10: Basic layout for locking a cavity to a laser: The reflected signal is sensed with a photodetector and is mixed with the local oscillator signal; the output of the mixer is sent to the actuator through a controller.

the laser beam before it enters a FP cavity. The modulation process generates side-bands around the main carrier frequency of the laser source. Thus, the electric field after the EOM can be expressed as:

$$E_{in} = E_0 e^{i(\omega t + \beta \sin \Omega t)}, \tag{2.32}$$

where ω represents the laser's (angular) frequency, Ω is the modulation frequency, and β represents the modulation index. To accurately control the length of an optical cavity, the carrier frequency is chosen to be resonant within the cavity, while the side-bands are chosen to be anti-resonant. Equation (2.32) can be expanded using Bessel functions $J_n(\beta)$ [65]. Thus, neglecting higher-order side-bands with smaller amplitudes, equation (2.32) becomes:

$$E_{in} = E_0 e^{i\omega t}(J_0(\beta) + iJ_1(\beta)e^{-i\Omega t} + iJ_1(\beta)e^{i\Omega t} + ...), \tag{2.33}$$

where $J_0(\beta)$ and $J_1(\beta)$ are the zeroth and first order Bessel functions, respectively. This means that the modulated electric field entering the cavity is represented by a carrier field and a pair of side-bands. The total power can be expressed as $P_0 \approx P_c + 2P_{sb}$, where $P_c = {J_0}^2(\beta)P_0$ is the power of the carrier, and $P_{sb} = {J_1}^2(\beta)P_0$ is the power of each side-band. The field reflected off the optical cavity can be expressed as:

$$E_{refl} = E_0 e^{i\omega t}\left(F(\omega)J_0(\beta) + F(\omega+\Omega)J_1(\beta)e^{i\Omega t} - F(\omega-\Omega)J_1(\beta)e^{-i\Omega t}\right), \tag{2.34}$$

where $F(\omega, \Omega)$ is the reflection coefficient, which depends on the laser angular frequency ω for the carrier and on Ω for the side-bands. It can be expressed as:

$$F(\omega,\Omega)=\frac{r(e^{i\phi}-1)}{1-r^2e^{i\phi}}, \tag{2.35}$$

where r is the reflectivity of the cavity mirrors, and ϕ is the phase that the beam acquires in a round trip, given by $\phi = 2\omega L/c$ for the carrier and by $\phi = 2(\omega \pm \Omega)L/c$ for the side-bands. In general, the phase acquired by the beam can be described in terms either of the laser frequency and the free spectral range of the cavity as $\phi = 2\pi f/\Delta f_{FSR}$; or of the round trip optical path in the cavity in light wavelengths as $\phi = 2\pi 2L/\lambda$.

A photo-detector is used to sense the power reflected from the cavity, which is expressed as:

$$\begin{aligned}P_{\text{refl}} &= P_c|F(\omega)|^2 + P_{sb}\left[|F(\omega+\Omega)|^2 + |F(\omega-\Omega)|^2\right]\\ &+ 2\sqrt{P_cP_{sb}}\Re\left[F(\omega)F^*(\omega+\Omega) - F^*(\omega)F(\omega-\Omega)\right]\cos(\Omega t)\\ &+ 2\sqrt{P_cP_{sb}}\Im\left[F(\omega)F^*(\omega+\Omega) - F^*(\omega)F(\omega-\Omega)\right]\sin(\Omega t)\\ &+ (\text{terms at } 2\Omega \text{ and higher}).\end{aligned} \tag{2.36}$$

Three waves with distinct frequencies are combined: the carrier at ω, and the upper and lower side-bands at $\omega+\Omega$ and $\omega-\Omega$. The outcome is a wave with frequency ω, characterized by an envelope that exhibits a beat pattern with two frequencies. The terms related to $\omega \pm \Omega$ result from the interference between the carrier and the side-bands, while the terms with 2Ω originate from the interference between the side-bands themselves. We focus on the two terms oscillating at the modulation frequency, since they sample the phase of the reflected carrier. Equation 2.36 includes both a sine term and a cosine term. Typically, only one of these terms will be significant, while the other will disappear. The modulation frequency determines which term vanishes and which persists. For low modulation frequencies the expression $F(\omega)F^*(\omega+\Omega) - F^*(\omega)F(\omega-\Omega)$ is purely real, and only the cosine term persists. On the other hand, at high modulation frequencies, i.e. when $\Omega \gg \Delta f_{FSR}/\mathcal{F}$ ($\mathcal{F}$ is the finesse of the cavity) and near resonance, this expression becomes purely imaginary, and only the sine term remains.

The signal recorded by the PD produces a voltage V_{refl} that is proportional to the reflected power P_{refl}. This voltage is then mixed with the signal from the local oscillator (LO), which operates at the same frequency (modulation frequency) as the one used for the EOM. The output from this mixing process is then passed through a Low Pass Filter (LPF), which isolates the terms

that are proportional to the beating between the carrier and the side-bands ($\omega \pm \Omega$) from higher frequency components. This filtered signal is the PDH error signal, denoted as e, used to control the length of a cavity, i.e. keeping the resonance condition of the cavity. The phase of the signal at the LO, denoted as ϕ_{LO}, can be adjusted. This adjustment allows the extraction of specific components of the mixed signal, effectively filtering out the desired signal component that is in-phase or quadrature (90 degrees out of phase) with the LO signal. Thus, after mixing and filtering, the output signal that is in-phase with the LO's modulation signal can be isolated. This in-phase component is directly proportional to the $\sin \Omega t$ term, then the error signal is expressed by:

$$e = 2\sqrt{P_c P_{sb}}\Im[F(\omega)F^*(\omega+\Omega) - F^*(\omega)F(\omega-\Omega)]. \tag{2.37}$$

In the fast modulation case and near resonance, which is the typical case in GW detectors, it is possible to assume that the reflection coefficients for the side-bands, $F(\omega+\Omega)$ and $F(\omega-\Omega)$, approach -1, signifying almost total reflection at these frequencies. Then, $F(\omega)F^*(\omega+\Omega) - F^*(\omega)F(\omega-\Omega) \approx -i2\Im[F(\omega)]$, resulting in an error signal given by:

$$e = 4\sqrt{P_c P_{sb}}\Im[F(\omega)]. \tag{2.38}$$

Near resonance, the phase acquired by the beam can be expressed as:

$$\phi \approx 2\pi N + 4\pi\frac{\delta L}{\lambda}, \tag{2.39}$$

where δL represents a slight deviation in the cavity length from resonance and N is an integer. This indicates that even very minor changes in the cavity length, as small as a fraction of a wavelength, can significantly affect the system. Then, rewriting the reflection coefficient $F(\omega)$ in terms of the small length displacement δL, it becomes:

$$F(\delta L) = \frac{r(e^{i4\pi\delta L/\lambda}-1)}{1-r^2e^{i4\pi\delta L/\lambda}} \approx \frac{r}{1-r^2}\left(i\frac{4\pi\delta L}{\lambda}\right) \approx i\frac{4\mathcal{F}}{\lambda}\delta L. \tag{2.40}$$

Finally, the error signal obtained with this technique is proportional to the change in the cavity length (or the frequency of the laser), and is given by:

$$e(\delta L) = -16\sqrt{P_c P_{sb}}\mathcal{F}\frac{\delta L}{\lambda}. \tag{2.41}$$

The linearity of the error signal near resonance enables the application of standard control theory tools to control the cavity length (or laser frequency).

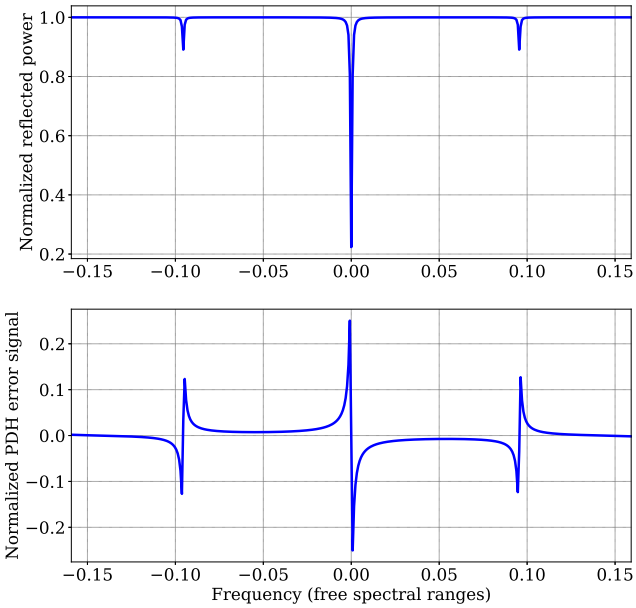

Figure 2.11: PDH error signal in free spectral ranges for a cavity with identical mirrors, a high demodulation frequency of 50 MHz and a modulation index $\beta = 0.7$.

The top plot of *Fig. 2.11* shows the reflected power of a FP cavity with identical mirrors without losses: the reflected power is minimum when the carrier crosses the resonance, meaning that all the power circulates in the cavity. Note that in real cases also the side-bands can be slightly resonant. The bottom plot of *Fig. 2.11* shows the PDH error signal: the error signal crosses zero when any of the beams, the carrier or the side-bands, achieve resonance within the cavity. Note that the sign of the slope is opposite for the carrier and the side-bands.

2.3 Advanced Virgo Plus detector

The Advanced Virgo Plus detector is a gravitational-wave detector located near Pisa, Italy. It employs a dual-recycling Fabry-Perot Michelson interferometer (DRFPMI) configuration, which incorporates a BS, a PRM, a SRM, and FP cavities, each with a length of 3 km in the arms of the Michelson interferometer.

This detector is part of a global network of gravitational-wave detectors, which includes the two LIGO observatories in the United States [1] and the KAGRA detector in Japan [55].

Advanced Virgo Plus represents an upgrade of the Advanced Virgo detector, implemented in two phases. Phase I, completed in 2020, aims at enhancing and shaping the detector's sensitivity. Key improvements includes increasing the power of the input laser beam to reduce the impact of the shot noise, installing a SRM to shape the detector's bandwidth, and implementing the frequency-dependent squeezing (FDS) system to effectively reduce the quantum noise impact across low, medium, and high frequency bands, thereby a broadband enhancement of the sensitivity.

Phase II focuses on minimizing mirror thermal noise to further increase the detector's sensitivity. This will be achieved by altering the beam geometry in the arm cavities to increase the beam size on the end mirrors, which reduces the thermal noise impact by averaging out the mirror surface vibrations over a larger area. Using larger beams implies the installation of larger and heavier end mirrors. Additionally, this phase plans to introduce improved coatings with lower mechanical losses to reduce the coating thermal noise. Together with an increase of the power of the laser beam, these upgrades aim to significantly enhance the detector's sensitivity.

The optical scheme for the Phase I configuration, implemented in view of the Observing Run 4 (O4), is shown in *Fig. 2.12*. The entire detector is divided into four main parts: the input optics system, the main interferometer, the output optics and the frequency-dependent squeezing system.

- **Input optics system**: The main beam of the interferometer is generated by a Nd:YAG laser system, its wavelength λ is 1064 nm. This system is designed to provide the laser beam with the required power, geometric shape, frequency and pointing stability to be matched into the interferometer. The frequency of the laser is pre-stabilized with a series of cavities, among which a triangular Input Mode Cleaner (IMC) cavity. Three EOMs are installed along the beam path to provide the modulation frequencies needed to control all the optical cavities. A mode matching telescope is installed to modify the properties of the input beam to match and inject it into the interferometer.

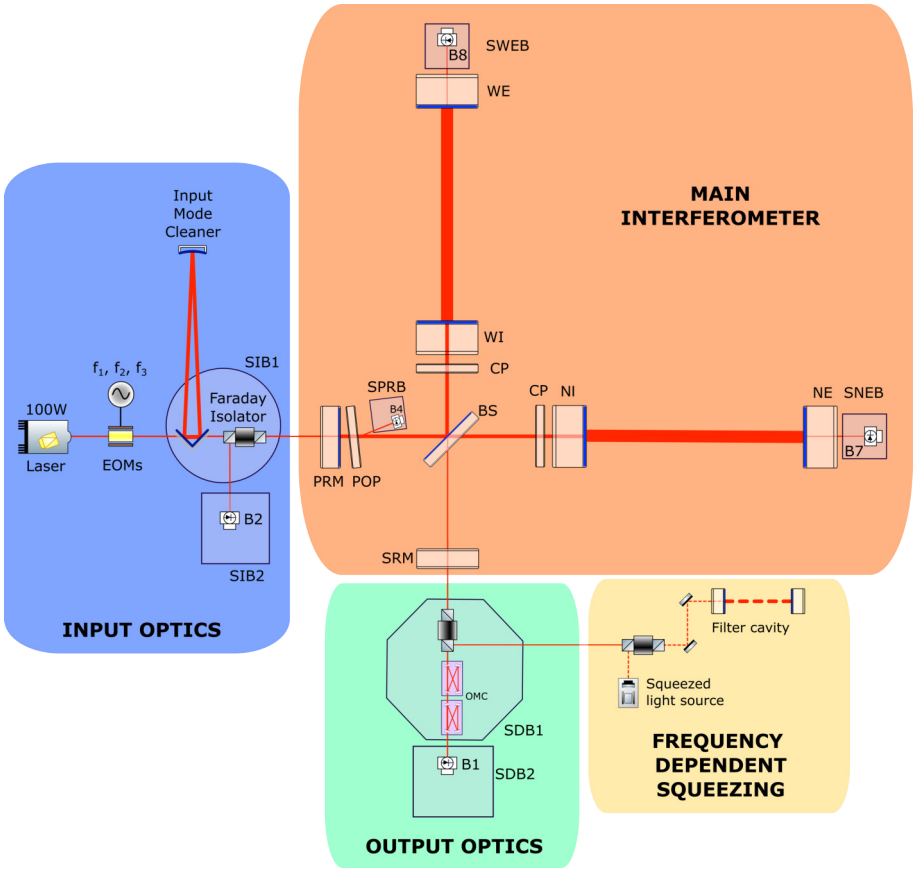

Figure 2.12: Advanced Virgo Plus optical configuration implemented in view of O4.

- **Main interferometer**: It consists of seven main mirrors: the PRM, the 50:50 BS, the SRM, the North Input (NI) mirror together with the North End (NE) mirror forming the FP cavity along the North arm, and the West Input (WI) mirror together with the West End (WE) mirror forming the FP cavity along the West arm. The shorter arms of the Michelson interferometer are formed by the BS, NI, and WI mirrors. The PRM together with the NI and WI mirrors forms the PRC, while the SRM together with the NI and WI mirrors forms the SRC.

- **Output optics**: At the output port of the interferometer the beam passes through the Output Mode Cleaner (OMC) cavity, placed in between the SRM and the photo-diodes used to detect GWs. This cavity is used to filter out control side-bands and higher-order-spatial modes [65], which can be generated by imperfections or misalignments of the main interferometer. A mode matching telescope is installed to adapt the properties of the interferometer beam to match it into the OMC.

- **Frequency Dependent Squeezing system**: It consists of a Frequency Independent Squeezing (FIS) source and a Filter Cavity with a length of 285 m. By injecting FDS light into the interferometer´s output through a Faraday isolator, before the OMC, the broadband quantum noise level can be reduced.

Fig. 2.12 shows also all the suspended benches and the names of the photo-diodes that sense the main beams extracted from the interferometer. These beams are summarized in *Table 2.1*.

Photo-diode	Measured beam
B1	Output beam from the interferometer.
B2	Reflected beam from the interferometer.
B4	Pick-off from the beam between the PRM and the BS.
B7	Transmitted beam through the North arm cavity.
B8	Transmitted beam through the West arm cavity.

Table 2.1: Main photo-diodes and beams in Advanced Virgo Plus.

The designed sensitivity curves for both Phase I and Phase II are shown in *Fig. 2.13*.

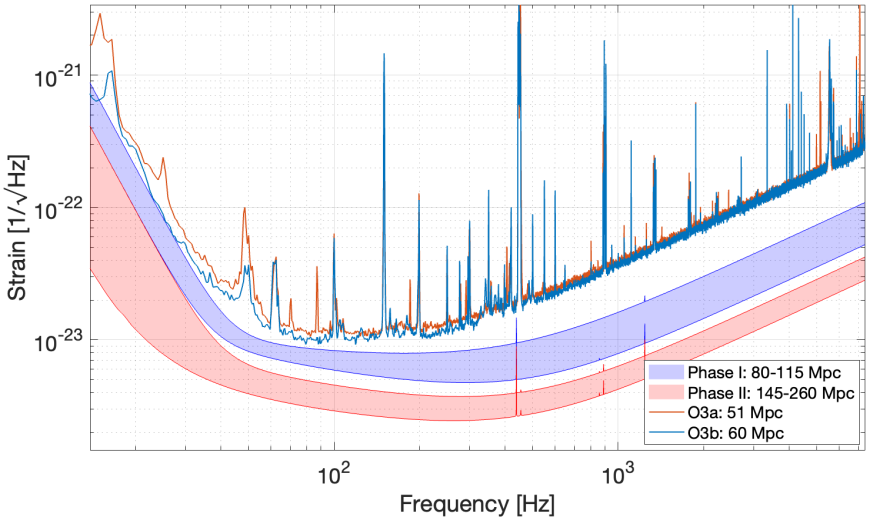

Figure 2.13: Advanced Virgo Plus designed sensitivity curves for Phase I and Phase II compared to the maximum sensitivities obtained during O3a and O3b.

In this figure the maximum obtained sensitivity curves during O3a and O3b are depicted in red and blue. The blue shaded region is the sensitivity achievable during Phase I depending on the configuration [66]: the upper limit means a low input power, injection of only FIS and no Newtonian noise mitigation, while the lower part means a higher input power, injection of FDS and implementation of Newtonian noise subtraction. The red shaded region is the sensitivity achievable during Phase II depending on the configuration [66]: the upper limit means the use of the current coatings for the mirrors and low input power, while the lower part means the use of improved coatings on the mirror reducing the impact of the thermal noise and higher input power.

2.3.1 Length sensing and control

Adding new mirrors, such as in the case of the upgrades of the Advanced Virgo Plus, increases the number of cavities and, therefore, the number of Degrees of Freedom (DoF) to be controlled. The correct working point of the interferometer is obtained when all the optical cavities are on resonance for the carrier beam to achieve maximum detector's sensitivity. In a Dual-Recycled Fabry-Perot Michelson Interferometer (DRFPMI) configuration, there are five main longitudinal DoFs defined as follows:

- **DARM** = $\frac{L_N - L_W}{2}$: **D**ifferential **ARM** length of the two FP cavities in the arms. This is the most crucial DoF, since it is the one sensitive to the passage of GWs.
- **CARM** = $\frac{L_N + L_W}{2}$: **C**ommon **ARM** length, average of the long arm lengths.
- **MICH** = $l_N - l_W$: Length difference between the lengths from the BS and, respectively, the NI and the WI mirrors, forming the **MICH**elson interferometer.
- **PRCL** = $l_{PR} + \frac{l_N + l_W}{2}$: **P**ower **R**ecycling **C**avity **L**ength.
- **SRCL** = $l_{SR} + \frac{l_N + l_W}{2}$: **S**ignal **R**ecycling **C**avity **L**ength.

The lengths of these various cavities, which form the above DoFs, are illustrated in *Fig. 2.14*, together with a list of the side-bands generated to control the full interferometer.

Note that not all the side-bands are resonant in all the cavities. By design, all the side-bands, except the ones multiple of f_4, are resonant in the IMC and pass through it going into the interferometer. The side-bands at f_4, which are reflected by the IMC, are used to control the IMC length. None of the side-bands is resonant inside the FP arm cavities. f_1 is defined to be resonant inside the PRC. f_2 is defined to be resonant inside the PRC and the SRC. Finally, f_3 is defined to be anti-resonant inside both the PRC and SRC.

The proper Length Sensing and Control (LSC) of a laser interferometric detector is crucial to meet and keep during the run its design sensitivity. The functionality and working point of these detectors depend on keeping the interferometric condition, which depends on both the optical lengths of the cavities and laser frequency of the detector. However, maintaining this condition is challenging due to constant disturbances. Without active control loops for both the optical cavity lengths and laser frequency, it becomes nearly impossible to maintain the requested interferometric condition and, thereby, to have sufficient sensitivity to detect the passage of GWs.

2.4 Limiting noises

The coupling into DARM of noises due to various sources can spoil the sensitivity. These random variations could mask a real GW signal or create a false

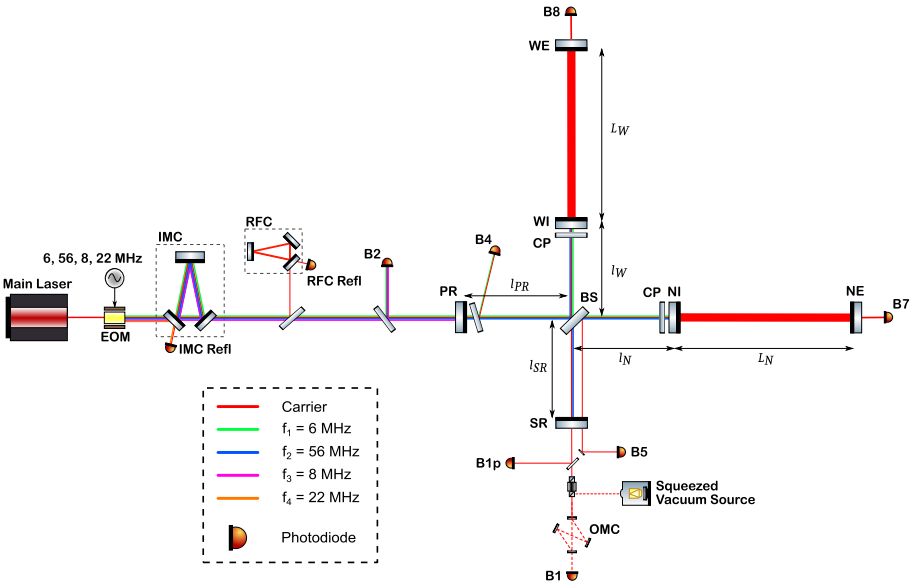

Figure 2.14: O4 Observing Run Optical Layout of Advanced Virgo Plus. The laser beam travels towards the interferometer. It passes through the IMC cavity and the PR mirror, then the laser beam is split at the BS and directed towards the North and West arms. Thereafter, the beams are reflected by the end mirrors of each arm and directed back to the BS, where the beams are recombined and split again towards the input port and output port passing through the SR mirror. The carrier is shown in red. The different side-bands f_1, f_2, f_3, f_4 are indicated in green, blue, pink and orange, respectively.

one. Therefore, all noises, disturbances and couplings must be characterized and studied. Typically, for GW detectors, these noises are characterized using their Amplitude Spectral Density (ASD), which is given by:

$$A(f) = \sqrt{S(f)}, \tag{2.42}$$

where $S(f)$ is the Power Spectral Density (PSD), which in turn is given by:

$$S(f) = \lim_{T\to\infty} \frac{2}{T} \left| \int_{-T}^{T} x(t) e^{-2i\pi ft} dt \right|, \tag{2.43}$$

where $x(t)$ is the noise signal and T is the time observation window. Moreover, for GW detectors, there is a typical distinction being made between fundamental and technical noises. Fundamental noises define the design sensitivity of the detector by the incoherent sum of all of them. On the other hand,

technical noises are due to the technology used in these detectors and to the infrastructure where they are hosted.

2.4.1 Design sensitivity

All these sources of fundamental noise impose limitations in GW detectors. Combining all the strains of these different fundamental noises it is possible to produce a design sensitivity curve. The estimated design sensitivity due to the limits imposed by the fundamental noises for Advanced Virgo Plus Phase I is shown in *Fig. 2.15*.

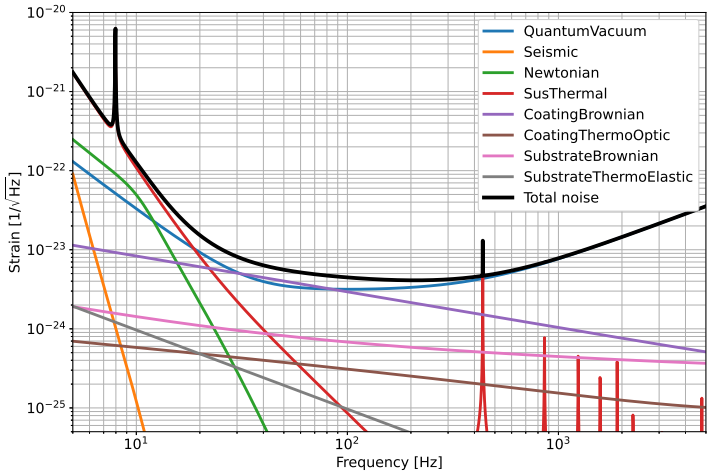

Figure 2.15: Design sensitivity of Advanced Virgo Plus configuration for O4.

2.4.2 Fundamental noises

Fundamental noises in GW detectors can originate from a range of different physical phenomena and impact the detectors in unique ways and in different frequency bands. The most significant fundamental noises are seismic noise, quantum noise, thermal noise and Newtonian noise. Understanding these noises is crucial for reducing their impact and, therefore, enhancing the detector's sensitivity. The quest to minimize these noises involves an effort that covers multiple disciplines, encompassing advancements in mechanical engineering, quantum optics, material science and environmental isolation techniques. In

this section, we delve into the details of the main fundamental noises, each subsection provides details on the nature and sources of the different noises and the mitigation strategies.

Seismic noise

Seismic noise arises from the natural vibrations of the Earth. These vibrations can originate e.g. from earthquakes, wind and ocean waves. Seismic noise affect the GW detectors mostly at lower frequencies (below 10 Hz).

A sensitivity of the order of 10^{-22} per $\sqrt{Hz}$ at 10 Hz and above, corresponds to a mirror motion of the order of $10^{-19}\,\mathrm{m}/\sqrt{\mathrm{Hz}}$ for the arm length of 3 km of Advanced Virgo Plus. For the Virgo and LIGO sites, the seismic motion at 10 Hz is of the order of $10^{-10}\,\mathrm{m}/\sqrt{\mathrm{Hz}}$ as shown in *Fig. 2.16*: dashed curves represent the upper and lower bounds of the ambient seismic noise levels, the so-called New High Noise Model (NHNM) and New Low Noise Model (NLNM), respectively. Additionally, the typical levels of seismic noise at the Virgo, LIGO Hanford and LIGO Livingston are depicted in red, green and blue, respectively. Figure taken from [67].

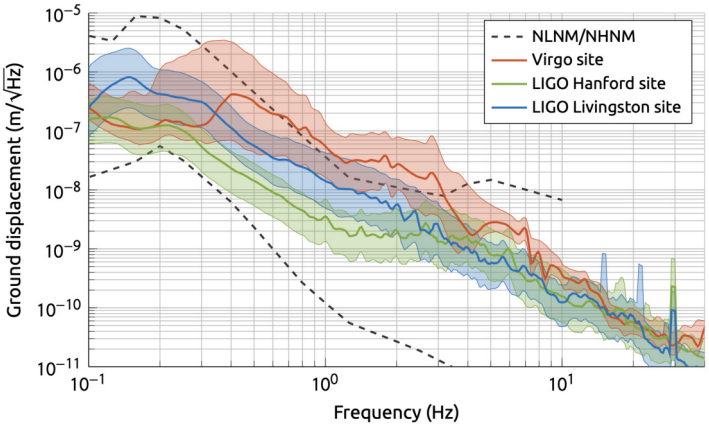

Figure 2.16: Horizontal motion spectra measured at LIGO and Virgo sites compared with the Peterson's high-noise (NHNM) and low-noise (NLNM) models.

Since the characteristic seismic motion for all the sites is of the order of $10^{-10}\,\mathrm{m}/\sqrt{\mathrm{Hz}}$ at 10 Hz, an attenuation of, at least, a factor of 10^9 is needed on the mirror motion to detect GW signals. To mitigate seismic noise, GW detectors employ active and passive isolation systems. Active isolation requires the use of sensors to monitor seismic motion and actuators to mitigate these

measured vibrations in real time. Passive isolation, typically, involves the use of pendula to suspend the mirrors and optical components. For a pendulum, the motion above its resonant frequency is significantly reduced. For a pendulum with length l, with a suspended mass m, its dynamics can be described as:

$$m\ddot{x} = \frac{mg}{l}(x - x_{gnd}), \tag{2.44}$$

where x denotes the displacement of the attached mass, x_{gnd} denotes the displacement from the suspension point and g represents the acceleration due to Earth's gravity. From the differential equation (2.44), the transfer function that relates the displacement of the mass and the displacement of the suspension point is given by:

$$\frac{x(f)}{x_{gnd}(f)} = \frac{f_0^2}{f_0^2 - f^2}, \tag{2.45}$$

where $f_0 = \sqrt{g/l}/2\pi$ is the resonance frequency of the pendulum. Finally, for frequencies higher than f_0, equation (2.45) can be approximated to:

$$\frac{x(f)}{x_{gnd}(f)} \approx \frac{f_0^2}{f^2}, \tag{2.46}$$

meaning that the motion at higher frequencies is attenuated as $1/f^2$. Using several stages of pendula in a seismic isolation system, one can effectively enhance the attenuation at frequencies above the resonant frequency. For a system with N stages, the overall transfer function between the top stage of the pendulum array and the bottom stage becomes:

$$\frac{x_{bottom}(f)}{x_{top}(f)} \approx \left(\frac{f_0^2}{f^2}\right)^N. \tag{2.47}$$

Therefore, implementing a multiple pendula chain allows to reach the attenuation factor of, at least, 10^9 needed to filter out the residual seismic motion, as shown in *Fig. 2.17*.

Active isolation systems are used in the Advanced LIGO detectors, while mainly passive ones are exploited in Advanced Virgo Plus and KAGRA. *Fig. 2.18* depicts the Advanced Virgo Plus isolation system, which features a complex multi-stage pendulum chain, an inverted pendulum (IP), and the

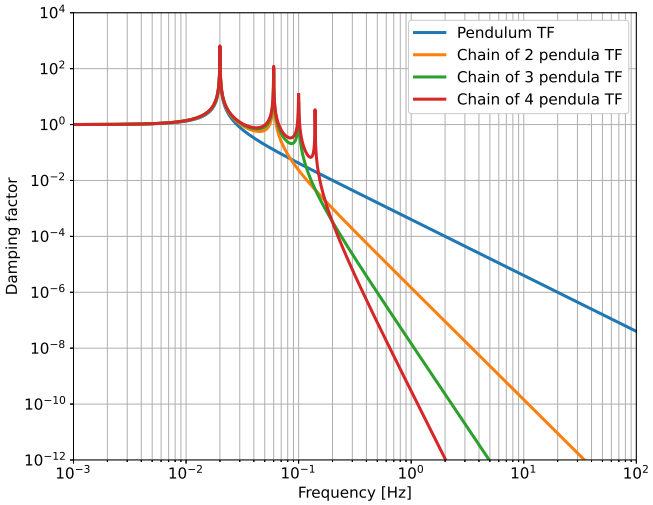

Figure 2.17: TF of a pendulum compared to the TFs of chains of multiple pendula characterized by different number of stages: Increasing the number of stages, the attenuation is improved above the resonance frequency.

payload that includes the suspended mirror. [1]

The IP is used to control the resonance modes of the entire chain, to pre-filter horizontal motion at low frequencies around the site's microseism peak, to provide inertial damping, and to position the entire suspension system. The chain of pendula acts as mechanical filters, each incorporating multiple pairs of concentric blade springs and magnetic anti-springs that reduce the coupling of vertical ground motion into the motion of the mirror. The payload, consisting of the marionetta and the mirror, is suspended from the final stage of the pendulum chain.

[1]The initial design included filters 1-7. However, this was before the inverted pendulum was introduced, which made a few filters unnecessary. Filter 7 was retained as the steering filter, but filters 5 and 6 were removed. Conversely, filter 0 was added to attenuate the vertical degree of freedom, a function not provided by the inverted pendulum.

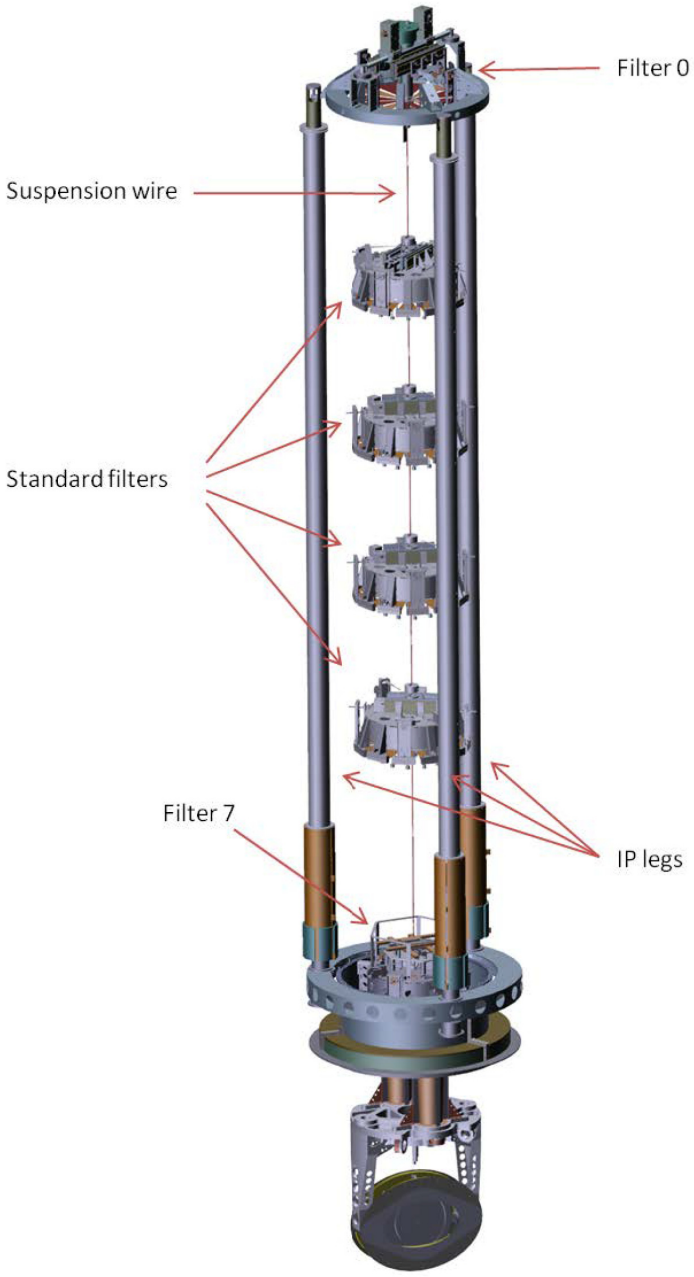

Figure 2.18: Sketch of the Advanced Virgo Plus isolation system.

Newtonian noise

Newtonian noise refers to the fluctuations in the gravitational field at the location of the GW detector due to local mass distributions. These fluctuations can originate from seismic activity, atmospheric pressure variations and oceanic tides. This fundamental noise interacts directly with the test masses and is not suppressed by the active or passive isolation systems. A simplified model for the amplitude spectral density of the seismic Newtonian noise can be expressed as:

$$h_{NN}(f) = \frac{G\rho x_g}{\sqrt{3}\pi L f^2}, \tag{2.48}$$

where ρ is the density of the soil surrounding the test masses, x_g is the distribution of the ground motion and L is the arm length of the detector. On the other hand, the atmospheric Newtonian noise is mainly affected by temperature and air flux changes.

There are some strategies aiming to reduce Newtonian noise. An initial approach consists of an offline subtraction of Newtonian noise from the strain data [68]. To implement this technique, seismometers and infra-sound microphones are placed in different locations inside the buildings that host the main optics of the interferometer. *Fig. 2.19* shows an example of the seismometers and infra-sound microphones installed in one the Advanced Virgo Plus buildings.

Figure 2.19: Seismometers and infra-sound microphones installed at the Advanced Virgo Plus site.

Another possible approach will be to construct future GW detectors underground, since it has been measured that surface seismic waves are significantly suppressed at some hundred of meters underground [69].

Quantum noise

In the context of interferometric GW detectors, quantum noise arises from the quantum-mechanical nature of the laser beam. Quantum noise in GW detectors consists of two components: shot noise and radiation pressure noise. It is described using its ASD calibrated in strain units (h_{QN}), that is the incoherent sum of shot noise and radiation pressure noise:

$$h_{QN} = \sqrt{h_{SN}^2 + h_{RPN}^2}. \tag{2.49}$$

Shot Noise (SN) arises from the quantized light, leading to fluctuations in the number of photons arriving on a photo-detector and follow a Poisson distribution. As a result, when a laser illuminates a photo-detector, the resulting photo-current time-series exhibits fluctuations. These fluctuations, known as shot noise, scale with the square root of the laser beam's optical power. In contrast, the sensitivity of a GW detector increases linearly with the optical power. Therefore, enhancing the optical power in a GW detector can effectively improve the signal-to-shot-noise ratio, scaling with the square root of the optical power within the GW interferometer. The ASD of photon shot noise in units of strain for the case of a Michelson interferometer is expressed as:

$$h_{SN} = \frac{1}{L}\sqrt{\frac{\hbar c\lambda}{2\pi P}}, \tag{2.50}$$

where L represents the average arm length of the interferometer, $\hbar$ denotes the reduced Planck constant, c stands for the speed of light, λ is the wavelength of the laser and P is the average optical power.

Additionally, photons carry momentum, and when they reflect off a free-falling test mass, they impart a radiation pressure force to the mirror. Since the photons reach the test mass at different intervals, the force exerted on the mirror and, consequently, its position fluctuates over time. This results in what is known as radiation pressure noise. The resulting ASD due to Radiation Pressure Noise (RPN) in the sensitivity band can be expressed as:

$$h_{RPN} = \frac{1}{mf^2L}\sqrt{\frac{\hbar P}{2\pi^3 c\lambda}}, \tag{2.51}$$

where f is the frequency and m is the mass of the mirrors. From equation (2.50), we can see that shot noise is frequency independent. On the other hand, from equation (2.51), we can see that RPN is inversely proportional to the square of the frequency. The sum of the SN and RPN is shown in *Fig. 2.20*: It can be noticed that RP mainly limits the detector sensitivity at low frequencies, while SN dominates at high frequencies.

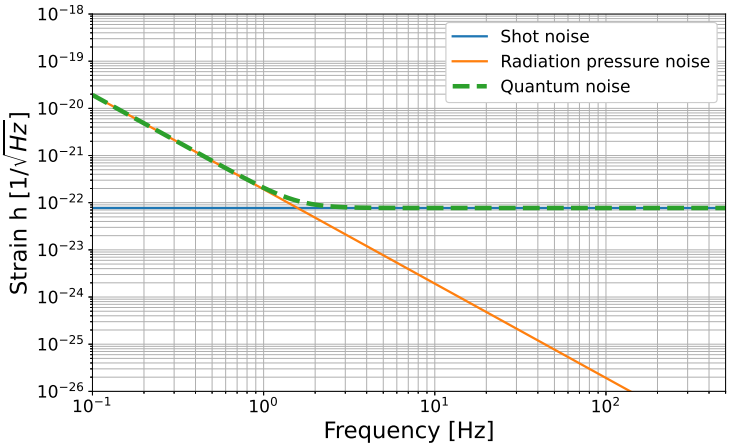

Figure 2.20: Sum of shot noise and radiation pressure noise for an interferometer characterized by $m = 40\,\text{kg}$, $L = 3\,\text{km}$ and $P = 100\,\text{kW}$.

For each frequency, we could find an optimal laser power to minimize the quantum noise, where the RPN and the SN have the same level. All these optimal points create a curve, crossing the whole detection spectrum, the Standard Quantum Limit (SQL), which is defined as:

$$h_{SQL} = \sqrt{\frac{\hbar}{m\pi^2 f^2 L^2}}. \tag{2.52}$$

For a GW interferometer with fixed arm lengths and mirror masses, the standard quantum limit defines its quantum sensitivity limit. The trend of the QN and the SQL for three different optical powers inside the interferometer is shown in *Fig. 2.21.* One can see that increasing the optical power the level of the SN improves, worsening the level of RPN.

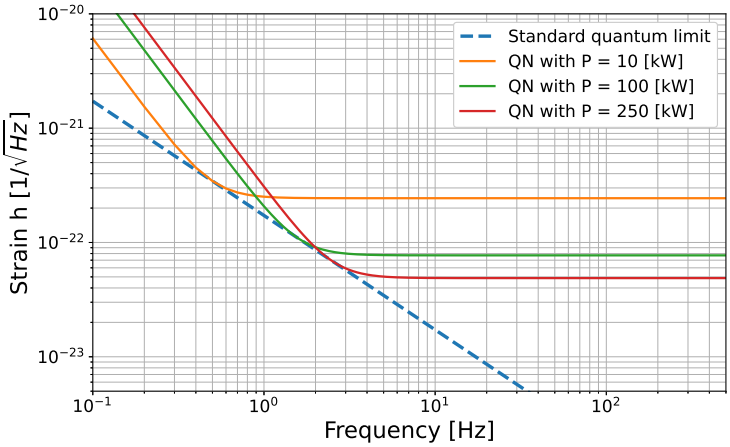

Figure 2.21: Effective strain quantum noise computed as the incoherent sum of shot noise and radiation pressure noise in a Michelson interferometer for different high circulating powers. Parameters are: $L = 3\,\mathrm{km}$, $\lambda = 1064\,\mathrm{nm}$, $P = 10, 100, 250\,\mathrm{kW}$ and $m = 40\,\mathrm{kg}$. Standard quantum limit, in dashed blue lines, shows the minimum strain limited by quantum noise.

Thermal noise

Thermal noise is the actual displacement of the mirrors due to the Brownian motion of the particles making up the test masses suspension, substrate and optical coating. Brownian noise is usually studied with the application of the fluctuation-dissipation theorem. Therefore, this section offers an introductory overview of the fluctuation-dissipation theorem, followed by a description of the different types of thermal noises affecting GW detectors. These include suspension thermal noise, substrate Brownian noise, substrate thermo-elastic noise and coating thermal noise.

The fluctuation-dissipation theorem was first articulated by Einstein to describe how particles suspended in a fluid undergo random movements due to thermal fluctuations [70] in 1905. Almost five decades later, the theorem was formulated in a more comprehensive version [71]: for a given coordinate $x(f)$ with speed given by $v(f)$, the theorem outlines the relationship between the applied fluctuating thermal force $F(f)$ and the complex impedance of the system $Z(f)$. The complex impedance of the system is described as:

$$Z(f) = \frac{F(f)}{v(f)} = \frac{F(f)}{i2\pi f x(f)}. \tag{2.53}$$

Then, the Fluctuation-Dissipation theorem is formulated as:

$$F^2(f) = 4k_B T \Re[Z(f)], \tag{2.54}$$

where k_B is the Boltzmann constant and T is the temperature. The thermal noise or the fluctuation of the generalized coordinate $X_{th}(f)$ within a system is given by:

$${X_{th}}^2(f) = \frac{4k_B T}{4\pi^2 f^2} \Re[Z(f)], \tag{2.55}$$

where $X_{th}(f)$ is the Fourier transform of an observable $x_{th}(t)$.

In GW detectors, mirrors and certain optical components are suspended like pendula using wires. The primary forces restoring these pendula are gravity, which is lossless, and the elasticity of the wires, which does incur losses. The elastic constant of the pendulum is calculated as follows:

$$k = \frac{Mg}{L} + N_w \frac{\sqrt{T_w EI}}{2L^2}(1 + i\phi_w) = k_g + k_y(1 + i\phi_w), \tag{2.56}$$

where L is the pendulum length, N_w is the number of supporting wires, M is the mass of the mirror, E is the Young's modulus of the wire, I is the moment of inertia of the wire's cross-section and ϕ_w is the loss angle due to wire elasticity, representing loss of energy as heat. k_g and k_y represent the elastic constants due to gravity and wire elasticity, respectively. Then, assuming gravitational forces dominate those from the wires, the overall pendulum elastic constant in equation (2.56) simplifies to:

$$k = k_g \left(1 + \frac{k_y}{k_g} + i\frac{k_y}{k_g}\phi_w\right) \approx k_g \left(1 + i\frac{k_y}{k_g}\phi_w\right). \tag{2.57}$$

The loss angle of the pendulum ϕ_p is defined as:

$$\phi_p = \frac{k_y}{k_g}\phi_w. \tag{2.58}$$

Finally, the pendulum thermal noise is expressed as:

$${X_{th}}^2(f) = \frac{4k_B T \phi_p}{128\pi^7 f_0^2 M f^5}, \tag{2.59}$$

where f_0 is the resonance frequency of the system. Equation (2.59) shows that pendulum thermal noise inversely correlates with the mirror mass and frequency across the overall bandwidth. Consequently, advanced GW detectors

aim for heavier and larger test masses to minimize noise and enhance detection capabilities.

In the initial Virgo detector, pendulum thermal noise was a significant limiting factor of the sensitivity at low frequencies, largely due to the high loss angle, of the order of 10^{-6}, associated with the steel wires used to suspend the mirrors. To address this issue, silica wires, which feature a considerably lower loss angle, were introduced. This change allowed for a reduction in the suspension loss angle by three orders of magnitude. The adoption of these silica monolithic suspensions decreased the pendulum thermal noise to the order of 10^{-9}. These suspensions are constructed using silica fibers that are welded to silica blocks, which are then silicate bonded directly to the mirror side. This design, shown in *Fig. 2.22*, significantly improved the sensitivity of the detector from the initial Virgo to Advanced Virgo Plus.

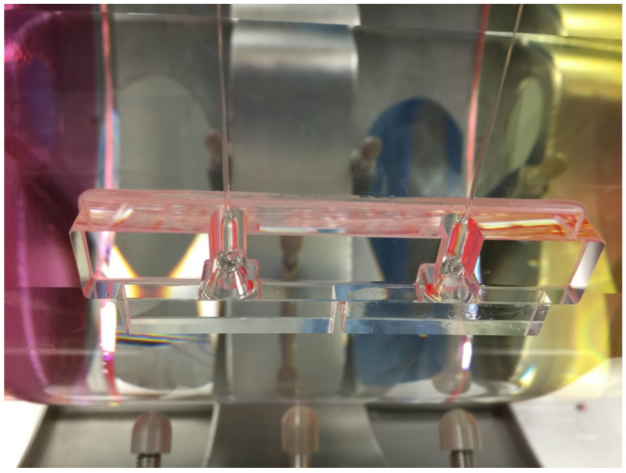

Figure 2.22: Monolitic suspension in Advanced Virgo Plus.

To describe the thermal noise in the substrate of the mirror test masses, one needs a comprehensive model that includes every possible vibration eigenmode. However, this approach demands substantial computational resources [72]. An alternate method was suggested by Levin in 1998 [73]. Using this novel approach it was possible to obtain an expression for the substrate thermal noise, given by:

$$x_{th}{}^2(\omega) = \frac{k_B T}{\omega} \frac{1-\sigma^2}{\sqrt{\pi} E_0 w} \phi, \tag{2.60}$$

where σ is the Poisson ratio, E_0 is the Young modulus of the substrate, ϕ represents the loss angle and w is the beam radius used in the method described in [73]. The loss angle depends primarily on the type of material used for the substrate. Therefore, selecting a substrate with lower losses is crucial to minimize this source of noise. Currently, fused silica is the preferred material for large-scale detectors because of its very low loss angle, potentially as low as 10^{-9}. Other materials considered for this purpose include sapphire, silicon, and calcium fluoride, all of which also exhibit favorable properties for GW detectors.

The substrate thermo-elastic noise can be analyzed also using the fluctuation-dissipation theorem. When a Gaussian beam hits the substrate surface, it converts energy to heat, which is absorbed by the substrate, reducing the restoring force. Then, the substrate thermo-elastic noise can be expressed as:

$$ {x_{th}}^2(\omega) = \frac{16 k_B T}{\omega^2} \frac{\alpha^2 (1+\sigma)^2 k T}{\sqrt{\pi} C \rho^2 w^3}, \tag{2.61} $$

where α represents the thermal expansion coefficient, k stands for the thermal conductivity, ρ is the density of the material and C denotes the specific heat per unit volume. Unlike fused silica, materials such as silicon and sapphire, which are strong candidates for future cryogenic gravitational-wave detectors, exhibit higher thermal conductivity and expansion coefficients, leading to increased thermo-elastic noise. However, experiments indicate that at cryogenic temperatures ($10 - 20\,\mathrm{K}$), these materials show better performance with significant reductions in mechanical losses and thermal expansion.

For optimal reflectivity, a substrate is layered with a coating that is several micrometers thick, involving 15 to 40 alternating layers of different materials such as doped silica (SiO2 with low refractive index) and doped tantala (Ta2O5 with high refractive index). The higher loss angle of tantala significantly raises the losses. Although the coating is much thinner than the substrate itself, it is the primary cause of thermal noise in the mirror. This predominance is because the majority of the energy from a Gaussian laser beam is concentrated at the surface where the coating is applied, making the losses from the coating more significant than other types of losses. The coating thermal noise can be expressed through the following equation:

$$ {x_{th}}^2(\omega) = \frac{4 k_B T}{\omega} \frac{1-\sigma^2}{\sqrt{\pi} E_0 w} \phi_{eff}(\omega), \tag{2.62} $$

where $\phi_{eff}(\omega)$ represents the effective coating loss, defined as:

$$\phi_{eff}(\omega) = \frac{d}{\sqrt{\pi}w}\left(\frac{E_0}{E_\perp}\phi_\perp(\omega) + \frac{E_\parallel}{E_0}\phi_\parallel(\omega)\right), \tag{2.63}$$

where d denotes the thickness of the coating, w is the beam radius, E_0 is the Young's modulus of the substrate, and $E_\perp$ and $E_\parallel$ correspond to the Young's modulus of the coating in the perpendicular and parallel orientations to the layers, respectively. $\phi_\perp$ and $\phi_\parallel$ represent the loss angles in these orientations. These parameters are determined by the thicknesses of the layers and the properties of the used materials.

Empirical studies have verified that coating thermal noise is consistent with theoretical predictions and significantly affects the sensitivity of advanced detectors in the mid-frequency range [74, 75]. Plans for future enhancements, such as in the Advanced Virgo Plus detector, include increasing the beam size to mitigate mirror thermal noise, as highlighted in equations (2.60) and (2.62).

Fig. 2.23 shows the contribution to the total thermal noise from the suspension thermal noise, the coating Brownian noise, the substrate Brownian noise, the coating thermo-optic noise and the substrate thermo-elastic noise for Advanced Virgo Plus. Note that the coating Brownian noise becomes the most dominant component of the total thermal noise above approximately 30 Hz.

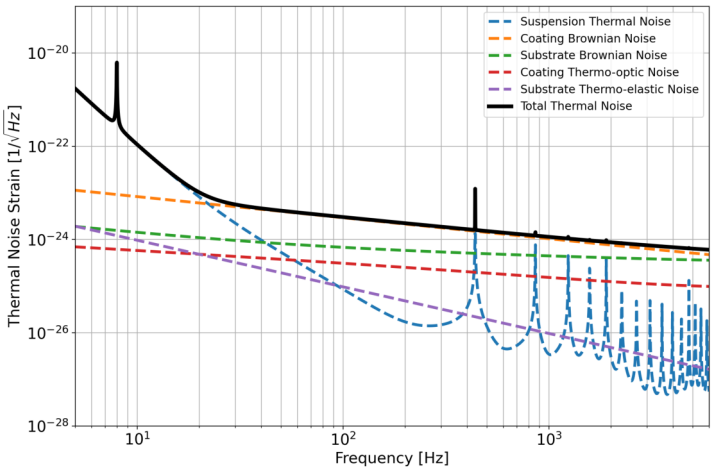

Figure 2.23: Thermal noise strain for Advanced Virgo Plus.

2.4.3 Technical noises

In addition to fundamental noises, which are intrinsic to the design of the interferometer, the detector's performance can be limited by technical noises. During the design of the various components of the detector, the goal is to have all contributions from technical noises, at least, a factor of 10 below the design sensitivity. Technical noises are not directly connected to the design of the detector but, as noted in previous observing runs of current GW detectors, they can limit their performance. A crucial part of the commissioning process involves suppressing or reducing various technical noises. Though not an exhaustive list, the following sections specifically describe some of the most important technical noises with focus on sensing noises.

Readout noise

The readout noise should be limited by the shot noise. This means that the noise due to the electronics in the detection chain should be lower than the shot noise. The electronic noise impacts the sensitivity in two primary ways, depending on the involved photo-diodes. First, the readout noises associated with the photo-diodes used to detect the B1 beam directly affect the measurement of the GW signal. Second, the error signals to control the different DoFs can propagate through the control loops and convert into mirror position noises, as explain in detail in Chapter 3.

The total signal at the modulation frequency Ω can be expressed in terms of its in-phase $V_I(t)$ and quadrature $V_Q(t)$ components as:

$$V_\Omega(t) = V_I(t) \cdot \cos(2\pi\Omega t) + V_Q(t) \cdot \sin(2\pi\Omega t). \tag{2.64}$$

This signal is processed using a demodulation board, which delivers the signals $V_I^{ch}(t) = \frac{V_I(t)}{2}$ and $V_Q^{ch}(t) = \frac{V_Q(t)}{2}$ for the in-phase and quadrature components, respectively.

The electronic noise at the detection chain output primarily comes from the quantization noise of the ADCs and the noise generated by the preamplifier. The quantization noise is a white noise with a spectral density of about $\sim 100\,\mathrm{nV}/\sqrt{\mathrm{Hz}}$. Generally, the electronic noise generated upstream of the demodulation board becomes dominant, especially at higher frequencies. Adjusting the gain of the demodulation board helps to minimize this noise.

On the other hand, the preamplifier noise propagates through the demodulation board, resulting in an electronic noise level slightly higher than $1\,\mu\mathrm{V}/\sqrt{\mathrm{Hz}}$.

The impact of readout noises on the detector's sensitivity depends on the signal-to-noise ratio at the output of the photo-diode acquisition chain. Thus, the contribution of readout noises can be reduced by increasing the power of the beam incident on the photo-diodes.

Note that the contribution of electronic noise to the sensitivity curve decreases as the incident power on the photo-diodes increases, while, the absolute level of shot noise rises with the square root of the power. Moreover, in GW detectors the contribution of electronic noise should be, at least, 10 times lower that the contribution of shot noise also to make use of Squeezing techniques [76].

Demodulation noise

During the demodulation process, relative phase fluctuations between the signal at the modulation frequency delivered by the photo-diode and the local oscillator signal can introduce noise into the demodulated signal, known as demodulation noise. The coupling mechanism for this phenomenon is described as follows: if the signal at the modulation frequency delivered by the photo-diode undergoes phase fluctuations $\delta\phi_\Omega(t)$, such that:

$$V_\Omega(t) = V_I(t)\cos(2\pi\Omega t + \delta\phi_\Omega(t)) + V_Q(t)\sin(2\pi\Omega t + \delta\phi_\Omega(t)), \tag{2.65}$$

and the local oscillator undergoes phase fluctuations $\delta\phi_{\mathrm{LO}}(t)$, resulting in:

$$V_{LO}(t) = \cos(2\pi\Omega t + \delta\phi_{LO}(t)), \tag{2.66}$$

the signal obtained at the output of the mixer of the in-phase channel V_I^{ch} is, then, given by:

$$\begin{aligned} V_I^{ch}(t) = &\frac{V_I(t)}{2}\cdot[\cos(4\pi\Omega t + \delta\phi_\Omega(t) + \delta\phi_{LO}(t)) + \cos(\delta\phi_\Omega(t) - \delta\phi_{LO}(t))] \\ &+ \frac{V_Q(t)}{2}\cdot[\sin(4\pi\Omega t + \delta\phi_\Omega(t) + \delta\phi_{LO}(t)) + \sin(\delta\phi_\Omega(t) - \delta\phi_{LO}(t))]\,. \end{aligned} \tag{2.67}$$

Filtering out the components at twice the modulation frequency from equation (2.67) and expanding the trigonometric functions to the first order, the signal $V_I^{ch}(t)$ at the output of the detection chain is written as:

$$V_I^{ch}(t) = \frac{V_I(t)}{2} + \frac{V_Q(t)}{2} \cdot \delta\phi_{\mathrm{dem}}(t), \tag{2.68}$$

where $\delta\phi_{\mathrm{dem}}(t)$ represents the relative phase fluctuations between the signal at the modulation frequency delivered by the photo-diode and the local oscillator signal, i.e. $\delta\phi_{\mathrm{dem}}(t) = \delta\phi_{\Omega}(t) - \delta\phi_{\mathrm{LO}}(t)$.

The previous calculation shows that relative phase fluctuations between the signal at the modulation frequency from the photo-diode and the local oscillator signal generate noise in the demodulated signal of the in-phase channel, with an ASD proportional to the signal induced on the quadrature channel. Analogously, this phenomenon is symmetrical for the quadrature channel. The demodulation phase noise $\delta\phi_{\mathrm{dem}}$ can have two different origins: it can be generated at the electronic level of the detection chain, or it can result from intrinsic phase noise of the generator that delivers the signal for the phase modulation of the laser beam.

Longitudinal sensing and control noise

Controls are essential for the operation of GW detectors. They are implemented on several systems of the detector to keep their proper working point. For instance they are used to maintain the longitudinal and angular position of the mirrors, to damp the modes of the suspension system, to continuously align the laser beam, among others. Unfortunately, without subtraction, or decoupling techniques, longitudinal control noise is the main limitation of GW detectors at low frequencies. This type of noise emerges from the sensor noise that is fed-back to the system to keep the interferometer in the proper working point. From the error signal derived from the PDH technique, described in section 2.2.2, the controls must keep the optics in the desired longitudinal position. To generate these error signals, the PDH technique uses photo-detectors, which are affected by electronic noise, ADC noise, shot noise, among others. Sensor noise is indistinguishable from real displacement noise and it dominates the noise floor above $\sim 50\,\mathrm{Hz}$. At the beginning of the lock acquisition procedure, the controllers are designed to be robust and strong to acquire the resonance state. Later, the bandwidth of the different control loops are dialed back, weakening the control action but reducing the re-injection of the sensor noise. However, this process alone is not enough due to optical cross-couplings, which transfer the noise from one channel to another of the different DoFs. This particular aspect is studied in detail in Chapter 3, where starting from an interferometer

simulation tool, the optical cross-coupling of all longitudinal DoF are studied and the effects on the sensitivity are explained. Furthermore, Chapter 3 covers the development of a full Multiple-Input Multiple-Output system, that allows to predict cross-couplings and helps to design decoupling filters to circumvent the re-injection of noise in current and future GW detectors.

Angular control noise

If the beam is well-aligned and centered with respect to the mirrors, at first order angular noise from a mirror does not affect the optical path length traveled by the beam, having no significant impact on the DARM DoF signal. However, if the beam is decentered relative to the mirrors, angular noise can couple to the output of the interferometer, thus limiting its sensitivity.

Suppose the incident beam is vertically decentered on the BS, as depicted in *Fig. 2.24*, where d denotes the beam decentering, and $\delta\theta$ denotes the Pitch angular noise of the mirror, around its horizontal axis.

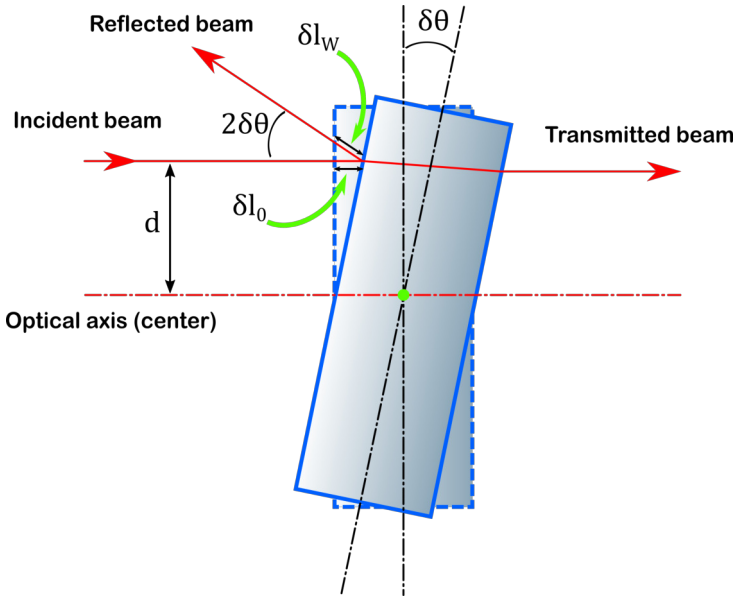

Figure 2.24: Effect of an Pitch displacement noise $\delta\theta$ of a mirror, in the hypothesis of a decentered beam relative to the optical axis.

The angular noise induces a variation in the optical path length of the beam reflected towards the West arm that can be expressed as:

$$\delta l_W \approx \delta l_0 = d\delta\theta, \tag{2.69}$$

where δl_0 denotes the longitudinal shift of the mirror with respect to its nominal position. On the other hand, the beam transmitted towards the North arm experiences a variation $\delta l_N = -\delta l_W$. Thus, the angular noise of the BS introduces an asymmetry between the lengths of the short arms of the Michelson interferometer, which can be expressed as:

$$\delta l_{MICH} \approx 2d\delta\theta. \tag{2.70}$$

This asymmetry produces a noise on the output signal, that is equivalent to a length difference δl between the two Fabry-Perot cavities, defined as:

$$\delta l = \frac{\pi}{2\mathcal{F}}\delta l_{MICH}, \tag{2.71}$$

where the factor $\pi/2\mathcal{F}$ represents the inverse of the number of round-trips made by the beam resonating in a FP cavity.

The origin of the noise introduced by angular control loops comes from the fact that some mirrors are independently controlled using only their local control systems, which allow to keep the mirrors in their nominal position with respect to only their local reference frames without considering their longitudinal and angular positions with respect to the other mirrors. On the other hand, a more accurate, and less noisy, angular control can be implemented using a wavefront sensing technique [77, 78], which considers the relative position of all the mirrors together.

For Advanced Virgo Plus, as described in [69], the angular DoFs did not spoil Virgo's sensitivity during O3 and remained at an acceptable level (within 1 order of magnitude of the designed sensitivity) in preparation for O4. However, this can become a problem for future GW detectors, such as the Einstein Telescope [79]. Addressing both longitudinal and angular control noises is an ongoing effort in the GW community and of paramount importance for the commissioning team and future observing runs. Therefore, a model for the full interferometer, covering longitudinal and angular DoFs, will significantly help to better understand the detector and exploit its capabilities. This model should be able to represent the interaction of cross-coupling between angular and longitudinal DoF and the re-injection of noise in closed-loop.

Monitoring lines

Temporal variations in the different control loop parameters, especially for the DARM DoF loop, can be tracked by injecting modulated excitations into the loop. These excitations generate peaks, or lines, at the modulation frequencies in the ASD of the corresponding error signal, with cross-coupling to others.

In Advanced Virgo Plus, several lines are introduced in different ways, either through a photon calibrator system or directly into the error signals of different control loops to monitor different properties of the interferometer such as the control loops UGFs, the coupling of some noises, the contrast defect, among others. For example, two photon calibrators induce modulated displacements on the ETMs (End Test Masses) through photon radiation pressure generated by an auxiliary laser with a wavelength of 1047 nm. The identification and cataloging of all these purely instrumental monitoring lines are crucial for the process of "offline cleaning" when searching for the effect of a passing GW.

Charging noise

Ideally there should be no charge on the test masses of Advanced Virgo Plus. However, residual charges may remain due to incomplete removal of the First Contact polymer used to protect the optics during transportation and installation, and to clean them. Additionally, UV photons from ion pumps in the vacuum system strip electrons from the test mass surfaces, and dust particles contribute to charging as well.

Charging noise couples to the measured GW signal through two mechanisms: Time-variant charge interacts with the metal cage around the test mass; and voltage fluctuations from grounded metal near the test mass create electric field fluctuations E that can apply a force F_{ch} on the test mass, given by:

$$F_{ch} = \int E\sigma dS, \tag{2.72}$$

where σ is the estimate of the charge density on the front and back surfaces of the test mass under examination.

The coupling of voltage fluctuations to sensitive signals can be reduced by discharging key optics, specially the test masses. Ion guns, which introduce positive and negative ions into the system can efficiently remove charge from surfaces. This is one of the future upgrades that will be implemented in Advanced Virgo Plus.

Mirror actuator noise

The correction signal from the control system is sent to a digital-to-analog converter (DAC). The voltage from the DAC output is applied to an amplifier connected to a coil. The current flowing through the coil generates a magnetic field, exerting a force on the magnets attached to the mirror or the marionetta, which is the isolation stage just above the mirror, allowing to steer it. The DAC and amplifier produce electronic noise, with an overall level of about $400\,\mathrm{nV}/\sqrt{\mathrm{Hz}}$. Additionally, if the DAC is not perfectly adjusted, this noise increases proportionally to the amplitude of the correction signal sent to the DAC. The electronic noise of the actuators causes a current in the coil, inducing a mirror position noise δL_{mirror}, expressed in the frequency domain as:

$$\delta L_{mirror}(f) = \mathcal{K} \cdot H(f) \cdot M(f) \cdot n(f), \tag{2.73}$$

where: $\mathcal{K}$ represents the static gain of the actuation chain, including the response of the electronics, the mechanical response of the mirror and its suspension system; $H(f)$ is the TF of the coil response; $M(f)$ is the TF of the mirror's mechanical response, which varies depending on whether the force is applied at the level of the marionetta or directly on the mirror; and $n(f)$ is the electronic noise level of the actuators.

The TF of the electrical response of the coil can be expressed by:

$$A(f) = \frac{1}{1 + i\frac{f}{f_{coil}}}, \tag{2.74}$$

where $f_{coil} = \frac{R_{circuit}}{L_{coil}}$, $R_{circuit}$ is the total resistance of the circuit connected to the coil and L_{coil} is the coil's inductance.

When the force is applied directly to the mirror, the mechanical system behaves like a pendulum resonating at a frequency $f_p \approx 0.7\,\mathrm{Hz}$ and the TF of the mirror's mechanical response can be expressed as:

$$M(f) = \frac{1}{1 + i\frac{f}{Qf_p} - \left(\frac{f}{f_p}\right)^2}, \tag{2.75}$$

where Q is the quality factor of the pendulum wires.

When the force is applied to the marionetta, the mechanical filtering between the marionetta and the mirror makes the noise from actuators acting on the marionetta negligible compared to the one of the actuators acting directly on the test mass. For the four mirrors in the arms, the longitudinal dis-

placement δL_{mirror} due to actuator noise induces a variation δL in the length difference between the FP cavities, similar to the effect of a passing GW.

Laser frequency and intensity noise

Current GW detectors use a high power Nd:YAG laser system to deliver the beam at the input of the interferometer. However, these laser systems are characterized by an intrinsic frequency noise of $\sim 10^4 f^{-1}\,\mathrm{Hz}/\sqrt{\mathrm{Hz}}$ [2] between 10 Hz and 5 kHz, while the requirement for GW detectors is of $\sim 10^{-6}\,\mathrm{Hz}/\sqrt{\mathrm{Hz}}$ between 10 Hz and 10 kHz. Therefore, before injecting this laser beam into the interferometer, its frequency must be stabilized. This is true also for the intensity, which fluctuates approximately at $\sim 10^{-4} f^{-1}\,1/\sqrt{\mathrm{Hz}}$ between 10 Hz and 5 kHz, while the requirement for GW detectors is of $\sim 10^{-8}\,1/\sqrt{\mathrm{Hz}}$ [3] between 10 Hz and 10 kHz. The stabilization of these two properties can be achieved by several active and passive control systems [80].

Frequency noise refers to the fluctuations in the laser light's frequency over time. Laser frequency noise can couple to the GW detector output by the chosen working point of the Michelson interferometer and due to imbalances in the reflectivity of the mirrors forming the FP cavities [81]. Frequency noise is primarily canceled at the output port by the Michelson interferometer's common-mode rejection. However, residual frequency noise couples into the GW channel, or DARM DoF, through intentional asymmetry introduced for the RF control side-bands, and through to the imbalances in the FP cavities pole frequencies.

Amplitude noise, or intensity noise, refers to the variations in the intensity or amplitude of the laser light. This noise coupling into the interferometer is due to a nonzero differential arm offset (ΔL), or Schnupp asymmetry [82], designed to enable the transmission of modulation side-bands through the interferometer to the output port. It also couples through mismatches in circulating arm powers and mirror masses, causing coupling through radiation pressure at low frequencies. Furthermore, imperfections in the mirrors can create a conversion of the fundamental mode of the laser into higher-order modes, thus contributing to the coupling of amplitude noise to the interferometer output. These last imperfections can be compensated using a Thermal Compensation System (TCS) [83].

[2] Typical frequency noise for a nominal frequency in the order of terahertz.

[3] Upper limit requirement, the shape of the noise can vary according to the noise suppression loop.

Scattered light noise

Scattered light noise in the GW readout has multiple origins. When the laser light interacts with both the main mirrors and the auxiliary optical components installed in the input and output optics systems, a fraction of it can scatter out, due to the imperfection of these optics. This scattered light can interact with mechanical components, and chamber walls and be reflected back into the main beam, modulating its phase and amplitude, thus, adding noise to the measured GW signal.

For example, the light scattered out from the main mirrors can be characterized using the Bi-directional Reflectivity Distribution Function (BRDF), which depends on the imperfections on the mirror surface, determining the amount and angle of scattered light. The power scattered out in a cone with an angle Φ, formed between the scattered light and the main beam, is approximated as follows:

$$\frac{dP_s}{P_{arm}} \approx BRDR_{mirror} \times d\Psi, \tag{2.76}$$

where $d\Psi = 2\pi\Phi d\Phi$ is the solid angle of scattering. Some of this scattered light hits the beam tube or mechanical components and it is reflected back into the main beam, coupling the motion of these elements into the measured GW signal. Therefore, the effect of the scattered light noise can be seen in the sensitivity curve as structures or bumps around the resonant frequencies of these mechanical components. An example of the effect on the sensitivity of the light scattered out by a sensor and re-coupled into the main beam can be seen in *Fig. 2.25*, taken from [84].

Mitigation strategies for scattered light noise include: High-quality optical coatings on test masses and auxiliary optics to minimize imperfections; Baffles strategically placed within the vacuum system or on optical benches to intercept scattered light, preventing its re-injection into the main beam; Vacuum chambers designed to minimize scattering surfaces and optimize the optical environment; Control systems actively monitoring and mitigating low-frequency motion of scattering surfaces; Installation of optics on seismically isolated benches.

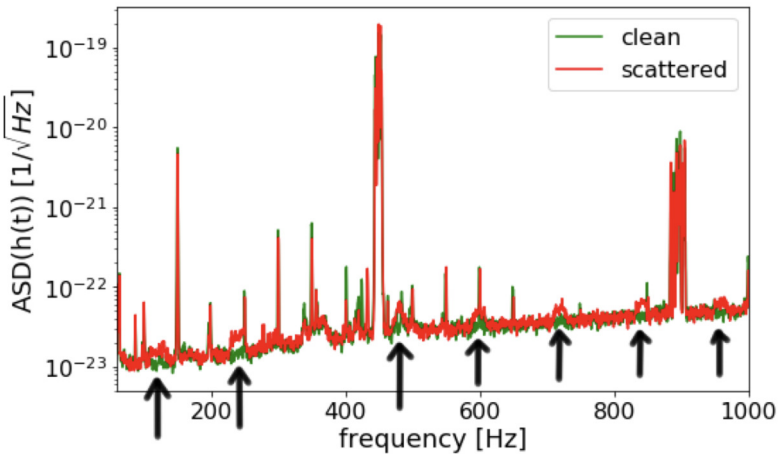

Figure 2.25: Effect of scattered light noise on the sensitivity curve in red, compared to the clean sensitivity curve in green.

Residual gas noise

Residual gas within vacuum chambers and tubes can influence the readout of GW detectors. Residual gas exerts a damping force on the test masses, which introduces displacement noise [85]. The noise can be estimated by applying the fluctuation-dissipation theorem or through Monte Carlo simulations. The type of gas present, including nitrogen, hydrogen, and water vapor, also influences the damping noise.

Furthermore, gas molecules moving through the laser beam in the arm cavities can cause phase noise by disturbing the optical phase of the beam. This phase noise is modeled by considering the impulsive disturbance caused by each molecule's transit through the laser beam. This effect can vary depending on the pressure distribution in the arm cavities and the profile of the laser beam, with the most significant contributions coming from the beam waist. Accurately reading out this noise is a challenge, as the exact composition of residual gases is unknown, and there is limited spatial resolution due to the limited number of vacuum gauges. Currently in Advanced Virgo Plus the residual gas pressure is of the order of 10^{-10} mbar in the arm tubes and of the order of 10^{-8} mbar in the mirror vacuum chambers.

Environmental noise

The environmental noise sources affecting Advanced Virgo Plus include seismic disturbances, acoustic noise, wind, and magnetic interference. Seismic disturbances arise from ground vibrations caused by various factors such as traffic, local human activity, and mechanical equipment within the buildings. These vibrations can affect the sensitivity of the interferometer by inducing unwanted motion in its suspended mirrors. Acoustic noise results from sound waves generated by vacuum pumps, motors, electronic equipment, and other sources within the surroundings of the interferometer. Wind-induced noise is caused by air movement around the buildings and structures of the detector. High winds can lead to increased acoustic and seismic noise levels, potentially impacting the interferometer's performance and even producing loss of control. Magnetic noise arises from surrounding metal structures in Advanced Virgo Plus that can generate eddy current due to electromagnetic disturbances, producing magnetic gradients that couple to the magnets of the mirrors, thus, exerting unwanted displacement of the optics, affecting their stability and potentially introducing noise into the GW signal readout.

For seismic noise, the superattenuator is utilized to isolate the interferometer from ground vibrations, equipped with active inertial damping to further suppress horizontal movements. Acoustic noise is addressed through acoustic isolation measures, such as placing sensitive components in isolated rooms and employing soundproofing materials, and installing most of the main components in vacuum. Wind-induced noise is managed by designing the interferometer's infrastructure to minimize its effects, such as using sturdy construction materials and locating sensitive components in areas less susceptible to wind disturbances. Magnetic interference is mitigated by employing magnetic shielding techniques to minimize the impact of external magnetic fields on interferometer components. Additionally, continuous monitoring and analysis of environmental noise characteristics help in further refinements of noise mitigation strategies.

2.5 Future GW detectors

Ground-based detectors, such as Advanced LIGO, Advanced Virgo Plus and KAGRA represent the second generation of GW detectors. In preparation for O4 and in perspective of O5 and future runs, these detectors are upgraded to

improve their sensitivity. However, they will reach eventually strict limitations due to the sites or the infrastructure where they are implemented. An effort is currently ongoing to design a new generation of GW detectors, which will overcome the limitations of the current observatories. The target is to improve the sensitivity and broaden the observation bandwidth. There are two proposed 3rd generation ground-based GW detectors: the Einstein Telescope (ET) [86] in Europe and the Cosmic Explorer (CE) [87] in the US. The science case of these future detectors, in addition to the further study of BBHs and BNSs, is to explore the origins of the universe by detecting primordial GWs [88, 23, 89] and possibly the observation of unexpected sources. Moreover, they will allow to test the principles of GR and investigate alternative theories of gravity.

The ET is an European enterprise that consists of three pairs of underground Michelson interferometers with 10 km arm length at an angle of 60 deg, forming a triangular observatory. This configuration allows to reduce the false alarm rate and to reconstruct both plus and cross polarizations of GW signals. As shown in *Fig. 2.26* [90], each vertex and corresponding arms of the equilateral triangle will host two Michelson interferometers: One is optimized for low frequencies and will work at low power and cryogenic temperature; the other one is optimized for high frequencies and will work at high power and at room temperature. On the other hand, the CE will inherit the design of current GW detectors but with an arm length 10-times longer, featuring a 40 km long, L-shaped interferometer.

The design sensitivity for these two proposed ground-based GW detectors, compared with the current GW detectors, is shown in *Fig. 2.27* [91]. The operation bandwidth of ground-based detectors spans from few Hz to a few kHz and it is primarily constrained by Seismic and Newtonian noises.

In parallel to the design of future ground-based GW detectors, also an effort to design and build space-based GW detectors is on going. Space-based detectors offer the potential to extend the bandwidth of GW detectors to much lower frequencies and, therefore, allowing to study massive black hole mergers [92]. Among various proposed space-based projects, the Laser Interferometer Space Antenna (LISA) [93] stands out as one of the most advanced and in a mature stage [94]. The science case for LISA is primarily focused on massive BH mergers, compact BNS within the Milky Way and extreme mass ratio inspirals. For this, LISA aims to operate at a bandwidth between 0.1 mHz and 1 Hz. A comparison of the different sensitivity bandwidths for ground-based detectors and LISA is shown in *Fig. 2.28* [95].

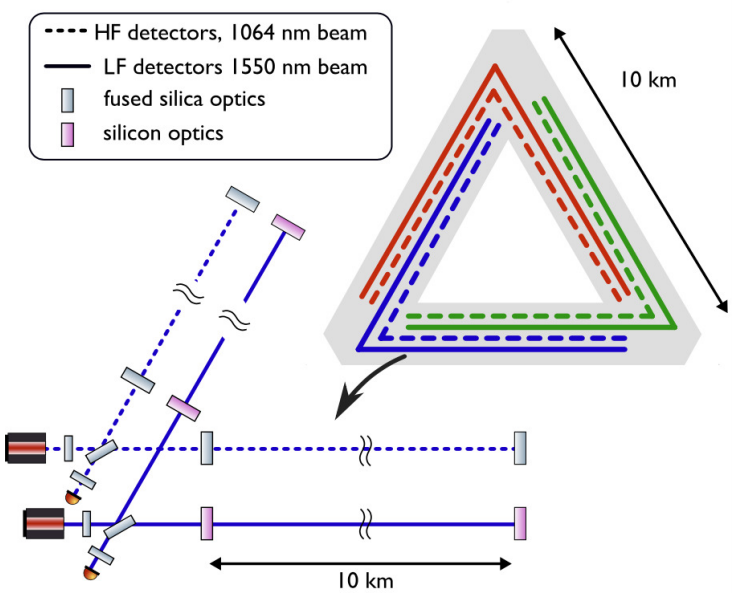

Figure 2.26: Einstein Telescope configuration with three pairs of interferometers: the ones optimized for Low Frequencies (LF) are shown in solid lines while the ones optimized for High Frequencies (HF) are shown in dashed lines.

The LISA configuration consists of three identical spacecrafts arranged in a triangular formation. Each spacecraft, separated by millions of kilometers, will host a pair of test masses that are free-floating and shielded from external disturbances, and a pair of lasers to get interferometric measurements of the distances between the test masses. A precursor of LISA was the LISA Pathfinder, launched by ESA in 2015 to demonstrate the key technologies necessary for the success of LISA [96]. Apart of demonstrating the concept of free-falling test masses in space, LISA Pathfinder also verified the operation at the Lagrange point, a gravitationally stable region in space where the gravitational forces of the Earth and the Sun balance out, allowing the spacecraft a relatively fixed position with minimal energy consumption. With these critical milestones achieved, LISA Pathfinder laid the ground for the realization of space-based GW detectors.

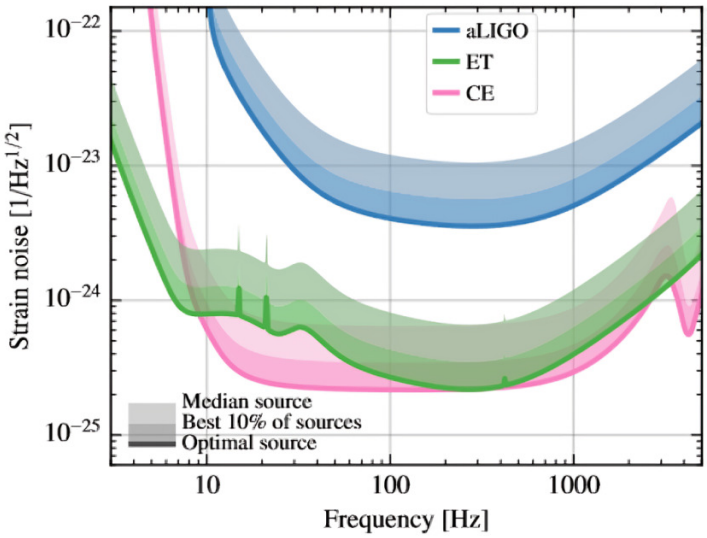

Figure 2.27: Comparison of the design sensitivity of third generation vs second generation of ground-based gravitational-wave detectors.

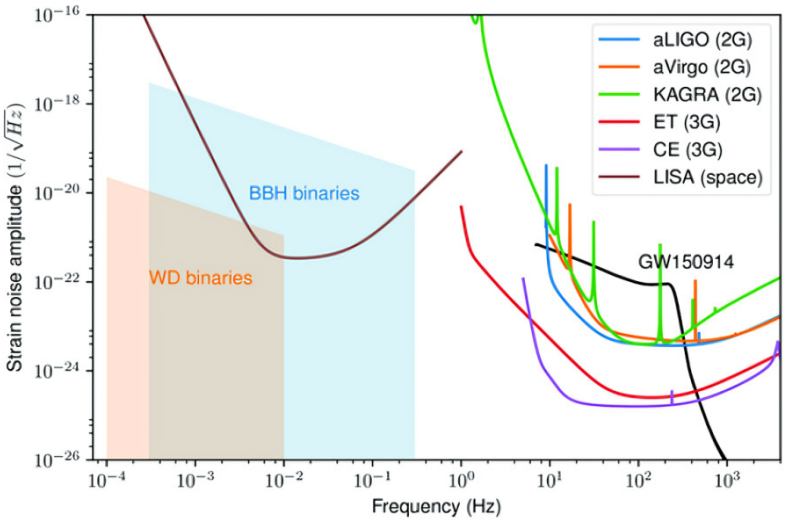

Figure 2.28: Comparison of the different bandwidths for ground-based and space-based GW detectors.

Chapter 3

A MIMO approach for longitudinal sensing and control noise projections of Advanced Virgo Gravitational-wave detector

The re-injection of sensing and control noises can constrain the sensitivity of gravitational-wave (GW) detectors. These noises originate from the control systems used to maintain the proper working point of the interferometric detector and can severely limit its sensitivity, if not properly mitigated. In the case of Advanced Virgo Plus [1], one of the key upgrades in view of the O4 observing run involves the installation of a signal recycling (SR) mirror. This mirror, installed at the output port of the detector, is designed to enhance and shape the sensitivity.

To address the challenges posed by the re-injection of sensing and control noises, we propose a multiple-input multiple-output (MIMO) approach for the control of the longitudinal degrees of freedom (DoFs) of the detector. This approach utilizes a comprehensive model of the interferometric detector, incorporating the coupling mechanisms between the different DoFs. By employing this model, we can predict the contribution of sensing and control noises to the overall detector sensitivity and develop strategies for noise mitigation.

Our methodology consist of implementing a MIMO model of the Advanced Virgo Plus detector, which takes into account the sensing noise sources and their interactions. The results obtained from these simulations provide valuable

[1] This paper refers to the configuration of the Advanced Virgo Plus, but for simplicity, it is referred to as Advanced Virgo in the text.

insights into the dominant noise contributors and their frequency-dependent behavior. Based on the MIMO model simulations, we have developed decoupling filters aimed at reducing the impact of sensing and control noises, particularly in the low-frequency region. These filters are designed to suppress the re-injection of sensing noises in the control loops and subtract them from the detector's output, thus enhancing the overall sensitivity. The effectiveness of these filters is validated through extensive simulations, demonstrating their potential to achieve the desired low control noise target.

In addition to test noise subtraction filters, this MIMO model serves as the core of a so-called noise budget tool. This tool will allow us to estimate the contribution of all the known noise sources to the measured sensitivity, providing a comprehensive understanding of the detector's noise environment.

This work is described in a paper that was published on August 21st, 2023, in the journal Classical and Quantum Gravity, Volume 40, Number 18. DOI: 10.1088/1361-6382/aceb4e.

A MIMO approach for longitudinal sensing and control noise projections of Advanced Virgo gravitational-wave detector

Enzo N. Tapia San Martín, M. Valentini, D. Bersanetti, M. Was, R. Maggiore, M. van Dael, J. W. Perry, B. L. Swinkels, M. Mantovani, A Freise.

Classical and Quantum Gravity, Volume 40, Number 18
IOP Science
DOI 10.1088/1361-6382/aceb4e
Published 21 August 2023

Abstract

So far, the sensitivity of gravitational-wave (GW) detectors, in the low-frequency and mid-frequency regions of its bandwidth, has been limited by technical noises. The re-injection of sensing and control noises can be one of the main limitations. After the end of the third observing run O3, in preparation for the fourth observing run O4, an upgrade phase started among all the km-scale GW detectors, namely LIGO, Virgo and KAGRA, with the aim of improving their sensitivity. In particular, for the case of Advanced Virgo, one of the most significant upgrades is the installation of a signal recycling (SR) mirror, introducing the signal recycling cavity. The main target of this signal recycling mirror is to shape the sensitivity curve of the detector. The installation of a signal recycling mirror adds an extra optical cavity and, thus, extra degrees of freedom (longitudinal and angular), that should be controlled to keep its working point, ultimately increasing the complexity of the whole control strategy. In order to have an accurate description of the interferometer, we have implemented a multiple-input multiple-output (MIMO) model in the frequency domain.

The target of this paper, after showing the Advanced Virgo configuration for the next observing run, is to describe the control scheme used for the main longitudinal degrees of freedom using a MIMO approach. In particular, we detail a useful matrix representation for the modeled system. Finally, we use the implemented model to project the sensing and control noises on the sensitivity curve. Following the obtained results, we propose noise subtraction filters to achieve the low control noise target in the low-frequency region of the sensitivity curve. Additionally, using this model, we have implemented the core of a noise budget tool, which will allow to estimate the contribution of all the known sources of noise on the measured sensitivity.

3.1 Introduction:

Gravitational-wave astronomy is now a consolidated research field. The first observation was done in 2015 [97] by the Advanced LIGO detectors [98] during the first observing run (O1). A total of three binary black hole (BBH) mergers were detected in O1 [99]. In 2017, during the last month of the second observing run (O2), Advanced Virgo [4] joined the network. During this second run, seven BBH mergers [100] were detected and also the first observation of a GW signal originated from the merger of neutron stars was achieved [101]. This detection gave rise to the era of the multi-messenger astronomy [102]. For the third observing run (O3) all the detectors were upgraded in order to improve their sensitivity and 79 GW signals have been detected [103, 104]. In view of the fourth observing run O4, all the detectors have gone through different upgrades with the aim of improving sensitivity [105].
The design sensitivity of GW detectors is limited by the so-called fundamental noises. In particular, at frequencies below 10 Hz, it is limited by seismic noise [106], Newtonian noise [107] and radiation pressure noise [108]. Between 10 Hz and $\sim$ 100 Hz, the sensitivity is limited by thermal noise, respectively of the suspensions and of the mirrors [109]. Finally, above 100 Hz, the sensitivity is limited by shot noise [110]. Unfortunately, the real sensitivity of all the detectors is partially limited by the so-called technical noises, related to the environment hosting the experiments and the technology used to implement them. One target of the commissioning activities done before the observing runs is to characterize and understand these noises and reduce them. Among the various technical noises, one important role is played by the sensing and control noises from the longitudinal and angular degrees of freedom (DoFs). Despite

the fact that during O3 these specific noises were not the main limitation in the low-frequency region of the sensitivity, they could become the main offender following the continuous upgrades implemented in the detectors. It could also impact the sensitivity of future detectors, such as the Einstein Telescope [111], considering that this detector will focus on getting its sensitivity improved for lower frequencies than the current detectors (1 Hz - 10 Hz).

This work will focus on the characterization of the longitudinal controls of Advanced Virgo, with the purpose to better understand and unravel the contribution of the control noises in preparation for O4. In particular, a multiple-input multiple-output (MIMO) approach [112], used to model these controls, will be presented. In this model, in contrast with a single-input single-output (SISO) approach, all the cross-coupling terms from the longitudinal DoFs are taken into account.

Similar models have been already developed in the past for LIGO to implement feed-forward filters from auxiliary DoFs to the GW strain channel. They are described in [113] and in [114] . In an analogous way, this technique has been implemented also for the Virgo detector and described in [115] and in [116]. In these works, MIMO models have been also used to implement feed-forward or noise subtraction filters in order to reduce the effect of the control noises of auxiliary DoFs to the signal sensitive to the passage of a GW. These methods typically start with a description of a reduced representation of a system using a MIMO model with two inputs and two outputs. From this model, one can design a subtraction filter to reduce the contribution of the control noise of one of the loops to the targeted DoF. In this paper, we describe in detail this method for the case of the Advanced Virgo configuration for O4, expanding it for the full interferometer, considering five DoFs. We focus on the couplings limiting the sensitivity, designing the related subtraction filters. We plug-in these noise subtraction filters in a MIMO model of the longitudinal DoFs of the detector in order to study the effects of more than one noise subtraction filter at the same time. In this way, the path by which these noises are propagated inside the loop and projected into the sensitivity can be studied and characterized. It will be shown that Advanced Virgo needs to use these decoupling filters in order to satisfy the requirements on the sensitivity curve for O4.

In general, not only sensing and control noises, but also other technical noises can limit the sensitivity of the detectors. For that reason, the model has been built in a way that can be upgraded to include also the estimated

projections of other typical noise sources. This model can serve as a core of a noise budget directly in the frequency domain by computing the noise projection on the DoF sensitive to GW from all the noises or perturbations entering the control loop through different points.

3.2 Advanced Virgo configuration for O4

For the next planned observing run (O4), the Advanced Virgo configuration will be a Dual-Recycled, Fabry-Perot, Michelson interferometer (DRFPMI) [4]. This configuration involves seven core optics: a power recycling mirror (PR), a signal recycling mirror (SR), a beam-splitter (BS), an input mirror and an end mirror for the arm West-pointing arm cavity (WI and WE, respectively) and an input mirror and an end mirror for the arm North-pointing arm cavity (NI and NE, respectively). The Michelson interferometer, formed by the BS and the two arms, is the typical core configuration of the current GW detectors. In order to increase the effective arm length and, most importantly, its sensitivity, Fabry-Perot (FP) cavities are added to each arm of the detector. The working point of the interferometer is tuned to have a destructive interference for the light beams coming back from the arm cavities, the so-called dark fringe (DF) configuration. Thus, most of the light is reflected back towards the input port of the interferometer and lost. However, by placing a semi-transparent mirror (PR) between the BS and the main laser, forming a power recycling cavity (PRC), one can recycle this light and inject it back into the interferometer. This increases the effective power circulating inside the interferometer and, therefore, improves its sensitivity, at the cost of adding another control DoF. The passage of a gravitational-wave causes a differential change in the arm length, inducing a phase-shift of the recombined laser at the output port. This out-of-phase beam leaks towards the output port and GWs can be detected. By placing a mirror (SR) between the BS and the output port of the detector, forming a signal recycling cavity (SRC), it is possible to shape and optimize the detector bandwidth for specific GW sources. Again this is at the cost of adding another DoF.
Some other systems and elements are needed to build a GW detector: for example, a high-power stabilized laser, electro-optic modulators (EOMs), photodiodes (PDs), a data acquisition system, electronics, seismic isolation systems and optical systems among others. The main pre-stabilized laser provides a coherent light beam, characterized by high power to reduce the impact of the

shot noise. The EOMs are used to modulate the main laser beam and generate sidebands of the carrier signal, which are used to control the different DoFs of the detector. An input mode cleaner cavity (IMC) filters out higher-order modes, in order to have only the fundamental Gaussian mode entering in the interferometer. A reference cavity (RFC), in combination with the IMC, is used to further stabilize the frequency of the main laser [117]. Various PDs are installed at different pick-off ports of the interferometer: $\mathrm{IMC_{REFL}}$ is located at the reflection port of the IMC; B1 is located at the output port of the interferometer; B2 is installed at the input port, in reflection of the PR cavity; B4, is located to acquire a pick-off beam from the light circulating inside the PR cavity; B7 and B8 are used to sense the transmission of the light from the FP cavities.

A sketch of the Advanced Virgo optical configuration is shown in *Fig. 3.1.*

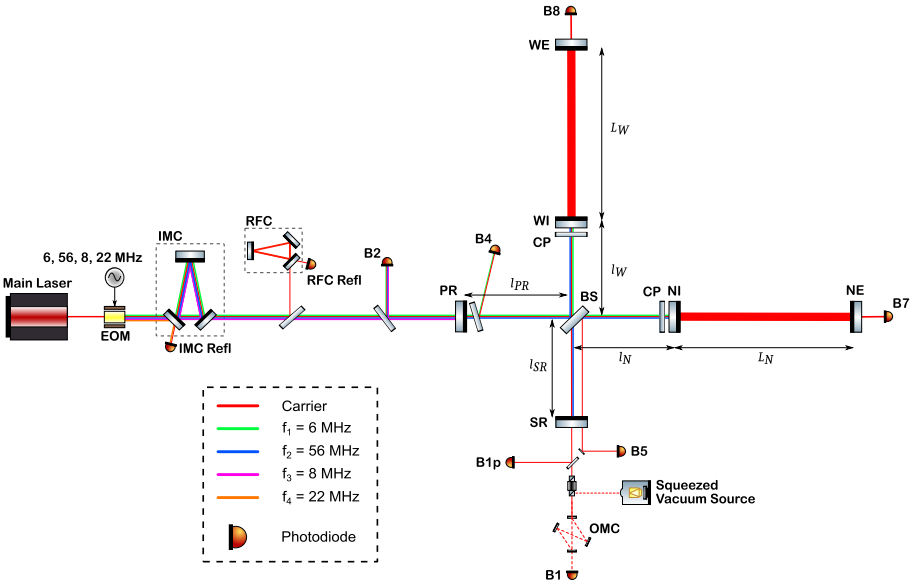

Figure 3.1: Advanced Virgo optical configuration for the O4 observing run. The laser beam travels towards the interferometer. It passes through the IMC cavity and the PR mirror, then the laser beam is split at the BS and directed towards the North and West arms. Then, the beams are reflected by the end mirrors of each arm and directed back to the BS, where the beams are recombined and split again towards the input port and output port passing through the SR mirror. The carrier is shown in red. The different sidebands f_1, f_2, f_3, f_4 are indicated in green, blue, pink and orange respectively.

3.2.1 Main longitudinal degrees of freedom

Adding additional cavities to the detector increases the number of DoFs that should be controlled to have the interferometer properly working to achieve the maximum sensitivity. The long arms, i.e. the FP cavities, are composed by WI and WE mirrors for the West arm and by the NI and NE mirrors for the North arm. The short arms of the Michelson interferometer are made by the BS, the NI and the WI mirrors. The power recycling cavity (PRC) is made by the PR, the NI and the WI mirrors. The signal recycling cavity (SRC) is made by the SR, the NI and the WI mirrors. The five main longitudinal DoFs of a DRFPMI configuration are defined as:

- **DARM** = $\frac{L_N - L_W}{2}$: **D**ifferential **ARM** length of the two FP cavities in the arms. This is the most crucial DoF, since it is the one sensitive to the passage of GWs.
- **CARM** = $\frac{L_N + L_W}{2}$: **C**ommon **ARM** length, average of the long arms length.
- **MICH** = $l_N - l_W$: Length difference between the lengths from the BS and, respectively, the NI and the WI mirrors, forming the **MICH**elson interferometer.
- **PRCL** = $l_{PR} + \frac{l_N + l_W}{2}$: **P**ower **R**ecycling **C**avity **L**ength.
- **SRCL** = $l_{SR} + \frac{l_N + l_W}{2}$: **S**ignal **R**ecycling **C**avity **L**ength.

The lengths of the different cavities forming these DoFs are shown in *Fig. 3.1.*

3.2.2 Modulation-Demodulation technique

As previously mentioned, in order to achieve maximum sensitivity and stability, the interferometer has to keep the FP, the PRC and the SRC cavities on resonance and the MICH degree of freedom in the DF configuration [4]. The error signals for these control loops are generated using a radio frequency (RF) modulation-demodulation technique, derived from the classical Pound-Drever-Hall (PDH) technique [118, 64]. In this technique, the light field is modulated at a certain frequency. Then, the error signals are obtained by demodulating the output of the PDs using a mixer at the same chosen frequencies.
For the Advanced Virgo case, the light field of the main laser is phase modulated at four different frequencies ($f_1 = 6\,\mathrm{MHz}$, $f_2 = 56\,\mathrm{MHz}$, $f_3 = 8\,\mathrm{MHz}$

and $f_4 = 22\,\mathrm{MHz}$) using EOMs, which are summarized as a single element in *Fig. 3.1.* These EOMs generate sidebands at multiples of the modulation frequencies. The interferometer, i.e. the length of the cavities, is designed and the modulation frequencies are chosen to allow or not the resonance of the different sidebands in the various cavities. By design, all the sidebands, except the ones multiple of f_4, are resonant in the IMC and pass through it going into the interferometer. The sidebands at f_4, which are reflected by the IMC, are used to control the IMC length. None of the sidebands is resonant inside the FP arm cavities. f_1 is defined to be resonant inside the PRC. f_2 is defined to be resonant inside the PRC and the SRC. Finally, f_3 is defined to be anti-resonant inside both the PRC and SRC. The resonant sidebands in the different cavities are shown in *Fig. 3.1.*

3.2.3 Longitudinal Sensing and Control scheme

The DARM DoF corresponds to the differential length of the North and West FP cavities. For the Advanced Virgo detector, this DoF is sensed using a DC readout scheme [119], extracting the error signal from the B1 photodiode used in DC. The signal is acquired and passes through a series of servo filters of the control loop. From the output of the servo filters, a correction signal is obtained and sent to the actuators of the system. The actuators used to control the position of the suspended mirrors are coil-magnet pairs, which can apply a force on the mirrors over a limited bandwidth defined by the coil-driver circuit. The magnets are glued almost at the edge of the anti-reflective face of the mirrors, while the coils are installed on the mechanical structure surrounding the mirrors. Therefore, it is necessary to consider also the pendulum dynamics in the actuation characterization. In the case of DARM, the actuation is applied to the end mirrors of the FP cavities, i.e. the NE and the WE mirrors. In a similar way, with the definition given in section 3.2.1, one can describe the feedback loop of the other DoFs.
The MICH DoF is sensed using the in-phase (0 rad) component of the B2 photodiode demodulated at f_2. This error signal is passed through a bank of filters properly designed for this DoF. The correction signal for this DoF is sent to the coil-magnet actuators of the BS. The same correction signal is sent also to the PR and SR mirrors, in order to compensate the length variation of l_{PR} and l_{SR} due to the motion of BS. Thus, these three mirrors are the actuators of MICH DoF.

The PRCL DoF is sensed using the in-phase component of the B2 photodiode demodulated at f_3. The correction signal of this DoF is sent to the coil-magnets of the PR mirror, which is the actuator of the PRCL DoF.
The SRCL DoF is sensed using the in-quadrature component of the B2 photodiode demodulated at f_2. The correction signal of this DoF is sent to the coil-magnets of the SR mirror, which is the actuator of the SRCL DoF.
A sketch of the Longitudinal Sensing and Control (LSC) scheme is shown in *Fig. 3.2*.

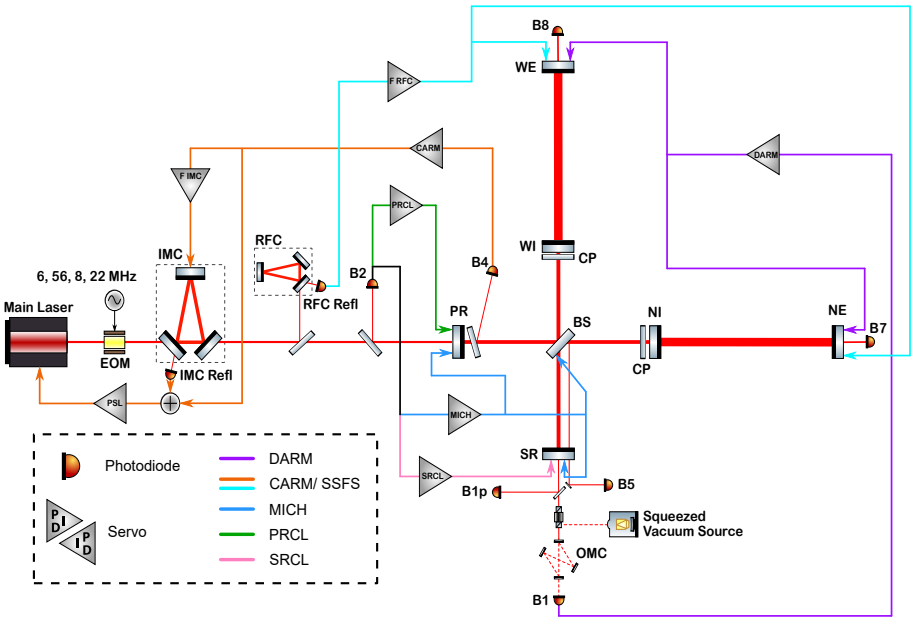

Figure 3.2: Longitudinal Sensing and Control scheme of Advanced Virgo for O4. A beat note signal between the partially reflected carrier field and the sidebands are measured by PDs located at different ports of the interferometer. By demodulating this beat note at one of the frequencies of the generated sidebands and with a low-pass filter, one gets an error signal to control a cavity. The connection between error signal, control filter and actuators of DARM is shown in purple. The connection of CARM/SSFS loop is shown in orange and calypso. The connection of MICH loop is shown in blue. The connection of PRCL loop is shown in green. The connection of SRCL loop is shown in pink.

On the other hand, the CARM DoF is sensed using the in-phase component of the B4 photodiode demodulated at f_1. This is a special case, since this error signal is sent towards the laser injection system to further stabilize the

frequency of the main laser. Then, another error signal taken from the reflection port of the RFC cavity is sent to the end mirrors of the FP cavities, i.e. the NE and the WE mirrors [120]. This control loop is described in detail in section 6.6.
The sensing and actuation of these five longitudinal DoFs are summarized in table 3.1.

DoF	PD and demod. frequency	Actuator
DARM	B1_DC	differentially NE and WE
CARM	B4_6 MHz_I	commonly NE and WE
MICH	B2_56 MHz_I	BS, PR and SR
PRCL	B2_8 MHz_I	PR
SRCL	B2_56 MHz_Q	SR

Table 3.1: Readout and actuators of longitudinal DoFs.

For the characterization and the design of a single DoF control loop, information about the different components are needed: the optical response in the frequency domain of the considered DoF or, in other words, the plant transfer function (TF); the photodiode response of the sensing, or the error signal; the pendulum dynamics of the actuator; the sign of the actuation. In general, this is the description of five DoFs controlled as a five separate Single-Input Single-Output (SISO) system, under the assumption of small couplings among them. This approach is also known as decentralized control scheme. However, for such a complex and sophisticated system, this should be revisited and studied in detail, considering, in particular, the cross-coupling effects among the five DoFs. Therefore, in this study we propose a model that takes into account all the cross-couplings among these DoFs with a Multiple-Input Multiple-Output (MIMO) approach. With this method we study the re-injection of sensing and control noises into the closed loop system of the particular case of Advanced Virgo. On top of that, this approach provides also guidance on the design of noise subtractions or decoupling filters to meet the requirements on the noise projections of these DoFs on the sensitivity curve.

3.2.4 Second Stage of Frequency Stabilization loop

As mentioned before, GW detectors need a very stable laser source. A pre-stabilization of the laser frequency is part of the early stages of the process implemented to control the whole experiment. In particular, the laser frequency is pre-stabilized using a fixed cavity as reference [121]. A further step

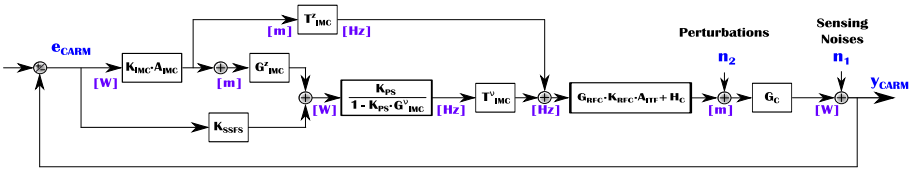

Figure 3.3: Block diagram of the SSFS/CARM loop.

is needed to improve the stabilization of the laser frequency. Therefore, when the FP optical cavities are controlled, they are used as a better reference. This further step is called Second Stage of Frequency Stabilization (SSFS) [120]. The SSFS is coupled to the control of CARM. In this section, we describe the CARM/SSFS DoF scheme using the block diagram shown in *Fig. 3.3*. After a block diagram reduction, the equivalent block between the error signal of CARM e_{CARM} and the perturbations n_2 can be considered as a controller of CARM DoF. Then, its equivalent plant of the loop is G_c. The final target of this block diagram reduction is to include it in the global MIMO control scheme.

The output of this scheme, y_{CARM}, is the power measured by the dedicated PD to sense CARM in units of [W]. All the blocks and variables are described below:

- G_C: Optical response from the motion of the NE and the WE mirrors to the SSFS error signal [W/m].
- H_C: Relation between the frequency fluctuations and the change of the length of the CARM DoF [m/Hz].
- A_{ITF}: Pendulum dynamics of the actuator of the end mirrors of the long optical cavities [m/V].
- K_{RFC}: Controller to correct the length of CARM for variations in the laser frequency [V/W].
- G_{RFC}: Response of the PD placed in reflection of the RFC cavity for the fluctuations in the laser frequency [W/Hz].
- T^{ν}_{IMC}: Optical transfer function of the IMC cavity which relates the input frequency noise to its output frequency noise [Hz/Hz].
- K_{PS}: Controller to correct the frequency of the main laser source [Hz/W].

- G^{ν}_{IMC}: Response of the PD placed in reflection of the IMC cavity for the fluctuations in the laser frequency [W/Hz].
- T^{z}_{IMC}: Transfer function from longitudinal motion of the IMC cavity to frequency noise in transmission [Hz/m].
- G^{z}_{IMC}: Optical response from the motion of the IMC end mirror to the IMC error signal [W/m].
- K_{IMC}: Controller acting on the IMC end mirror for frequencies below 200 Hz in [V/W]. This bandwidth is enough to stabilize the low frequency motion of the mirror.
- A_{IMC}: Pendulum dynamics of the actuator of the end mirror of the IMC cavity[m/V].
- K_{SSFS}: SSFS controller using the CARM error signal above 200 Hz and serving as reference signal for the pre-stabilization loop [W/W].

In the scheme of *Fig. 3.3*, the error signal for the SSFS is represented by e_{CARM}. this signal is taken from the in-phase component of the B4 photodiode demodulated at f_3. Sensing noises n_1 and perturbations n_2 are also included in this diagram and will be addressed in detail in section 3.4.

3.3 Multiple-Input Multiple-Output scheme for the longitudinal controls

A MIMO scheme of the longitudinal loops is presented in *Fig. 3.4*. In this scheme, the vector of the discrete-time error signals is represented by $e(nT_s)$, for $n = 0, ..., N-1$, where N is the number of samples and T_s is the sample time. The vector of the discrete-time outputs measured by the PDs is represented by $y(nT_s)$. Different discrete-time noise sources have been included in this diagram as $n_i(nT_s)$, where $i = 1, ..., 6$. For this tool only six types of noise or perturbations have been considered (sensing noise, perturbations/calibration, perturbations, driver noise, DAC noise and ADC noise), but it can be upgraded to include more different noises.

The blocks, or matrices, of this scheme are described below:

- $\mathbf{G}(j\omega_k)$, where $\omega_k = 2\pi f_k$ and $f_k = k/NT_s$, is the "Optical response matrix". It defines all the relations, including cross-coupling, among the

change of length of the different optical cavities and the power readout by the dedicated PDs. Since there are five main longitudinal DoFs for Advanced Virgo in the O4 configuration, this matrix has five rows and five columns of transfer functions (TFs). These TFs are estimated using the tool FINESSE [122, 123].

- $\mathbf{C}(j\omega_k)$ is the "Control matrix". It contains all the designed control filters used to control each longitudinal DoF. Since a SISO system approach is typically used to design these filters, this is a diagonal matrix.

- $\mathbf{B}(j\omega_k)$ is the "Decoupling filter matrix". If needed, this matrix is used to include filters to decouple the other DoFs from DARM, which is sensitive to GWs. When no decoupling filters are applied, this matrix is the Identity, therefore each DoF is controlled independently by its own control filter. In Section 3.5 the presence of coupling will be described and this matrix will be modified to include decoupling filters.

- $\mathbf{D}$ is the "Driving matrix". It provides a coordinate transformation from the longitudinal DoF to the individual mirror motion. It is used to select the output signals of the control filters that is sent to a set of mirror actuators.

- $\mathbf{H}(j\omega_k)$ is the "Coil Driver matrix". It includes the low-pass filters present in the coil drivers of the magnet-coil actuators of the mirrors. This is a diagonal matrix.

- $\mathbf{A}(j\omega_k)$ is the "Pendulum dynamics matrix". It includes the dynamics of the actuator that follows a double pendulum shape in frequency, due to its seismic isolation system. This is also a diagonal matrix.

- $\mathbf{O}$ is the "Geometrical matrix". It provides a coordinate transformation from the mirror motion to the longitudinal DoF motion. It is the inverse of the driving matrix $\mathbf{D}$.

- $\mathbf{I}$ is the "Sensing matrix". It passes the error signal obtained with the PDs to the different DoFs. Each signal of the dedicated PD is passed directly to the respective DoF error signal, therefore this is a diagonal matrix.

The elements of these matrices are represented as Frequency Response Functions (FRFs) of N frequency bins. Therefore, these blocks are three-dimensional complex arrays of size $5x5xN$. In the calculations, each frequency

bin is treated separately and standard matrix operations can be used. All described matrices are square.

There is no actuation applied on the NI and WI mirrors, therefore the geometrical matrices **O** and **D** are square instead of having a dimension of $5x7xN$ and $7x5xN$ respectively. The elements of the matrices **D** and **O** are frequency independent.

FINESSE, the tool used to estimate the optical transfer function matrix $\mathbf{G}(j\omega_k)$, can compute the behaviour of light beams inside different optical systems. These computations are performed in the frequency domain. The first step is implementing a model of the interferometer in FINESSE. Next, a working point is defined and the lengths of the optical cavities are tuned to maximize the optical gain. In this way the TFs from the motion of the mirrors corresponding to a motion of one DoF at the time can be estimated, obtaining the TFs to the readout of all the five DoFs. With this process a total of 25 Optical TFs is obtained. Thus, for the longitudinal DoFs DARM, CARM, MICH, PRCL and SRCL with corresponding subindices $1, ..., 5$, the "Optical Response Matrix" has the following representation:

$$\begin{pmatrix} DARM_{output} \\ CARM_{output} \\ MICH_{output} \\ PRCL_{output} \\ SRCL_{output} \end{pmatrix} = G(j\omega_k) \cdot \begin{pmatrix} DARM_{input} \\ CARM_{input} \\ MICH_{input} \\ PRCL_{input} \\ SRCL_{input} \end{pmatrix}. \tag{3.1}$$

Using the same procedure, also the other blocks of the scheme shown in *Fig. 3.4* can be estimated. $\mathbf{C}(j\omega_k)$, $\mathbf{H}(j\omega_k)$ and $\mathbf{A}(j\omega_k)$ are diagonal matrices.

3.4 MIMO transfer function matrices

In this section we will describe the properties of the useful transfer function matrices for the LSC model shown in block diagrams in *Fig. 3.4*. Typically, a control loop is characterized by its open loop transfer function (OLTF), which is the response obtained by opening the loop at a certain node, injecting noise on that node and measuring the signal at the same node after passing through

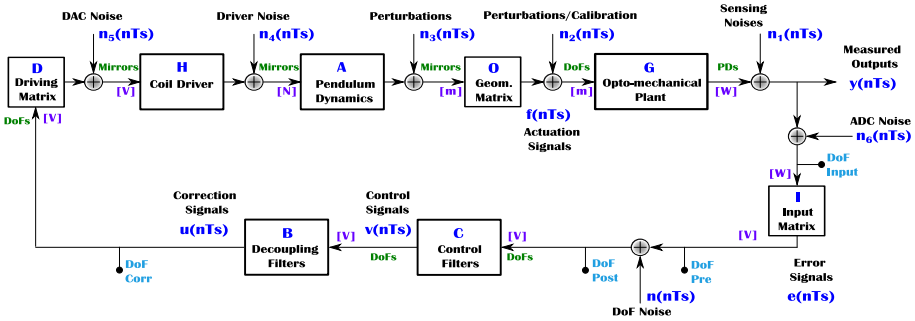

Figure 3.4: Block diagram of the LSC loops in a MIMO representation.

all the blocks of the loop. The result of the OLTF is the product of all the blocks specified in the control system scheme. In the case of Advanced Virgo, the nodes used for the TF estimations are called "DoF Pre" and "DoF Post". These names are due to fact that they are taken at the points before and after the node of noise injections. The noise is injected in the node "DoF Noise". Other nodes are available for the LSC loops, called "DoF Input" and "DoF Corr", which are used during commissioning and serve, respectively, to check the status of the error signals and to check the applied correction sent to actuators. However, these nodes are not relevant for the present study. Another property of a control loop is the closed loop transfer function (CLTF), which is measured at the output and determines the effect on the measured output when the feedback system is closed. Other TFs provide information about noise and disturbance rejection. Since these TFs are studied for a MIMO system, they are matrices. They are the sensitivity function matrix $\mathbf{S}$ and the complementary sensitivity function matrix $\mathbf{T}$. All these TFs are useful to study the stability, the controllability, the observability, the robustness, the disturbance the rejection, and the optimization of the system.

Assuming that all the elements of the blocks of the diagram in *Fig. 3.4* are linear and time-invariant, the relation of the variables of the system can be analysed using the Discrete Fourier transform (DFT) [124]. The output signal $y(nTs)$ of the diagram in *Fig. 3.4* can be represented in the frequency domain as:

$$Y(k) = \frac{1}{\sqrt{N}} \sum_{n=0}^{N-1} y(nT_s) e^{-j2\pi nk/N}. \tag{3.2}$$

For the case without noises and perturbations, taking the DFT of the rest of the signals, the relations among the signals $Y(k)$, $F(k)$, $U(k)$, $V(k)$ and $E(k)$

can be obtained. For these signals, passing through the blocks of the system and omitting the term $j\omega_k$ for simplicity, the OLTF matrix is:

$$L(j\omega_k) = G \cdot O \cdot A \cdot H \cdot D \cdot B \cdot C \cdot I. \tag{3.3}$$

In a similar way, also the CLTF matrix can be computed. In a typical control system scheme, the error signal is obtained by subtracting the fed-back signal $Y(k)$ of the loop from a target reference value $R(k)$. For the control of optical cavities, the error signal is obtained demodulating the signal measured by the PDs as mentioned in section 6.4. The ratio between the measured output and this reference signal is the CLTF:

$$\frac{Y(k)}{R(k)} = L(j\omega_k) \cdot (1 + L(j\omega_k))^{-1}. \tag{3.4}$$

The vector $Y(k)$ is not the true output of the system, because these signals are perturbed by the intrinsic sensing noise of the PDs, denoted by $N_1(k)$. Therefore, for the study of noises, the relation between the different noise sources and the measured outputs in closed loop should be estimated. The relation between the sensing noise of the photo-diodes and the vector of the measured outputs is given by the sensitivity function matrix **S**:

$$S(k) = \frac{Y(k)}{N_1(k)} = (1 + L(j\omega_k))^{-1}. \tag{3.5}$$

In a similar way, the relation between a perturbation on a DoF, denoted by $N_i(k)$ at the level of the DoF motion, and the vector of the measured outputs $Y(k)$ is given by the complementary sensitivity function matrix $T_i(j\omega_k)$. For example, for perturbation $N_2(k)$, a related complementary sensitivity function matrix $T_2(j\omega_k)$ is:

$$T_2(j\omega_k) = \frac{Y(k)}{N_2(k)} = G(j\omega_k) \cdot (1 + L(j\omega_k))^{-1}. \tag{3.6}$$

Note that a calibration procedure of DARM can also be considered as a perturbation applied and producing a DARM motion.

The same computation can be done for other types of noises or perturbations entering from different nodes of the closed loop system. All these relationships are summarized in table 3.2.

	Name of matrix	TF	Source
L	Open loop transfer function	L	-
CLTF	Closed loop transfer function	$L \cdot (1+L)^{-1}$	R
S	Sensitivity function	$(1+L)^{-1}$	N_1
T_2	Complementary sensitivity	$G \cdot (1+L)^{-1}$	N_2
T_3	Complementary sensitivity	$GO \cdot (1+L)^{-1}$	N_3
T_4	Complementary sensitivity	$GOA \cdot (1+L)^{-1}$	N_4
T_5	Complementary sensitivity	$GOAH \cdot (1+L)^{-1}$	N_5
T_6	Complementary sensitivity	$GOAHDBCI \cdot (1+L)^{-1}$	N_6

Table 3.2: Transfer function matrices for the Advanced Virgo MIMO model.

This is a subset of the technical noises entering in the control loops of Advanced Virgo and affecting the main DoFs of the interferometer. Using this MIMO model it is possible to produce a core for a noise budget tool, as described in details in section 3.6.

3.5 Sensing and control noise projections

Noises or perturbations are normally characterized locally, meaning that they are characterized at the level of where they enter in the control loop. These noises are shaped by the CLTF and affect the DoF output. Considering the MIMO closed loop system representing the Advanced Virgo detector, DARM is the DoF sensitive to the passage of GWs. For this reason, all the projections of the different noises are compared to DARM. Referring to *Fig. 3.4* and, specifically for the sensing and control noises, the projections are estimated with the following procedure. As a first step, this tool computes the in-loop effect of the amplitude spectral density (ASD) [125] $\tilde{N}_1(f_k)$ of the sensing and control noise $n_1(nTs)$ of the PDs at the output node. For this purpose, the sensitivity function matrix $\mathbf{S}$ is used to transfer the sensing noise of the PDs to the equivalent noise at the output node taking into account the effect of the closed loop.

$$\tilde{N}_1^{in-loop}(f_k) = |S(f_k)| \begin{pmatrix} \tilde{N}_1^{DARM}(f_k) \\ \tilde{N}_1^{CARM}(f_k) \\ \tilde{N}_1^{MICH}(f_k) \\ \tilde{N}_1^{PRCL}(f_k) \\ \tilde{N}_1^{SRCL}(f_k) \end{pmatrix}. \tag{3.7}$$

Since we are interested in the noise projected on DARM, only the row corresponding to the in-loop noise from the different DoFs to DARM is considered. Therefore, only the first row of the matrix **S** is used:

$$\tilde{N}_1^{DARM\ in-loop}(f_k) = |S^{DoF}(f_k)|\tilde{N}_1(f_k). \tag{3.8}$$

Next, the input-referred noise, i.e. the equivalent noise at the input of the block $\mathbf{G}(j\omega_k)$ from the sensing noise entering in the loop at the output of the optical response matrix, should be checked. For this purpose, the previous result is divided by the first term of the complementary sensitivity function matrix $T_2(f_k)$. This denominator corresponds to the TF from the DARM motion to the DARM error signal in closed loop:

$$\tilde{N}_1^{Proj}(f_k) = \frac{|S^{DoF}(f_k)|\tilde{N}_1(f_k)}{|T_2^{DARM}(f_k)|}. \tag{3.9}$$

Finally, these last results in units of $\frac{\mathrm{m}}{\sqrt{\mathrm{Hz}}}$ are divided by the length of the arms of Advanced Virgo to make a comparison with the strain sensitivity h. In the long-wavelength approximation [126], h is given by the differential arm length of the interferometer over the arm length of the FP cavities L_0 ($L_0 =$ 3km for Advanced Virgo):

$$h = \frac{L_N - L_W}{L_0} = \frac{\Delta L}{L_0}. \tag{3.10}$$

3.5.1 Noise projections without decoupling filters

In order to produce the sensing noise projections on the sensitivity curve, we need the level of sensing noise present in the PDs used to sense the optical fields inside, in reflection or in transmission of the different optical cavities of

the interferometer. One of the noises that enter from the sensing noise node is the quantum noise. The quantum noise in GW detectors is composed by two types of noises: shot noise and radiation pressure noise. Shot noise arises from the number of photons impinging on the PD for a constant power level and a fixed measuring time. On the other hand, radiation pressure noise arises from the number of the photons of a laser beam impinging on a mirror with finite mass. The quantum noise level of the PDs used for Advanced Virgo controls is shown in *Fig. 3.5*. Since B1 is sensitive to the motion of DARM, it can sense the effect of radiation pressure [127] due to high power build-up inside the FP cavities. For the PDs B2 and B4 the shot noise is predominant.

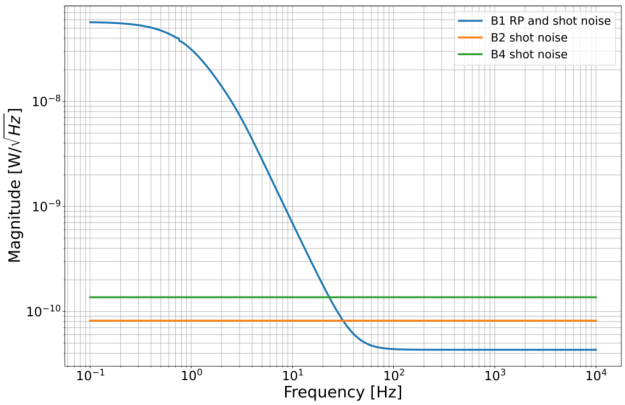

Figure 3.5: Quantum noise level on photo-diodes used for the longitudinal controls. B1 PD is sensitive to DARM, so it can see both radiation pressure and shot noise. B2 and B4 PDs only see shot noise since, not sensing DARM, they do not see any effect of radiation pressure in the 3km FP cavities.

Using this information and the equations 3.7, 3.8, 3.9 and 3.10 one can estimate the sensing noise projections of the main longitudinal DoFs and compare them to the design sensitivity.

Fig. 3.6 shows the Advanced Virgo target sensitivity for O4 (blue region), corresponding to a binary neutron star (BNS) range of $80 - 115$Mpc [128]. As general requirement, all the technical noises should be, at least, a factor of ten below the sensitivity to be sure that the detector is not limited by them. This safety margin corresponds to the orange region in *Fig. 3.6*.

Moreover, the control noise projections from the re-injection of the PDs sensing noise are estimated for the main longitudinal DoFs (CARM, MICH, PRCL, SRCL) and compared to the target sensitivity and the safety margin

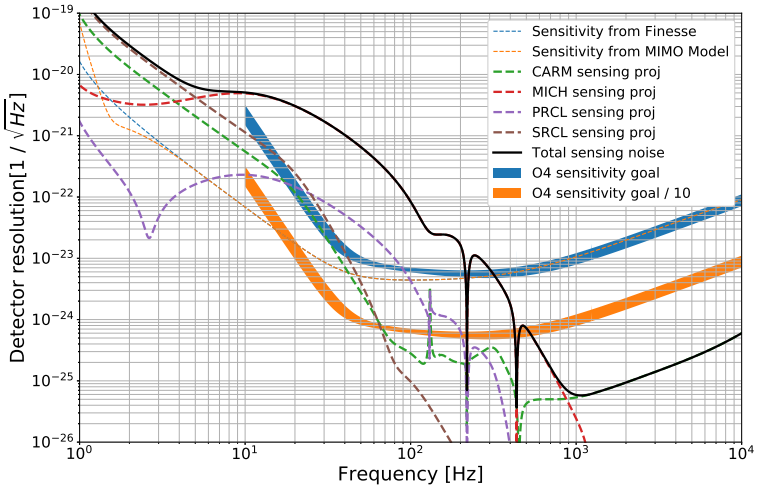

Figure 3.6: Sensing noise projections for the LSC control loops compared to designed sensitivity without any noise subtraction filter.

in *Fig. 3.6*. The MICH noise projection is shown in red: it is clearly not compliant with the sensitivity target. Its shape is defined by the matrix **S**. Moreover, also the noise projection of SRCL, shown in brown, is slightly above the target sensitivity at low frequencies. In the bandwidth $20 - 90$Hz, also the noise projection of PRCL, shown in purple, is above the target sensitivity. The CARM/SSFS noise projection, shown in green, is inside the target sensitivity region at low frequencies, while its shape at high frequencies is given by the coupling between CARM and DARM DoFs due to the imperfect common mode rejection. Additionally, also the quantum-noise limited sensitivity estimated with FINESSE and the quantum-noise limited sensitivity estimated with the MIMO tool from the Optical TFs are shown in *Fig. 3.6*, respectively in the dashed blue and dashed orange lines, and compared to the target sensitivity and the LSC noise projections.

It is clear that the sensitivity target for O4 is spoiled by the re-injection of sensing and control noises from the PDs of the main longitudinal DoFs. Therefore, to reduce these noises, it is necessary to introduce decoupling filters in the control loop.

3.5.2 Decoupling filters

As mentioned before, a GW detector is a complex system full of cross-coupled DoFs. In principle, all the cross-couplings can be tackled with a full $\mathbf{B}(j\omega_k)$ decoupling matrix. With the aim of reducing or removing the interactions from the control signals $V(k)$ to measured outputs $Y(k)$ of *Fig. 3.4*, the following product should be a diagonal matrix, namely $\mathbf{Q}(j\omega_k)$:

$$G \cdot O \cdot A \cdot H \cdot D \cdot B = Q. \tag{3.11}$$

Commonly, when the matrix $\mathbf{Q}(j\omega_k)$ is not diagonal, the diagonal elements of the plant matrix $\mathbf{G}(j\omega_k)$ can be chosen in order to obtain $\mathbf{Q}(j\omega_k)$, which simulates a plant without cross-couplings:

$$Q(j\omega_k) = diag[G(j\omega_k)]. \tag{3.12}$$

Then, $\mathbf{B}(j\omega_k)$ can be chosen to obtain the following relation:

$$B(j\omega_k) = (G \cdot O \cdot A \cdot H \cdot D)^{-1} \cdot Q. \tag{3.13}$$

This technique is known as generalized decoupling, which is possible if the model is perfect and, thus, it is not feasible in practice. Therefore, if a subset of DoF couplings are more critical than others, a possible solution is to implement a partial decoupling. In order to do this, a model of N inputs and N outputs is reduced to a $2x2$ MIMO model between the variables that should be decoupled. Following a procedure similar to the one shown in [129], decoupling filters for the main LSC DoFs spoiling the sensitivity curve have been designed.

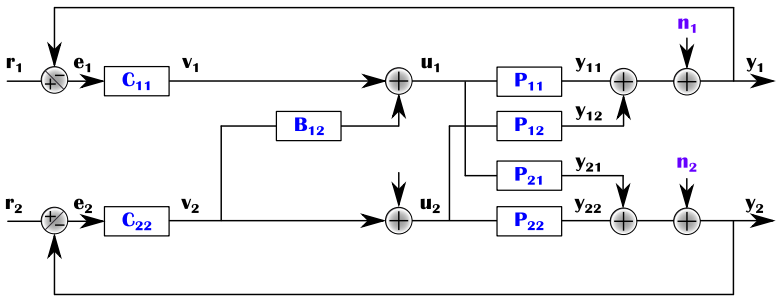

Figure 3.7: 2x2 MIMO scheme with decoupling filter included.

Fig. 3.7 shows a 2x2 MIMO system. The controllers of the two DoFs are defined as C_{11} and C_{22}. A filter B_{12} is included to decouple the dynamics of the lower loop to the upper loop. Finally, the blocks P_{11}, P_{12}, P_{21} and P_{22} represent the plant including cross-coupling terms. In this way, it is possible to write the OLTF of the scheme as:

$$P \cdot B \cdot C = \begin{pmatrix} P_{11} & P_{12} \\ P_{21} & P_{22} \end{pmatrix} \cdot \begin{pmatrix} 1 & B_{12} \\ 0 & 1 \end{pmatrix} \cdot \begin{pmatrix} C_{11} & 0 \\ 0 & C_{22} \end{pmatrix} \tag{3.14}$$

$$= \begin{pmatrix} P_{11} & P_{12} \\ P_{21} & P_{22} \end{pmatrix} \cdot \begin{pmatrix} C_{11} & x = B_{12}C_{22} \\ 0 & C_{22} \end{pmatrix} \tag{3.15}$$

$$= \begin{pmatrix} P_{11}C_{11} & P_{11}x + P_{12}C_{22} \\ P_{21}C_{11} & P_{21}x + P_{22}C_{22} \end{pmatrix}. \tag{3.16}$$

In order to decouple the interactions from the lower loop to the upper one shown in *Fig. 3.7*, one forces $P_{11}x + P_{12}C_{22} = 0$. Thus, the decoupling matrix $\mathbf{B}(j\omega_k)$ turns in:

$$B(j\omega_k) = \begin{pmatrix} 1 & \frac{-P_{12}}{P_{11}} \\ 0 & 1 \end{pmatrix}. \tag{3.17}$$

As a consequence, the OLTF of this scheme becomes:

$$P \cdot B \cdot C = \begin{pmatrix} P_{11}C_{11} & 0 \\ P_{21}C_{11} & \frac{-P_{12}C_{22}P_{21}}{P_{11}} + P_{22}C_{22} \end{pmatrix}. \tag{3.18}$$

The decoupling filters can be included in the MIMO scheme, specifically in the block $\mathbf{B}(j\omega_k)$ from *Fig. 3.4*. Following the previously described procedure, we have designed decoupling filters for interactions from MICH to DARM and from SRCL to DARM.

3.5.3 MICH2DARM decoupling filter

First, following the procedure described in section 3.5.2 for a simplified MIMO model, we add a "mich2darm" decoupling filter in the first row and third column of matrix $\mathbf{B}(j\omega_k)$ of the full 5x5 MIMO model. The filter "mich2darm" is computed as $\frac{-G_{13}}{G11}$ from the optical response matrix $\mathbf{G}(j\omega_k)$. Its shape is shown in *Fig. 3.8*.

Fig. 3.9 shows the LSC noise projections compared to the target sensitivity including the "mich2darm" decoupling filter: it is possible to see that, with

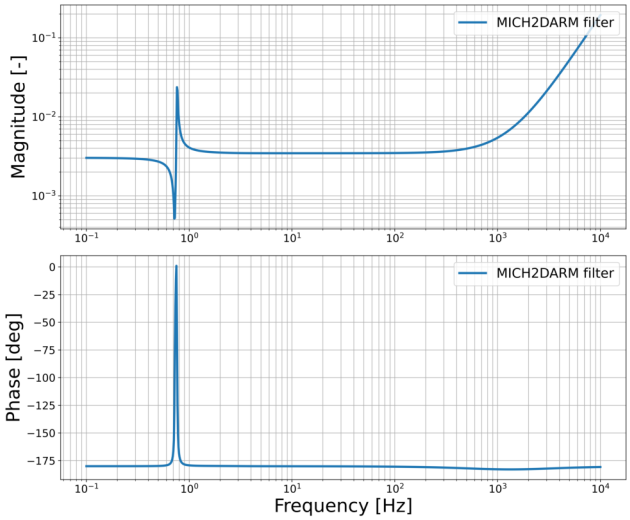

Figure 3.8: Computed decoupling "mich2darm" filter from MIMO model.

the implementation of the filter, the sensing noise from MICH projected onto DARM is reduced. Moreover, also the shape of the other projections changes. This is due to the not diagonal 5x5 Optical matrix. Therefore, all the elements of the matrix $\mathbf{S}(j\omega_k)$ are modified by the addition of the "mich2darm" filter. Additionally, with this configuration, the SRCL sensing and control noise projection limits the sensitivity in the low-frequency region.

3.5.4 SRCL2DARM decoupling filter

It is possible to reduce the sensing and control noise projection of SRCL by adding a "srcl2darm" filter in the first row and fifth column of the decoupling matrix $\mathbf{B}(j\omega_k)$. The filter "srcl2darm" is computed as $\frac{-G_{15}}{G11}$ from the optical response matrix $\mathbf{G}(j\omega_k)$. Its shape is shown in *Fig. 3.10*.

With the implementation of the "srcl2darm" decoupling filter, the sensing noise from SRCL projected onto DARM is reduced. However, the other sensing and control noise projections do not change much and the sensitivity is mostly spoiled by the MICH noise projection as shown in *Fig. 3.11*. Therefore, adding a filter to decrease only the SRCL cross-coupling to DARM is not sufficient to satisfy the requirements.

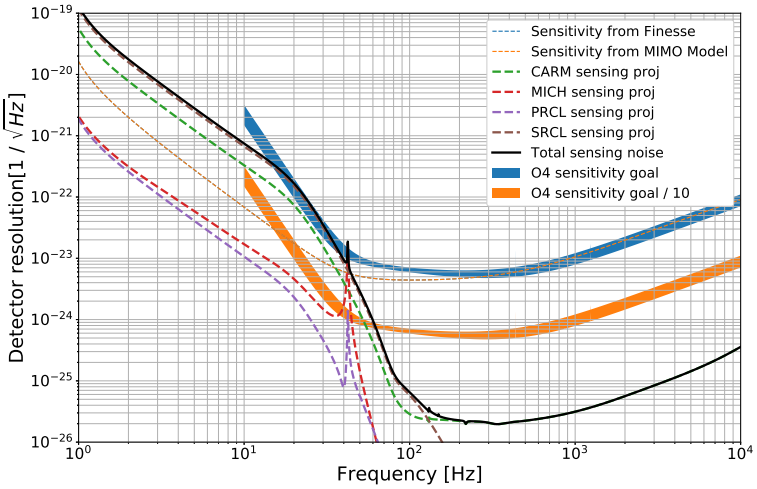

Figure 3.9: Sensing noise projections from LSC control loops compared to the designed sensitivity with the "mich2darm" decoupling filter.

3.5.5 Noise projections with decoupling filters

Adding both "mich2darm" and "srcl2darm" filters in the matrix $\mathbf{B}(j\omega_k)$ can effectively reduce MICH and SRCL cross-couplings to DARM. Therefore, the decoupling filter matrix becomes:

$$B = \begin{pmatrix} 1 & 0 & mich2darm & 0 & srcl2darm \\ 0 & 1 & 0 & 0 & 0 \\ 0 & 0 & 1 & 0 & 0 \\ 0 & 0 & 0 & 1 & 0 \\ 0 & 0 & 0 & 0 & 1 \end{pmatrix}. \tag{3.19}$$

All the elements of the matrix $\mathbf{S}(j\omega_k)$ are modified by the addition of the "mich2darm" and "srcl2darm" filters in the matrix $\mathbf{B}(j\omega_k)$. Finally, the implementation of these filters in the scheme results in a cleaner DARM signal and, therefore, a cleaner sensitivity curve, as shown in *Fig. 3.12*.

This last result might be overoptimistic: even though the terms of the optical response needed to compute the "mich2darm" and "srcl2darm" decoupling filters are available in the model over a wide range of frequencies, in practice, only a limited bandwidth of the measured plant is available. Therefore, the filters implemented in the actual detector might not be as good as the model over the entire observation frequency band. However, this could be improved

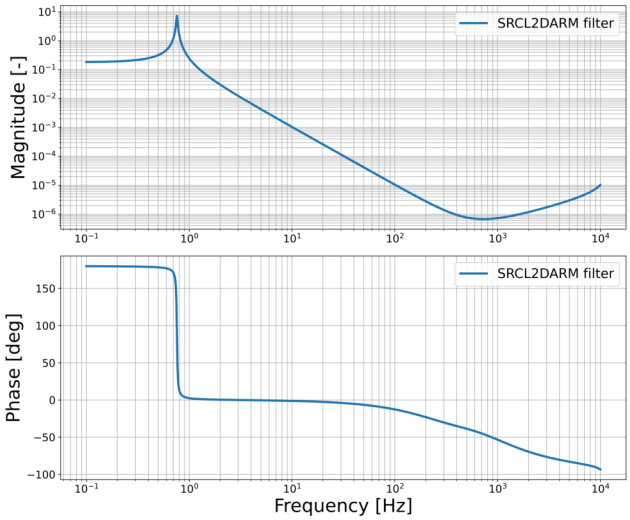

Figure 3.10: Computed decoupling "srcl2darm" filter from MIMO model.

with a swept sine system identification procedure. Although the noise present in the measurements will ultimately limit the identification of the system plus errors from fitting a FRF with a zero-pole-gain model.

3.6 Advanced Virgo Noise Budget tool

As mentioned before, ultimately, the ideal sensitivity of the GW detectors is given by the sum of fundamental noises. However, during the previous observation runs, the real sensitivity curve was spoiled by technical and not-understood noises. In particular, the low and mid frequency bands were spoiled. This result pointed out the importance of having an always updated model for the understanding of the interferometer limits, which can help to identify and characterize most of the noise sources entering the detector at different points.
In section 3.5 the projection of the intrinsic sensing noise of the PDs was presented: the sensitivity is mainly covered by the projection of the coupling of MICH into DARM and of SRCL into DARM sensing noise. Therefore, a first step is to reduce this re-injection of noise as much as possible using a noise subtraction or decoupling filters technique. Once these filters are applied, the resulting sensitivity curve is no longer limited by the longitudinal control noises. However there may be other noises hidden beneath the projection of longitudinal noises. Thus, a tool to identify and disentangle these noises is needed,

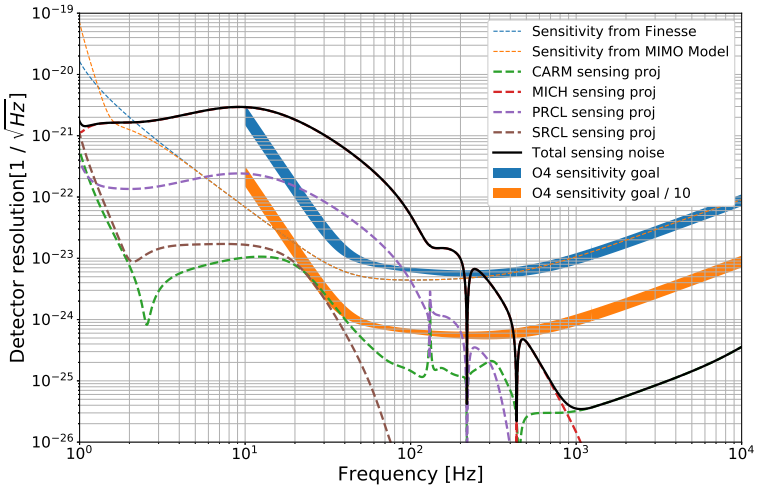

Figure 3.11: Sensing noise projections from LSC control loops compared to the designed sensitivity with the "srcl2darm" decoupling filter.

in particular in the commissioning phase, when the limiting noises are studied. Such a tool was available for Advanced Virgo for O3, but it needed a relatively long time to compute the noise projections. With a noise budget in real time or in almost real time, it would be easier to identify the sources of noise.

Using the MIMO approach in the frequency domain presented in this work, in order to estimate noise projections, only the computation of the different transfer function matrices relating the noise entering from one node to the projected noise on the DARM DoF is needed. The computation of these transfer function matrices requires no real time processing. Only time of data collection is required from the different sensors to finally compute the projection of the noises. Therefore, with this approach, a noise budget tool can compute almost in real time the sensitivity.

In order to get a more realistic model, that can be used as a noise budget tool, we need to be able to obtain the full matrix $\mathbf{G}(j\omega_k)$ over a wide frequency range. For this, several noise injections are required. Once this matrix is obtained, it is possible to estimate noise projections with a MIMO approach as discussed in sections 3.4 and 3.5.

Finally, with the aim of using this MIMO model of the interferometer as a noise budget tool, one needs to consider several other noises that can enter the control loop, either in the same six nodes previously described or in other nodes. Moreover, some noises could enter the loop in a way that would force

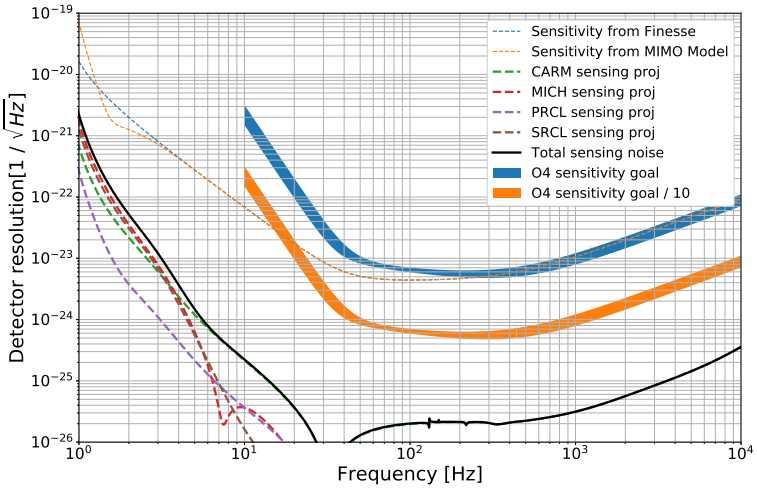

Figure 3.12: Sensing noise projections from LSC control loops onto designed sensitivity with "mich2darm" and "srcl2darm" decoupling filters.

modifications of the model to include them. Apart from that, this model has to be calibrated in order to project other types of noises into the sensitivity curve, since this was calibrated to show the projections of sensing noises so far. The target is to conclude the calibration of the model in order to include the projections of the different identified noises to have the most complete description possible of the sensitivity of Advanced Virgo.

3.7 Conclusions

During the previous data taking periods, Advanced Virgo was mainly limited by technical noises in the low and mid frequency regions of the detection band i.e. between 10 Hz and $\sim$ 100 Hz. With the aim of getting a better understanding of the interferometer, we have developed a simplified MIMO model of the Advanced Virgo detector. With this model we have produced projections of the sensing and control noises of the main longitudinal DoFs onto the gravitational-wave strain sensitivity, taking into account all the cross-coupling terms of the optical plant. Then, we have shown that the re-injection of these noises limits the detector sensitivity for Advanced Virgo in O4. Next, using the optical response we have designed noise subtraction filters in order to get a cleaner sensitivity curve. Finally we have used the MICH to DARM and SRCL to DARM decoupling filters to demonstrate that the re-injection of noise from

these channels can be reduced below the safety margin for technical noises of the sensitivity curve. Ultimately, it has also been highlighted that the core of a noise budget tool can be fabricated using this approach, since several nodes where noise or perturbation can enter the control loop have been considered. This simplified noise budget tool could compute the level of some noises of the real interferometer almost in real time, which can speed up the commissioning process and also help to identify sources of noise that could be limiting the sensitivity during the next observing run.

Chapter 4

Longitudinal cross-couplings in Advanced Virgo Plus

As shown in Chapter 3, a critical point lies within complex systems as Advanced Virgo Plus: the cross-coupling among the different longitudinal degrees of freedom. This behaviour, while inherently sophisticated, is extremely important in the interferometer's performance, impacting the level of sensitivity that can be achieved. In this chapter, we look into the cross-couplings observed among all the longitudinal DoFs mainly focusing on the DoF sensitive to the passage of gravitational waves (DARM). In Chapter 3, we worked with a simulation tool implemented for the O4 configuration of Advanced Virgo Plus, here instead we obtain the cross-coupling terms with experimental measurements. By combining real data and simulation methods, this chapter aim to understand the main offenders of the sensitivity of the detector among the longitudinal DoF couplings. However, the final goal is not only to understand these cross-couplings, but also to find ways to counter act these effects, by employing decoupling filters and, thus, improving the sensitivity of the detector. Examining the longitudinal DoFs of Advanced Virgo Plus as a MIMO system in the frequency domain provides essential insights about their complex interactions. This study sets a base to study different decoupling filters and their effects, which are not only limited to one DoF to DARM, but also among the other longitudinal DoFs. These decoupling filters are vital for the operation of the detector and to achieve an optimal sensitivity.

4.1 Cross-couplings among the longitudinal DoFs

As detailed in Chapter 3, Advanced Virgo Plus has five longitudinal DoFs, respectively named DARM, CARM, MICH, PRCL and SRCL. These DoFs are defined as combinations of the lengths of the different optical cavities in the interferometer, as explained in section 6.3. To have such an interferometer working as a GW detector, all the five DoFs have to be controlled to achieve the intended interferometric state. The procedure to reach this state is known as lock acquisition, for which new techniques have been developed for the second generation of GW interferometers [130]. The error signals that are used to control these DoFs can be optimized by fine tuning the demodulation phase used in the PDH technique. From here, optimal signals are selected for each DoF. However, once all the five DoFs are controlled, the sensitivity of the detector is spoiled by the sensing and control noises being re-injected into DARM through all the other DoFs. This is due to the fact that the error signals do not purely measure one DoF, but a combination of all the others as a result of the intrinsic cross-couplings of the opto-mechanical plant. As shown in Chapter 3, the longitudinal DoFs of Advanced Virgo Plus can be considered as a MIMO system, where all the DoFs are interconnected and influence each other through cross-coupling mechanisms. A characterization as a MIMO system is crucial for considering the complex interactions among these DoFs and to design the decoupling filters required to obtain an optimal performance. For this study, we have implemented a MIMO representation of the longitudinal DoFs of Advanced Virgo Plus in the frequency domain. A sketch for the dynamics of the system with five inputs and five outputs, interconnected with one another, is depicted in *Fig. 4.1*; y_n, u_n, e_n and r_n, respectively indicate the output, input signal, error signal and reference of each "n" DoF. Additionally for each DoF, perturbations are denoted as d_n, noise injection signals are denoted as x_n and sensing noises are denoted as n_n^1. Furthermore, the cross-coupling terms of the plant are denoted as $G_{nm}(s)$ to represent a coupling from a DoF "m" to a DoF "n". Finally, filters and decoupling filters are depicted as $C_{nn}(s)$ and $C_{nm}(s)$, respectively.

Solving analytically the expressions of a complex system with five inputs and five outputs can become unfeasible. However, using a MIMO system identification approach, we can measure all the 25 resulting Open-Loop Transfer Functions (OLTFs) of this system. Subsequently, we develop a structure in

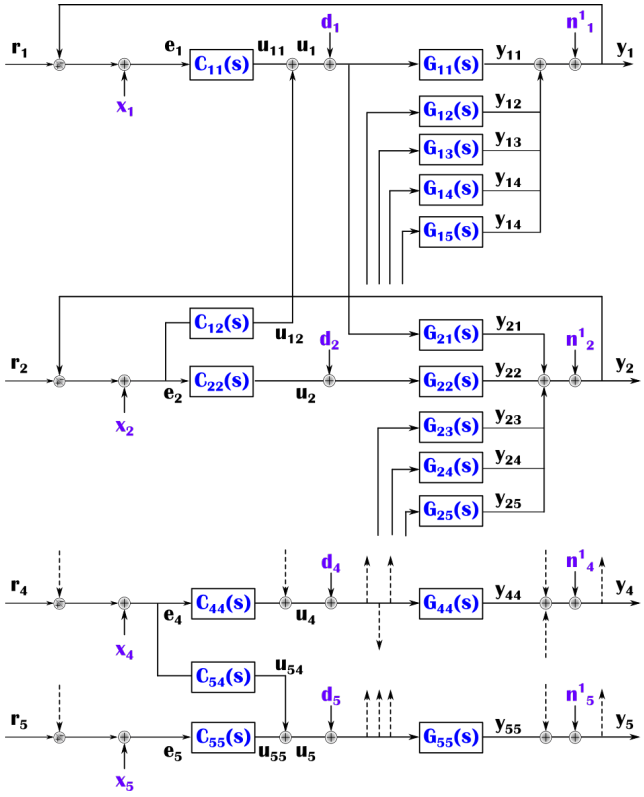

Figure 4.1: Visual representation of a 5×5 MIMO system. Some example of decoupling filters are included.

the frequency domain which describes the complete opto-mechanical system in multidimensional arrays (5×5×N), where N is the number of frequency bins.

4.2 System identification technique

The task of identifying a complex system within a closed-loop condition is notably challenging. Adding additional feedback loops often leads to biased results [131]. To address this issue, estimating the Frequency Response Function (FRF) is the starting point for this system identification method. To give a visualization of the method, we present a general opto-mechanical scheme in *Fig. 4.2*. In this scheme the block "G_0" represents the physical plant, optical cavities for the case of GW detectors; the block "A" represents the actuator dynamics of the mirrors; the block "C" depicts the control filter used to maintain a working point as well as the closed loop operation, and the block "H" represents the dynamics of the sensor readout. Additionally, the representation of the array of the discrete-time input signals of the plant is denoted as $u(nT_s)$, the error signal $e(nT_s)$ is derived with the PDH technique, the noise injection node is represented by $x(nT_s)$, $e'(nT_s)$ indicates the point after the noise injection node, the outputs are denoted as $y(nT_s)$ and the disturbances are labeled as $d(nT_s)$. Here n ranges from 0 to $N-1$, with N representing the number of samples and T_s depicts the sample time. In the frequency domain, the Discrete Fourier Transform (DFT) [132] of the array of the input signals is given by:

$$U(k) = \frac{1}{\sqrt{N}} \sum_{n=0}^{N-1} u(nT_s) e^{-j2\pi nk/N}, \tag{4.1}$$

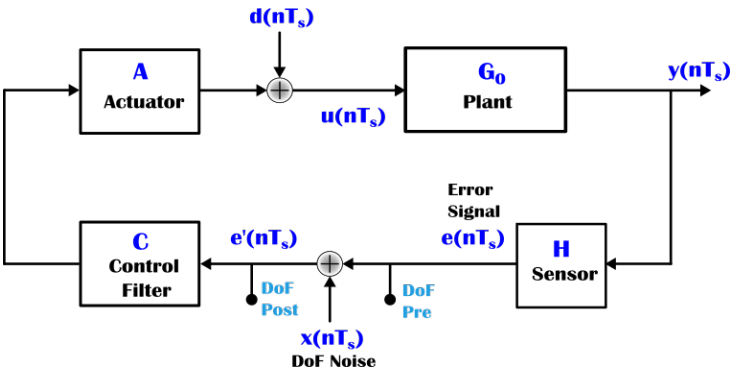

Figure 4.2: General closed-loop system, where the PDH technique has been used to obtain an error signal.

For a Linear Time Invariant (LTI) system and in the open-loop working

configuration, an empirical transfer function estimation can be derived from the observed data of the output $Y(k)$, which is the DFT of the output of the system, and the input signal $U(k)$. Thus, the plant transfer function (TF) can be estimated and expressed as $\hat{G}(\omega_k) = \frac{Y(k)}{U(k)}$, where $\omega_k = 2\pi f_k$, $f_k = k/NT_s$ is the frequency at index k in the discrete frequency domain and k is the index of the frequency bin. The impact of noise can be diminished if this computation is averaged for several segmented portions of input and output signals. While with a different approach, a TF estimation of the plant can be derived also from the estimated cross-power spectrum of its input and output signals ($\hat{\Phi}_{yu}$) along with the estimated auto-power spectrum of its input signal ($\hat{\Phi}_{uu}$) [133]. This computation also involves a segmentation into smaller sections of both signals, minimizing spectral leakage. The estimated cross-power and estimated auto-power spectra are given by:

$$\hat{\Phi}_{yu} = \frac{1}{W} \sum_{w} Y_w(k) U_w^H(k) \tag{4.2}$$

and

$$\hat{\Phi}_{uu} = \frac{1}{W} \sum_{w} U_w(k) U_w^H(k), \tag{4.3}$$

correspondingly. Where w is the window function applied to process the data, W is the total amount of window functions and $*^H$ represents the hermitian transpose of a matrix. Hence, the plant TF estimation is given by $\hat{G'}(\omega_k) = \frac{\hat{\Phi}_{yu}}{\hat{\Phi}_{uu}}$.

When these LTI systems are in a closed-loop working condition, they are set to operate in a precise working point. Then, it is possible to estimate the TFs of the system in closed-loop using a vector of noise injections "x", and taking measurements at the nodes "*pre*" and "*post*", see *Fig. 4.2*, of the error signal of each DoF [134, 135]. In this context the estimated TF of the real plant, depicted in *Fig. 4.2*, is given by:

$$\hat{G'}(\omega_k) = \frac{\hat{\Phi}_{yu}}{\hat{\Phi}_{uu}} = \frac{G_0(\omega_k)\Phi_{xx} - C(\omega_k)\Phi_{dd}}{\Phi_{xx} + |C(\omega_k)|^2 \Phi_{dd}}. \tag{4.4}$$

When the noise injections dominate among the sources of noise in the system, equation (4.4) reduces to the real plant $G_0(\omega_k)$. However, the problem arises when disturbances dominate the noises entering the loop. In this case, equation (4.4) reduces to $-\frac{1}{C(\omega_k)}$. When neither x nor d are zero, the result

of (4.4) is a mix of both contributions. In contrast with the different methods previously explained, we can apply an indirect approach [136], which consists of computing various closed-loop TFs, i.e. the sensitivity function matrix $S(\omega_k)$ and the complementary sensitivity function matrix $T(\omega_k)$. The relation between them is given by:

$$S(\omega_k) + T(\omega_k) = I, \tag{4.5}$$

where I is the identity matrix.

For this system, the estimated sensitivity function $\hat{S}'(\omega_k)$ and the estimated complementary sensitivity function $\hat{T}'(\omega_k)$ are given by:

$$\hat{S}'(\omega_k) = \frac{\hat{\Phi}_{e'x}}{\hat{\Phi}_{xx}} = \frac{1}{1 + \hat{L}'(\omega_k)} \tag{4.6}$$

and

$$-\hat{T}'(\omega_k) = \frac{\hat{\Phi}_{ex}}{\hat{\Phi}_{xx}} = -\frac{\hat{L}'(\omega_k)}{1 + \hat{L}'(\omega_k)}, \tag{4.7}$$

where $\hat{L}'(\omega_k)$ is the estimated OLTF of the system depicted in *Fig. 4.2*, and is given by the product of all the in-loop elements, i.e. $L(\omega_k) = H \cdot G_0 \cdot A \cdot C$. Ultimately, an unbiased estimation of the OLTF matrix is obtained from these measurements in closed-loop as:

$$\hat{L}'(\omega_k) = \hat{T}'(\omega_k) \cdot (\hat{S}'(\omega_k))^{-1}. \tag{4.8}$$

Lastly, since the controllers of this system are known, the dynamics of the actuators and the responses of the photo-diode sensors are well understood, then the unbiased opto-mechanical plant TF can be derived from (4.8).

Thus, following the idea presented in Chapter 3 for Advanced Virgo Plus, we develop a model of the interferometer that includes all the cross-coupling terms of the opto-mechanical plant. For this, the mirror actuators are described using the models already cross-checked for previous observing runs [61], where all the opto-mechanical components were characterized and further updated with the inclusion of the model for the Signal Recycling mirror [137]. The filters used to acquire the lock of the optical cavities are known and can be imported from the Virgo Process Monitoring (VPM) software interface, described in Chapter 2. However the opto-mechanical TFs are not previously known and have to be measured. Therefore, the data obtained using the system identification

technique described above allow us to represent the interferometer detector as a MIMO system in the frequency domain using its measured Frequency Response Functions (FRFs), with opto-mechanical TFs based on measurements. A scheme that represents the model obtained from measurements is depicted in *Fig. 4.3*. This scheme is the particular case for focusing only on sensing noise (n_1). A more general scheme describing all its elements, input and outputs, is shown in *Fig. 3.4* in Chapter 3. Note that each denoted signal is actually a vector of multiple signals.

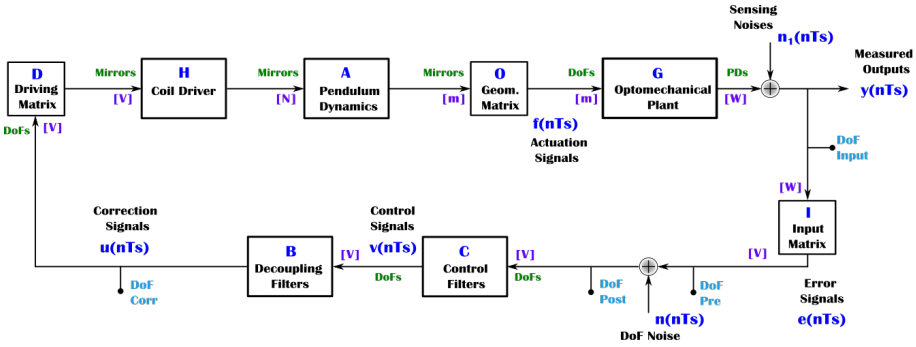

Figure 4.3: MIMO block diagram representation of the longitudinal DoFs of Advanced Virgo Plus. Each block is a multidimensional array of five rows, five columns and N frequency bins.

The 25 resulting FRFs obtained with this approach are shown in *Fig. 4.4*. The first row on this figure, shows the different effects of moving all the longitudinal DoFs and recording the output of the DARM DoF. The second, third, fourth and fifth rows show the effect of moving all the longitudinal DoFs and recording the signals for CARM, MICH, PRCL and SRCL DoFs, respectively. Not all the elements get to have a high coherence during the measurements, meaning that their cross-coupling can, in principle, be neglected.

Nevertheless, after the locking process and when the interferometer is fully controlled, the DARM error signal is almost completely covered by noise re-injected through other DoFs. Using the data obtained during the noise injections "x", we identify the sources of noise due to cross-couplings on the DARM signal. An example of this working condition, and an initial DARM noise budget, is depicted in *Fig. 4.5*. Each cross-coupling contribution to the DARM DoF error signal is depicted with a different color, these different contributions are denoted as "CARM2DARM", "MICH2DARM", "PRCL2DARM" and "SRCL2DARM". The dominant contribution limiting the DARM signal is MICH2DARM.

Since the opto-mechanical matrix $G(\omega_k)$ is not diagonal, we focus on the re-injection of the sensing noise (n_1) in the loop scheme shown in *Fig. 4.3*, which includes the experimental measurements of the various TFs. Therefore, the error signals obtained with their dedicated photo-diodes are affected by the cross-coupled dynamics that lie in the off-diagonal terms of $G(\omega_k)$. Nonetheless, it is possible to mitigate these re-injections of noise by implementing decoupling filters (in the decoupling filter matrix $B(\omega_k)$) between the correction signals coming from the locking filters (placed in the control filter matrix $C(\omega_k)$) and the driving signal (from the Driving Matrix D).

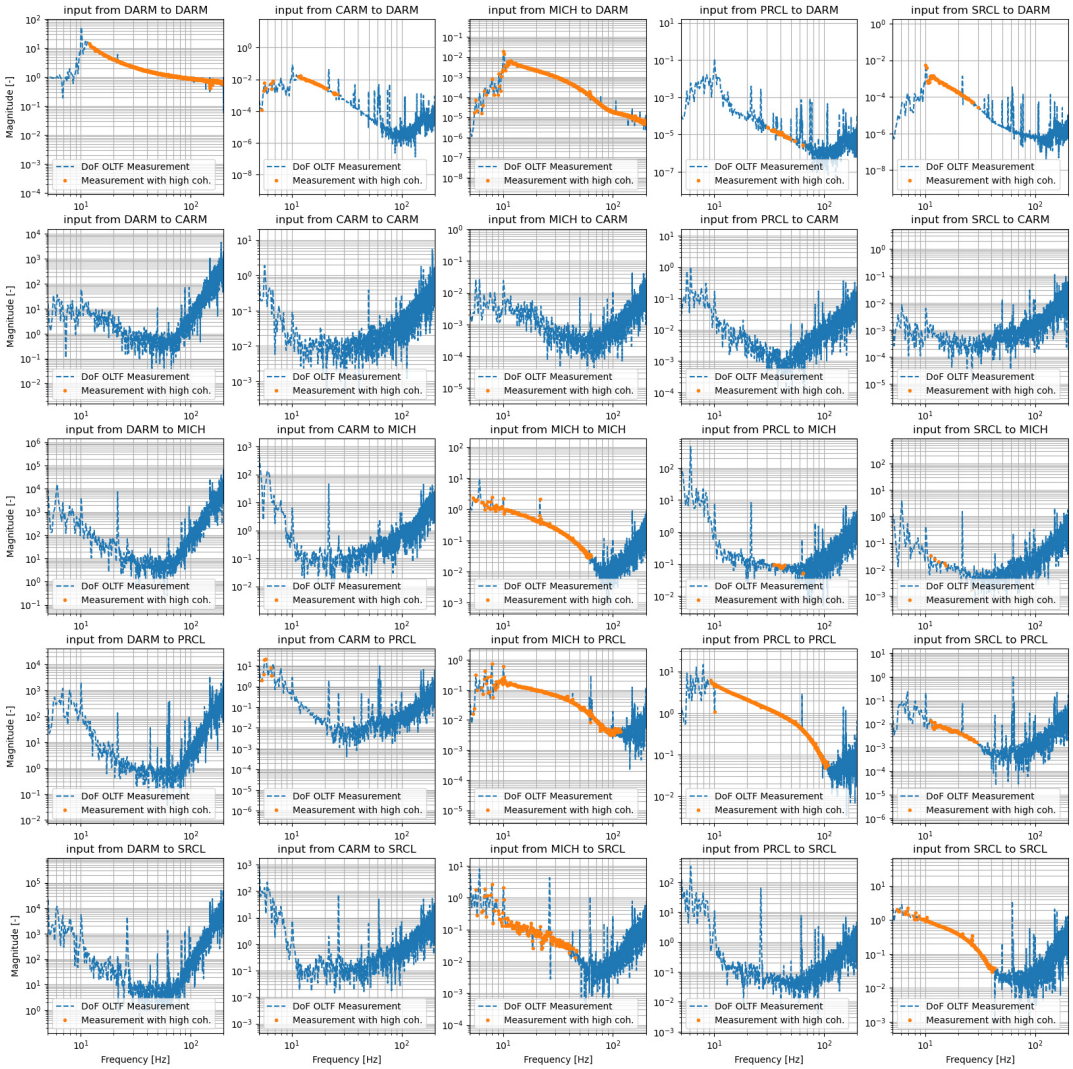

Figure 4.4: Measurement of all the 25 OLTFs resulting from the noise injections at 5 different nodes and 5 outputs. The measured TFs are depicted in blue. When the TFs exhibit high coherence, they are depicted in orange.

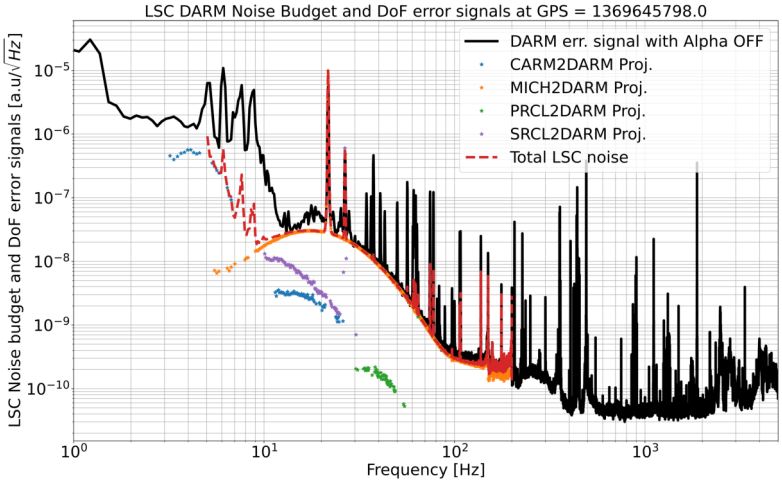

Figure 4.5: Pure DARM noise budget without the implementation of any decoupling filter.

4.3 Decoupling filters

As detailed in Chapter 3, we identified and foresaw plausible couplings that could affect the DARM signal, and therefore, spoil the sensitivity of the detector. The study concluded that the main offenders due to cross-couplings for the O4 sensitivity target are from MICH, CARM and SRCL DoFs. In Advanced Virgo Plus, the decoupling filters used to mitigate these effects are denoted by Greek letter names [138], this list describes them:

- *Alpha*: Decoupling filter for MICH to DARM coupling;
- *Beta*: Decoupling filter for PRCL to DARM coupling;
- *Gamma*: Decoupling filter for CARM to DARM coupling;
- *Delta*: Decoupling filter for SRCL to DARM coupling.

It is important to underline that neither the previous study using simulations nor measurements stated the need to implement a decoupling filter for PRCL to DARM cross-interaction. In the following sections, the three mentioned decoupling filters are described.

4.4 MICH to DARM coupling

As highlighted in *Fig. 4.5*, the main limit to the DARM noise budget is the re-injection of the MICH sensing and control noises. For this reason, a decoupling filter to mitigate the re-injection of this noise has to be implemented. As detailed in Chapter 3, the decoupling filter is designed to cancel the contribution from MICH to DARM. The filter is obtained by the ratio of the TF $G_{12}(\omega_k)$ over the TF of DARM $G_{11}(\omega_k)$. These TFs together with the empirically derived and the implemented decoupling filter are depicted in *Fig. 4.6*. The left plots represent the magnitude and the phase of the opto-mechanical DARM TF and the TF from MICH to DARM DoFs. The plot on the right side represents the ratio of these two TFs and the implemented filter in the system.

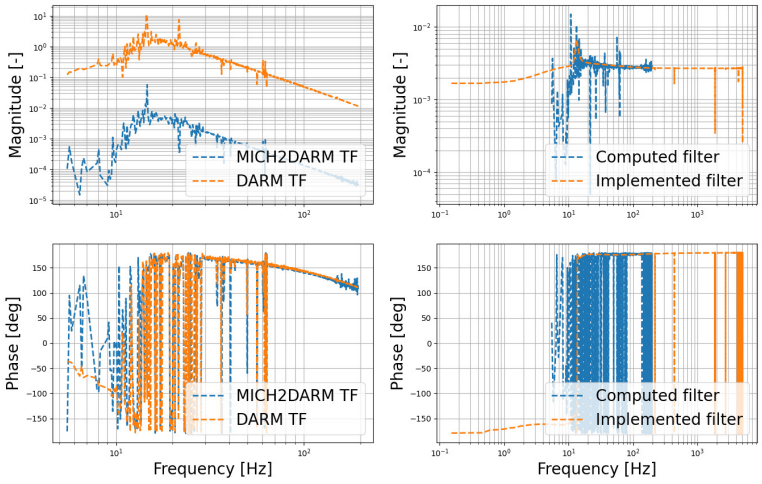

Figure 4.6: MICH coupling to DARM and DARM TFs. The ratio between these TFs is the decoupling filter implemented to mitigate MICH coupling to DARM.

Following the procedure described in Chapter 3, we implement this filter in between the correction sent to the MICH DoF and the DARM DoF. In the model, this filter is placed in the first row and third column of $B(\omega_k)$. A comparison of the 25 OLTFs before and after the implementation of a decoupling filter for MICH to DARM coupling is shown in *Fig. 4.7*. In the first row and third column, it can be seen that the coupling from the MICH to DARM DoF was reduced by a factor of 20 at $\sim 30\,\mathrm{Hz}$.

After the implementation of this Alpha filter, we check the spectrum of the error signal of DARM again to see its effect. The resulting DARM error signal is shown in *Fig. 4.8*. When *Alpha* is implemented, the DARM error signal is reduced by a factor of 13 at $\sim 30\,\mathrm{Hz}$. However, this still has room for improvement, as it will be shown in the following sections.

By implementing an initial *Alpha* filter, the contribution from MICH2DARM decreases by a factor of 20 but it is still limiting the DARM signal in the frequency range between ~ 30 and $\sim 70\,\mathrm{Hz}$. Furthermore, additional decoupling filters can be computed from the cross-coupling terms of the measured opto-mechanical matrix. In order to illustrate this, in the following sections, the effects of implementing different decoupling filters are addressed.

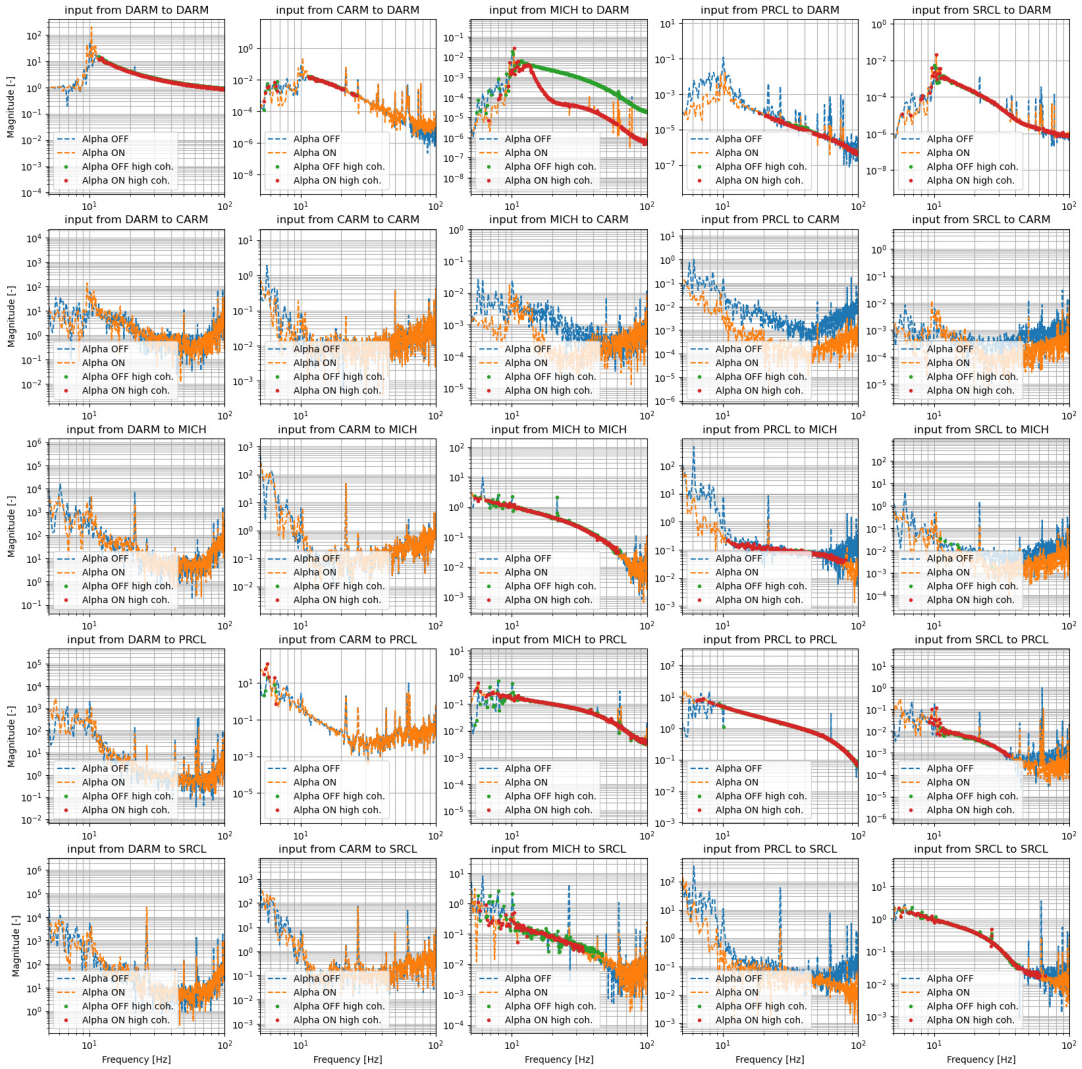

Figure 4.7: Measurement of all the 25 OLTFs resulting from the noise injections at 5 different nodes and 5 outputs. The measured TFs are depicted in blue. When the TFs exhibit high coherence, they are depicted in green and red.

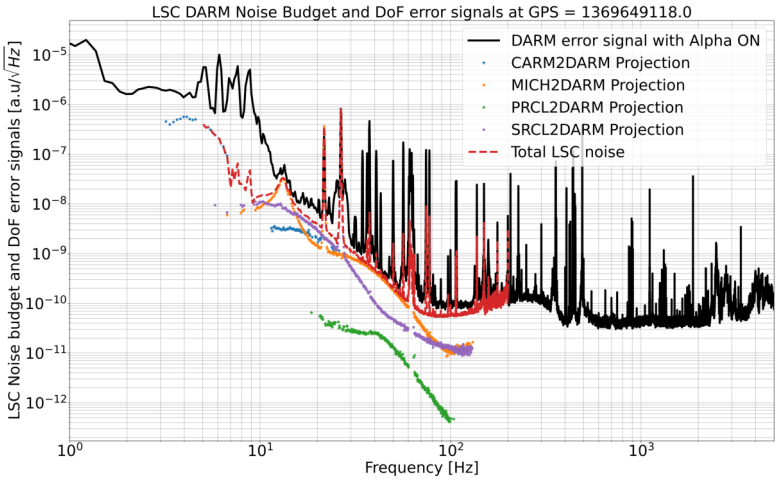

Figure 4.8: DARM noise budget with a MICH2DARM (*Alpha*) filter ON.

4.5 CARM to DARM coupling

Analogously, the coupling from the CARM DoF to the DARM error signal is obtained. Thus, a decoupling filter to mitigate this effect is implemented. Again, by employing the MIMO model approach in the frequency domain, we evaluate and anticipate the impact of a *Gamma* filter on the DoF error signal sensitive to the passage of GW. *Fig. 4.9* illustrates the scenario wherein a *Gamma* filter is introduced alongside the existing *Alpha* filter. With the implementation of a perfect *Gamma* filter, the CARM2DARM cross-coupling could be reduced up to a factor of 40 at $\sim 20\,\mathrm{Hz}$.

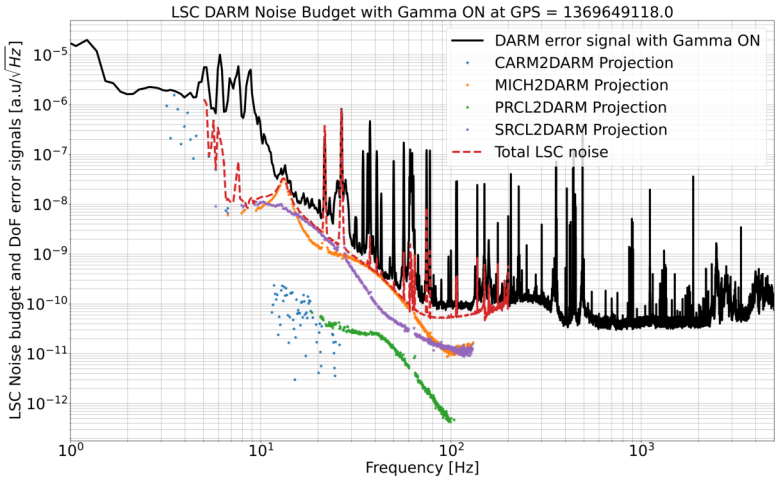

Figure 4.9: DARM noise budget with the implemented MICH2DARM (*Alpha*) and the computed CARM2DARM (*Gamma*) filters ON.

4.6 SRCL to DARM coupling

For the same set of noise injections previously used, we estimate the coupling from the SRCL DoF to the DARM error signal. Therefore, it is possible to compute a decoupling filter to mitigate this effect. Using this MIMO model approach in the frequency domain, we check and predict the effect the filter should have on the DoF error signal sensitive to the passage of GW. *Fig. 4.10* depicts the situation when a *Delta* filter is implemented together with the already implemented *Alpha* filter. It can be seen that with the implementation of a perfect *Delta* filter, the SRCL2DARM cross-coupling could be reduced up to a factor of 500 at $\sim 30\,\mathrm{Hz}$.

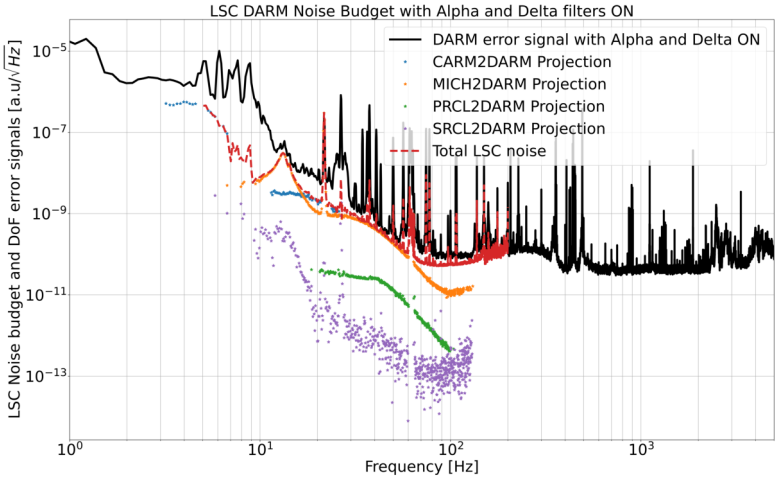

Figure 4.10: DARM noise budget with the implemented MICH2DARM (*Alpha*) and the computed SRCL2DARM (*Delta*) filters ON.

4.7 *Alpha*, *Gamma* and *Delta* implementation

Implementing all the three decoupling filters provides a cleaner DARM error signal, an example of this scenario is depicted in *Fig. 4.11*. Here the current *Alpha* filter was implemented together with computed *Gamma* and *Delta* filters. With these filters, SRCL and CARM contributions to DARM error signal could be reduced up to a factor of 500 and 40 at $\sim 30\,\mathrm{Hz}$, respectively. But now, the limiting noise contribution is again from MICH, therefore a new *Alpha* filter has to be computed, as already mentioned in section 4.4.

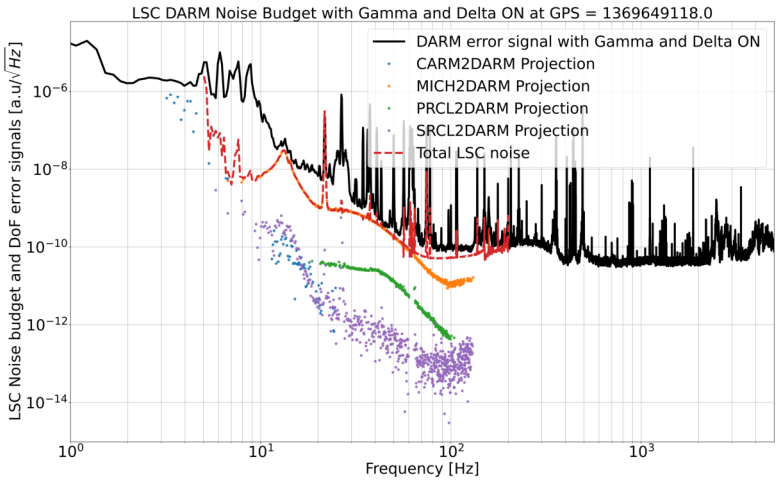

Figure 4.11: DARM noise budget with the implemented MICH2DARM (*Alpha*) and the computed CARM2DARM (*Gamma*) and SRCL2DARM (*Delta*) filters ON.

Then, with an updated *Alpha* filter implemented together with the *Gamma* and *Delta* filters previously showed, the re-injection of noise can be minimized, achieving a level of noise 10 times lower than the current DARM error signal noise level, as shown in *Fig. 4.12*. Moreover, it can be seen that the DARM error signal gets cleaned up. The total noise contribution from all the other DoFs is reduced by a factor of 25 at $\sim 30\,\mathrm{Hz}$.

Finally, *Fig. 4.13* serves as a comparison between the starting point of the DARM error signal without any decoupling filters and with the exploration of different decoupling filters. It can be seen that the level of noise in DARM was reduced by a factor of ~ 10 between 20 Hz and $\sim 100\,\mathrm{Hz}$. In this scenario

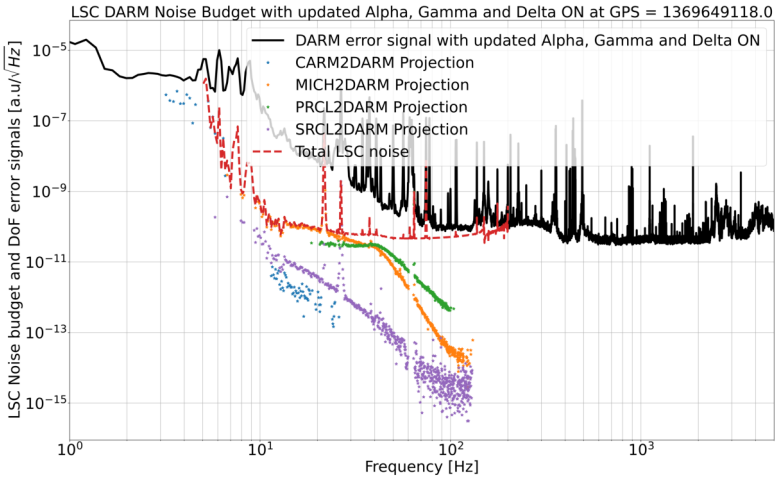

Figure 4.12: DARM noise budget with the updated MICH2DARM (*Alpha*) and the computed CARM2DARM (*Gamma*) and SRCL2DARM (*Delta*) filters ON.

the DARM signal is affected by other technical noises and a process of noise hunting started in preparation for O4. Using the information obtained in this process it is possible to generate a noise budget of the signal sensitive to GWs and explain its limitations.

Finally, *Fig. 4.13* serves as a comparison between the initial DARM error signal without any decoupling filters and the signal with various decoupling filters applied. It can be seen that the noise level in DARM was reduced by a factor of approximately 10 between 20, Hz and around 100, Hz. In this scenario, the DARM signal is affected by other technical noises, prompting the initiation of a noise hunting process in preparation for O4. Using the information obtained from this noise hunting process, it is possible to generate a noise budget for the signal sensitive to GWs and explain its limitations.

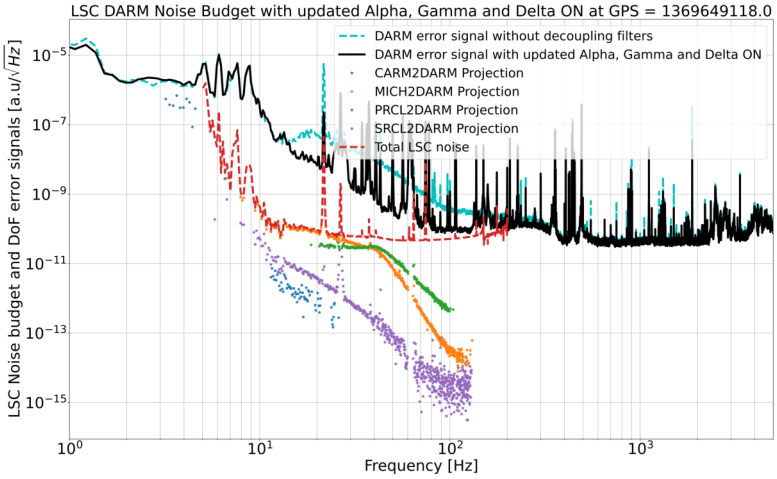

Figure 4.13: Comparison of DARM error signal with and without decoupling filters.

Chapter 5

Frequency domain noise budget tool for Advanced Virgo Plus

Even the most minuscule disturbances can mask the signals that GW detectors seek to observe. To identify these signals from a vast array of noise, LIGO, Virgo and KAGRA employ comprehensive noise budgets [139]. A noise budget is an essential tool that outlines and quantifies all known noise sources within a system, providing a road-map for noise mitigation and enabling the isolation of true GW signals from noise. A noise budget is typically represented as a graph plotting the ASD of the different noises (in strain sensitivity) over frequency. Each major noise is graphically represented, helping to identify and understand the predominant noise sources at different frequencies. This meticulous process of noise budgeting is critical to enhance the sensitivity of the detectors and to ensure the validity of the detected signals.

GW detectors are capable to detect variations in distance as small as 10^{-18} m over a frequency range from about 10 Hz to a few kHz. However, numerous sources of noise can interfere with the detection of GWs. As detailed in Chapter 2, the primary categories of noise, referred to as fundamental noise sources in these detectors, include quantum noise, thermal noise, seismic noise, and Newtonian noise. The interplay of these noise sources determines the overall design sensitivity of GW detectors. Each type of noise has a characteristic frequency dependence. Therefore, a starting point is to generate an initial noise budget that defines the maximum achievable sensitivity of the detector, given its infrastructure, materials, and primary parameters.

One pivotal tool used by LIGO, Virgo and KAGRA collaborations for generating and managing their design sensitivity and, thus, their initial noise bud-

gets is the Gravitational-Wave Interferometer Noise Calculator (GWINC) [140]. This open-source software helps predict and analyze noise sources in GW interferometers. Through the input of various parameters, GWINC calculates the expected level of (fundamental) noises across frequencies. For the Advanced Virgo Plus configuration for O4 and its corresponding parameters, the noise budget of fundamental noise or *designed sensitivity* computed with GWINC is shown in *Fig. 5.1*, which was shown also in Chapter 2.

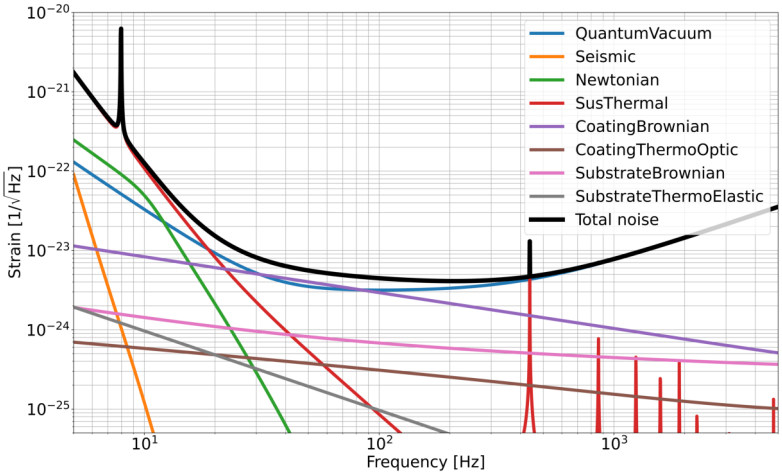

Figure 5.1: Design sensitivity and fundamental noises for O4 Advanced Virgo Plus configuration.

GWINC is not limited to study current detectors; it is also applicable in the preliminary design stages of future detectors, offering insights into how changes in design parameters can affect sensitivity. While GWINC is powerful, during the operation of GW detectors, scientists and engineers also need to identify dynamic factors that could degrade sensitivity. Therefore, a tool for the real-time assessment of detector limitations becomes essential. This tool would enable the monitoring of fluctuating noise sources, such as seismic fluctuations and temperature fluctuations related to different weather conditions or human activities, ensuring optimal detector performance.

Robust frameworks for analyzing noise in GW detectors have been developed using MATLAB and Simulink [141]. These tools import signals in the time domain and process them with internal modeled dynamics of the interferometer, that are included in block diagrams using Simulink. While very

accurate, these software programs require considerable time and computing power, making the processing rather slow. An example of the plots produced using these tools is shown in *Fig. 5.2*. Despite their strengths, these tools often come with limitations, such as a steep learning curve and difficulties in sharing work within large collaborations. Typically, only a handful of experts have a deep understanding of these tools, posing challenges in their maintenance and restricting cooperative efforts. Consequently, shifting from specialized, proprietary platforms to ones more open and encouraging to collaboration is essential. Moreover, tools delivering a dynamic noise budget that can compute and tell which noise limits the sensitivity at any moment are crucial.

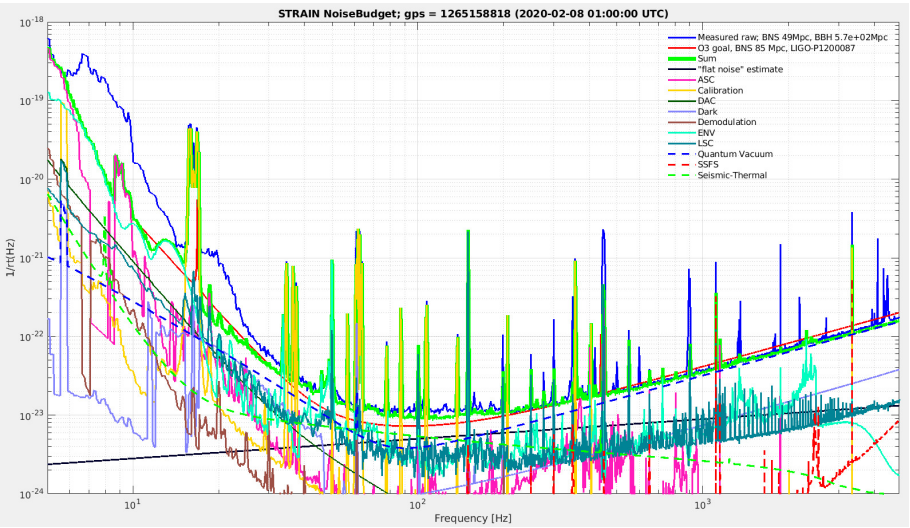

Figure 5.2: Noise budget of Advanced Virgo produced using a MATLAB Simulink tool.

Several types of noise can degrade the sensitivity of a GW detector. As described in previous chapters, for the Advanced Virgo Plus detector, one of the primary offenders is the re-injection of sensing noise into the control loop of its longitudinal DoFs. To study and mitigate this effect, a MIMO model was developed. This model includes the sensing noises from each longitudinal DoF as sources of technical noise. These noises are introduced at a specific node within the MIMO model. This chapter is dedicated to the development of a noise budget tool for Advanced Virgo Plus, derived from the framework established in previous chapters and expanded to include several noises. The core of this model is a *snapshot* of the real interferometer when it is fully controlled.

This means that the noise budget tool is based on intrinsic measurements. Furthermore, this tool can also work with a simulated model of the interferometer, as outlined in Chapter 3.

The tool uses Python and addresses two main objectives: increasing speed, as all data are already imported in the frequency domain and formatted as previously computed multidimensional matrices; and enhancing user-friendliness by facilitating contributions in an open-source environment and allowing for parallel collaboration.

5.1 From the astrophysical event to the reconstructed strain to study the detector

5.1.1 Reconstructed strain (H_{REC})

As mentioned in Chapter 1, a GW produces a strain $h(t)$ in space-time which, on Earth, can be detected thanks to the GW detectors described in Chapter 2. For a passing GW, the detector produces an effect on the DARM DoF $e_{DARM}(t)$ through the detector's response R. Ultimately, $e_{DARM}(t)$ is processed to get a reconstructed strain $h_{REC}(t)$ through a calibration process (R^{-1}). *Fig. 5.3* shows a sketch of detecting a GW signal and producing a reconstructed strain. The signal used for parameter estimation of GW sources is $h_{REC}(t)$. Therefore, calibration of the detector will always be a fundamental constraint on the precision of astrophysical parameter estimation.

The complexity of both calibrating the detector and creating a noise budget for the measured strain lies in the fact that this signal is contained within the DARM DoF, meaning that it is part of a closed-loop control system that continuously adjusts the interferometer working point. To obtain the reconstructed strain $h_{REC}(t)$ signal from this closed-loop system, a specific process must be followed using calibration data [142]. This process generates an error signal that impose deviations of the current state from the desired state of the interferometer arms. This error signal captures the influence of passing GW along with other disturbances. However, for the purpose of developing a noise budget in the frequency domain, the reconstructed strain $H_{REC}(f)$ would be sufficient. An accurate estimated reconstructed strain $\hat{H}_{REC}(f)$ can be obtained by *unfolding* the error signal of DARM. In this context, *unfold* means to extract the measured strain from the closed-loop of the DARM DoF.

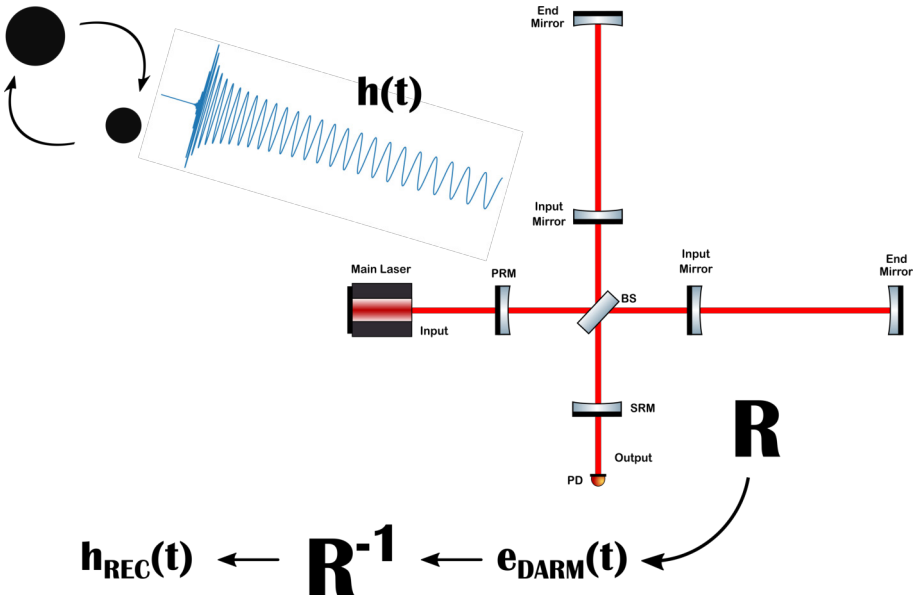

Figure 5.3: Diagram of a GW detection, from the astrophysical signal to the reconstructed strain for parameter estimation and data analysis.

5.1.2 Unfolding DARM error signal

As it has been mentioned before, the DoF sensitive to GW is DARM. By unfolding the DARM DoF from its closed-loop state one obtains an estimate of $H_{REC}(f)$. This is done by transferring the closed-loop error signal of DARM in $\mathrm{V}/\sqrt{\mathrm{Hz}}$ back to the DARM DoF motion in $\mathrm{m}/\sqrt{\mathrm{Hz}}$ and, then, dividing this quantity by the length of the arms.

Mathematically, the estimated $\hat{H}_{REC}(f)$ can be obtained from the DARM error signal in the following way:

$$\hat{H}_{REC}(f) = \frac{e_{DARM}(f)}{3\,\mathrm{km}} \cdot \frac{(1 + L_{DARM}(f))}{I_{DARM}(f) \cdot G_{DARM}(f)}, \tag{5.1}$$

where $e_{DARM}(f)$ is the DARM error signal, $L_{DARM}(f)$ is the closed-loop TF of the DARM DoF, $I_{DARM}(f)$ corresponds to the DARM error signal conversion factor in V/W, and $G_{DARM}(f)$ is the optical response of DARM in W/m. An illustrative diagram to help the visualization of this process is shown in *Fig. 5.4* [1]. This figure represents the block diagram of the closed-loop MIMO model of the longitudinal DoFs of Advanced Virgo Plus. Point A is the

[1] Description of each of these blocks can be found in Chapter 3.

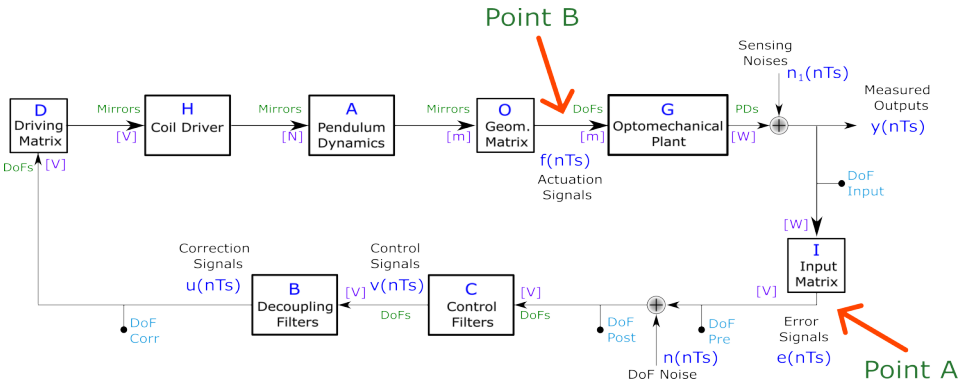

Figure 5.4: Visual representation of how to convert DARM error signal in closed-loop onto $\hat{H}_{REC}$ in the frequency domain.

closed-loop error signal of DARM in $\mathrm{V}/\sqrt{\mathrm{Hz}}$ and point B corresponds to the DARM DoF motion in $\mathrm{m}/\sqrt{\mathrm{Hz}}$. A comparison between the estimated strain $\hat{H}_{REC}(f)$ and the measured $H_{REC}(f)$ obtained with the full calibration and reconstruction process is shown in *Fig. 5.5*.

It can be seen that this method provides a useful estimate of $H_{REC}(f)$ for the purpose of producing the noise projections, that are used to construct a noise budget.

5.2 Nodes for noise projections

Different types of noise can couple to the primary output, i.e. DARM DoF, of the interferometer throughout various mechanisms. These noises can be included in the model illustrated in Chapters 3 and 4 by adding nodes at different points of the closed loop diagram, shown in *Fig. 5.4*. In the previous chapters, only two nodes where considered in the MIMO model: a node n used for injecting noise for system identification, located at the error signal point of the closed loop and used to measure OLTFs; and a node n_1 that summarizes the sensing noises entering all the DoF readouts. However, as unveiled in Chapter 2, we know that these are not the only types of noise that can spoil the sensitivity of the detector. Therefore, we have upgraded the closed-loop MIMO model to take into account more types of noise by expanding the number of nodes. An updated scheme, that includes several nodes, is shown in *Fig. 5.6*.

Note that the model includes the possibility for future changes and upgrades, thus more nodes can be added if necessary. Regardless, the current

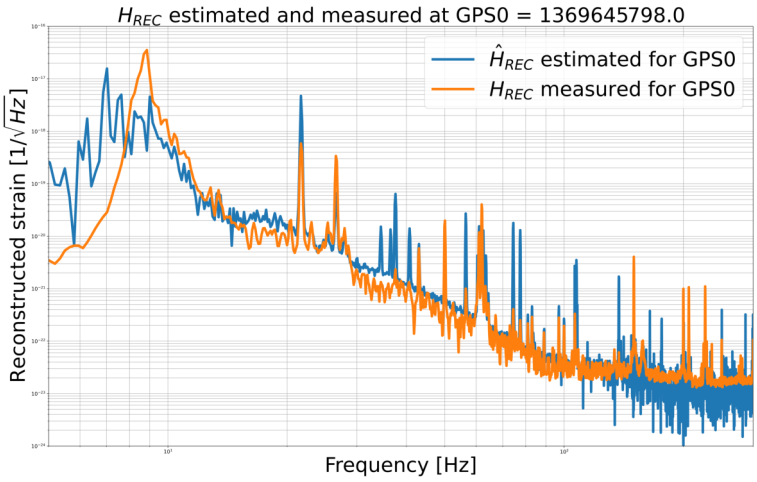

Figure 5.5: Comparison of the estimated reconstructed strain $\hat{H}_{REC}$ and the measured reconstructed strain H_{REC}.

model accounts for six nodes, which can be used to add the following types of noise:

- Sensing noises (n_1): Noise at the level of the photo-diode, such as dark noise, shot noise, demodulation phase noise, scattered light noise.
- Perturbations on DoFs (n_2): Noise at the level of the DoFs, such as Newtonian noise, Photon Calibration injections, Newtonian Calibration injections, magnetic noise, acoustic noise, seismic noise, radiation pressure noise, angular control noise, frequency noise.
- Perturbations on Mirrors (n_3): Magnetic noise, acoustic noise, unbalanced actuators, seismic noise, thermal noise, radiation pressure noise, angular control noise, frequency noise.
- Actuation noise (n_4): Magnetic noise, amplifier noise.
- DAC Noise (n_5): Operational amplifier noise, electronics noise.
- ADC Noise (n_6): Electronic thermal noise, quantization noise.

Note that this is not an exhaustive list and more noises can be included in the existent nodes. Note that in the list some noises are repeated, because

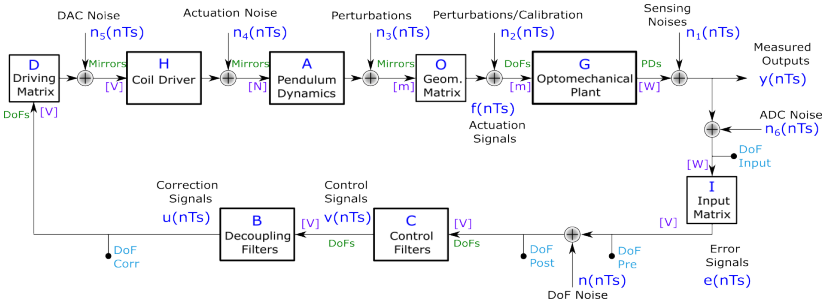

Figure 5.6: Updated closed loop scheme, which includes more nodes in between matrix elements of the model.

certain types of noise could affect the optics of the interferometer either locally or broadly, or both. Also note that the angular corrections, which are pivotal for the control of the interferometer, are considered as residual motion on the longitudinal axis of the mirrors.
This model is the core of this noise budget tool, meaning that it can be further modified to include different mechanisms or ways that different noises could enter the interferometer.

5.3 Recipe for noise projections

The model described before is used to study the effects of different types of noise entering the detector at different nodes (or points). Here we present a recipe to study the effect on the DARM DoF or on $\hat{H}_{REC}(f)$ of a noise entering the interferometer through one of these nodes. To study the effect of a certain noise in the interferometer, one first has to select (or install) a sensor that can measure such type of noise locally in its corresponding units. Then, one has to identify and select one of the nodes where this noise could enter the detector. If the units do not match with the ones shown in *Fig. 5.6*, then one has to include a coupling factor or a coupling matrix in the case of a vector of different noises. This coupling can be computed by a series of noise injections throughout the detector, using $H_{REC}(f)$ and a local sensor as monitors. Then, using the corresponding pre-computed closed-loop TF matrices, i.e. $S(\omega_k)$ and $T(\omega_k)$ described in Chapter 4, it is possible to project this type of noise or noises on the sensitivity curve.

An active campaign is ongoing to characterize different type of couplings from environmental noises to $H_{REC}(f)$. The plan of this campaign is detailed

in the report of environmental noises in Advanced Virgo Plus [143, 144]. As detailed in these reports, the first step to characterize a certain type of noise and its coupling to $H_{REC}(f)$ is to compute a coupling coefficient CF by injecting noise near the main optics and measure the effect of this noise on $H_{REC}(f)$. The $CF(f)$ is given by:

$$CF(f) = \sqrt{\frac{[Y_{inj}(f)]^2 - [Y_{bkg}(f)]^2}{[X_{inj}(f)]^2 - [X_{bkg}(f)]^2}}, \tag{5.2}$$

where Y_{inj} and X_{inj} are the ASDs of H_{REC} and the witness sensor, respectively, during the noise injection period; Y_{bkg} and X_{bkg} are the ASDs of H_{REC} and the witness sensor, respectively, during a quiet period.

This tool also provides the option to study the coupling from different noises not only to DARM, but also to the other four longitudinal DoFs, i.e. CARM, MICH, PRCL and SRCL.

5.3.1 Example of noise projection recipe

As an example, we consider the case of the magnetic noise coupling at the level of the mirrors, which enters in the loop through the node between blocks A and O in the scheme in *Fig. 5.6*, i.e. perturbations on mirrors n_3. A coupling TF has to be computed with dedicated magnetic noise injections at different points of the interferometer, typically near the main optics. Then, by using $H_{REC}(f)$ as an observer, a TF is computed between a local sensor for magnetic noise and $H_{REC}(f)$ [143]. Finally, using the pre-computed matrix T_3, which is the closed loop TF matrix that relates n_3 noises to the error signal of the different DoFs and is given by:

$$T_3(j\omega_k) = S(j\omega_k) \cdot I(j\omega_k) \cdot G(j\omega_k) \cdot O(j\omega_k), \tag{5.3}$$

then, the projection on the different longitudinal DoFs can be studied with the following expression:

$$\tilde{N}_3^{in-loop}(f_k) = |T_3(f_k)| \begin{pmatrix} \tilde{N}_3^{NE}(f_k) \\ \tilde{N}_3^{WE}(f_k) \\ \tilde{N}_3^{BS}(f_k) \\ \tilde{N}_3^{PR}(f_k) \\ \tilde{N}_3^{SR}(f_k) \end{pmatrix}. \tag{5.4}$$

Note that the effect of magnetic noises on the different main optics can be studied for all the longitudinal DoFs with $\tilde{N}_3^{in-loop}(f_k)$. For example, the first row of $\tilde{N}_3^{in-loop}(f_k)$ corresponds to the effect of these noises on DARM and the third row of $\tilde{N}_3^{in-loop}(f_k)$ corresponds to the effect of these noises on MICH. Therefore, this approach can serve to study coupling of different type of noises to each main longitudinal DoF of the interferometer.

In the following sections, different types of technical noises are explored and coupling factors are computed to integrate them in the noise budget core.

5.4 Noise projections results

In this section, we present the current preliminary results obtained with the developed Python-based noise budget tool. As the tool is still in active development, the results discussed here correspond only to a small subset of the noise sources that have been integrated thus far. These findings offer an initial insight into the potential capabilities and performance of the tool. They also serve as groundwork for future improvements and future integration of more noise sources. The computed closed-loop TFs are derived from the measured opto-mechanical TF matrix $G(j\omega_k)$. This matrix was derived from data obtained in June 2023, when several noise injections were performed to study the working point of the interferometer. Once all the pieces are put together and all the needed matrices are computed, one can test the tool. For this, we used several noise injections, which were performed in an equivalent state of the interferometer and we compared the projected noise using this method with the measured output of the interferometer. In the next subsections, we present two examples, together with the integration of shot noise, which help also as a demonstration of how this tool can be used.

5.4.1 Magnetic noise injections

Several noise injections at various locations within the buildings of the Virgo site where the interferometer is held were performed during the last two years. These injections were performed by the Environmental Noise team of Advanced Virgo Plus. Using these instances, we have tested the capabilities of this tool. At first we describe the noise injections performed [143, 145]: small coils were placed at different times near the base of the different vacuum towers where the mains optics are suspended, for example near the input optics and output

optics towers, NI and WI towers, BS tower and, finally, WE and NE towers. For both NE and WE towers, the coupling functions are simpler to obtain, since there are no other nearby main interferometer optics either in West-end or North-end buildings. Thus, no extra magnetic coupling contributions have to be taken into account.

Fig. 5.7 illustrates the location of the coil placed near one of the towers for this campaign of noise injections. Noise injections occurred around the WE tower in July 2023 and around the NE tower in September 2023. These were "shaped" noise (signal whose PSD varies with frequency, unlike white noise which has equal power across all frequencies) injections with a frequency range from 8 to 330 Hz and a duration of 600 s. Furthermore, the coil used for the injections was placed in three different orientations: along the E-W axis, along the N-S axis, and in the vertical direction. The magnetic noise generated by these coils is expected to couple with the magnets installed on the main optics of Advanced Virgo Plus.

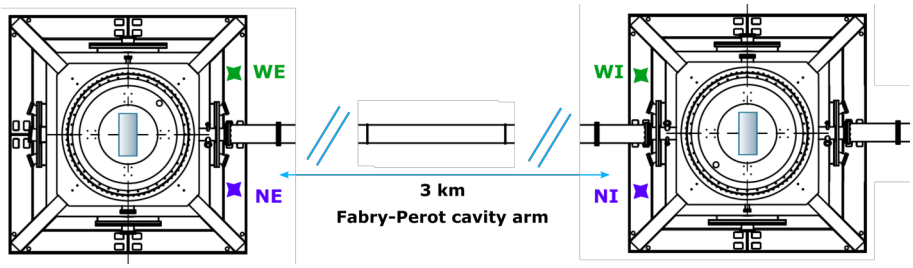

Figure 5.7: Location of the coils used for magnetic injections near the towers along one Fabry-Perot arm. The sketch shows the external magnetic coil locations for the NE and WE towers, as well as for the WI and NI towers, with the main mirror at the center.

Using the coupling functions computed for WE and NE during their corresponding noise injections and adding them to the node n_3 in the model shown in *Fig. 5.6*, we have computed their noise projections on the DARM DoF. The results obtained following the recipe mentioned in section 5.3 for these noise injections and projections on the DARM DoF are presented in *Fig. 5.8* and in *Fig. 5.9*: both figures show the effect of a magnetic injection in one of the end buildings of Advanced Virgo Plus. In both of them, the projections of magnetic noise on all the main mirrors is shown. We can note that in *Fig. 5.8* the level of $e_{DARM}(f)$ is explained by the noise projection of the WE magnetic noise, while in *Fig. 5.9* the level of $e_{DARM}(f)$ is explained by the noise projection of

the NE magnetic noise. In both cases, the DARM error signal is superposed with the noise projections of these magnetic injections, meaning that there is a strong coupling of magnetic noise.

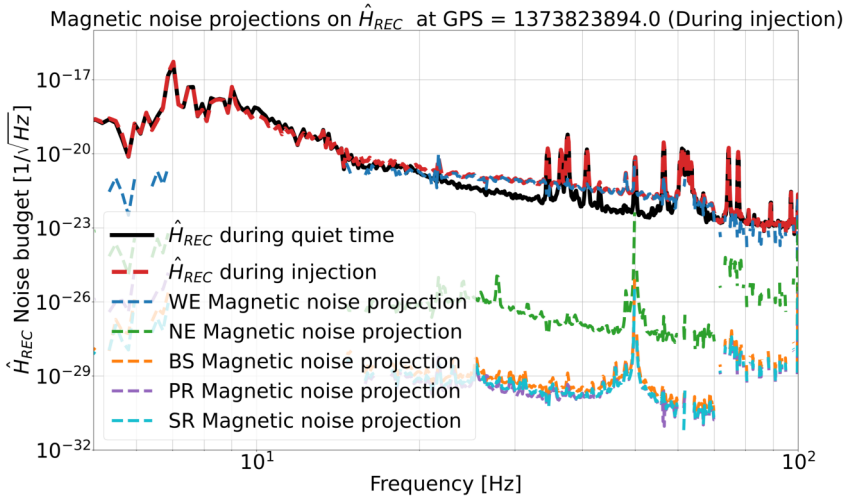

Figure 5.8: Noise projections of the WE magnetic noise injections onto $\hat{H}_{REC}$.

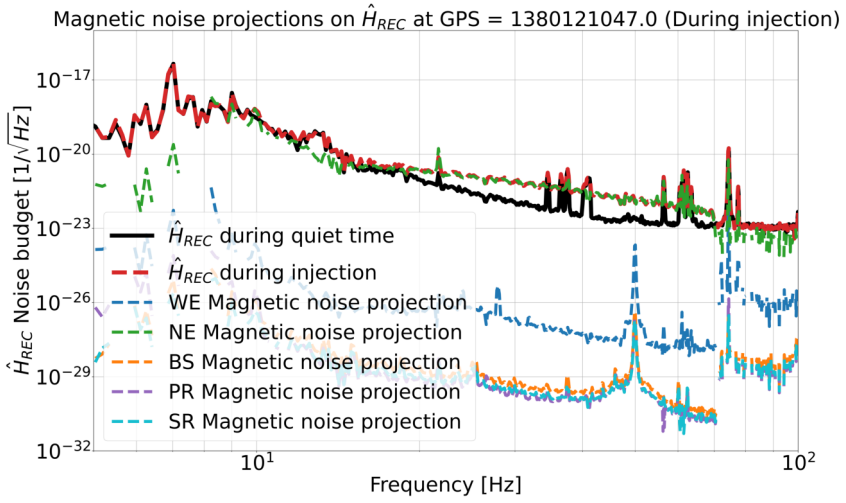

Figure 5.9: Noise projections of the NE magnetic noise injections onto $\hat{H}_{REC}$.

5.4.2 Calibration noise injections

One of the methods for the calibration of the Advanced Virgo Plus detector is performed using a photon calibrator [146]: this actuator exerts a controlled force on the end test masses of the interferometer using laser radiation. By directing a known amount of photon momentum on the mirrors, the calibration procedure replicates the physical effect of a passing GW, allowing a precise characterization of the response of the detector. Significant aspects of this calibration process are the establishment of the correct sign of the response of the detector and the cross-checks of systematic uncertainties. During the calibration campaign for O4, several measurements were performed with the interferometer fully controlled to contrast the mirror motion along its longitudinal axis z with and without the noise injection of the photon calibrator. For the WE and NE mirrors the injections in their longitudinal axes occurred in September 2023. Since in this case of noise injections the optics are perturbed directly, the closed loop matrix that relates the noises in n_4 to the error signals of the different DoFs T_4 is given by:

$$T_4(j\omega_k) = S(j\omega_k) \cdot I(j\omega_k) \cdot G(j\omega_k) \cdot O(j\omega_k) \cdot A(j\omega_k). \tag{5.5}$$

Using equation (5.5) and following the recipe detailed in section 5.3 one can compute the noise projections onto the error signal of the DARM DoF. The obtained results are shown in *Fig. 5.10* and *Fig. 5.11*: both figures show the effect of a photon calibrator injection on one of the end mirrors of Advanced Virgo Plus. In both of them, the projections of the photon calibrator noise on all the main mirrors is shown. We can note that in *Fig. 5.10* the level of $e_{DARM}(f)$ is explained by the noise projection of the WE photon calibrator noise, while in *Fig. 5.11* the level of $e_{DARM}(f)$ is explained by the noise projection of the NE photon calibrator noise.[2]

Note that there are also several "lines" or spikes at different frequencies that are always being injected in the optics and they serve for continuous calibration and monitoring.

[2]Due to the noisy measurements of the optical plant at higher frequencies, the noise projections are shown in the frequency band from 5 Hz to 100 Hz.

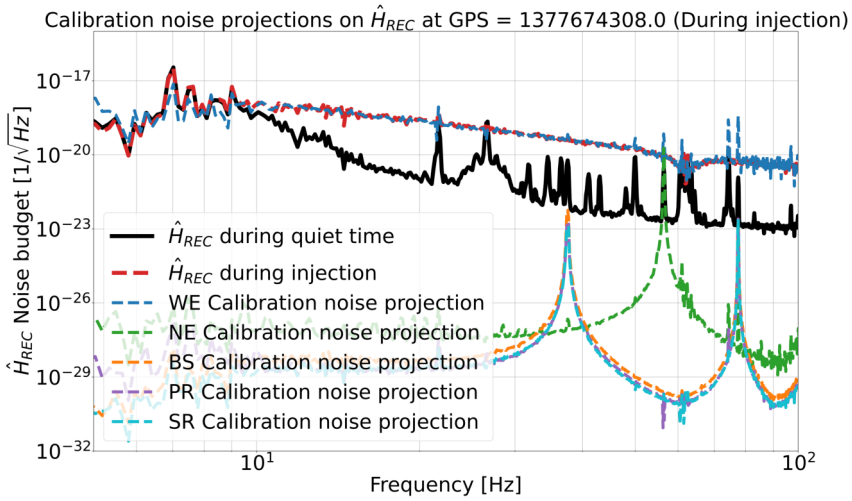

Figure 5.10: Noise projections of the WE photon calibrator noise injections onto $\hat{H}_{REC}$.

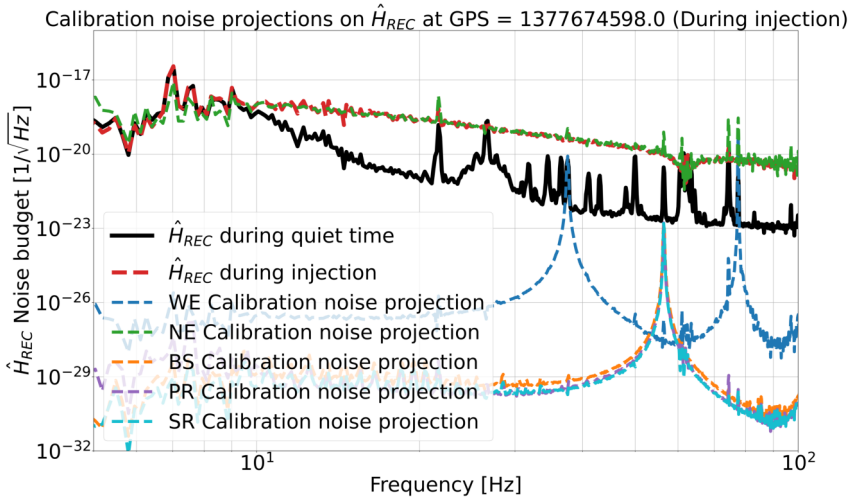

Figure 5.11: Noise projections of the NE photon calibrator noise injections onto $\hat{H}_{REC}$.

5.5 Integration of noises and future work

In the development of the noise budget tool, progress has been made to enhance its number of nodes and capabilities for noise analysis. The tool now integrates magnetic noise, calibration lines, longitudinal DoF sensing noise (including shot noise, electronic noise, and read-out noise) and longitudinal DoF UGFs monitoring lines. These additions make the noise budget tool a valid but still very preliminary resource for identifying and quantifying various noise contributions on the sensitivity curve of the detector. An example of the output of the current results of this noise budget tool is shown in *Fig. 5.12*: measured H_{REC} and estimated strain $\hat{H}_{REC}$ with the noises integrated in the tool so far are presented. The level of H_{REC} is mainly covered by the re-injection of the noise from the MICH DoF. Several peaks at different frequencies in H_{REC} can be explained by the projections of the noise from UGF monitoring lines of the longitudinal DoFs and calibration lines of WE and NE. Note that the results cover up to about 200 Hz, because the *snapshot* of the physical TF of the interferometer has high coherence in the measured OLTFs in this region.

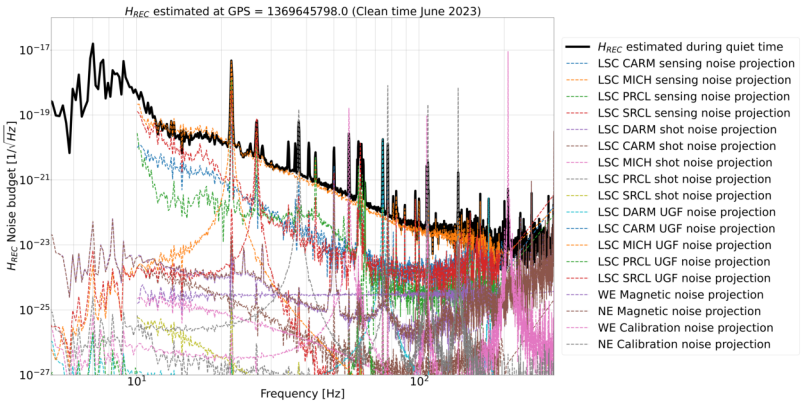

Figure 5.12: Estimated $\hat{H}_{REC}$ with the current set of noises integrated in the noise budget tool.

Fig.5.13 shows the sums of the different types of noise integrated so far in this tool, i.e. the total sensing noise, total shot noise, total magnetic noise, total calibration noise, and total UGF monitoring noise. Several of the spikes in frequency are intentionally injected signals used for calibrating different optics and monitoring the detector's status. These lines are effectively projected onto the sensitivity plot using this noise budget tool; however, many still need to

be integrated. Note that these known lines are removed in the data processing pipelines for data analysis.

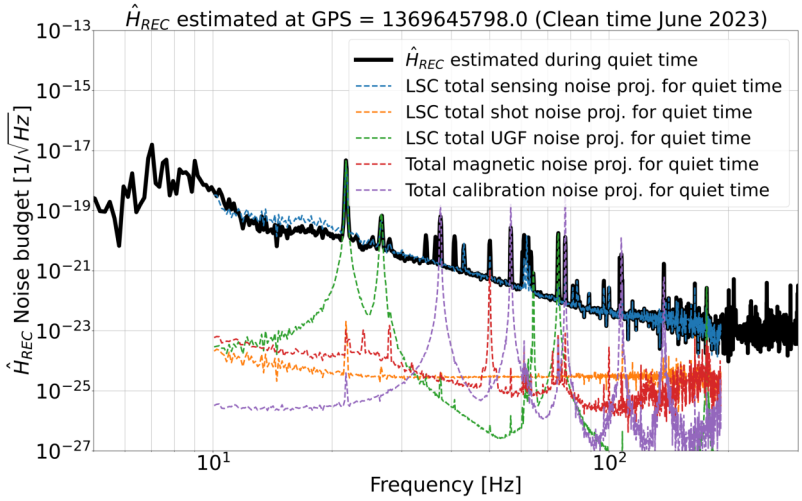

Figure 5.13: Estimated $\hat{H}_{REC}$ with the sum of the current types of noise integrated in the noise budget tool.

In the next months, several other noises will be included in this tool in collaboration with the different teams studying the various noises impacting the sensitivity of Advanced Virgo Plus. Note that this tool currently uses a snapshot of the Advanced Virgo Plus interferometer to produce these noise projections. However, it is possible to replace the block of the measured optomechanical TFs $G(j\omega_k)$ by simulation results to study the contribution of noises in different configuration and working points of the interferometer.

Chapter 6

A MIMO system identification approach for the longitudinal control of the Filter Cavity of the Advanced Virgo Gravitational-wave Detector

One of the main challenges in gravitational-wave (GW) detection is overcoming various sources of noise that can obscure the signals from distant astronomical events. Among these, quantum noise is a significant limiting factor. Quantum noise in GW detectors has two primary components: radiation pressure noise, which predominates at low frequencies, and shot noise, which dominates at high frequencies. The integration of a frequency-dependent squeezed system into these detectors aims to reduce the quantum noise across the entire detection bandwidth.

The injection of squeezed vacuum states through the detector's dark port can enhance sensitivity. These squeezed states, manipulated via a detuned Filter Cavity (FC), undergo a frequency-dependent rotation that effectively mitigates quantum noise across the entire accessible frequency band. However, achieving the precise longitudinal control of the FC is crucial for maximizing this noise suppression. This involves the simultaneous active correction of both the cavity length and the squeezing laser frequency, transforming the setup into a complex Multiple-Input Multiple-Output (MIMO) system.

This research addresses the need for an effective identification approach for the MIMO loop of the longitudinal control of the Filter Cavity in the Ad-

vanced Virgo Plus detector [1]. Traditional Single-Input Single-Output (SISO) methodologies fall short in this complex control scenario. Our work demonstrates that adopting a MIMO system identification framework provides deeper insights into the underlying dynamics of the Filter Cavity's longitudinal control and facilitates better control strategies. By improving the duty-cycle, by making the controllers robust, our approach directly contributes to the enhanced sensitivity of the detector.

Our study is structured as follows: we first present an overview of the fundamental principles of quantum noise in GW detectors and the role of frequency-dependent squeezing in mitigating this noise. We then delve into the specific challenges associated with the longitudinal control of the Filter Cavity, highlighting the limitations of traditional SISO approaches. Following this, we introduce our MIMO system identification framework, detailing the theoretical underpinnings and practical implementation of our method. The following sections of the manuscript provide a thorough analysis of the experimental setup, data acquisition, and system modeling techniques employed in our research. We also present the results of our identification process. Finally, we discuss the broader implications of our findings for the field of GW detectors and outline potential directions for future research. This work is detailed in a paper that has been submitted to the journal Physical Review Applied.

[1] This paper refers to the configuration of the Advanced Virgo Plus, but for simplicity, it is referred to as Advanced Virgo in the text.

A MIMO system identification approach for the longitudinal control of the Filter Cavity of the Advanced Virgo Gravitational-Wave Detector

Enzo N. Tapia San Martín, Y. Guo, M. Vardaro, Y. Zhao, E. Capocasa, R. Flaminio, M. Tacca

Physical Review Applied.
Sent for publication.

Abstract

The sensitivity of the second generation ground-based gravitational-wave detectors is mainly limited by fundamental noises. Among them, the main contribution is due to the quantum noise that has two different components: radiation pressure noise, limiting the low frequency sensitivity and shot noise, limiting at high frequencies. It was shown that the injection of frequency dependent squeezed vacuum states through the detector dark port brings to a whole bandwidth reduction of the quantum noise. For this reason, in the break between the third and the fourth scientific observing runs, the LIGO and Virgo detectors implemented a Frequency Dependent Squeezing source. This system is based on a detuned linear cavity, the Filter Cavity, that reflects frequency independent squeezed states, impressing on them a frequency dependent rotation. The lock precision of the longitudinal control of the Filter Cavity is one of the key parameters affecting the quantum noise suppression factor. The target lock precision was achieved by simultaneously actively correcting both the cavity length and the frequency of the squeezing main laser. In this scenario, the setup turns into a highly coupled-structure and it was necessary to consider it as a Multiple-Input Multiple-Output system. In this work, we demonstrate that following a Single-Input Single-Output approach to describe this setup leads to inconsistencies while, with the use

of Multiple Input Multiple-Output system identification techniques we can not only effectively characterize the system but also improve its robustness. Ultimately, we show that with the proper design of the filters it is possible to ensure the required robustness and locking precision to provide frequency dependent squeezed states of light for the Advanced Virgo interferometer.

6.1 Introduction

After the landmark observation of a gravitational-wave (GW) emitted by the coalescence of a Binary Black Hole (BBH) system [97] in 2015, the detection of a GW arisen from a Binary Neutron Star (BNS) system [147] and multiple GW observations have been performed [103, 104]. After the completion of the third scientific Observing Run (O3) in 2020, all the ground-based gravitational-wave (GW) detectors, Advanced LIGO [1], Advanced Virgo [4], KAGRA [148] and GEO600 [149], have gone through several upgrades to increase their sensitivity. During O3, Advanced LIGO and Advanced Virgo were mainly limited by quantum noise, in particular by the shot noise component at high frequencies. Therefore, a technique called Frequency Independent Squeezing (FIS) [150, 151], which limits the impact of the quantum shot noise (above $\sim 50\,\mathrm{Hz}$), was implemented. The downside of the FIS injection is that excessively high squeezing levels, while enhancing the sensitivity of the detector at high frequencies, leads to a degradation at low frequencies. This is a consequence of the increase of the radiation pressure noise, which is the second component of quantum noise, as measured by both LIGO and Virgo detectors [152, 108]. This effect is connected to the Heisenberg's uncertainty principle, which imposes limitations on the ability to precisely determine a pair of measurements, i.e. position and momentum on a quantum system [153].

In gravitational-wave detectors, quantum noise is originated by the vacuum fluctuations entering from the output port. Furthermore, these fluctuations can mask or spoil the GW signal. However, with the use of proper squeezed vacuum states, both quantum noise components can be modified manipulating the entering vacuum state. Thus, in preparation for the fourth Observing Run (O4), a Frequency Dependent Squeezing (FDS) [154] system has been implemented in both Advanced LIGO and Advanced Virgo detectors [155, 156]. FDS systems are designed to provide a stable source of squeezed states of light to be injected into the output port of the Dual-Recycled, Fabry-Perot, Michelson interferometer. Using the FDS technique a reduction of quantum

noise of about 4.5 dB at high frequencies and about 2 dB at low frequencies is expected for Advanced Virgo during O4. The frequency dependent squeezed field is produced with a phase rotation of a squeezed field coming from a FIS source, by means of the reflection from a detuned high-finesse Fabry-Perot linear cavity, denoted as Filter Cavity (FC). In Advanced Virgo, the control of the FC is achieved through different steps. Initially, the lock of the cavity is obtained using an auxiliary laser beam, also generated by the FIS source. This secondary laser beam is characterized by a wavelength different from the one of the main squeezed beam, for which the finesse of the cavity is lower. Then, to further improve the lock precision of the cavity, a second loop is implemented by acting on the working point of the phase-locked loop (PLL) used to ensure that the frequency of the squeezer main laser is the same as the frequency of the main laser of the detector.

In this work, we present a new scheme developed to fully characterize the control of the FC of the Advanced Virgo FDS system via a Multiple-Input Multiple-Output (MIMO) approach [157]. A MIMO scheme, in contrast to a Single-Input Single-Output (SISO) approach [158], can disentangle the system dynamics and its cross-coupled terms. At first, we briefly introduce the Advanced Virgo FDS system. Then, we describe a model of the FC control system characterizing it and comparing measured transfer functions (TFs) with theoretical ones. Finally, we used this MIMO approach to develop a new model of the control system. Furthermore, we use these results to design robust controllers for the system without spoiling the locking precision, which is crucial to achieve the proper squeezing level to be injected into the interferometer.

6.2 Quantum noise and Squeezing

In second generation GW detectors, quantum shot noise and quantum radiation pressure noise are dynamically correlated [159]. In interferometers quantum noise is described using its amplitude spectral density calibrated in strain units (h_{QN}) [160], consisting in the incoherent sum of shot noise (SN) and radiation pressure noise (RPN):

$$h_{QN} = \sqrt{h_{SN}^2 + h_{RPN}^2}. \tag{6.1}$$

The amplitude spectral density of these components can be expressed as:

$$h_{SN} = \frac{1}{L_0}\sqrt{\frac{\hbar c \lambda}{2\pi P}} \tag{6.2}$$

for the shot noise, and:

$$h_{RPN} = \frac{1}{mf^2L_0}\sqrt{\frac{\hbar P}{2\pi^3 c\lambda}}, \tag{6.3}$$

for the radiation pressure noise, where L_0 represents the average arm length of the interferometer, $\hbar$ denotes the reduced Planck constant, c stands for the speed of light, λ is the wavelength of the laser, P is the average optical power, f is the frequency and m is the mass of the mirrors. SN is frequency-independent, while RPN follows a $1/f^2$ shape. Therefore, QN is dominated by RPN at low frequencies and by SN at high frequencies. For each frequency, we could find an optimal laser power to minimize the quantum noise, where the RPN and the SN have the same level. All these optimal points create a curve, crossing the whole detection spectrum, the Standard Quantum Limit (SQL), which is defined as:

$$h_{SQL} = \sqrt{\frac{\hbar}{m\pi^2 f^2 L_0^2}}. \tag{6.4}$$

For a GW interferometer with fixed arm lengths and mirror masses, the standard quantum limit defines its sensitivity limit. The trend of the QN and the SQL for three different optical powers inside the interferometer is shown in *Fig. 6.1.* One can see that increasing the optical power the level of the SN improves, worsening the level of RPN.

RPN arises from the quantum fluctuations in the light's amplitude, causing the mirrors in the detector to move unpredictably. Amplitude squeezing reduces the quantum uncertainty in the number of photons, thereby decreasing the fluctuations in the motion of the mirrors [161], but increasing the impact of the SN. This reduction in RPN enhances the detector sensitivity in the low-frequency range. While SN arises from the random and discrete arrival of photons on the photo-diodes, resulting in fluctuations of the phase of the light beam. Phase squeezing helps in making the arrival times of photons on the photo-diode more uniform, thus reducing SN, but increasing the RPN. The effect of injecting phase squeezing is equivalent to increasing the input power of the interferometer, as shown in *Fig. 6.1.* Therefore, to obtain a full bandwidth reduction of the QN of GW detectors, the squeezing ellipse should rotate at the SQL frequency of the system, i.e. generating a frequency dependent squeezed state. A description of the squeezed states can be found in the appendix.

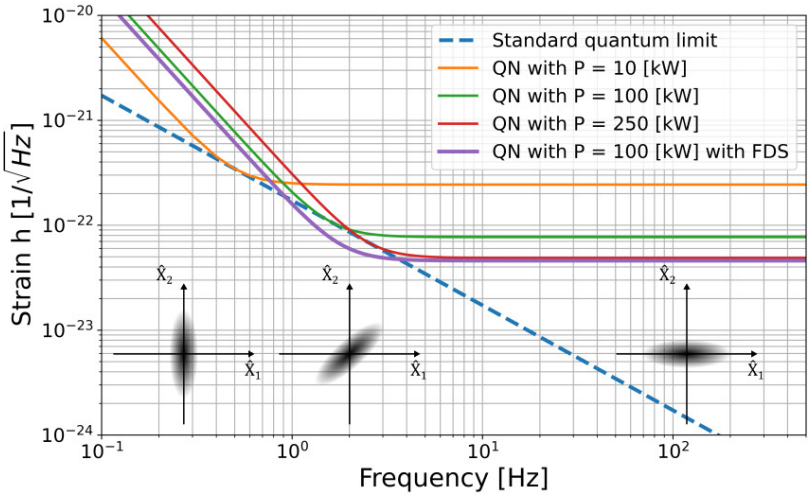

Figure 6.1: Effective strain quantum noise computed as the incoherent sum of shot noise and radiation pressure noise in a Michelson interferometer for different high circulating powers. Parameters are: $L_0 = 3\,\mathrm{km}$, $\lambda = 1064\,\mathrm{nm}$, $P = 10, 100, 250\,\mathrm{kW}$ and $m = 40\,\mathrm{kg}$. Standard quantum limit, in dashed blue lines, shows the minimum strain limited by quantum noise. The purple trace shows the effect of injecting Frequency Dependent Squeezing (4.5 dB of phase squeezing and 2 dB of amplitude squeezing) into a Michelson interferometer with a circulating power of 100 kW: the QN improves in the full bandwidth. The rotation of the squeezed states is shown in the bottom of the figure, phase squeezing at high frequencies, while amplitude squeezing at low frequencies.

6.3 Advanced Virgo Frequency Dependent Squeezing System

In preparation for O4, a FDS system has been implemented in Advanced Virgo with the target of achieving a QN reduction of about 4.5 dB at high frequencies and about 2 dB at low frequencies. In order to meet these values, strict requirements have been imposed on both the losses and phase noise. In this particular case, the spectra of SN and RPN meet in the region between 20 to 30 Hz. Therefore, the optimal rotation of the squeezing ellipse has been designed to be ~ 25 Hz [156]. A sketch of the frequency dependent rotation of the squeezing ellipse is shown in *Fig. 6.1*: at low frequencies the uncertainty of $\hat{X}_1$ is smaller than the one of $\hat{X}_2$, while the contrary happens at high frequencies. As detailed in the previous section, in order to reduce QN at low frequencies, amplitude squeezing is required, while phase squeezing is needed for the reduction of QN at high frequencies. Therefore, the injection of both amplitude squeezing at low frequency and phase squeezing at high frequency is required. The rotation of the angle of the squeezing ellipse for different frequencies is achieved by reflecting a squeezed light state off the Filter Cavity. The source of squeezing used in Advanced Virgo is the same FIS source already installed and operational during O3 [162], set to deliver phase squeezed states. The system operates with a wavelength of 1064 nm as the main interferometer. The squeezed states are generated using an independent laser from the interferometer. However, to have an impact on the sensitivity, the squeezed states should be at the same frequency of the interferometer main laser. Thus, a PLL is implemented to match the frequency of the laser of the FIS source with the one of the Virgo main laser [150]. A Filter Cavity, consisting of two suspended mirrors, has been installed along one of the main arms of Advanced Virgo during the upgrade break between O3 and O4. It has been shown that a cavity length of the order of hundreds of meters is less influenced by losses than cavities with lengths of tens of meters [163], since they are characterized by a lower finesse value. Considering this input and the infrastructural configuration of the Virgo site, a length of 285 m has been chosen. In order to achieve the target squeezing ellipse rotation, the FC works in a detuned configuration, meaning that its resonance is deliberately shifted by a few Hertz away from the carrier frequency. The detuning frequency of this FC has been defined to be of 25 Hz. In order to achieve it, the required linewidth of the optical cavity is also 25 Hz. According to the measured linewidth, the estimated finesse for the IR

(Infrared) laser is $\mathcal{F}_{IR} = 9695 \pm 4$ [156]. A simplified scheme of the Advanced Virgo detector with the FDS system is shown in *Fig. 6.2*.

6.3.1 Longitudinal control of the Filter Cavity

Having such a notable finesse value for the IR beam, the acquisition of the control of the FC turns into a difficult task. Therefore, the full longitudinal control of the cavity is achieved in two subsequent steps: at first, the cavity is locked using an auxiliary green laser; then, the longitudinal control is moved to an IR beam. Moreover, one of the crucial factors to achieve the required level of FDS is to have a high level of locking precision. The target lock precision level is below 1 Hz RMS, which effectively minimizes the fluctuations on the detuning of the FC and, therefore, reduces the degradation of the FDS, as described in [164]. In order to achieve this value of lock precision, the actuation of the control loop is divided in two parts according to the frequency range: the correction signals below 100 Hz are sent to the output mirror of the FC, while the corrections at higher frequencies are used to stabilize the frequency of the laser source, as described in sections 6.3.2 and 6.3.3. A scheme of the FC length control and frequency stabilization of the laser source plus all its relevant components is shown in *Fig. 6.3*.

6.3.2 Length control loop

The lock of the FC is initially achieved with an auxiliary green laser (532 nm). This laser beam is produced through a Second Harmonic Generation process [165], a non-linear optical phenomenon, where two photons of identical wavelength interact inside a specific material to get a new photon at half the original wavelength. The Second Harmonic Generator (SHG) is installed in the FIS source [162] and is doubling the main squeezer laser frequency. The FC finesse for the green beam is $\mathcal{F}_G \sim 100$, much lower than the one for the IR beam. To keep the FC on resonance, the Pound-Drever-Hall (PDH) modulation-demodulation technique [64] is used. First, side-bands are generated with an electro-optic modulator (EOM) at 5.5 MHz, then an error signal is derived demodulating the beam reflected by the cavity and passed through a low pass filter. This signal is then used to close the loop with a control filter, which produces a correction signal sent to the actuators, consisting of pair of coils-magnets, of the output mirror of the FC. Once the FC is controlled, the detuning of the carrier beam in relation to the resonant condition is actively

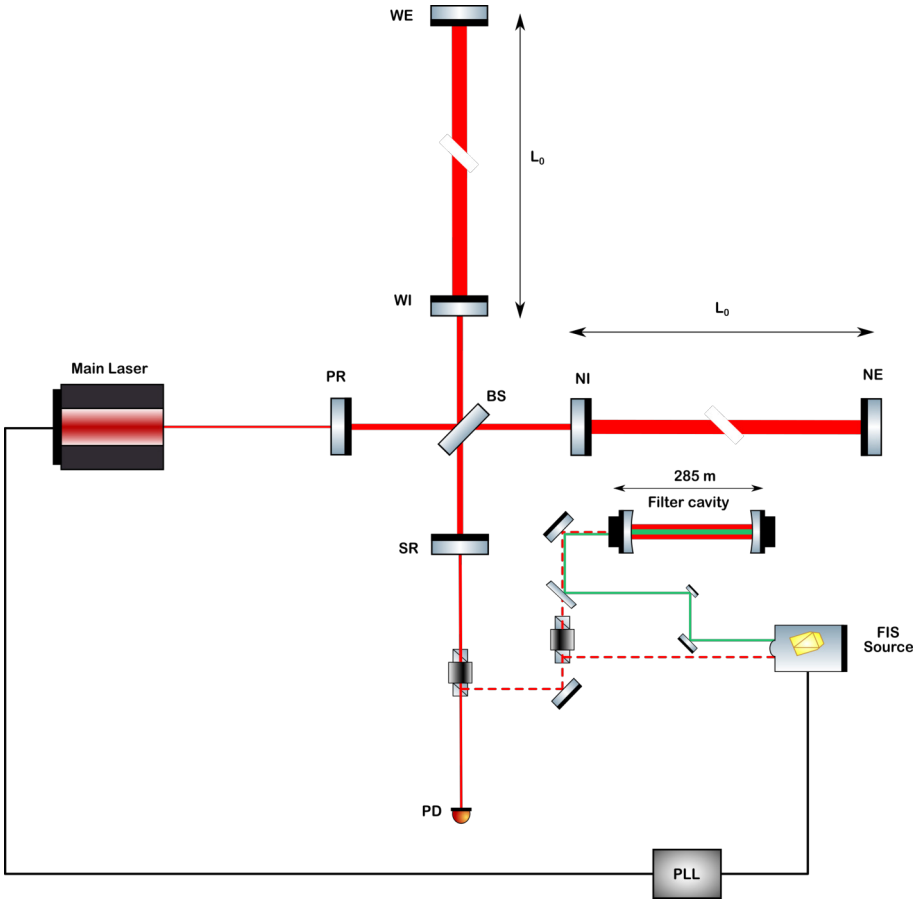

Figure 6.2: Simplified scheme of the Advanced Virgo detector optical configuration with the FDS system for O4 run. The main laser beam first goes through a power recycling (PR) mirror, then is split at the Beam Splitter (BS) mirror and directed towards the North and West arms passing through the North Input (NI) and West Input (WI) mirrors. These beams travel along the arm cavities and are reflected back by the North End (NE) and West End (WE) mirrors to be recombined at the BS. The recombined beam passes through a Signal Recycling (SR) mirror before reaching the output photo-diode (PD). This scheme includes some of the key components of the FDS system: the FIS source; the PLL between the main laser and the Squeezing laser; and the Filter Cavity installed along the North arm of the detector. The Squeezed beam is injected at the output of the interferometer through a Faraday isolator.

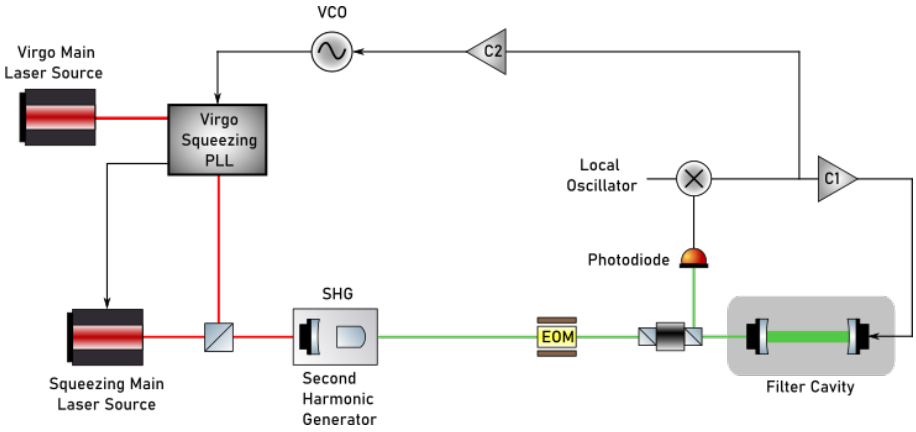

Figure 6.3: Scheme of the longitudinal control loop of the FC. For both the length control and frequency control loops, the error signal is derived from the same photo-diode with a modulation-demodulation technique. For the cavity length and frequency control loops, the control filters are denoted as C_1 and C_2, respectively. The first loop controls the length of the cavity using the coil-magnet actuators of the end mirror. The second loop controls the PLL working point using a VCO.

controlled using an Acousto-Optic Modulator (AOM) installed along the green optical path. To achieve the required level of locking precision (RMS < 1 Hz) with the IR beam, the first step is to improve the locking precision using the green beam.

6.3.3 Frequency stabilization loop

In the early stages of the commissioning of the FDS system, only the control of the length of the FC was foreseen. However, this strategy resulted in a level of locking precision not compliant with the requirement: most of the measured RMS of the locking precision came from additional noise around ~ 100 Hz and the bandwidth of the loop was limited by delays of the digital system. Therefore, an additional loop was implemented acting in the high frequency band (above ~ 100 Hz) on the squeezing main laser frequency, through the same actuator of the PLL, already implemented to lock the frequency of the main squeezing laser to the one of the main Virgo laser. The error signal for this loop is the same PDH signal extracted from the reflection of the FC. After passing through a controller, it is used to closed the loop by acting on the PLL working point through a Voltage-Controlled Oscillator (VCO).

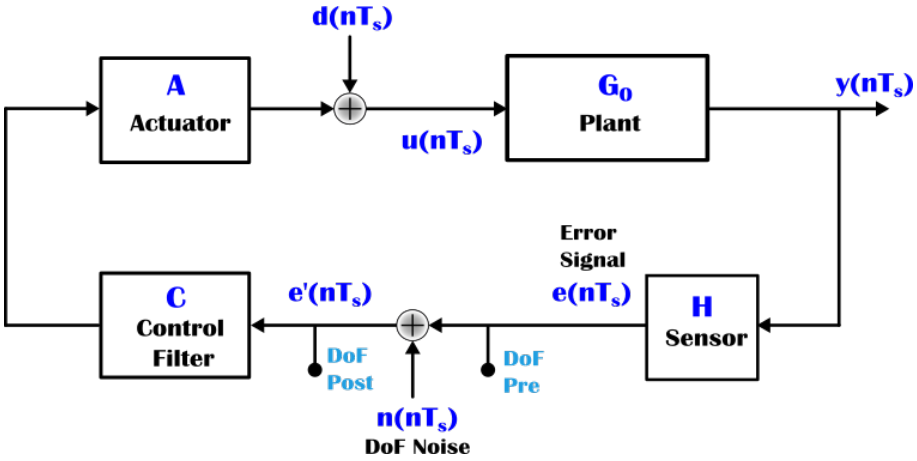

Figure 6.4: General closed loop system, where a modulation-demodulation technique has been used to obtain an error signal.

6.4 Modelling the system

As described in section 6.3, the control system of the Filter Cavity of the FDS system of Advanced Virgo consists of two feedback loops working together to achieve the high required level of locking precision, both for the green and IR beams. Control systems are typically described in the frequency domain by their Open Loop Transfer Functions (OLTFs). The OLTFs can be derived from differential equations or block diagrams including all the components of the loop. Furthermore, this description provides insights of the system stability, resonances, bandwidth and overall performance. A block diagram for a generic opto-mechanical control loop is shown in *Fig. 6.4*: G_0 represents the opto-mechanical plant; H represents the sensor; C stands for the controller and A is the representation of the actuator. Note that each block can be either a single component or a matrix, i.e. each block can be either a Single-Input Single-Output (SISO) system or a Multiple-Input Multiple-Output (MIMO) one. Moreover, Y and U are the output and input signals respectively, n represents the noise used to characterize the loop, d stands for the perturbations that can disturb the system, finally, assuming that the error signal is derived with a modulation-demodulation technique, e and e' stand for the error signals before and after the noise injection node.

Considering the control loop of the FC length based on the PDH technique, the Transfer Functions of the various elements with the corresponding units

are the following:

- $G_{FC}\,[\frac{\mathrm{W}}{\mathrm{m}}]$: Optical cavity, representing the longitudinal motion.
- $A_{FC}\,[\frac{\mathrm{m}}{\mathrm{V}}]$: Made of two components, $A_{coil}\,[\frac{\mathrm{N}}{\mathrm{V}}]$, for the coil actuator and $A_{pend}\,[\frac{\mathrm{m}}{\mathrm{N}}]$ for the pendulum dynamics.
- $H_{FC}\,[\frac{\mathrm{V}}{\mathrm{W}}]$: Photo-diode response.
- $C_{FC}\,[\frac{\mathrm{V}}{\mathrm{V}}]$: FC length control filter.

In the same way, also the elements of the control loop of the frequency stabilization part can be defined as:

- $G_{Laser}\,[\frac{\mathrm{W}}{\mathrm{Hz}}]$: Frequency response of the main squeezing laser.
- $A_{Laser}\,[\frac{\mathrm{Hz}}{\mathrm{V}}]$: VCO dynamics.
- $H_{Laser}\,[\frac{\mathrm{V}}{\mathrm{W}}]$: Photo-diode response.
- $C_{Laser}\,[\frac{\mathrm{V}}{\mathrm{V}}]$: Squeezing laser frequency stabilization control filter.

To validate theoretically estimated OLTFs, a comparison with their respective experimentally measured equivalents is needed. A comparison of the theoretical and measured OLTFs of the two parts of the Advanced Virgo FC control loop is depicted in *Fig. 6.5*. The measured and the theoretical OLTFs are shown, respectively, in blue and in orange . It can be seen that the measured OLTFs differ from the theoretically modeled OLTFs for both the segments of the loop. For the FC length control loop, the Unity Gain Frequency (UGF), the Phase Margin (PM) and the Gain Margin (GM) are different between the model and the measurement. For the Squeezing main laser frequency control loop, the shape is different below few hundreds of Hz. In general, this difference can be due to various reasons: either the system exhibits uncertainties and parameter variations or there are limitations in the measurements. In the case of the Advanced Virgo FDS, all the components of the FC operate in highly controlled environments. Furthermore, the system has been well-characterized and its parameters are accurately known. Therefore, in this scenario the case of uncertainties and parameter variations can be ruled out or, at least, neglected until a certain degree. Thus, a possible explanation of the difference between the theoretical and the measured OLTFs can be the way to perform the measurements.

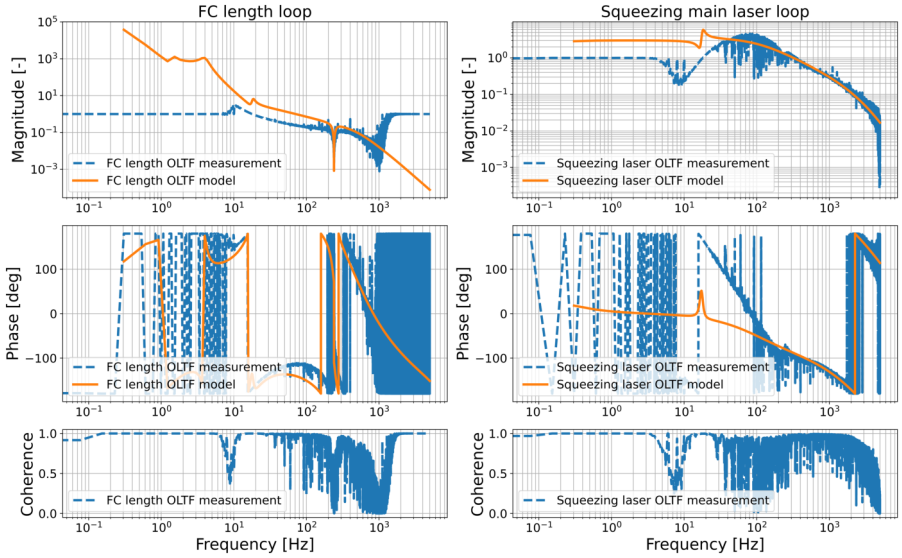

Figure 6.5: Bode plots of the modeled and measured OLTFs for both the length control of the FC (left) and the frequency control (right). The orange line represents the theoretical model, while the blue dashed lines depict the measurements of the OLTFs obtained with a SISO system identification approach.

6.5 MIMO model and system identification technique

A SISO system approach was initially used to design the control filters of the two parts of the FC control loop. With this approach, discrepancies arose comparing measured with modeled OLTF, as shown in *Fig. 6.5*. Furthermore, the system exhibited instabilities, i.e. sudden loss of control, that could not be explained in a first instance. Therefore, in order to better understand the dynamics of the full opto-mechanical system, two steps have been made: at first, a system identification approach that can unfold the cross-coupled dynamics[2] when measuring the system OLTF has been used; then, a MIMO approach including the cross-coupling terms has been considered to model the system.

6.5.1 System identification technique

Identifying a complex system within a closed-loop condition is notably challenging. Characterizing complex systems with multiple control loops, as the FC of the FDS system of Advanced Virgo, leads to measurements that could not be explained with simple SISO OLTF models. Therefore, adding extra feedback loops often leads to biased measured results [131]. To better understand the results, and to get unbiased OLTFs, a MIMO system identification approach should be considered. Obtaining the Frequency Response Function (FRF) is the starting point for this method. Considering the general opto-mechanical scheme shown in *Fig. 6.4*, the representation of the array of the discrete-time input signals of the plant, is denoted as $u(nT_s)$. n ranges from 0 to $N-1$, with N representing the number of samples, while T_s is the sample time. In the frequency domain, with the application of the Discrete Fourier Transform (DFT) [132], the array of the input signals is given by:

$$U(\omega_k) = \frac{1}{\sqrt{N}} \sum_{n=0}^{N-1} u(nT_s) e^{-j2\pi nk/N} \tag{6.5}$$

where $\omega_k = 2\pi f_k$, $f_k = k/NT_s$ is the frequency at index k in the discrete frequency domain and k is the index of the frequency bin. Note that these are array of signals, so they count for multiple-inputs. Furthermore, for a Linear Time Invariant (LTI) system in open loop, an empirical transfer function

[2]The cross-coupled dynamics lie in the off-diagonal elements of the opto-mechanical plant matrix.

estimation can be derived from the observed data of the output $Y(\omega_k)$ and input signals $U(\omega_k)$. Thus, the plant TF can be estimated and expressed as $\hat{G}(\omega_k) = \frac{Y(\omega_k)}{U(\omega_k)}$. The error of the measurement can be diminished if this computation is averaged for several segmented portions of input and output signals. While with a different approach, a TF of the plant can be derived from the cross-power spectrum of its input and output signals (Φ_{yu}) along with the auto-power spectrum of its input signal (Φ_{uu}) [132]. This computation involves as well segmentation into smaller sections of both signals, which minimizes spectral leakage. Hence, the TF estimate is given by $\hat{G'}(\omega_k) = \frac{\Phi_{yu}}{\Phi_{uu}}$. However, when these LTI systems are in a closed loop condition to operate in a precise working point, such as the case of the FC of the FDS system, it is possible to estimate the TFs of the system in closed loop using the array of excitation inputs $n(nT_s)$, and measuring the signals before and after the noise injection node. These measurements are performed for both the controls of the length of the FC and the frequency of the main squeezing laser. In this context the estimated TF of the real plant is given by [134]:

$$\hat{G'}(\omega_k) = \frac{\Phi_{yu}}{\Phi_{uu}} = \frac{G_0(\omega_k)\Phi_{nn} - C(\omega_k)\Phi_{dd}}{\Phi_{nn} + |C(\omega_k)|^2\Phi_{dd}}. \tag{6.6}$$

When noise injections dominate among the sources of noise of the loop, equation (6.6) reduces to the real plant $G_0(\omega_k)$. However, the problem arises when disturbances dominate the noises entering the loop. In this case, equation (6.6) reduces to $-\frac{1}{C(\omega_k)}$. When neither n nor d are zero, then the result of (6.6) is a mix of both contributions, Φ_{yu} and Φ_{uu}. In contrast with the different methods previously explained, we can apply an indirect approach [136], which consists of computing closed loop TFs, i.e. Sensitivity function ($S'(\omega_k)$) and complementary sensitivity function ($T'(\omega_k)$) of this system, which are given by:

$$\hat{S'}(\omega_k) = \frac{\hat{\Phi}_{e'n}}{\hat{\Phi}_{nn}} = \frac{1}{1 + \hat{L'}(\omega_k)} \tag{6.7}$$

and:

$$-\hat{T'}(\omega_k) = \frac{\hat{\Phi}_{en}}{\hat{\Phi}_{nn}} = -\frac{\hat{L'}(\omega_k)}{1 + \hat{L'}(\omega_k)}, \tag{6.8}$$

where $\hat{L'}(\omega_k)$ is the estimated OLTF of the system depicted in Fig. 6.4, given by the product of all the elements in the loop, i.e. $L(\omega_k) = H{\cdot}G_0{\cdot}A{\cdot}C$. Ultimately, the estimation of the OLTF can be obtained from these measurements in closed

loop as:

$$\hat{L}'(\omega_k) = \hat{T}'(\omega_k)(\hat{S}'(\omega_k))^{-1}. \tag{6.9}$$

Lastly, since the controllers of this system are known, the dynamics of the actuators and the response of the photo-diode are well understood, then the matrix of the unbiased opto-mechanical plant TFs can be derived starting from (6.9).

6.5.2 MIMO model of the system

A MIMO block diagram scheme of the FC opto-mechanical system is depicted in *Fig. 6.6*. In the scheme, the opto-mechanical plant that involves the control of the length of the optical cavity and the PLL that controls the frequency of the main squeezing laser are represented by the four elements (G_{11}, G_{12}, G_{21} and G_{22}) of the real opto-mechanical plant matrix, $\mathbf{G_0}(j\omega_k)$. In particular, G_{11} represents the dynamics of the optical cavity length, G_{12} represents the cross-coupling dynamics of the optical cavity length to the frequency of the squeezing laser, G_{21} is the cross-coupling dynamics of the frequency of the squeezing laser to the optical cavity length and G_{22} stands for the dynamics of the main squeezing laser frequency. The actuator dynamics matrix $\mathbf{A}(j\omega_k)$, a diagonal matrix, has two non-zero elements: the dynamic of the mirror actuators (A_{11}), and the Voltage-Controller Oscillator (VCO) dynamic (A_{22}). The sensing response matrix $\mathbf{H}(j\omega_k)$ has two identical elements H_{11} and H_{22}, representing the response of the photo-diode placed in reflection of the cavity. Finally, this scheme also includes the control filters used for the cavity length control (C_{11}) and for the frequency stabilization (C_{22}), which are the non-zero elements of the diagonal control matrix $\mathbf{C}(j\omega_k)$.

6.5.3 Model results

The combination of the system identification technique presented in section 6.5.1 and the detailed MIMO scheme shown in section 6.5.2 allows to not neglect the re-injection of noise from one control loop to another, as explained in [166]. This approach facilitates the estimation of all cross-coupling elements within this complex system, which are included in the non-diagonal terms of the OLTF matrix $\mathbf{L}(j\omega_k)$. Meanwhile, the diagonal terms of $\mathbf{L}(j\omega_k)$ represent the pure dynamics of both the FC length and the squeezing main laser frequency, i.e. not affected by re-injection of noise. Thus, it can be used to explain the difference

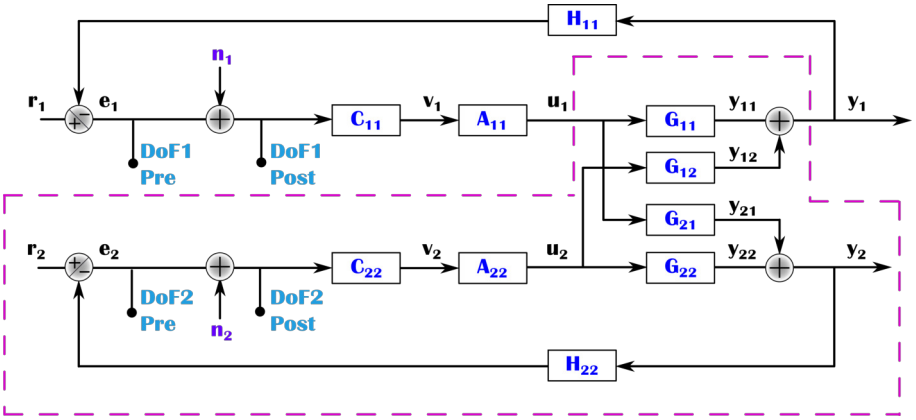

Figure 6.6: Schematic representation of a 2x2 MIMO control system. The system has two nodes for noise injections, used for characterization and performance check-up. A_{11} and A_{22} represent the actuator dynamics of each branch. The sensor response is characterized by the TFs H_{11} and H_{22}. The control filters for these loops are denoted as C_{11} and C_{22}. The interaction between these two loops is due to the plant cross-coupled dynamics denoted as G_{11}, G_{12}, G_{21} and G_{22}. The dashed pink line denotes the equivalent plant that is "seen" by the upper loop, when these two loops work in closed loop condition.

between the theoretical and experimental OLTFs shown in *Fig. 6.5*. Indeed, we could validate the model detailed in section 6.4, as shown in *Fig. 6.7*: green curves are the performed measurements analyzed with the MIMO approach and the orange curves are the model. Finally, the model fits the measurement.

Furthermore, it was possible to explain the measurement results obtained in the first analysis performed with a SISO approach, shown in blue in *Fig. 6.5*. To reproduce these measurement results, we need to introduce the concept of equivalent plant. In the case of the Advanced Virgo FC, the equivalent plant of one loop takes into account also the dynamics of the other loop working in closed-loop condition. The equivalent plant of the FC length control G_{11}^{eq} is shown inside the dashed pink section of *Fig. 6.6* and is given by:

$$G_{11}^{eq} = G_{11} - \frac{G_{21}H_{22}C_{22}A_{22}G_{12}}{1 + G_{22}H_{22}C_{22}A_{22}}. \tag{6.10}$$

Note that G_{11}^{eq} deviates from the plant G_{11} due the interaction of these two loops, expressed in the second term of equation (6.10). Analogously, we can estimate the equivalent plant of the squeezing main laser frequency control G_{22}^{eq}.

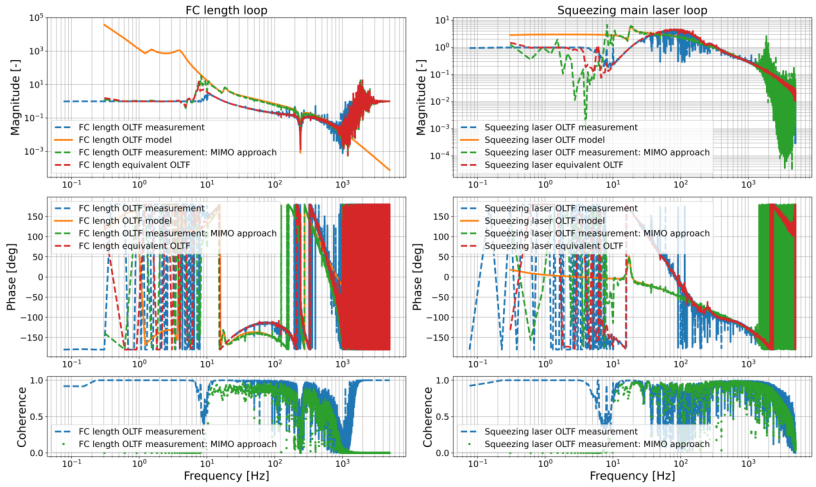

Figure 6.7: Bode plot analysis of the FC length and frequency control loops. The solid orange lines depict the model of the system and the dashed blue lines show the measurements performed with a SISO approach. The dashed green lines depict the results of the measurements obtained using a MIMO approach. The dashed red lines represent the OLTFs when the equivalent plant is included in the model, explaining the results of the measurements obtained with the SISO approach.

The OLTFs estimated using the equivalent plants are shown in red in *Fig. 6.7* and they fit the measurement results obtained with the SISO approach.

6.6 Robustness analysis

To deliver the target level of FDS, the full system should meet the required level of locking precision and be stable and robust. The initial set of implemented control filters allowed to achieve the required level of lock precision. However, the target working condition was not always feasible due to the loss of control of the FC, indicating instabilities in the system. Since the initial controllers were designed using a SISO approach, possible intrinsic cross-couplings were neglected. Thus, they could not necessarily perform as expected, explaining the instabilities of the system. To understand this behaviour, we analyze with the Nichols chart the stability of the MIMO opto-mechanical system, because it has been shown that they are valid in particular conservative scenarios [167]. The Nichols charts of the four elements of the OLTF matrix $\mathbf{L}(j\omega_k)$ for this system are presented with the blue curves in *Fig. 6.8*. It can be seen that the OLTFs of the diagonal terms, i.e. L_{11} and L_{22}, are robust and stable. However, inspecting the Nichols chart of the off-diagonal terms, i.e. L_{12} and L_{21}, of the OLTF matrix, it can be observed that their phases are below $-180\,\mathrm{deg}$, indicating instability. Therefore, minor disturbances or noise sources entering the loop could introduce instabilities in the system unlocking the optical cavity.

In this analysis, our focus was understanding the behaviour and ensuring the stability of the MIMO system. Therefore we optimized the filters to gain overall stability and robustness, without affecting the level of the achieved locking precision. Note that both the current and new control filters have been designed in a decentralized architecture [158] due to the limitations imposed by the installed hardware and software. The Nicholas chart for the OLTFs estimated using the new control filters are shown with the orange curves in *Fig. 6.8*. It can be noticed that with the new set of control filters, the system has a sufficient level of stability margin.

6.7 Conclusions

In the break between the Observing Runs O3 and O4, the ground-based GW detectors have gone through several upgrades to improve their sensitivity. In

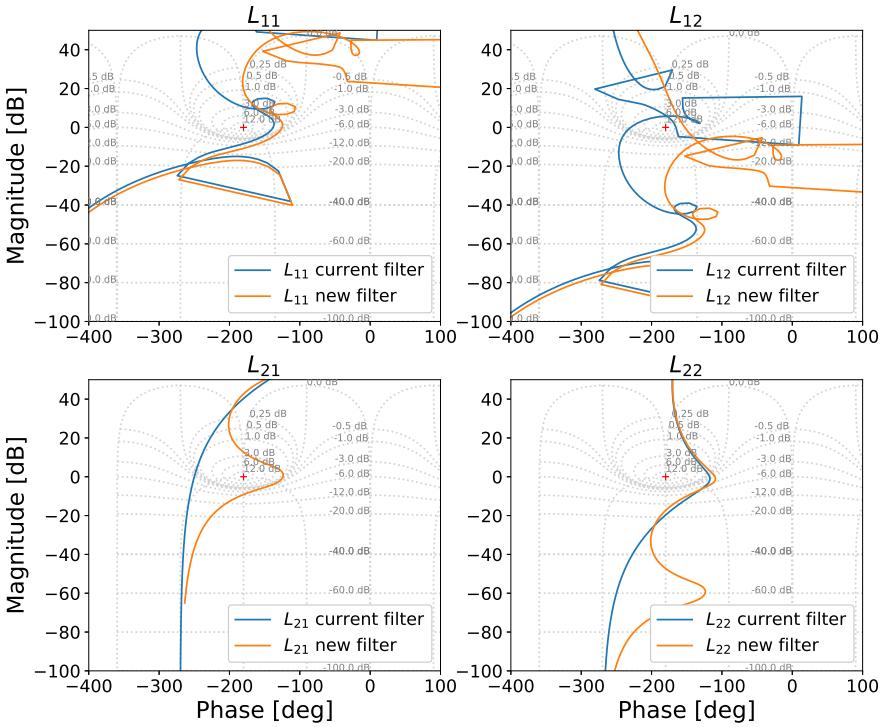

Figure 6.8: Nichols plot comparison for two sets of control filters. The blue curves represent the OLTFs with the current implemented filters, while the orange curves denote the updated OLTFs for redesigned control filters. The red "plus" represents the point of unity gain and -180 deg of phase, the critical point for stability studies. The modification of these filters aims to enhance both the stability and robustness of the longitudinal control of the FC system.

Advanced Virgo, among the various upgrades, a FDS system has been implemented to obtain a reduction of the impact of the Quantum Noise in the full detection bandwidth. The frequency dependent squeezed field is produced with a rotation of a squeezing ellipse coming from a FIS source, by reflecting it from a detuned high-finesse Fabry-Perot linear cavity, called Filter Cavity (FC). To achieve the target of a QN reduction of about 4.5 dB at high frequencies and about 2 dB at low frequencies, strict requirements have been imposed on both the losses and phase noise of the system. In particular, to obtain the required level of phase noise, the target lock precision level for the longitudinal control of the FC was set to be below 1 Hz RMS. In the Advanced Virgo detector, the control of the FC is achieved through different steps. Initially, the lock of the cavity is obtained using an auxiliary laser beam. Since it was not possible to reach this level of locking precision acting only on the mirrors of the cavity, a second control loop, acting on the frequency of the squeezing main laser has been implemented.

A SISO system approach was initially used to design the control filters of the two parts of the FC control loop. With this approach, discrepancies arose comparing measured with modeled OLTFs. Therefore, to better understand the dynamics of the full opto-mechanical system, two steps have been made: at first, a system identification approach that can unfold the cross-coupled dynamics when measuring the system OLTF has been used; then, a MIMO approach including the cross-coupling terms has been considered to model the system. Using the MIMO model we were able to explain the difference between the theoretical and experimental OLTFs. Moreover, the investigation revealed that the initial longitudinal controllers, while effective in achieving a high level of precision, exhibited instabilities when studying cross-coupled terms, leading to lock losses of the system. To mitigate these issues, we performed robustness analyses and, subsequently, redesigned the filters to enhance the stability margins of the FC system.
Thanks to this result, we achieved the target lock precision required in the control of the filter cavity only using the auxiliary beam in the low finesse configuration, simplifying the control scheme. The current study has underscored the importance of employing a suitable system identification technique to understand the behavior of complex feedback systems. This work also aims to open avenues for future research directed toward enhancing control strategies.

Acknowledgments

The authors gratefully acknowledge the Quantum Noise Reduction (QNR) team of Advanced Virgo for having implemented and commissioned the Frequency Dependent Squeezing (FDS) system in Advanced Virgo. In particular, the authors are grateful to J.P. Zendri, M. De Laurentis, F. Sorrentino, R. Bonnand and A. Bertolini for having managed the realization of the FDS system; H. Vahlbruch and M. Mehmet for having implemented the squeezing source; M. Barsuglia for his help in controlling the Filter Cavity. A special thanks go to the staff of the European Gravitational Observatory (EGO) for the relevant role in the logistic, in the implementation of the structural changes, in the installation of the vacuum environment and in the electronics cabling.

Appendix: Squeezed states

The quantum noise in interferometers can be described also using the quantum mechanics notation expressing a laser beam as an electromagnetic field at a frequency ω in terms of creation ($a^\dagger_\omega$) and annihilation operators ($\hat{a}_\omega$) [168, 169]. This notation will be useful to introduce and describe the concept of squeezed states. Since annihilation and creation operators are not Hermitian, they cannot be used to describe observable quantities. Therefore, we introduce Hermitian quadrature operators as a way to represent the amplitude and phase components of the electromagnetic field. Quantization of light imposes uncertainties when measuring either of these two observables. Then, the amplitude quadrature operator is defined as [170]:

$$\hat{X}_1 = \hat{a}_\omega + a^\dagger_\omega \tag{6.11}$$

while the phase quadrature operator is defined as:

$$\hat{X}_2 = i(a^\dagger_\omega - \hat{a}_\omega). \tag{6.12}$$

The uncertainty principle imposes restrictions on the variances of these operators as:

$$\langle(\Delta\hat{X}_1)^2\rangle\langle(\Delta\hat{X}_2)^2\rangle \geq 1, \tag{6.13}$$

meaning that measuring both the amplitude and phase quadratures precisely at the same time is not possible. Using this notation we can first defined the

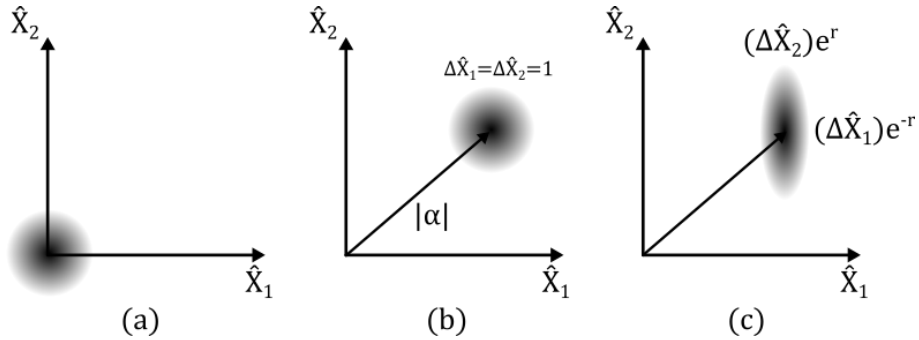

Figure 6.9: Phasor representation of different quantum states: (a) Vacuum state, (b) Coherent state, (c) Squeezed state along $\hat{X}_1$.

vacuum state $|0\rangle$, the state of a field where no photons are present, shown in *Fig. 6.9*(a). Then we can introduce coherent states, which refer to the eigenstates of the annihilation operator. A coherent state can be represented as $|\alpha\rangle$, where α, the complex field amplitude, is the eigenvalue that corresponds to the eigenstate, and is related to the number of photons.

A way to describe a laser beam as a coherent state is by applying a displacement operator ($\hat{D} = e^{\alpha\hat{a}-\alpha^* a^\dagger}$) to the vacuum state. Thus, the representation of a laser beam as a coherent state, can be expressed as:

$$|\alpha\rangle = \hat{D}(\alpha)|0\rangle \tag{6.14}$$

For a coherent state, the product defined in equation (6.13) is minimized to 1, meaning that the variances for the amplitude and phase quadrature are identical. This leads to a spherically symmetric uncertainty distribution as shown in *Fig. 6.9*(b). Giving that the product in equation (6.13) must hold, the uncertainties can be redistributed between the two quadratures. This can be achieved by deforming the spherical distribution of the uncertainties into an ellipse. This is denoted as the process of squeezing a coherent state, resulting in a squeezed state of light, as shown in *Fig. 6.9*(c). Hence, a state squeezed in its phase-quadrature exhibits a reduced uncertainty in $\hat{X}_2$ at the expense of an increased uncertainty in $\hat{X}_1$. A squeezed state can be obtained applying the unitary squeezing operator ($\hat{S}(re^{i\Phi})$) to a coherent state, with a squeezing degree r and a squeezing angle Φ ($\Phi = 0$ denotes amplitude squeezing, whereas $\Phi = \pi/2$ defines phase squeezing).

Chapter 7

Toward direct measurement of Coating Thermal Noise for Future Gravitational-wave Detectors

In the second generation of GW detectors, the fundamental noise limiting the sensitivity in the mid-frequency range is the Brownian coating thermal noise. Indeed, this noise could also limit the sensitivity of the 3^{rd}-generation of detectors. Thermal noise is present not only in the coating but also in the substrate of the mirrors and in their suspension wires. In order to overcome the barrier of this fundamental noise, the plan for Einstein Telescope is to replace the current fused-silica mirrors with silicon mirrors and cool them down to 10 K for the interferometer focused on improving the sensitivity at low frequencies. Since this is a new material at a new operation temperature for GW detectors, two things are extremely essential. The first one is to measure directly the thermal noise of the coatings at cryogenic temperatures and the second one is to characterize the coating materials that are intended to be used for this new generation of detectors. To directly measure the thermal noise of the coatings, optical techniques can be used. Unfortunately, this kind of direct measurements has several complications. Firstly, if the vacuum level is insufficient, residual gases risk to condense and freeze on the sample mirror surface due to the cryogenic environment and will thereby spoil the measurement. Secondly, the noise floor of the electronics used for the control and measurements in this setup must be well below the expected noise level related to the coating thermal noise itself. Implementing such a kind of experiment will help in answering the following questions:

- Is it possible to directly measure the Coating Thermal Noise (CTN) for the 3^{rd}-generation GW detectors?
- What coating material should be used to maximize the sensitivity of these detectors?
- What would be the maximum sensitivity for these detectors?

To support research and development for 3^{rd}-generation GW detectors, we started to design and develop an advanced optical setup to directly measure the CTN at cryogenic temperatures. The optical design is derived from the one completed at MIT by Gras and Evans [171, 172]. We decided to integrate the core of the optical experiment into a seismic isolation system to minimize vibrations and external disturbances, ensuring accurate measurements and reliable testing results. With this setup we could profit of a quiet environment at cryogenic temperature to test and characterize also new sensors and actuators that could be exploited by the Einstein Telescope.

By providing a controlled and stable environment, our setup is poised to play a crucial role in advancing the development of next-generation GW detection technologies, contributing to the continuous progress of the field.

In this chapter we present the conceptual design of the optical cavity and the preliminary design of the control architecture of this optical setup. The commissioning of the full setup and the first CTN measurement results are expected for the next year.

7.1 Working principle of the optical setup

We use an optical setup to characterize the CTN of a high-reflectivity sample mirror. In GW detectors, the internal thermal noise of the test mass mirrors is defined as the fluctuations in the longitudinal motion of the optical axis. These fluctuations are produced by the internal damping inside the test mass, as described in Chapter 2. Internal damping of mirrors refers to the intrinsic energy dissipation within the mirror material due to internal friction and structural rearrangements when it deforms. This damping affects the mirror's performance by reducing its quality factor (Q-factor) and increasing thermal noise. At first, we install a sample mirror inside a folded high-Finesse optical cavity. Then, this cavity must allow the co-resonance of three modes: The fundamental mode of the laser beam (TEM00) and two higher-order modes (TEM02

and TEM20). Under those circumstances CTN appears as a fluctuation in the resonant frequency difference between the two higher-order modes (HOM). The fundamental Gaussian mode (TEM00), and two Hermite-Gaussian modes (TEM02 and TEM20) are shown in *Fig. 7.1.*

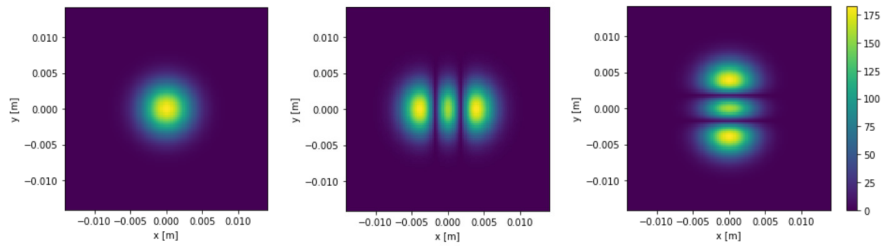

(a) TEM00 (b) TEM20 (c) TEM02

Figure 7.1: Shape of the far field intensity of (a) the fundamental mode (TEM00) and higher-order modes (b) TEM20 and (c) TEM02. Intensity in W/m^2.

The thermal noise level that is sensed by the TEM02 mode is different from the thermal noise level sensed by the TEM20 mode because they do not explore the same area of the sample mirror coating. On the contrary, these HOMs and the fundamental mode sense the same common noises. These noises, are for example: cavity length noise, frequency noise and substrate thermal noise of the mirror. Thus, the fundamental mode can be used to decouple the common noises from the CTN measurement, and we can obtain a clean CTN measurement. In this experiment, the CTN is obtained as a result of the beat note signal from the resonant frequencies of the TEM02 and TEM20 modes. While multiple dissipation mechanisms within the coating can cause the observable to fluctuate, we focus on the primary one: mechanical loss of the coating materials. Although this constitutes only a portion of all coating thermal noises, we will denote the noise associated with this mechanism as CTN. Knowing this information one can better understand and update the sensitivity achievable by future detectors.

7.2 Optical experimental setup

This optical setup is composed by two main parts. The first one aims to generate the three beams that are injected into the folded cavity and to detect the reflected and transmitted beams needed for the various control loops and

for the measurement of the CTN. It is composed of a 1550 nm fiber laser source and various optical components and electro-optical devices. The second one is an in-vacuum high-finesse multi resonant cavity. The general scheme is shown in *Fig. 7.2*.

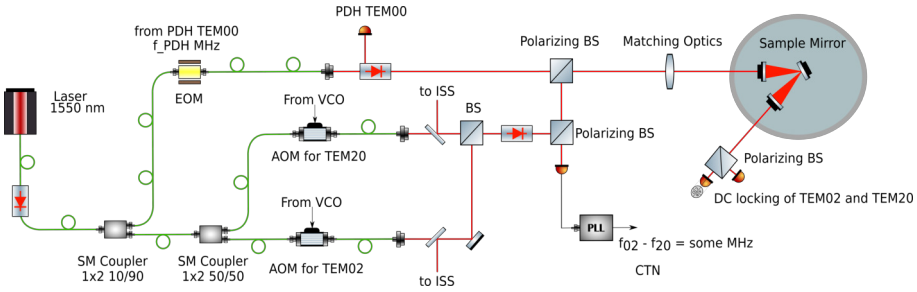

Figure 7.2: Sketch of the optical setup to measure CTN.

The laser beam is split in three components: one is injected in an Electro-Optic Modulator (EOM) to be phase modulated; the other two are injected into two Acousto-Optic Modulators (AOMs) to shift their frequency, allowing the resonance of the HOMs within the cavity. At the output of the modulators the three beams, propagating in free space, are superposed, sent through a mode matching telescope and injected into the cavity.

As for the controls, the main laser is stabilized in frequency by locking the TEM00 mode to the folded cavity length using a Pound-Drever-Hall (PDH) loop in reflection, while the TEM02 and TEM20 are DC locked to the folded cavity. In addition to that, the two beams shifted in frequency are also stabilized in intensity actuating on the AOMs, by using Intensity Stabilization Servo (ISS) loops. Each loop for the two frequency shifted beams includes a Voltage-Controlled Oscillator (VCO). It is important to note that all the beams are in their fundamental mode all the time outside the folded cavity. The conversion of the frequency shifted beams into TEM02 and TEM20 takes place only inside the cavity. A key of the experiment is that the radius of curvature (RoC) of the input and output couplers of the cavity are slightly different. Therefore, by tuning the orientation of the input mirror, with respect to the output one, one can get the two HOMs co-resonating, together with the TEM00, inside the folded cavity. This happens since, in contrast to an ideal situation, the Transverse Mode Spacing (TMS) differs for them. In other words, the frequencies of the TEM20 and TEM02 modes are separated by a few MHz. Another key point is that the "fixed" resonant frequencies difference of these modes changes

due to the coating thermal noise.

7.3 Folded optical cavity

The optical cavity is installed in-vacuum at a temperature of 10 K. It is composed of the input and output couplers characterized by a nominal RoC of 50 mm, reflectance $R = r^2 = 0.9998$, transmittance $T = t^2 = 200$ ppm and losses $\mathcal{L} = 25 \cdot 10^{-6}$, where r and t stand for the amplitude reflection and transmission coefficients, respectively, with $0 \leq r$ and $t \leq 1$ and $r^2 + t^2 < 1$. The length of the cavity is $L = 97.6$ mm. The waist w of the beam is placed on the sample mirror to maximize the effect of the thermal noise (CTN $\propto 1/w$). In order to align the folded cavity, the mirrors are provided with actuators to adjust them in specific Degrees of Freedom (DoF):

- Sample Mirror: Transverse (T), Pitch (P) and Yaw (Y).
- Input Coupler: Longitudinal (L), Pitch (P) and Yaw (Y).
- Output Coupler: Longitudinal (L), Pitch (P) and Yaw (Y).

This is summarized in *Fig. 7.3*.

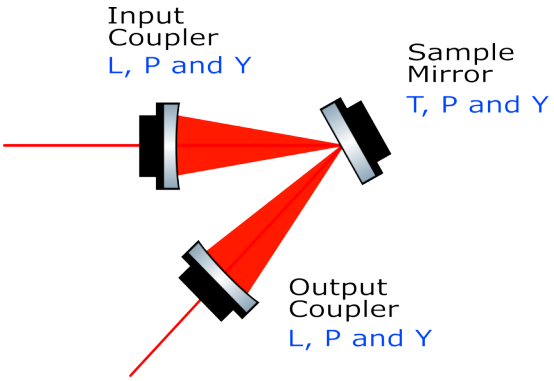

Figure 7.3: Controllable DoFs of the folded cavity

7.3.1 Simulations

With the objective of testing, understanding and speeding up the commissioning of the optical setup, the folded cavity has been simulated using FINESSE [122, 123] simulation tool. These simulations help to refine design parameters

and minimize risks. Using the design parameters of the optics and laser and a frequency modulation of $f_m = 15\,\text{MHz}$, we have checked the resonance condition, linewidth, finesse and cavity pole. The results are shown in *Fig. 7.4a* and *Fig. 7.4b*. *Fig. 7.4a* shows the transmitted, reflected and circulating powers around the resonance condition of the cavity: Everything works as expected. *Fig. 7.4b* shows the transfer function of the cavity, the cavity pole is at $f_c = 55981\,\text{Hz}$. The computed finesse with this tool is $\mathcal{F} = 13717$.

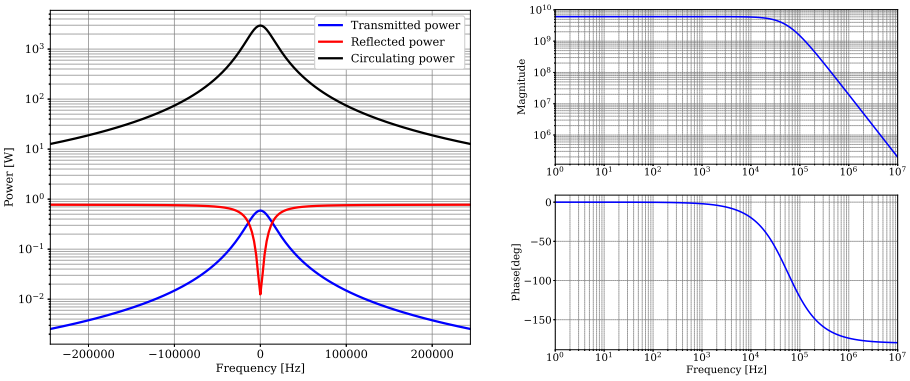

(a) (b)

Figure 7.4: (a) Transmitted (blue), circulating (black) and reflected (red) powers of the folded cavity for frequencies near the resonance frequency. (b) Transfer function of the cavity for the fundamental mode.

The main laser is stabilized in frequency by locking the TEM00 mode to the folded cavity length using a PDH loop in reflection: the error signal to lock the fundamental mode using the PDH technique can and must be optimized. *Fig. 7.5a* shows a preliminary study to find the optimal demodulation phase using the PDH technique: Depending on the demodulation phase, the error signal linear range can be maximized.

Since the RoC of the input and output couplers of the cavity are slightly different, by tuning the orientation of the input mirror with respect to the output mirror, one can get the three modes co-resonating inside the folded cavity. In the simulation, this effect is mimicked by adding astigmatism to one of the mirrors. *Fig. 7.5b* shows a preliminary study of modes co-resonating inside the folded cavity varying the level of astigmatism applied on the output coupler: scan of the cavity shows multiple peaks, corresponding to the resonance of the fundamental (TEM00) mode and the TEM 02/20 modes.

Fig.7.6 shows a photo of the assembled folded cavity.

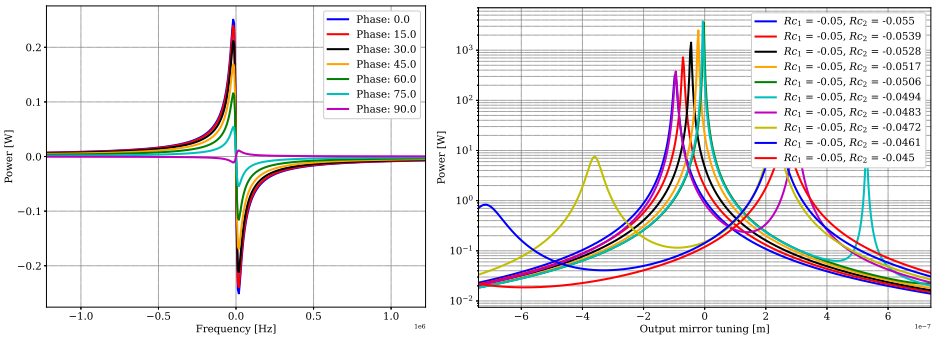

(a) (b)

Figure 7.5: (a) Optimization of PDH error signal: Scan of different demodulation phases. (b) Circulating power corresponding to the fundamental and HOMs for different astigmatism in the output mirror.

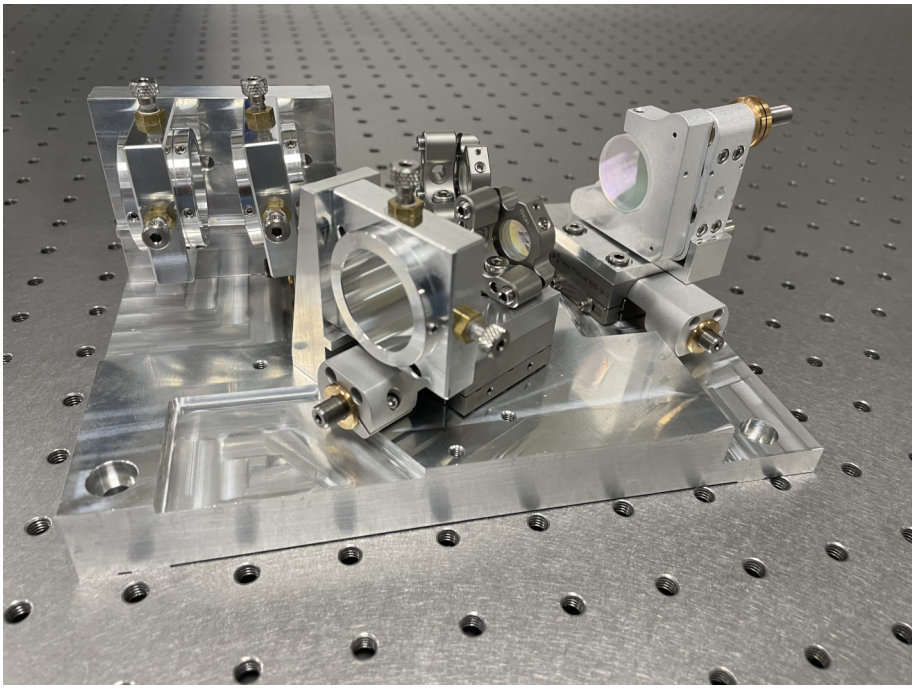

Figure 7.6: Photo of the folded cavity for the CTN experiment.

7.4 Control schemes

As mentioned before, the main laser is stabilized in frequency using the TEM00 resonating inside the cavity with a PDH loop as shown in *Fig. 7.7*: The error signal is derived from the reflection port of the folded cavity. A slow, large dynamic range loop is used to find the resonant region. A fast loop is used to continuously adjust the laser frequency to maintain the beam resonating in the cavity.

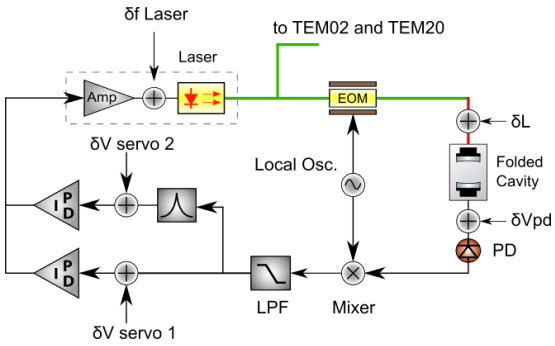

Figure 7.7: PDH loop diagram to lock the laser frequency on the cavity length.

The TEM02 and TEM20 modes are controlled using a technique known as DC locking. The error signals are derived from the intensity signals obtained from the cavity's transmission port. *Fig. 7.8* shows a sketch of the DC-locking: The signal in transmission from the folded cavity is used to keep the TEM02 and TEM20 resonating inside the cavity by controlling the RF frequency generators that drive the AOMs, which runs in parallel to the control of the loop for the TEM00.

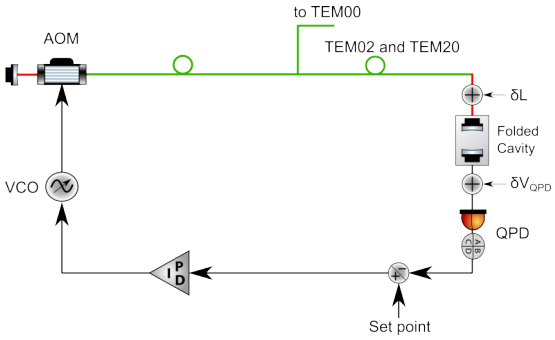

Figure 7.8: Block diagram of the DC locking scheme. TEM02 and TEM20 are frequency locked to the cavity.

In addition to DC locking, intensity stability loops are also used to maintain the stability of the optical intensity injected into the cavity. A pick-off from the beam the output of each AOM is used as error signal; the intensity is stabilized by modulating the amplitude of the VCO output by means of a RF mixer. The set up uses two intensity stabilization loops, one for TEM20 and other for TEM02. A sketch of one of the intensity stabilization loops is shown in *Fig. 7.9*.

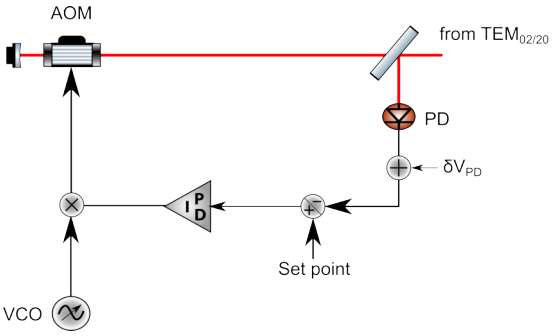

Figure 7.9: Block diagram of the intensity stability servo loop for the control of each HOM. TEM02 and TEM20 are stabilized in intensity with VCOs and AOMs.

Since beams shifted in frequency are frequency-locked to the TEM02 and TEM20 frequencies of the folded cavity, the CTN of the sample mirror can be measured by the frequency of the beat note between these beams. It's worth noting that the input coupler has been rotated with respect to the output coupler to establish a "fixed" difference between the TEM02 and TEM20 mode frequencies. This frequency difference is measured by analyzing the beat note signal of the two beams. Subsequently, fluctuations in the beat note are tracked using a Phase-Locked Loop (PLL) setup, as illustrated in Figure 7.10.

Finally, the oscillations in the beat signal frequency are transformed into a corresponding variation in cavity length by applying the conversion factor $L\lambda/c$, where L is the total length of folded cavity, λ is the wavelength of the laser light and c is the speed of light. The Amplitude Spectral Density (ASD) of this adjusted signal contains the coating thermal noise alongside fundamental and technical noises. These extra noises, apart from the CTN, will have to be reduced within the relevant frequency range of the CTN measurement to enhance the accuracy and reliability of the results.

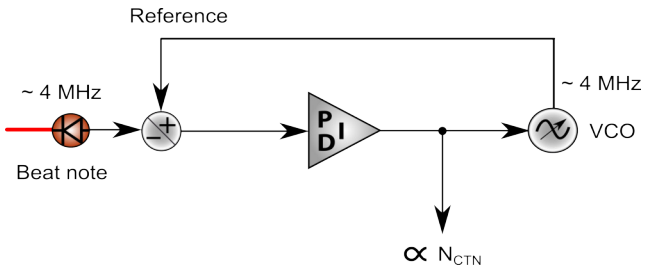

Figure 7.10: Phase Locked loop diagram to track the difference in frequencies of the beat note of the two HOMs.

7.5 Vibration isolation and cryogenic system

The optical bench is cooled down to 10 K using cooling wires connected to a Thermal Storage Unit (TSU), as shown in *Fig. 7.11*. Furthermore, in order to suppress undesirable vibrations and to minimize the vibration induced by the thermal link on it, the optical bench is suspended by three maraging steel wires. These wires are connected to three Geometric Anti Spring (GAS) filters, which are mounted on a movable top plate. These filters provide vertical vibration isolation to the optical bench [173]. Three flexible inverted pendulum (IP) legs support the top movable plate. Altogether, this entire system is situated inside a vacuum tank to reduce the fluctuations produced by air and the acoustic noise.

Mounted on the IP legs, the top plate has three Linear Variable Differential Transformers (LVDTs) circumferentially arranged. Each LVDT is colocated to a voice coil actuator to sense and adjust the position of the top plate. Thus, the optical bench can be adjusted in longitudinal, transverse and yaw DoFs. Moreover, each GAS filter unit also has one LVDT with a co-located voice coil actuator. Consequently it is possible to adjust the position of the optical bench in vertical, pitch and roll DoFs. To summarize, the optical bench can be moved in all six DoFs.

In order to sense the position of the optical bench for the alignment with respect to the input and output of the optical experiment, we will use a quadrant photo-diode installed along the path of the beam transmitted by the cavity.

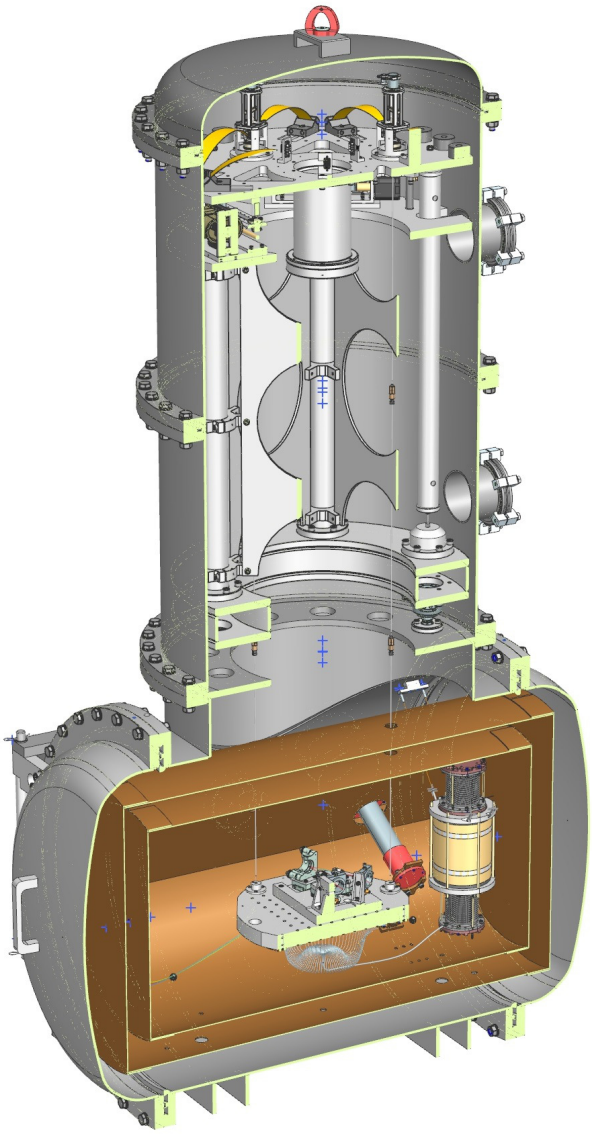

Figure 7.11: Vibration isolation system and cryogenics for the CTN optical bench.

7.6 Conclusions and future work

In the next steps of the project, the focus will shift to analyzing and reducing the impact of noises on the experimental setup. This will involve characterizing and quantifying various noise contributions such as seismic vibrations, thermal fluctuations, and laser stability to refine common mode rejection techniques.

Having a convenient optical setup for testing current and new coatings designed for future GW detectors would be a significant asset. This setup is specifically designed to work with a main laser wavelength of 1550 nm. Initially it will be tested at room temperature and later at cryogenic temperatures, to directly measure the coating thermal noise in the working conditions planned for the Einstein Telescope.

Closure

Up to 2015 the Universe was observable for us only through electromagnetic waves, high energy particles, and neutrinos. The direct detection of gravitational waves (GWs) opened another window to observe it.

This thesis has explored the capabilities of ground based interferometer to detect GWs, focusing on the Advanced Virgo Plus detector. The thesis first provides an overview of the foundation of gravitational radiation, setting the stage by emphasizing the importance of precise detection capabilities in GW observatories. It was revealed early on that noise is the principal antagonist in the tale of GW detection. Various sources of noise, from seismic disturbances to thermal fluctuations, quantum noise and most importantly, technical noises, were explored in detail. Through this exploration, the thesis not only highlighted the challenges faced by current GW detectors but also framed the necessity for innovative noise reduction techniques that were later discussed and implemented.

In response to these challenges, the study of the implementation of a Multiple-Input Multiple-Output (MIMO) control system in Advanced Virgo Plus was detailed. This sophisticated system was designed to enhance the detector's ability to discriminate against noise without compromising the integrity of GW signals. The effectiveness of the MIMO system was underscored by extensive simulations and real-time operational adjustments, which demonstrated its capacity to significantly reduce the re-injection of noise in the detector's data output. This was not just a theoretical enhancement but a practical upgrade to Advanced Virgo Plus operation. The next step will be to revisit all controllers in place to account for the intrinsic cross-couplings and reduce the re-injection of noise among all these degrees of freedom.

The thesis also delved into the implementation of a reliable MIMO system identification framework. This was tested for the Filter Cavity of the frequency dependent squeezing system, designed to reduce the impact of quantum noise.

The results from these experiments provided compelling evidence supporting the effectiveness of frequency dependent squeezing, facilitated by the MIMO control system identification and design. The next step will be to optimize these longitudinal control filters, as the current implementation ensures robustness but allows for improvement.

Further discussions included the development of a frequency domain noise budget tool, a framework for identifying and quantifying noises at various frequencies. This tool proved its capabilities for ongoing tests and assessments of the detector's sensitivity and will be essential in pinpointing specific noise sources that could be targeted for further mitigation. Being a real-time snapshot of the detector's noise, this tool can provide insights into the noises that limit or could limit the sensitivity of the detector, thereby enhancing signal clarity and detection confidence. This is, however, just the start, since many of the known noises have to be integrated and this will be a collaborative effort.

A portion of the research was dedicated to the design and preliminary work towards directly measuring coating thermal noise at cryogenic temperatures for future GW detectors. By designing and implementing a new experimental setup, the research can provide directions for the direct measurement of this critical noise source. Once ready, this setup will not only contribute to a better understanding of thermal noise characteristics but also to test new materials and technologies that could lead to improvements in future GW detectors. This is just a preliminary design to complete the experiments. In the near term, after the completion of the experiment, these direct measurements will clarify the directions to take for coatings in future GW detectors.

Looking forward, the thesis outlines several pathways for further research. The refinement of the MIMO control systems, the efficient system identification frameworks and the design of an optical setup to explore new materials for the coatings of the main mirrors of these detectors. The ongoing development of next-generation detectors, such as the proposed Einstein Telescope, will benefit also from the findings and methodologies developed in this research. The advancements made through this thesis in the field of GW detection represent a substantial progress toward the integration of advanced noise reduction techniques, sophisticated control systems, and innovative experimental setups, marking a key transition in our approach to observing the cosmos.

Summary

The detection of gravitational waves has marked a monumental leap in our ability to perceive and understand the Universe. These waves, ripples in space-time caused by massive celestial events like black-hole and neutron star mergers, were first predicted by Albert Einstein in his theory of general relativity. Their detection provides a new way of looking at the Universe, differing from traditional electromagnetic observations. However, capturing these faint signals requires extraordinarily sensitive instruments capable of distinguishing gravitational waves in a world of background noise. This thesis focuses on the challenges and advancements in detecting gravitational waves, emphasizing noise reduction techniques and sophisticated control systems to enhance the sensitivity of detectors.

What are gravitational waves?

Gravitational waves are distortions in space-time generated by massive astrophysical events, such as black hole mergers, neutron star collisions, and even from the Big Bang. These waves propagate outward from their source at the speed of light, carrying information about the dynamics of the process that generated them. The detection of gravitational waves allows scientists to study these colossal events, providing a new method of exploring the Universe that complements traditional electromagnetic observations.

How do we measure gravitational waves?

Interferometric gravitational-wave detectors are highly sophisticated instruments designed to measure the minute distortions in space-time caused by the passage of gravitational waves. The primary detectors in use today are large-scale interferometers like LIGO, Virgo and KAGRA. These detectors use the principle of a Michelson Interferometer enhanced with Fabry-Perot and Recycling Cavities to measure small changes in the distance between suspended

mirrors, caused by gravitational waves stretching and compressing the space-time.

- **Michelson Interferometer:** Splits a laser beam into two perpendicular paths. When gravitational waves pass through, they cause tiny changes in the length of these paths, which can be detected as shifts in the interference pattern of the recombined beams.
- **Fabry-Perot Cavity:** Increases the interaction time of the laser beams with gravitational waves by reflecting the beams multiple times between mirrors, enhancing the sensitivity of the detector.
- **Recycling Cavities:** Reuse the power that gets reflected back to the source and recycle and enhance the gravitational-wave signal.

Fig. 1 depicts two typical configurations of current gravitational-wave detectors. The use of additional optical cavities enhances the detector's sensitivity but adds complexity due to the introduction of extra degrees of freedom per added mirror.

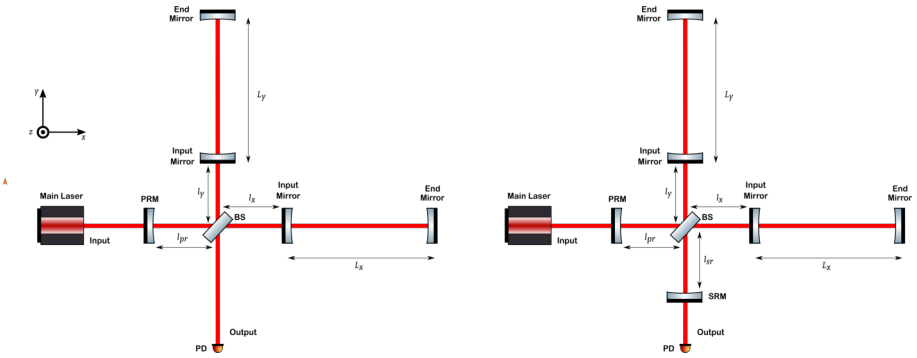

Figure 1: Left: Power Recycling Fabry-Perot Michelson interferometer. Right: Dual (power, PRM, and signal, SRM) Recycling Fabry-Perot Michelson interferometer.

The most important degree of freedom in these detectors is the Differential Arm (DARM) motion, which is sensitive to the passage of gravitational waves. For a passing GW, the detector produces an effect on the DARM degree of freedom $e_{DARM}(t)$ through the detector's response R. Ultimately, $e_{DARM}(t)$ is processed to get a reconstructed strain $h_{REC}(t)$ through a calibration process (R^{-1}). *Fig. 2* shows a sketch of detecting a gravitational-wave signal and producing a reconstructed strain. The different degrees of freedom of the detector

can be affected by various types of noise, and due to their intrinsic cross-couplings to the DARM degree of freedom, they can affect the measurement of gravitational-wave signals.

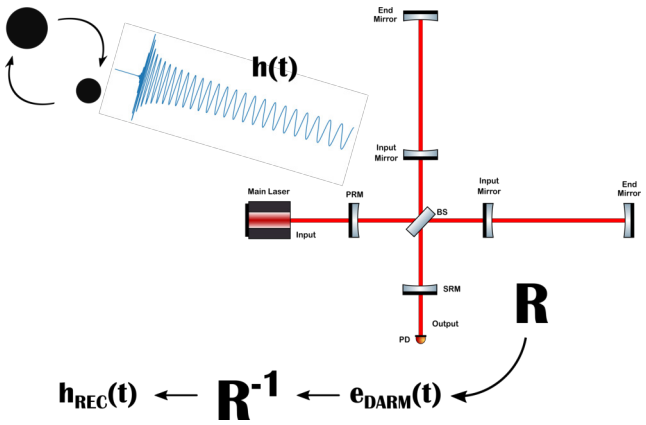

Figure 2: Diagram of a GW detection, from the astrophysical signal to the reconstructed strain for parameter estimation and data analysis.

Performance limitations of gravitational-wave detectors.

The detection of gravitational waves can be significantly affected by various types of noise that can obscure the faint signals. This thesis explores several key sources of noise and their impact on detector performance:

- **Seismic Noise:** Vibrations from the Earth's surface, such as those caused by natural seismic activity or human activities.
- **Thermal Noise:** Random fluctuations generated by the natural motion of particles at the atomic level within the materials of the detector.
- **Quantum Noise:** Inherent uncertainties in the measurement process due to quantum nature of light.
- **Technical Noises:** Imperfections in the instrumentation and control systems used in the detectors.

Multiple-Input Multiple-Output (MIMO) Dynamic Systems.

The operation of gravitational-wave detectors is a complex task. Multiple sensors and actuators located at various places of the interferometer are used to measure and assess the correct working point of the interferometric

detector. This thesis has a special focus on implementing a Multiple-Input Multiple-Output (MIMO) control system model for the Advanced Virgo Plus detector. This sophisticated model is used to design de-coupling filters which can significantly reduce the noise being re-injected by the control system of the detector. This practical upgrade not only improved the sensitivity of the Advanced Virgo Plus but also established a framework for future enhancements in gravitational-wave detection technology.

For this study, we have implemented a MIMO representation of the longitudinal degrees of freedom of Advanced Virgo Plus in the frequency domain. A sketch for the dynamics of the system with five inputs and five outputs, interconnected with one another, is depicted in *Fig. 3*; y_n, u_n, e_n and r_n indicate the output, input signal, error signal and reference of each "n" degree of freedom, respectively. Additionally for each degree of freedom, perturbations are denoted as d_n, noise injection signals are denoted as x_n and sensing noises are denoted as n_n^1. Furthermore, the cross-coupling terms of the plant are denoted as $G_{nm}(s)$ to represent a coupling from a degree of freedom "m" to another degree of freedom "n". Finally, filters and decoupling filters are depicted as $C_{nn}(s)$ and $C_{nm}(s)$, respectively.

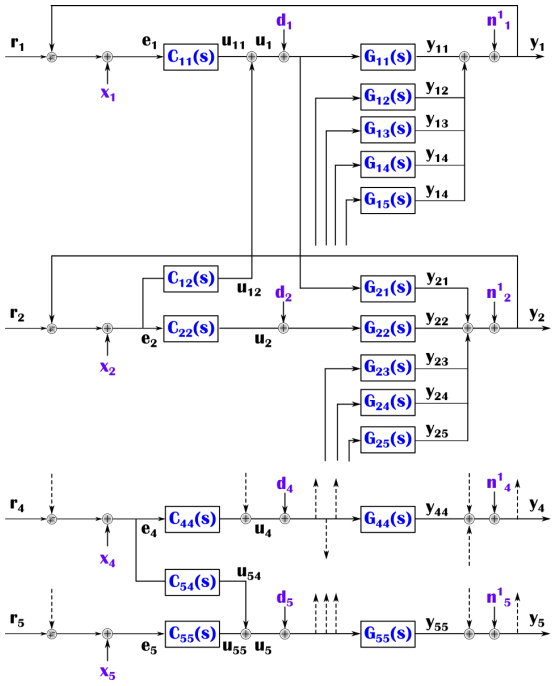

Figure 3: Visual representation of a 5×5 MIMO system. Some examples of decoupling filters are included.

Reducing technical noises.

This thesis explores techniques to reduce technical noises, focusing on the development of a reliable MIMO model and system identification framework. Additionally, using this model as a core, a noise budget tool was developed. In this tool several sources of noise can be included to understand the noises that can limit sensitivity in almost real-time. Furthermore, the MIMO model framework and the MIMO system identification approach was tested for the Filter Cavity of the Frequency Dependent Squeezing system. The results were promising, demonstrating the capability of the MIMO model to understand highly coupled systems across different degrees of freedom and to analyze its performance in a closed-loop configuration.

The research also delves into the development of optical setups for testing new materials and coatings designed to minimize thermal noise. These materials are crucial for future detectors, which aim to operate at higher sensitivities and at cryogenic temperatures.

Where do we go from here?

Looking ahead, the thesis outlines several key areas for future research and development. These include:

- **Characterization and Quantification of Noise:** Continued efforts to understand and measure various noise contributions, such as seismic vibrations, thermal fluctuations, and laser stability. This knowledge is vital for refining noise mitigation techniques.
- **System Identification:** Studying new approaches for system identification, especially for multiple-input multiple-output systems in closed-loop and with highly cross-coupled terms.
- **Optical Setup for Coating Tests:** Completion of the optical setup to test new coatings for future detectors. This setup will be tested both at room temperature and cryogenic temperatures. The goal is to measure coating thermal noise under conditions similar to those expected in the Einstein Telescope, a next-generation gravitational-wave observatory.

Samenvatting

De detectie van zwaartekrachtgolven heeft een monumentale sprong betekend in ons vermogen om het Universum waar te nemen en te begrijpen. Deze golven, rimpelingen in de ruimtetijd veroorzaakt door massieve kosmische gebeurtenissen zoals botsingen van zwarte gaten en neutronensterren, werden voor het eerst voorspeld door Albert Einstein in zijn algemene relativiteitstheorie. Hun detectie biedt een nieuwe manier om het Universum te bekijken, verschillend van traditionele elektromagnetische waarnemingen. Het vastleggen van deze zwakke signalen vereist echter buitengewoon gevoelige instrumenten die in staat zijn zwaartekrachtgolven te onderscheiden in een wereld vol achtergrondgeluid. Dit proefschrift richt zich op de uitdagingen en vooruitgangen in de detectie van zwaartekrachtgolven, met nadruk op technieken voor ruisonderdrukking en geavanceerde regelsystemen om de gevoeligheid van detectoren te verbeteren.

Wat zijn zwaartekrachtgolven?

Zwaartekrachtgolven zijn vervormingen in de ruimtetijd die worden gegenereerd door massieve astrofysische gebeurtenissen, zoals botsingen van zwarte gaten, botsingen van neutronensterren en zelfs door de oerknal. Deze golven verspreiden zich vanaf hun bron met de snelheid van het licht en dragen informatie over de dynamiek van het proces dat ze veroorzaakte. De detectie van zwaartekrachtgolven stelt wetenschappers in staat deze kolossale gebeurtenissen te bestuderen en biedt een nieuwe methode om het Universum te verkennen die traditionele elektromagnetische waarnemingen aanvult.

Hoe meten we zwaartekrachtgolven?

Interferometrische zwaartekrachtgolven-detectoren zijn zeer geavanceerde instrumenten die zijn ontworpen om de kleine vervormingen in de ruimtetijd te meten die worden veroorzaakt door de doorgang van zwaartekrachtgolven. De

primaire detectoren die tegenwoordig in gebruik zijn, zijn grootschalige interferometers zoals LIGO, Virgo en KAGRA. Deze detectoren gebruiken het principe van een Michelson-interferometer, verbeterd met Fabry-Perot- en recyclingcavities, om kleine veranderingen in de afstand tussen opgehangen spiegels te meten, veroorzaakt door zwaartekrachtgolven die de ruimtetijd rekken en samendrukken.

- **Michelson-interferometer:** Splitst een laserstraal in twee loodrechte paden. Wanneer zwaartekrachtgolven passeren, veroorzaken ze kleine veranderingen in de lengte van deze paden, die kunnen worden gedetecteerd als verschuivingen in het interferentiepatroon van de gerecombineerde stralen.

- **Fabry-Perot Cavity:** Verhoogt de interactie tijd van de laserstralen met zwaartekrachtgolven door de stralen meerdere keren tussen spiegels te reflecteren, wat de gevoeligheid van de detector verhoogt.

- **Recycling Cavities:** Hergebruiken de kracht die wordt teruggekaatst naar de bron en recyclen en versterken het zwaartekrachtgolf-signaal.

Fig. 1 toont twee typische configuraties van huidige zwaartekrachtgolvendetectoren. Het gebruik van extra optische cavities verhoogt de gevoeligheid van de detector, maar voegt complexiteit toe door de introductie van extra vrijheidsgraden per toegevoegde spiegel.

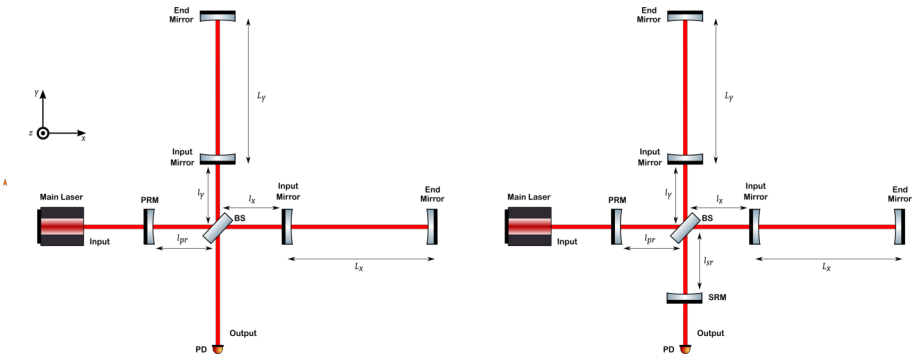

Figure 1: Links: Power Recycling FP Michelson-interferometer. Rechts: Dual Recycling FP Michelson-interferometer.

De belangrijkste vrijheidsgraad in deze detectoren is de Differential Arm (DARM) beweging, die gevoelig is voor de doorgang van zwaartekrachtgolven.

Voor een passerende zwaartekrachtgolf produceert de detector een effect op de DARM-vrijheidsgraad $e_{DARM}(t)$ via de respons van de detector R. Uiteindelijk wordt $e_{DARM}(t)$ verwerkt om een gereconstrueerde rek $h_{REC}(t)$ te verkrijgen via een kalibratie-proces (R^{-1}). *Fig. 2* toont een schets van het detecteren van een zwaartekrachtgolf-signaal en het produceren van een gereconstrueerde rek. De verschillende vrijheidsgraden van de detector kunnen worden beïnvloed door verschillende soorten ruis en door hun intrinsieke kruisverstrengeling met de DARM-vrijheidsgraad kunnen ze de meting van zwaartekrachtgolf-signalen beïnvloeden.

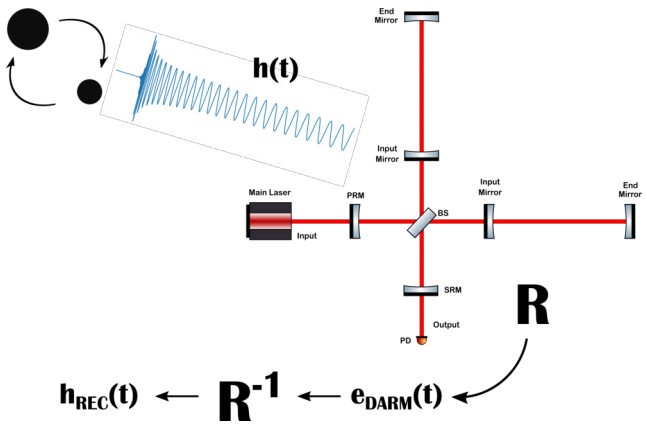

Figure 2: Diagram van een zwaartekrachtgolf-detectie, van het astrofysische signaal tot de gereconstrueerde rek voor parameter estimatie en data-analyse.

Prestatiebeperkingen van zwaartekrachtgolvendetectoren.

De detectie van zwaartekrachtgolven kan aanzienlijk worden beïnvloed door verschillende soorten ruis die de zwakke signalen kunnen verdoezelen. Dit proefschrift onderzoekt verschillende belangrijke bronnen van ruis en hun impact op de prestaties van de detector:

- **Seismische ruis:** Trillingen van het aardoppervlak, zoals die veroorzaakt door natuurlijke seismische activiteit of menselijke activiteiten.
- **Thermische ruis:** Willekeurige fluctuaties die worden veroorzaakt door de natuurlijke beweging van deeltjes op atomair niveau binnen de materialen van de detector.
- **Kwantuumruis:** Inherente onzekerheden in het meetproces vanwege de kwantum natuur van licht.

- **Technische ruis:** Onvolkomenheden in de instrumentatie en regelsystemen die in de detectoren worden gebruikt.

Multiple-Input Multiple-Output (MIMO) dynamische systemen. Het bedienen van zwaartekrachtgolven-detectoren is een complexe taak. Meerdere sensoren en actuatoren, geplaatst op verschillende locaties van de interferometer, worden gebruikt om het juiste werkpunt van de interferometrische detector te meten en te beoordelen. Dit proefschrift richt zich in het bijzonder op de implementatie van een Multiple-Input Multiple-Output (MIMO) regelsysteemmodel voor de Advanced Virgo Plus detector. Dit geavanceerde model wordt gebruikt om ontkoppelingsfilters te ontwerpen die de door het regelsysteem van de detector gereïnjecteerde ruis aanzienlijk kunnen verminderen. Deze praktische upgrade verbeterde niet alleen de gevoeligheid van de Advanced Virgo Plus, maar stelde ook een raamwerk vast voor toekomstige verbeteringen in de zwaartekrachtgolf-detectie technologie.

Voor deze studie hebben we een MIMO-representatie van de longitudinale vrijheidsgraden van Advanced Virgo Plus in het frequentiedomein geïmplementeerd. Een schets van de dynamiek van het systeem met vijf ingangen en vijf uitgangen, onderling met elkaar verbonden, wordt weergegeven in *Fig. 3*; y_n, u_n, e_n en r_n geven respectievelijk de uitgang, het ingangssignaal, het foutsignaal en de referentie van elke "n" vrijheidsgraad aan. Bovendien worden voor elke vrijheidsgraad verstoringen aangeduid als d_n, ruisinjectiesignalen als x_n en sensor ruis als n_n^1. Verder worden de kruisverstrengelingstermen van de plant aangeduid als $G_{nm}(s)$ om een koppeling van een vrijheidsgraad "m" naar een andere vrijheidsgraad "n" te vertegenwoordigen. Tot slot worden filters en ontkoppeling filters weergegeven als $C_{nn}(s)$ en $C_{nm}(s)$, respectievelijk.

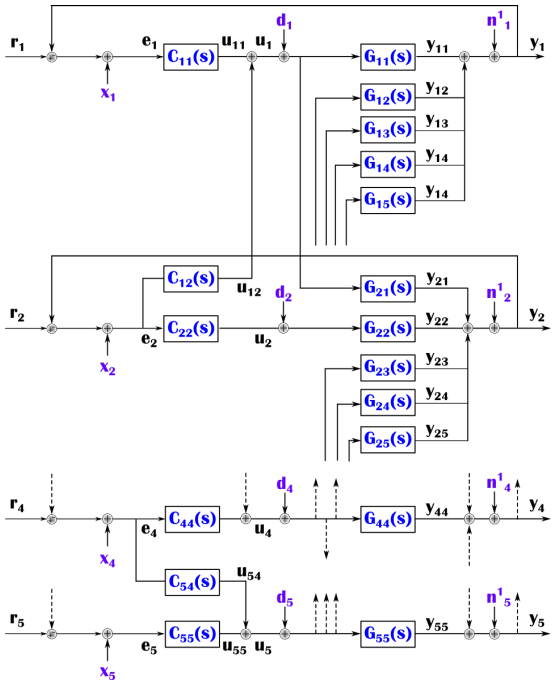

Figure 3: Visuele representatie van een 5×5 MIMO-systeem. Enkele voorbeelden van ontkoppeling filters zijn inbegrepen.

Verminderen van technische ruis.

Dit proefschrift onderzoekt technieken om technische ruis te verminderen, met een focus op de ontwikkeling van een betrouwbaar MIMO-model en systeemidentificatiekader. Daarnaast werd, met dit model als kern, een ruisbudgettool ontwikkeld. In deze tool kunnen verschillende ruisbronnen worden opgenomen om bijna real-time de ruis te begrijpen die de gevoeligheid kan beperken. Bovendien werd het MIMO-modelkader en de MIMO-systeemidentificatieaanpak getest voor de Filter Cavity van het Frequency Dependent Squeezing systeem. De resultaten waren veelbelovend en toonden de capaciteit van het MIMO-model aan om sterk gekoppelde systemen over verschillende vrijheidsgraden te begrijpen en de prestaties ervan in een gesloten-lusconfiguratie te analyseren.

Het onderzoek gaat ook in op de ontwikkeling van optische opstellingen voor het testen van nieuwe materialen en coatings die zijn ontworpen om thermische ruis te minimaliseren. Deze materialen zijn cruciaal voor toekomstige detectoren, die streven naar een hogere gevoeligheid en werking bij cryogene temperaturen.

Waar gaan we vanaf hier naartoe?

Vooruitkijkend schetst het proefschrift verschillende belangrijke gebieden voor toekomstig onderzoek en ontwikkeling. Deze omvatten:

- **Karakterisering en Kwantificering van Ruis:** Voortdurende inspanningen om verschillende ruisbijdragen te begrijpen en te meten, zoals seismische trillingen, thermische fluctuaties en laserstabiliteit. Deze kennis is van vitaal belang voor het verfijnen van technieken voor ruisonderdrukking.
- **Systeemidentificatie:** Het bestuderen van nieuwe benaderingen voor systeemidentificatie, vooral voor multiple-input multiple-output systemen in gesloten-lus en met sterk gekoppelde termen.
- **Optische Opstelling voor Coatingtests:** Voltooiing van de optische opstelling om nieuwe coatings voor toekomstige detectoren te testen. Deze opstelling zal worden getest bij zowel kamertemperatuur als cryogene temperaturen. Het doel is om de thermische ruis van de coating te meten onder omstandigheden die vergelijkbaar zijn met die verwacht worden in de Einstein Telescope, een next-generation zwaartekrachtgolven-observatorium.

Bibliography

[1] B P Abbott et al. LIGO: the laser interferometer gravitational-wave observatory. *Reports on Progress in Physics*, 72(7):076901, jun 2009.

[2] B. P. Abbott et al. Observation of gravitational waves from a binary black hole merger. *Phys. Rev. Lett.*, 116:061102, Feb 2016.

[3] Albert Einstein. Die Feldgleichungen der Gravitation. *Sitzungsberichte der Königlich Preußischen Akademie der Wissenschaften (Berlin*, pages 844–847, January 1915.

[4] Fausto Acernese et al. Advanced Virgo: a second-generation interferometric gravitational wave detector. *Classical and Quantum Gravity*, 32:024001, 01 2015.

[5] B. P. Abbott et al. Gw170817: Observation of gravitational waves from a binary neutron star inspiral. *Phys. Rev. Lett.*, 119:161101, Oct 2017.

[6] David J. Thompson and Colleen A. Wilson-Hodge. Fermi Gamma-ray Space Telescope. 10 2022.

[7] Pietro Ubertini and Angela Bazzano. The INTErnational Gamma Ray Astrophysics Laboratory: INTEGRAL Highlights. *Nucl. Instrum. Meth. A*, 742:47–55, 2014.

[8] B. P. Abbott et al. Multi-messenger observations of a binary neutron star merger*. *The Astrophysical Journal Letters*, 848(2):L12, oct 2017.

[9] I. Newton. *Philosophiae naturalis principia mathematica*. Early English books online. Jussu Societas Regiæ ac typis Josephi Streater, prostant venales apud Sam. Smith, 1687.

[10] Albert Einstein. Zur Elektrodynamik bewegter Körper. *Annalen der Physik 17: 891*, pages 891–921, June 1905.

[11] Katerina Chatziioannou, Nicolás Yunes, and Neil Cornish. Model-independent test of general relativity: An extended post-einsteinian framework with complete polarization content. *Phys. Rev. D*, 86:022004, Jul 2012.

[12] Éanna É Flanagan and Scott A Hughes. The basics of gravitational wave theory. *New Journal of Physics*, 7(1):204, sep 2005.

[13] Sidney Bergh. *The Galaxies of the Local Group*. Cambridge Astrophysics. Cambridge University Press, 2000.

[14] M. Bailes et al. Gravitational-wave physics and astronomy in the 2020s and 2030s. *Nature Rev. Phys.*, 3(5):344–366, 2021.

[15] Frans Pretorius. Evolution of binary black-hole spacetimes. *Phys. Rev. Lett.*, 95:121101, Sep 2005.

[16] R. A. Hulse and J. H. Taylor. Discovery of a pulsar in a binary system. , 195:L51–L53, January 1975.

[17] Joel M. Weisberg and Joseph H. Taylor. The Relativistic binary pulsar B1913+16. *ASP Conf. Ser.*, 302:93, 2003.

[18] S. W. Hawking and W. Israel, editors. *Three hundred years of gravitation*. 1987.

[19] Reinhard Prix. *Gravitational Waves from Spinning Neutron Stars*, pages 651–685. Springer Berlin Heidelberg, Berlin, Heidelberg, 2009.

[20] Keith Riles. Searches for continuous-wave gravitational radiation. *Living Rev. Rel.*, 26(1):3, 2023.

[21] Nelson Christensen. Stochastic Gravitational Wave Backgrounds. *Rept. Prog. Phys.*, 82(1):016903, 2019.

[22] Bruce Allen and Joseph D. Romano. Detecting a stochastic background of gravitational radiation: Signal processing strategies and sensitivities. *Phys. Rev. D*, 59:102001, Mar 1999.

[23] Michele Maggiore, Chris Van Den Broeck, Nicola Bartolo, Enis Belgacem, Daniele Bertacca, Marie Anne Bizouard, Marica Branchesi, Sebastien Clesse, Stefano Foffa, Juan García-Bellido, Stefan Grimm, Jan Harms,

Tanja Hinderer, Sabino Matarrese, Cristiano Palomba, Marco Peloso, Angelo Ricciardone, and Mairi Sakellariadou. Science case for the Einstein Telescope. *Journal of Cosmology and Astroparticle Physics*, 2020(03):050, mar 2020.

[24] B. S. Sathyaprakash and Bernard F. Schutz. Physics, astrophysics and cosmology with gravitational waves. *Living Reviews in Relativity*, 12, March 2009.

[25] B P Abbott et al. A guide to LIGO–Virgo detector noise and extraction of transient gravitational-wave signals. *Classical and Quantum Gravity*, 37(5):055002, feb 2020.

[26] F.J. Harris. On the use of windows for harmonic analysis with the discrete fourier transform. *Proceedings of the IEEE*, 66(1):51–83, 1978.

[27] John G. Proakis and Dimitris G. Manolakis. *Digital Signal Processing (3rd Ed.): Principles, Algorithms, and Applications*. Prentice-Hall, Inc., USA, 1996.

[28] B. P. Abbott et al. GW170814: A three-detector observation of gravitational waves from a binary black hole coalescence. *Phys. Rev. Lett.*, 119:141101, Oct 2017.

[29] J. Veitch, V. Raymond, B. Farr, W. Farr, P. Graff, S. Vitale, B. Aylott, K. Blackburn, N. Christensen, M. Coughlin, W. Del Pozzo, F. Feroz, J. Gair, C.-J. Haster, V. Kalogera, T. Littenberg, I. Mandel, R. O'Shaughnessy, M. Pitkin, C. Rodriguez, C. Röver, T. Sidery, R. Smith, M. Van Der Sluys, A. Vecchio, W. Vousden, and L. Wade. Parameter estimation for compact binaries with ground-based gravitational-wave observations using the LALInference software library. *Phys. Rev. D*, 91:042003, Feb 2015.

[30] R. Abbott et al. Observation of gravitational waves from two neutron star–black hole coalescences. *The Astrophysical Journal Letters*, 915(1):L5, jun 2021.

[31] R. Abbott and others. Gw190412: Observation of a binary-black-hole coalescence with asymmetric masses. *Phys. Rev. D*, 102:043015, Aug 2020.

[32] Lionel London, Sebastian Khan, Edward Fauchon-Jones, Cecilio García, Mark Hannam, Sascha Husa, Xisco Jiménez-Forteza, Chinmay Kalaghatgi, Frank Ohme, and Francesco Pannarale. First higher-multipole model of gravitational waves from spinning and coalescing black-hole binaries. *Phys. Rev. Lett.*, 120:161102, Apr 2018.

[33] R. Abbott and others. GW190521: A binary black hole merger with a total mass of 150 $M_{\odot}$. *Phys. Rev. Lett.*, 125:101102, Sep 2020.

[34] Jonathan R. Gair, Ilya Mandel, M. Coleman Miller, and Marta Volonteri. Exploring intermediate and massive black-hole binaries with the Einstein Telescope. *General Relativity and Gravitation*, 43(2):485–518, February 2011.

[35] R. Abbott et al. GWTC-3: Compact binary coalescences observed by LIGO and Virgo during the second part of the third observing run. 11 2021.

[36] Charles Meegan, Giselher Lichti, P. N. Bhat, Elisabetta Bissaldi, Michael S. Briggs, Valerie Connaughton, Roland Diehl, Gerald Fishman, Jochen Greiner, Andrew S. Hoover, Alexander J. van der Horst, Andreas von Kienlin, R. Marc Kippen, Chryssa Kouveliotou, Sheila McBreen, W. S. Paciesas, Robert Preece, Helmut Steinle, Mark S. Wallace, Robert B. Wilson, and Colleen Wilson-Hodge. The Fermi Gamma-ray Burst Monitor. , 702(1):791–804, September 2009.

[37] A. Goldstein, P. Veres, E. Burns, M. S. Briggs, R. Hamburg, D. Kocevski, C. A. Wilson-Hodge, R. D. Preece, S. Poolakkil, O. J. Roberts, C. M. Hui, V. Connaughton, J. Racusin, A. von Kienlin, T. Dal Canton, N. Christensen, T. Littenberg, K. Siellez, L. Blackburn, J. Broida, E. Bissaldi, W. H. Cleveland, M. H. Gibby, M. M. Giles, R. M. Kippen, S. McBreen, J. McEnery, C. A. Meegan, W. S. Paciesas, and M. Stanbro. An ordinary short gamma-ray burst with extraordinary implications: Fermi-GBM detection of GRB 170817A. *The Astrophysical Journal Letters*, 848(2):L14, oct 2017.

[38] V. Savchenko et al. INTEGRAL detection of the first prompt gamma-ray signal coincident with the gravitational-wave event GW170817. *The Astrophysical Journal Letters*, 848(2):L15, oct 2017.

[39] C. Winkler, O. Pace, and S. Volonté. INTEGRAL - the International Gamma-Ray Astrophysics Laboratory. *ESA Journal*, 17(3):207–223, January 1993.

[40] B. P. Abbott et al. Gravitational waves and gamma-rays from a binary neutron star merger: GW170817 and GRB 170817A. *The Astrophysical Journal Letters*, 848(2):L13, oct 2017.

[41] F. Di Mille, K. Boutsia, L. Infante, D. Osip, P. Palunas, and M. Phillips. Las Campanas Observatory. In *Observatory Operations: Strategies, Processes, and Systems VII*, volume 10704 of *Society of Photo-Optical Instrumentation Engineers (SPIE) Conference Series*, page 107041S, July 2018.

[42] Daniel E. Holz and Scott A. Hughes. Using gravitational-wave standard sirens. *The Astrophysical Journal*, 629(1):15, aug 2005.

[43] A. Palmese, C. R. Bom, S. Mucesh, and W. G. Hartley. A standard siren measurement of the Hubble constant using gravitational-wave events from the first three LIGO/Virgo observing runs and the DESI Legacy Survey. *The Astrophysical Journal*, 943(1):56, jan 2023.

[44] S. J. Smartt et al. A kilonova as the electromagnetic counterpart to a gravitational-wave source. , 551(7678):75–79, November 2017.

[45] M.G. Aartsen et al. The IceCube Neutrino Observatory: instrumentation and online systems. *Journal of Instrumentation*, 12(03):P03012, mar 2017.

[46] G. Giacomelli. The ANTARES Neutrino Telescope. In Viktor Begun, László L. Jenkovszky, and Aleksander Polański, editors, *Progress in High-Energy Physics and Nuclear Safety*, pages 129–137, Dordrecht, 2009. Springer Netherlands.

[47] The Pierre Auger Cosmic Ray Observatory. *Nuclear Instruments and Methods in Physics Research Section A: Accelerators, Spectrometers, Detectors and Associated Equipment*, 798:172–213, 2015.

[48] J. Weber. Detection and generation of gravitational waves. *Physical Review*, 117(1):306–313, 1960.

[49] W. O. Hamilton, W. W. Johnson, O. D. Aguiar, and E. Mauceli. The ALLEGRO gravitational wave detector: performance and prospects. In *Proceedings of the 7th Marcel Grossmann Meeting on recent developments in theoretical and experimental general relativity, gravitation, and relativistic field theories*, pages 1609–1615. World Scientific, 1994.

[50] A. Vinante, L. Baggio, M. Bignotto, M. Bonaldi, M. Cerdonio, L. Conti, P. Falferi, N. Liguori, S. Longo, R. Mezzena, A. Ortolan, G. A. Prodi, F. Salemi, L. Taffarello, G. Vedovato, S. Vitale, and J. P. Zendri. The AURIGA detector: 2005 operation with a high sensitivity configuration. *Classical and Quantum Gravity*, 23(8):S103, 2006.

[51] D. G. Blair, E. N. Ivanov, M. E. Tobar, P. J. Turner, F. van Kann, and I. S. Heng. High sensitivity gravitational wave antenna with parametric transducer readout. *Physical Review Letters*, 74(12):1908, 1995.

[52] Rainer Weiss. Electromagnetically coupled broadband gravitational antenna. Quarterly Progress Report 105, Massachusetts Institute of Technology, Research Laboratory of Electronics, April 1972. Available at MIT Libraries.

[53] Kimio Tsubono. 300-m laser interferometer gravitational wave detector (TAMA300) in Japan. *First Edoardo Amaldi Conference on Gravitational Wave Experiments*, pages 112–114, 1995. Conference Proceedings.

[54] K Danzmann and the GEO Team. GEO 600 a 600-m laser interferometric gravitational wave antenna. In *First Edoardo Amaldi Conference on Gravitational Wave Experiments*, pages 100–111. World Scientific, 1994.

[55] Yoichi Aso, Yuta Michimura, Kentaro Somiya, Masaki Ando, Osamu Miyakawa, Takanori Sekiguchi, Daisuke Tatsumi, Hiroaki Yamamoto, and the KAGRA Collaboration. Interferometer design of the KAGRA gravitational wave detector. *Physical Review D*, 88(4):043007, 2013.

[56] Albert A. Michelson and Edward W. Morley. On the relative motion of the earth and the luminiferous ether. *American Journal of Science*, 34(203):333–345, 1887.

[57] Jean-Yves Vinet, Brian Meers, Catherine Nary Man, and Alain Brillet. Optimization of long-baseline optical interferometers for gravitational-wave detection. *Phys. Rev. D*, 38:433–447, Jul 1988.

[58] G. Vajente. Lectures on gravitational waves experimental techniques. TRISEP 2018 - Tri-Institutional Summer School on Elementary Particles, 2018. Waterloo, ON, Canada.

[59] R. Weiss and J. Bragg. Interferometer techniques for gravitational-wave detection. *Physical Review Letters*, 24(12):737–738, 1970.

[60] Michele Maggiore. *Gravitational Waves. Vol. 1: Theory and Experiments*. Oxford University Press, 2007.

[61] Julia Casanueva Diaz. *Control of the gravitational wave interferometric detector Advanced Virgo*. Theses, Université Paris Saclay (COmUE), September 2017.

[62] Ilaria Nardecchia. Detecting Gravitational Waves with Advanced Virgo. *Galaxies*, 10(1):28, 2022.

[63] Katsuhiko Ogata. *Modern Control Engineering*. Prentice Hall, 5 edition, 2010.

[64] Eric D. Black. An introduction to Pound–Drever–Hall laser frequency stabilization. *American Journal of Physics*, 69:79–87, 2001.

[65] Anthony E. Siegman. *Lasers*. University Science Books, 1986.

[66] The Virgo Collaboration. Advanced Virgo Plus Phase I - Design Report. VIR-0596A-19 URL: `https://tds.virgo-gw.eu/ql/?c=14430`, 6 2019.

[67] B Boom. *Acceleration sensing at the nano-g level: Development and characterisation of low-noise microseismometers for next generation gravitational wave detectors*. PhD thesis, 2020.

[68] Soumen Koley et al. Design and implementation of a seismic Newtonian noise cancellation system for the Virgo gravitational-wave detector. *Eur. Phys. J. Plus*, 139(1):48, 2024.

[69] M.K.M. Bader. *Seismic and Newtonian noise modeling for Advanced Virgo and Einstein Telescope*. PhD-Thesis - Research and graduation internal, Vrije Universiteit Amsterdam, 2021.

[70] A. Einstein. Über die von der molekularkinetischen Theorie der Wärme geforderte Bewegung von in ruhenden Flüssigkeiten suspendierten Teilchen. *Annalen Phys.*, 322(8):549–560, 1905.

[71] Herbert B. Callen and Theodore A. Welton. Irreversibility and generalized noise. *Phys. Rev.*, 83:34–40, Jul 1951.

[72] F. Bondu and J. Y. Vinet. Mirror thermal noise in interferometric gravitational wave detectors. *Phys. Lett. A*, 198:74–78, 1995.

[73] Yu. Levin. Internal thermal noise in the LIGO test masses: A direct approach. *Phys. Rev. D*, 57:659–663, Jan 1998.

[74] Eric D. Black et al. Direct observation of broadband coating thermal noise in a suspended interferometer. *Phys. Lett. A*, 328:1–5, 2004.

[75] S. Gras and M. Evans. Direct measurement of coating thermal noise in optical resonators. *Phys. Rev. D*, 98:122001, Dec 2018.

[76] M Mehmet and H Vahlbruch. High-efficiency squeezed light generation for gravitational wave detectors. *Classical and Quantum Gravity*, 36(1):015014, dec 2018.

[77] D. Z. Anderson. Alignment of resonant optical cavities. , 23(17):2944–2949, September 1984.

[78] Euan Morrison, Brian J. Meers, David I. Robertson, and Henry Ward. Automatic alignment of optical interferometers. *Appl. Opt.*, 33(22):5041–5049, 1994.

[79] R. Maggiore. *Adventures in Gravitational Wave Detector Control: A Round-Trip Journey.* PhD-Thesis - Research and graduation internal, Vrije Universiteit Amsterdam, 2024.

[80] F. Acernese et al. Advanced Virgo: a second-generation interferometric gravitational wave detector. *Classical and Quantum Gravity*, 32(2):024001, January 2015. Submitted to Classical and Quantum Gravity. 53 pages, 29 figures.

[81] K. Izumi and D. Sigg. Frequency response of the aLIGO interferometer: part1. LIGO Technical Report LIGO-T1500325–v3, Laser Interferometer Gravitational-Wave Observatory, 2016.

[82] S Hild, H Grote, J Degallaix, S Chelkowski, K Danzmann, A Freise, M Hewitson, J Hough, H Lück, M Prijatelj, K A Strain, J R Smith, and B Willke. DC-readout of a signal-recycled gravitational wave detector. *Classical and Quantum Gravity*, 26(5):055012, feb 2009.

[83] A Rocchi, E Coccia, V Fafone, V. Malvezzi, Y Minenkov, and L. Sperandio. Thermal effects and their compensation in Advanced Virgo. *Journal of Physics: Conference Series*, 363, 06 2012.

[84] L van der Schaaf. *The Phase Cameras of Advanced Virgo*. PhD thesis, 2020.

[85] R. Dolesi, M. Hueller, D. Nicolodi, D. Tombolato, S. Vitale, P. J. Wass, W. J. Weber, M. Evans, P. Fritschel, R. Weiss, J. H. Gundlach, C. A. Hagedorn, S. Schlamminger, G. Ciani, and A. Cavalleri. Brownian force noise from molecular collisions and the sensitivity of advanced gravitational wave observatories. *Phys. Rev. D*, 84:063007, Sep 2011.

[86] M. Punturo et al. The Einstein Telescope: a third-generation gravitational wave observatory. *Classical and Quantum Gravity*, 27(19):194002, October 2010.

[87] D. Reitze, R. Adhikari, S. Ballmer, and et al. The Cosmic Explorer Project: Current Progress and Plans for Gravitational-wave Astronomy and Fundamental Physics. *Journal of Physics: Conference Series*, 610:012021, 2015.

[88] B. S. Sathyaprakash, M. Abernathy, et al. The Einstein Telescope: A Third-Generation Gravitational Wave Observatory. *Classical and Quantum Gravity*, 29(12):124013, 2012.

[89] Cosmic Explorer Collaboration. The Cosmic Explorer: Exploring the universe with gravitational waves. *Physical Review D*, 100:084034, 2019.

[90] Samuel Rowlinson, Artemiy Dmitriev, Aaron W. Jones, Teng Zhang, and Andreas Freise. Feasibility study of beam-expanding telescopes in the interferometer arms for the Einstein Telescope. *Phys. Rev. D*, 103:023004, Jan 2021.

[91] Vicky Kalogera et al. The Next Generation Global Gravitational Wave Observatory: The Science Book. working paper or preprint, November 2021.

[92] J. Baker and Joan Centrella. Impact of LISA's low frequency sensitivity on observations of massive black hole mergers. *Class. Quant. Grav.*, 22:S355–S362, 2005.

[93] Pau Amaro-Seoane et al. LISA: The space-based gravitational wave observatory. *Living Reviews in Relativity*, 21(1):4, 2018.

[94] European Space Agency. ESA's LISA mission selected for implementation. *ESA*, Bulletin(162):22, 2015.

[95] Jose María Ezquiaga and Miguel Zumalacarregui. Dark energy in light of multi-messenger gravitational-wave astronomy. *Frontiers in Astronomy and Space Sciences*, 5, 12 2018.

[96] M. Armano et al. LISA Pathfinder: mission and status. *Classical and Quantum Gravity*, 33(19):195001, September 2016.

[97] B. P. Abbott et al. Observation of gravitational waves from a binary black hole merger. *Phys. Rev. Lett.*, 116:061102, Feb 2016.

[98] B P Abbott et al. LIGO: the laser interferometer gravitational-wave observatory. *Reports on Progress in Physics*, 72(7):076901, jun 2009.

[99] B. P. Abbott et al. Binary black hole mergers in the first Advanced LIGO observing run. *Phys. Rev. X*, 6:041015, Oct 2016.

[100] B. P. Abbott et al. GWTC-1: A gravitational-wave transient catalog of compact binary mergers observed by LIGO and Virgo during the first and second observing runs. *Phys. Rev. X*, 9:031040, Sep 2019.

[101] B. P. Abbott et al. GW170817: Observation of gravitational waves from a binary neutron star inspiral. *Phys. Rev. Lett.*, 119:161101, Oct 2017.

[102] B. P. Abbott et al. Multi-messenger observations of a binary neutron star merger. *The Astrophysical Journal*, 848(2):L12, oct 2017.

[103] R. Abbott et al. GWTC-2: Compact binary coalescences observed by LIGO and Virgo during the first half of the third observing run. *Phys. Rev. X*, 11:021053, Jun 2021.

[104] R. Abbott et al. GWTC-3: Compact binary coalescences observed by LIGO and Virgo algo during the second part of the third observing run, 11 2021. submitted to Phys Rev X. arXiv preprint 2111.03606.

[105] B. Abbott et al. Prospects for observing and localizing gravitational-wave transients with advanced LIGO, advanced Virgo and KAGRA. *Living Reviews in Relativity*, 21, 12 2018.

[106] F Acernese et al. Properties of seismic noise at the Virgo site. *Classical and Quantum Gravity*, 21(5):S433, feb 2004.

[107] M Beccaria et al. Relevance of Newtonian seismic noise for the Virgo interferometer sensitivity. *Classical and Quantum Gravity*, 15(11):3339, nov 1998.

[108] F. Acernese et al. Quantum backaction on kg-scale mirrors: Observation of radiation pressure noise in the Advanced Virgo detector. *Phys. Rev. Lett.*, 125:131101, Sep 2020.

[109] P. Amico, L. Carbone, C. Cattuto, L. Gammaitoni, M. Punturo, F. Travasso, and H. Vocca. Thermal noise limit in the Virgo mirror suspension. *Nuclear Instruments and Methods in Physics Research Section A: Accelerators, Spectrometers, Detectors and Associated Equipment*, 461(1):297–299, 2001. 8th Pisa Meeting on Advanced Detectors.

[110] F. Acernese et al. Increasing the astrophysical reach of the Advanced Virgo detector via the application of squeezed vacuum states of light. *Phys. Rev. Lett.*, 123:231108, Dec 2019.

[111] M. Punturo, Matthew Abernathy, Fausto Acernese, Bruce Allen, Nils Andersson, K. Arun, Fabrizio Barone, B. Barr, M. Barsuglia, Mark Beker, Nicola Beveridge, S. Birindelli, Snehasish Bose, L. Bosi, S. Braccini, C Bradaschia, Tomasz Bulik, Enrico Calloni, Giancarlo Cella, and Kazami Yamamoto. The Einstein Telescope: A third-generation gravitational wave observatory. *Classical and Quantum Gravity*, 27, 10 2010.

[112] Graham C. Goodwin, Stefan F. Graebe, and Mario E. Salgado. *Control System Design*. Prentice Hall PTR, USA, 1st edition, 2000.

[113] Grant David Meadors, Keita Kawabe, and Keith Riles. Increasing LIGO sensitivity by feedforward subtraction of auxiliary length control noise. *Classical and Quantum Gravity*, 31(10):105014, may 2014.

[114] D. V. Martynov et al. Sensitivity of the Advanced LIGO detectors at the beginning of gravitational wave astronomy. *Phys. Rev. D*, 93:112004, Jun 2016.

[115] Bas Swinkels, Enrico Campagna, Gabriele Vajente, Lisa Barsotti, and Matt Evans. Longitudinal noise subtraction: the alpha-, beta- and gamma-technique. *VIR-0050A-08*, 06 2008.

[116] F. Acernese et al. Performances of the Virgo interferometer longitudinal control system. *Astroparticle Physics*, 33(2):75–80, 2010.

[117] R.W.P. Drever, John Hall, F. Kowalski, James Hough, G.M. Ford, A.J. Munley, and Hywel Ward. Laser phase and frequency stabilization using an optical resonator. *Appl. Phys. B*, 31:97–105, 06 1983.

[118] Brian J. Meers and Kenneth A. Strain. Modulation, signal, and quantum noise in interferometers. *Phys. Rev. A*, 44:4693–4703, Oct 1991.

[119] S Hild, H Grote, J Degallaix, S Chelkowski, K Danzmann, A Freise, M Hewitson, J Hough, H Lück, M Prijatelj, K A Strain, J R Smith, and B Willke. DC-readout of a signal-recycled gravitational wave detector. *Classical and Quantum Gravity*, 26(5):055012, feb 2009.

[120] Fausto Acernese et al. Control of the laser frequency of the Virgo gravitational wave interferometer with an in-loop relative frequency stability of 1.0 × 1021 on a 100 ms time scale. In *2009 IEEE International Frequency Control Symposium Joint with the 22nd European Frequency and Time forum*, pages 760 – 763, 05 2009.

[121] François Bondu, A Brillet, F Cleva, H Heitmann, M Loupias, and Catherine Man. The Virgo injection system. *Class. Quantum Grav*, 19:1829–1833, 04 2002.

[122] Daniel D. Brown, Philip Jones, Samuel Rowlinson, Sean Leavey, Anna C. Green, Daniel Töyrä, and Andreas Freise. Pykat: Python package for modelling precision optical interferometers. *SoftwareX*, 12:100613, 2020.

[123] Daniel David Brown and Andreas Freise. Finesse. `http://www.gwoptics.org/finesse`, May 2014. You can download the binaries and source code at `http://www.gwoptics.org/finesse`.

[124] Rik Pintelon and Johan Schoukens. *System identification: a frequency domain approach*. John Wiley & Sons, 2012.

[125] Gerhard Heinzel, Albrecht Rüdiger, and R Schilling. Spectrum and spectral density estimation by the Discrete Fourier transform (DFT), including a comprehensive list of window functions and some new flat-top windows. *Public technical note*, 12, 01 2002.

[126] M. Rakhmanov, Joseph Romano, and J. Whelan. High-frequency corrections to the detector response and their effect on searches for gravitational waves. *Classical and Quantum Gravity*, 25, 09 2008.

[127] Daniel D. Brown. Interactions of light and mirrors: advanced techniques for modelling future gravitational wave detectors. *PhD Thesis*, 2016.

[128] B. Abbott, R. Abbott, T. Abbott, Matthew Abernathy, F. Acernese, K. Ackley, C. Adams, Teneisha Adams, Paolo Addesso, R. Adhikari, V. Adya, C. Affeldt, M. Agathos, Kazuhiro Agatsuma, Nancy Aggarwal, Odylio Aguiar, L. Aiello, Anirban Ain, P. Ajith, and John Zweizig. Prospects for observing and localizing gravitational-wave transients with Advanced LIGO, Advanced Virgo and KAGRA. *Living Reviews in Relativity*, 21, 12 2018.

[129] Annalisa Allocca, Diego Bersanetti, Julia Casanueva Diaz, Camilla De Rossi, Maddalena Mantovani, Alain Masserot, Loïc Rolland, Paolo Ruggi, Bas Swinkels, Enzo Nicolas Tapia San Martin, Marco Vardaro, and Michal Was. Interferometer sensing and control for the Advanced Virgo experiment in the O3 scientific run. *Galaxies*, 8(4), 2020.

[130] Kiwamu Izumi. *Multi-Color Interferometry for Lock Acquisition of Laser Interferometric Gravitational-wave Detectors*. PhD thesis, Tokyo U., 2012.

[131] Enzo Evers, Robbert Voorhoeve, and Tom Oomen. On frequency response function identification for advanced motion control. pages 1–6, 09 2020.

[132] Rik Pintelon and Johan Schoukens. System identification: A frequency domain approach. 2012.

[133] Lennart Ljung. *System Identification (2nd Ed.): Theory for the User*. Prentice Hall PTR, USA, 1999.

[134] Lennart Ljung. *System Identification: Theory for the User*. Prentice-Hall, Inc., USA, 1986.

[135] M. Deistler. System Identification T. Söderström and P. Stoica Prentice Hall International, 1989. *Econometric Theory*, 10(3-4):813–815, 1994.

[136] Paul M.J. Van Den Hof and Ruud J.P. Schrama. An indirect method for transfer function estimation from closed loop data. *Automatica*, 29(6):1523–1527, 1993.

[137] P. Ruggi and E. Majorana. Virgo logbook entry 49674, 2020.

[138] B. Swinkels, E. Campagna, G. Vajente, L. Barsotti and M. Evans. Longitudinal noise subtraction: the alpha-, beta- and gamma-technique. VIR-0050A-08 URL: `https://tds.virgo-gw.eu/ql/?c=2055`, 6 2008.

[139] C. Wipf. Noise budgeting for advanced detectors. LIGO Technical Report LIGO-G1400587, Laser Interferometer Gravitational-Wave Observatory, 2014.

[140] LIGO Scientific Collaboration. GWINC (Gravitational Wave Interferometer Noise Calculator). `https://git.ligo.org/gwinc`. Accessed on 2024-04-01.

[141] The MathWorks Inc. Matlab version: 9.13.0 (r2022b), 2022.

[142] Paul Lagabbe. *Improving the Advanced Virgo+ calibration with the photon calibrator for the 04 run.* PhD thesis, Laboratoire d'Annecy de Physique des Particules, France, Annecy, LAPP, 2023.

[143] M. Tringali, I. Fiori, F. Paoletti, A. Chincarini, P. Spinicelli, C. Miritescu, A. Romero, M. Lalleman, O. Nauwelaers. Environmental report - (Virgo week). VIR-0991A-23 URL: `https://tds.virgo-gw.eu/ql/?c=19862`, 11 2023.

[144] M. Tringali, I. Fiori, F. Paoletti, G. Quéméner, A. Chincarini, F. Bucci, C. Miritescu, F. Carbognani, R. Poulton, R. De Rosa. Magnetic injections: overview and plans (Commissioning meeting). VIR-0300A-24 URL: `https://tds.virgo-gw.eu/ql/?c=20360`, 3 2024.

[145] M.C. Tringali, A. Chincarini, B. D'Angelo, R.DeRosa, I. Fiori, C. Miritescu, F. Paoletti, G. Quemener. Near field sweep magnetic injections - an update. VIR-0584A-23 URL: `https://tds.virgo-gw.eu/ql/?c=19455`, 6 2023.

[146] F. Acernese et al. Calibration of advanced virgo and reconstruction of the gravitational wave signal $h(t)$ during the observing run O2. *Classical and Quantum Gravity*, 35(20):205004, 2018.

[147] B. P. Abbott et al. GW170817: Observation of gravitational waves from a binary neutron star inspiral. *Phys. Rev. Lett.*, 119:161101, Oct 2017.

[148] T. Akutsu et al. KAGRA: 2.5 Generation Interferometric Gravitational Wave Detector. *Nature Astron.*, 3(1):35–40, 2019.

[149] B Willke et al. The GEO 600 gravitational wave detector. *Classical and Quantum Gravity*, 19(7):1377, mar 2002.

[150] F. Acernese et al. Increasing the astrophysical reach of the Advanced Virgo detector via the application of squeezed vacuum states of light. *Phys. Rev. Lett.*, 123:231108, Dec 2019.

[151] M. Tse et al. Quantum-enhanced Advanced LIGO detectors in the era of gravitational-wave astronomy. *Phys. Rev. Lett.*, 123:231107, Dec 2019.

[152] Haocun Yu, L. McCuller, Mhyrrah Tse, Lorenzo Barsotti, N. Mavalvala, J. Betzwieser, C. Blair, S. Dwyer, A. Effler, M. Evans, A. Fernandez-Galiana, P. Fritschel, V. Frolov, N. Kijbunchoo, Fabrice Matichard, David McClelland, T. McRae, A. Mullavey, and D. Sigg. Quantum correlations between the light and kilogram-mass mirrors of LIGO. *Nature*, 02 2020.

[153] W. Heisenberg. *Über den anschaulichen Inhalt der quantentheoretischen Kinematik und Mechanik*, pages 478–504. Springer Berlin Heidelberg, Berlin, Heidelberg, 1985.

[154] H. J. Kimble, Yuri Levin, Andrey B. Matsko, Kip S. Thorne, and Sergey P. Vyatchanin. Conversion of conventional gravitational-wave interferometers into quantum nondemolition interferometers by modifying their input and/or output optics. *Phys. Rev. D*, 65:022002, Dec 2001.

[155] D. Ganapathy et al. Broadband quantum enhancement of the LIGO detectors with frequency-dependent squeezing. *Phys. Rev. X*, 13:041021, Oct 2023.

[156] F. Acernese et al. Frequency-dependent squeezed vacuum source for the Advanced Virgo gravitational-wave detector. *Phys. Rev. Lett.*, 131:041403, Jul 2023.

[157] Graham C. Goodwin, Stefan F. Graebe, and Mario E. Salgado. *Control System Design*. Prentice Hall PTR, USA, 1st edition, 2000.

[158] Katsuhiko Ogata. *Modern Control Engineering*. Prentice Hall PTR, USA, 4th edition, 2001.

[159] Alessandra Buonanno and Yanbei Chen. Quantum noise in second generation, signal-recycled laser interferometric gravitational-wave detectors. *Phys. Rev. D*, 64:042006, Jul 2001.

[160] Stefan L. Danilishin and Farid Ya. Khalili. Quantum Measurement Theory in Gravitational-Wave Detectors. *Living Rev. Rel.*, 15:5, 2012.

[161] Carlton M. Caves. Quantum-mechanical radiation-pressure fluctuations in an interferometer. *Phys. Rev. Lett.*, 45:75–79, Jul 1980.

[162] Moritz Mehmet and Henning Vahlbruch. The squeezed light source for the Advanced Virgo detector in the observation run O3. *Galaxies*, (4), 2020.

[163] Marc Eisenmann. *Use of squeezed states of light for the reduction of quantum noise in Advanced Virgo*. PhD thesis, Université Savoie Mont Blanc, November 2020.

[164] P. Kwee, J. Miller, T. Isogai, L. Barsotti, and M. Evans. Decoherence and degradation of squeezed states in quantum filter cavities. *Phys. Rev. D*, 90:062006, Sep 2014.

[165] Robert W. Boyd. Chapter 1 - the nonlinear optical susceptibility. In Robert W. Boyd, editor, *Nonlinear Optics (Third Edition)*, pages 1–67. Academic Press, Burlington, third edition edition, 2008.

[166] E. N. Tapia San Martín, M Valentini, D Bersanetti, M Was, R Maggiore, M van Dael, J W Perry, B L Swinkels, M Mantovani, A Freise, and M Tacca. A MIMO approach for longitudinal sensing and control noise projections of Advanced Virgo gravitational wave detector. *Classical and Quantum Gravity*, 40(18):185008, aug 2023.

[167] Jing Pei and Jerry R. Newsome. Robust stability analysis of the space launch system control design: A singular value approach. 2015.

[168] D. F. Walls. Squeezed states of light. *Nature*, 306:141–146, 1983.

[169] Carlton M. Caves. Quantum-mechanical noise in an interferometer. *Phys. Rev. D*, 23:1693–1708, Apr 1981.

[170] *Quantum Models of Light*, chapter 4, pages 93–137. John Wiley & Sons, Ltd.

[171] S. Gras et al. Audio-band coating thermal noise measurement for Advanced LIGO with a multimode optical resonator. *Phys. Rev.*, 2017.

[172] S. Gras and M. Evans. Direct measurement of coating thermal noise in optical resonators. *Phys. Rev.*, 2018.

[173] J. V van Heijningen, A. Bertolini, E. Hennes, M. G. Beker, M. Doets, H. J. Bulten, K. Agatsuma, T. Sekiguchi, and J. F J. Van Den Brand. A multistage vibration isolation system for Advanced Virgo suspended optical benches. *Class. Quant. Grav.*, 36(7):075007, 2019.